NESDIS

GOES & POES

Geostationary Operational Environmental Satellite

Polar-orbiting Operational Environmental Satellite

Programs

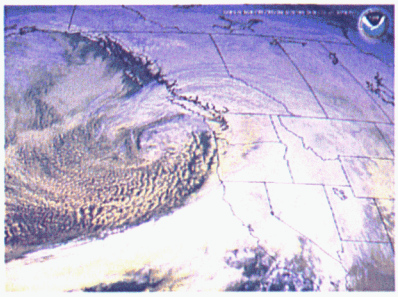

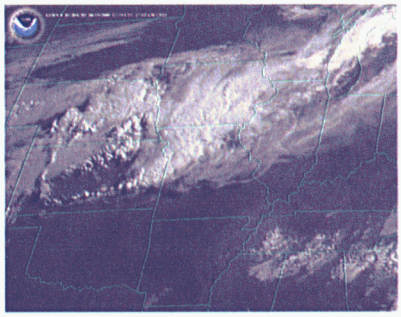

Papers prepared for the 82nd Annual Meeting of the American Meteorological Society

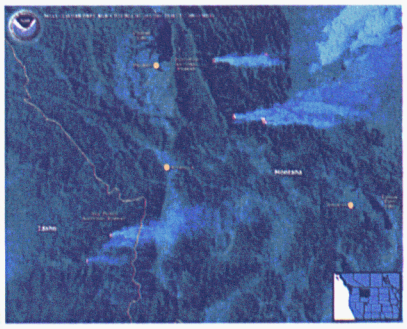

Orlando, Florida
January 13-17, 2001

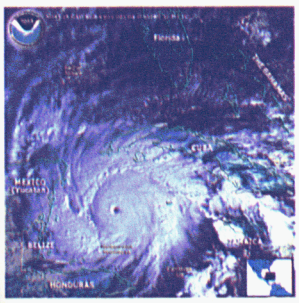

QC
879.4
.A44
2002

Table of Contents

Conference		Page
	1. Introduction	1
2.1 (IIPS)	An Overview of the Initial Joint Polar-orbiting System (IJPS) and Its Impact on the NOAA/NESDIS POES Program Diane Holmes, Stacy L. Bunin, and H. James Silva	2
2.2 (IIPS)	An Overview Of the NOAA/NESDIS Product Processing ~~Plans For The Initial Joint Polar~~ System Era Stacy L. Bunin, Diane Holmes, and Pamela M. Taylor	5
2.3 (IIPS)	NOAA'S GOES Satellite Program - Status And Plans Gerald J. Dittberner	8
2.4 (IIPS)	NOAA Polar Instrument Data Generation For Level 1B Use Arlington R. Morgan and Emily D. Harrod	11
2.5 (IIPS)	Recent Developments In QuikSCAT Near-Real-Time Processing at NOAA/NESDIS Jeffrey M. Augenbaum and Raymond W. Luczak, and Gene Legg	14
2.6 (IIPS)	Evolution of NANOOK, the NOAA/NESDIS Near-Real-Time MODIS Processing System Paul Haggerty, Kristina Sprietzer, Gene Legg, and Ray Luczak	17
J3.10 (IIPS)	AWIPS for Satellite-Derived Hydrometeorological Applications Roderick A. Scofield, Robert J. Kuligowski, Shuang Qiu, and Clay Davenport	20
P1.3 (IIPS)	NESDIS IPD Model for Developing Production Monitoring Software Richard Kelley	23
P1.16 (IIPS)	Applications of NOAA MODIS Near-Real-Time Data Kristina Sprietzer, Paul Haggerty, Gene Legg, Ray Luczak	24
3.11 (IOS)	GOES Users' Conference Recommendations For The Advanced Baseline Imager And Sounder James J. Gurka, Gerald J. Dittberner, and Timothy J. Schmit, NOAA/NESDIS	25
4.3 (IOS)	A Comparison Of GOES and AMSU Based Total Precipitable Water Retrievals Jaime Daniels and Ralph Ferraro	29
2.2 (HYDRO)	Status And Outlook Of Operational Satellite Precipitation Algorithms For Extreme Precipitation Events Roderick A. Scofield and Robert J. Kuligowski	31
P2.4 (HYDRO)	Satellite Rainfall Estimation Over South America: Evaluation Of Two Major Events Daniel A. Vila, Roderick A. Scofield, and J. Clay Davenport	36
3.10 (HYDRO)	Error Analysis Of Microwave Land Rainfall Estimation Algorithms Jeffrey R. McCollum and Ralph R. Ferraro	40
3.11 (HYDRO)	A Comparison Of Total Precipitable Water Observations From Satellite And Reanalysis Climatologies Ralph Ferraro and Arnold Gruber	43

LIBRARY
JUL 17 2003
National Oceanic &
Atmospheric Administration
U.S. Dept. of Commerce

National Oceanic and Atmospheric Administration
TIROS Satellites and Satellite Meteorology

ERRATA NOTICE

One or more conditions of the original document may affect the quality of the image, such as:

Discolored pages
Faded or light ink
Binding intrudes into the text

This has been a co-operative project between the NOAA Central Library and the Climate Database Modernization Program, National Climate Data Center (NCDC). To view the original document contact the NOAA Central Library in Silver Spring, MD at (301) 713-2607 x124 or Library.Reference@noaa.gov.

HOV Services
Imaging Contractor
12200 Kiln Court
Beltsville, MD 20704-1387
January 26, 2009

3.13 (HYDRO)	Incorporating Numerical Weather Prediction Model Parameters into the Retrieval of Precipitation from the Special Sensor Microwave/Imager Robert J. Kuligowski, Wanchun Chen, Ralph R. Ferraro, and Russ Treadon	45
P1.4 (OBSERV)	Improving The Incoproration Of Polar Satellite Passive Microwave Precipitation Estimates into the NCEP Global Data Assimilation System Robert J. Kuligowski, Russ Treadon, Wanchun Chen, and Ralph R. Ferraro	47
1.2 (SATMET)	An Overview of Active Fire Detection and Monitoring Using Meteorological Satellites Elaine M. Prins, Joleen M. Feltz, Chris C. Schmidt	49
P1.13 (SATMET)	A Comparison of the GOES-8 ABBA and INPE AVHRR Fire Products for South America From 1995-2000 Joleen M. Feltz, Elaine M. Prins, and Alberto W. Setzer	57
P1.14 (SATMET)	Principal Component Image Analysis of MODIS for Volcanic Ash Donald W. Hillger and James Clark	61
P 1.15 (SATMET)	Loss of the 12.0 mm "Split Window" Band on GOES-M: Impacts on Volcanic Ash Detection Gary P. Ellrod	67
P3.10 (SATMET)	Assimilation of GOES Sounder Cloud Top Pressure in NCEP's 48km ETA Mesoscale Model James A. Jung, Robert M. Aune, Timothy J. Schmit, and Tom H. Zapotocny	71
P3.29 (SATMET)	Cloud-Drift and Water Vapor Winds in the Polar Regions from MODIS Jeffrey R. Key, David Santek, Christopher S. Velden, and W. Paul Menzel	75
P3.37 (SATMET)	A Validation Study of the GOES Sounder Cloud Top Pressure Product James A. Hawkinson, Wayne Feltz, Timothy J. Schmit, Anthony J. Schreiner, and Steven A. Ackerman	79
P3.38 (SATMET)	Is the Resolution of GOES Sounder Data Sufficient to Support Single Field of View Retrievals and Derived Products? Gail M. Bayler, Suzanne Wetzel Seemann, Jun Li, and Timothy J. Schmit	82
P3.40 (SATMET)	An Evaluation of Several Years of CIMSS and NESDIS GOES Sounder Data James P. Nelson III, Timothy J. Schmit, and W. Paul Menzel	86
P3.47 (SATMET)	The NESDIS Satellite QPE Verification Program Robert J. Kuligowski, Shuang Qiu, Roderick Scofield, and Arnold Gruber	90
P3.51 (SATMET)	Validation of GOES-11 Data Xiangqian Wu and Timothy J. Schmit	92
P3.60 (SATMET)	Derived Cloud Products from the GOES-M Imager Anthony J. Schreiner and Timothy J. Schmit	96
P4.2 (SATMET)	Intercalibration of Geostationary and Polar-orbiting Infrared Window and Water Vapor Radiances Mathew M. Gunshor, Timothy J. Schmit, and W. Paul Menzel	100

P4.20 (SATMET)	Validation of GOES and MODIS Atmospheric Products and Radiances Using Department of Energy Atmospheric Radiation (DOE ARM) Measurement Data Wayne F. Feltz, Timothy J. Schmit, Jim Hawkinson, David Tobin, and Suzanne Wetzel-Seeman	104
P5.5 (SATMET)	Channel Selection for the Next Generation Geostationary Advanced Imagers Timothy J. Schmit, W. Paul Menzel, Mathew M. Gunshor, and James P. Nelson III	107
P5.23 (SATMET)	Simulation of GOES-M 5-Band Imager Using MODIS Data for Volcanic Ash Donald W. Hillger and James Clark	111
P5.35 (SATMET)	NOAA/NESDIS Operational Advanced-TOVS (ATOVS) Polar Orbiter Sounding Products Anthony L. Reale and Americo S. Allegrino	115
P5.38 (SATMET)	Retrieval of Atmospheric Inversions Using Geostationary High-Spectral-Resolution Sounder Radiance Information Jun Li, Timothy J. Schmit, Hung-Lung Huang, and Harold M. Woolf	119
	A Method for Correlated Noise Modeling in Satellite Radiance Simulation Thomas J. Kleespies and David Crosby	122
	An Impact Study of Five Remotely Sensed and Five In-situ Data Types in the ETA Data Assimilation System Tom H. Zapotocny, W. Paul Menzel, James P. Nelson III, and James A. Jung	125
	5. NOAA/NESDIS GOES and POES Product Web Sites	129

Introduction

This document is a compendium of papers prepared for several conferences at the American Meteorological Society's 82nd annual meeting, held 13-17 January 2002 in Orlando, Florida. The conferences included in this compendium are: the 18th International Conference on Interactive Information and Processing Systems (IIPS) for Meteorology, Oceanography, and Hydrology, the 16th Conference on Hydrology, the 6th Symposium on Integrated Observing Systems, the Symposium on Observations, Data Assimilation, and Probabilistic Prediction, and the Interactive Symposium on the Advanced Weather Interactive Processing System (AWIPS). In addition, papers are included from the 11th Conference on Satellite Meteorology and Oceanography, held 15-18 October 2001 in Madison, Wisconsin.

The papers within this compendium are directly related to the NOAA/NESDIS GOES and Polar Programs. This document has been prepared by the National Environmental Satellite, Data, and Information Service for distribution to the meteorological community and other interested individuals and organizations. Readers are authorized and encouraged to further distribute this information within their organizations. Use of any material within this document should be appropriately referenced.

On the cover:

All significant event images are courtesy of NOAA/NESDIS.

1. A storm over the West Coast spread snow through the mountains of Washington, Oregon, and northern California. This GOES-10 image showing the storm is from November 28, 2001.
   http://www.osei.noaa.gov/Events/Storms/US_Northwest/STMusNW332_G10.jpg

2. Severe thunderstorms produced tornadoes over Missouri. This GOES-8 image is from June 19, 2001.
   http://www.osei.noaa.gov/Events/Severe/US_Midwest/SVRusMW170_G8.jpg

3. Heat signatures (red) and smoke (light blue haze) are visible from fires burning in Montana and Idaho. This image was generated from NOAA-12 on October 1, 2001.
   http://www.osei.noaa.gov/Events/Fires/US_Northwest/FSMHSusMT275_N2.jpg

4. Hurricane Michelle was located over the Caribbean Sea on November 3, 2001, with winds estimated at 110 knots and gusts to 135 knots. This image was generated from NOAA-15 data.
   http://www.osei.noaa.gov/Events/Tropical/Atlantic/TRCmichelle307_N5.jpg

2.1 AN OVERVIEW OF THE INITIAL JOINT POLAR-ORBITING SYSTEM (IJPS) AND ITS IMPACT ON THE NOAA/NESDIS POES PROGRAM

Diane Holmes* and Stacy L. Bunin
Mitretek Systems, Inc., Falls Church, Virginia

H. James Silva
NOAA/NESDIS, Washington, D.C

1. INTRODUCTION

The overall mission objectives of the Polar-orbiting Operational Environmental Satellite (POES) system are to provide continuous daily global observations of weather patterns and environmental measurements of the Earth's atmosphere, its surface and cloud cover, and the proton and electron flux at satellite altitude. To fulfill these mission objectives, the National Environmental Satellite, Data, and Information Service (NESDIS), part of the National Oceanic and Atmospheric Administration (NOAA), has operated the current POES system since 1978, with a two satellite constellation in circular, near-polar, sun synchronous morning (7:30AM) and afternoon (2:00PM) orbits. However, the POES program is undergoing a transformation. The POES system is transitioning to the Initial Joint Polar-orbiting System (IJPS). IJPS will be a means for sharing polar satellite assets between the US and Europe.

IJPS is a cooperative effort between the United States and the Europeans to share responsibility for polar satellite operations and derived products. The details of IJPS can be found in The Agreement Between the United States National Oceanic and Atmospheric Administration and the European Organization for the Exploitation of Meteorological Satellites on an Initial Polar-orbiting Operational Satellite System, signed in November 1998. IJPS will be supported by US satellites, NOAA-N and -N', in the afternoon orbit and European satellites, MetOp-1 and -2, in the mid-morning orbit. As part of the IJPS agreement, NOAA and EUMETSAT are required to support each other's operational satellite through their respective ground segments for commanding, receiving telemetry and global data, monitoring their respective on-orbit status, and exchanging data between the two polar satellite systems. In order to meet the requirements of IJPS, the NOAA Polar Ground System is undergoing numerous changes. This paper provides an overview of several elements of IJPS with a focus on the changes to and the benefits of IJPS on the NOAA Polar Ground System.

* *Corresponding author address*: Diane Holmes, Mitretek Systems; 3150 Fairview Park Drive South; Fall Church, Virginia 22042; e-mail: DHolmes@Mitretek.org.

2. CURRENT STATUS/PLANS

NOAA currently operates a morning and an afternoon polar-orbiting series of weather satellites as part of the POES program. In the current series, NOAA-15 and NOAA-16 are the morning and afternoon satellites, respectively, and NOAA-M is planned for launch in March 2002 into a mid-morning orbit (10:00AM). A follow-on satellite series, NOAA-N and -N', are scheduled for launch in June 2004 and March 2008. NOAA monitors each satellite's orbit, health and safety data, and also provides direct readout and stored instrument science data to users.

MetOp-1 is scheduled for launch in 2005. Once it is declared operational in 2006, the MetOp satellite will assume the mid-morning orbit. EUMETSAT will be responsible for operating the MetOp-1 satellite as well as distributing the environmental data to its members. As part of the IJPS agreement, NOAA will receive environmental data from the common set of instruments carried on both the NOAA and MetOp satellites as well as the data from the MetOp unique instruments.

3. POES GROUND SYSTEM

The current POES ground system includes the following elements:

- Satellite Operations including:
  - CDA-Command and Data Acquisition Station (Fairbanks, AK and Wallops, VA)
  - SOCC- Satellite Operations Control Center (Suitland MD)
- Information Processing Systems including:
  - CEMSCS- Central Environmental Meteorological Satellite Computer System Suitland, MD
- Product Generation and Distribution
- Archive including:
  - NCDC- National Climatic Data Center, Asheville, North Carolina,
  - NODC- National Oceanographic Data Center, Silver Spring, Maryland
  - SAA- Satellite Active Archive, Suitland, MD

Satellite health and safety and instrument science data are received at the CDAs and then transmitted to the SOCC via a DOMSAT link. The SOCC processes

satellite health and safety data and sends instrument science data to the CEMSCS for information/product processing. The CEMSCS ingests the Level 0 data and processes it to NOAA Level 1b data sets (raw instrument data with ancillary data appended). The Level 1b data sets are then accessed by numerous product processing systems for environmental product generation (NOAA Levels 2 and 3) and near real-time distribution to users. Level 1b and selected products are available via the SAA. All NOAA Level 1b and operational data sets are transmitted to the NOAA data centers for long term archiving and distribution.

NOAA's participation in IJPS will require upgrades to the existing POES ground system due to the differences between the POES and MetOp satellites and the new interface requirements. These upgrades will address new instruments, new operating modes, and new technologies which are part of IJPS.

3.1 Instruments

During IJPS, NOAA-N and -N' and MetOp-1 and –2 will carry a common set of core instruments. These instruments include: AVHRR/3, HIRS/4, AMSU-A, MHS, SEM/2, SARSAT, and DCS. In addition to the core instruments, each satellite will carry instruments unique to its mission. For the NOAA satellites, the unique instrument is the SBUV/2. The MetOp-unique instruments are:

- Infrared Atmospheric Sounding Interferometer (IASI) which will retrieve high resolution atmospheric profiles of temperature and humidity with its 8461 channels
- Global Ozone Monitoring Experiment (GOME) which is an ozone profiler and total ozone measurement instrument
- Global Navigation Satellite System Receiver for Atmospheric Sounding (GRAS) which is a GPS type atmospheric sounding system
- Advanced Scatterometer (ASCAT) which is an instrument for measuring sea surface wind speed and direction.

Additionally, the MetOp spacecraft will have the capability to record full resolution 1km global data from the AVHRR/3. NOAA will continue to provide 4km global data from the AVHRR/3 throughout IJPS.

The common and unique instruments will require changes/upgrades to polar ground systems throughout NESDIS. The POES ground system will have the ability to control all instruments on the POES satellites, regardless of origin, to maintain the safety of the instrument and satellite as well as ensure that the common set of environmental instruments continue to collect and provide meteorological data. Modifications to current product processing systems will accommodate the changes associated with processing of satellite instrument data from the NOAA instruments on the MetOp satellite as well as the four MetOp-unique instruments. New algorithms will be developed for the MetOp-unique instruments so that data from these instruments can be used to produce new and improved products. Upgrades to NCDC, NODC, and SAA are required to support the increased data volume associated with MetOp 1km AVHRR and products from the four new MetOp instruments.

3.2 Satellite Operations

Via the SOCC and CDAs, the POES ground system will have the ability to command, control, and receive data from both the NOAA and MetOp satellites. Similarly, EUMETSAT will have the capability to support the MetOp and NOAA satellites from a control center in Darmstadt, Germany and a CDA station in Svalbard, Norway. At each control center, an interface will be established as a single point of entry through which all environmental data, health and safety data for satellites and instruments, satellite commands, and general voice communications will pass.

During IJPS, NOAA and EUMETSAT will provide cross-support during various operating scenarios. Two such scenarios are blind orbit and contingency operations.

Blind Orbit Support: Until IJPS is implemented, data acquired during POES blind orbits, i.e. orbits in which the satellite is not visible from the Fairbanks or Wallops CDA stations, is stored on the satellite and retrieved on the next visible pass. This results in the data not meeting the timeliness requirements established by the user community. To meet the user timeliness requirements, Level 2 products must be made available within 3 hours of observation. During IJPS, data from POES blind orbits will be retrieved at Svalbard and forwarded through Darmstadt to NOAA for processing. This blind orbit support will allow NOAA access to data from all orbits in near real-time thereby meeting the user timeliness requirements.

Contingency Support: During the IJPS era, the NOAA and EUMETSAT ground systems will have the capability to support each other's satellites in the event of an emergency or other contingency situations. In the case of contingency support for NOAA, health and safety data from the satellite/instruments as well as the environmental data will be downlinked to Svalbard and forwarded through Darmstadt to Suitland. The system will also allow NOAA to forward commands through the EUMETSAT ground system for transmission to the POES satellites via the Svalbard CDA. Similar capability will exist within the POES ground system to support MetOp satellites via the Fairbanks CDA.

While NOAA will benefit from having this virtual extension of its ground system, numerous upgrades are planned at the Fairbanks CDA and at SOCC to support the IJPS operations. Defining the upgrades to individual processing systems and supporting infrastructure is beyond the scope of this paper. However, at a minimum, the following functionality will be added to the POES ground system:

- Ability to receive, archive, and distribute to EUMETSAT all health and safety telemetry and global environmental data from the MetOp satellite;
- Ability to receive commands from EUMETSAT and transmit them to the MetOp satellite;
- Ability to receive, process, and distribute products derived from MetOp HRPT.

3.3 IJPS Technologies

IJPS will introduce several new technological advancements to the current POES ground system. While many of these advancements will be incorporated into the POES ground system for use during IJPS, many will be used in parallel with POES existing systems. These advancements include the following:

Pipeline Processing: Data will be delivered in pipeline mode to NOAA from EUMETSAT, which means data will be delivered in a constant flow as opposed to the current "burst" delivery method. Currently, POES data is received and stored at the CDA until all data for the pass has been downlinked. The data is then packaged together and "burst" back to SOCC. NESDIS will integrate pipeline processing into the POES ground system, providing the capability for processing NOAA data in the same mode.

Pipeline processing requires less bandwidth to transfer an equal amount of data. However, it is a much slower transfer process. To meet data timeliness requirements, the Svalbard CDA will begin to transfer the data almost immediately upon its receipt. Additionally, processing of the data will begin almost immediately upon its receipt at NOAA. MetOp data will arrive at the NESDIS ingestor in granules, or small subsets, of the orbit. Level 1 data will be produced in pipeline format to allow for the simultaneous processing of each granule to meet dataset timeliness requirements. The polar product processing systems will also process the Level 1 data into Level 2 products via a pipeline format in order to meet user timeliness requirements.

X-Band frequency data reception: Throughout IJPS, POES satellites will maintain S-band uplink and S- and L- band downlink capability. However, the MetOp satellites require X-band for downlinking data from the satellites. X-band downlink is required to accommodate the high rate unique instruments on the MetOp satellites, e.g. IASI.

X-band provides a much greater downlink capacity than L-band, yielding more data in the acquisition window. More data offers the potential to produce new and improved products.

CCSDS data format: MetOp data will utilize the Consultative Committee for Space Data Systems (CCSDS) standards. CCSDS is a communication protocol, optimized for satellite to ground communications. The CCSDS data format creates frames of fixed size, which are compatible with a forward error correction system. This system adds specially coded bits to each frame, which allows the ground system to identify errors in the data.

Creating parallel systems for processing X-band and CCSDS data formats will allow operators and engineers to expand their technical breadth and gain operating experience, which may reduce operational risks as NOAA moves into the next phase of Polar satellites, the National Polar-orbiting Operational Environmental Satellite System (NPOESS).

4. CONCLUSION

Activities are ongoing at NOAA to define and develop changes to the POES ground system that will allow NOAA to continue to meet its mission objectives and support the terms of the IJPS agreement. To ensure that NOAA is prepared to support IJPS operations, all upgrades, including a new communications system, archiving system, and data processing system, must be designed, integrated, and tested prior to the launch of MetOp-1.

IJPS will provide significantly improved operational capabilities and benefits to satellite heath and safety through the elimination of blind orbits and additional support during contingency situations. NOAA's participation in IJPS will form the baseline for future planned national and international Polar programs and ensures continuous support to a variety of users.

Additional IJPS information is available at the IJPS website: http://discovery.osd.noaa.gov/ijps/

REFERENCES

Mignogno, M. and J. Silva: *POES Program Status and NOAA Participation in the Initial Joint Polar Satellite System,* prepared for the MAXI Review 2001, September 18-20, 2001.

Silva, J. and L. A. Deem. *Transitioning the Polar-orbiting Operational Satellite Program to the New Millennium with Participation in the Initial Joint Polar-orbiting Operational Satellite System*, Preprints 14th IIPS, Phoenix, AZ, Amer. Meteor. Soc., paper 3.16.

Bunin, S. L., D. Holmes, and P. M. Taylor: *An Overview of the NOAA/NESDIS Product Processing Plans for the Initial Joint Polar System Era*, Preprints 18th IIPS, Orlando, FL, Amer. Meteor. Soc., paper 2.2.

Polar Operational Environmental Satellite Ground Segment Upgrade Description & Requirements for Initial Joint Polar Satellite System (RDN5), Version 1a, May 2000.

IJPS website: http://discovery.osd.noaa.gov/ijps/.

2.2 AN OVERVIEW OF THE NOAA/NESDIS PRODUCT PROCESSING PLANS FOR THE INITIAL JOINT POLAR SYSTEM ERA

Stacy L. Bunin* and Diane Holmes
Mitretek Systems, Inc., Falls Church, Virginia

Pamela M. Taylor
NOAA/NESDIS, Washington, D.C

1. INTRODUCTION

The National Oceanic and Atmospheric Administration (NOAA) and the European Organization for the Exploitation of Meteorological Satellites (EUMETSAT) signed a Memorandum of Agreement in November of 1998 for participation in the Initial Joint Polar System (IJPS). IJPS is a cooperative effort between the United States and the Europeans to share responsibility for environmental polar satellite operations and to provide the continuity of observations from polar-orbiting satellites for operational meteorological and environmental objectives.

IJPS consists of two independent, but fully coordinated, environmental polar-orbiting satellite systems. In support of IJPS, NOAA satellites NOAA-N and -N' will be flown in a polar orbit with an afternoon (2:00 PM) equatorial crossing time. The National Environmental Satellite, Data, and Information Service (NESDIS) will continue to operate these afternoon operational NOAA satellites, as well as generate, distribute, and archive an extensive suite of environmental products. EUMETSAT, working together with the European Space Agency (ESA), will develop the Meteorological Operational (MetOp) series of satellites to be flown in a polar orbit with a mid-morning (9:30 AM) equatorial crossing time. The mid-morning and afternoon satellites will each carry a set of common instruments along with additional instruments specific to each orbit and operating agency. Through the use of these satellites, NOAA and EUMETSAT will support the generation of products and services for their respective user communities.

2. CURRENT SATELLITE STATUS AND PLANS

Currently NESDIS has two operational polar-orbiting satellites. NOAA-K, now designated NOAA-15, was launched into an early morning orbit (7:30 AM) in May 1998. NOAA-L, now designated NOAA-16, was launched into an afternoon (2:00 PM) orbit in September 2000. The next satellite in the series, NOAA-M, is scheduled for a March 2002 launch to replace NOAA-15 but will be put into a mid-morning orbit (10:00 AM). NOAA-M's new mid-morning orbit will allow for increased temporal coverage and production of numerous imagery-based products, such as aerosol and vegetation index, currently not available from early morning orbits due to sun angle constraints. The new channel 3a (1.6 micron) added to the NOAA-KLM series for enhanced discrimination between snow/ice and clouds is also optimized in the mid-morning orbit. Additionally, NOAA-M at 10:00 AM allows for a transition to and validation of the NOAA heritage instruments and their derived products scheduled for MetOp-1. The planned launch dates for the NOAA and MetOp satellites during the IJPS era follows:

NOAA-N – June 2004
MetOp-1 – December 2005
NOAA-N' – March 2008
MetOp-2 – August 2010

The first MetOp satellite is planned to become operational in 2006 after an extensive checkout period.

3. IJPS INSTRUMENTS

The core environmental instrument set used for product processing on the NOAA and MetOp satellites in the IJPS era are listed below. In addition, sensors for search and rescue and data collection are also part of the core instrument suite.

- Advanced Microwave Sounding Unit-A (AMSU-A) is a microwave sounder with 15 channels in the 23-90 GHz range. This instrument is used primarily for derivation of temperature soundings along with several surface and hydrological parameters.
- Advanced Very High Resolution Radiometer (AVHRR/3) is an imaging radiometer with six channels (3 visible/near infrared and 3 infrared) in the range of 0.6-12 microns. The MetOp spacecraft will have the capability to record full resolution 1-km global imagery. In addition to imagery this instrument supports the production of numerous ocean, land, and ice parameters along with hazard (fire, volcano) detection and monitoring.
- High Resolution Infrared Radiation Sounder (HIRS/4) is a temperature sounder with 19 infrared channels in the 3-15 micron range, and one visible channel. The HIRS/4 is an upgrade from the HIRS/3 currently orbiting aboard the NOAA-KLM series of satellites. The HIRS/4 has a smaller field of view at 10-km, compared to 20-km on the HIRS/3 model.
- Microwave Humidity Sounder (MHS) is a microwave sounder with five channels at 89, 157, and around 183 GHz supporting production of humidity profiles and other hydrological products.

* *Corresponding author address*: Stacy L. Bunin, Mitretek Systems; 3150 Fairview Park Drive South; Falls Church, Virginia 22042; e-mail: sbunin@mitretek.org.

- Space Environment Monitor (SEM/2) is a multi-channel charged-particle spectrometer.

In addition to the core instruments, the NOAA satellites will also carry:

- Solar Backscatter-Ultraviolet Radiometer (SBUV/2) is a spectral radiometer with 12 channels in the 252.0-322.3 nm in discrete mode and 160-400 nm in scan mode, used for generating ozone profiles.

The MetOp satellites will carry four new instruments:

- Advanced Scatterometer (ASCAT) is a pulsed C-band radar at 5.255 GH, used to generate ocean surface wind products.
- Global Ozone Monitoring Experiment (GOME-2) is a nadir-viewing spectrometer with four channels in the range of 0.240-0.790 microns.
- Global navigation satellite system Receiver for Atmospheric Sounding (GRAS) is a radio occultation receiver that uses signals from the global navigation satellite systems. GRAS will only initially be used by NESDIS for research applications including atmospheric temperature and moisture profiles.
- Infrared Atmospheric Sounding Interferometer (IASI) is a Michelson interferometer covering the 3.6-15.5 micron range. The IASI will be used initially by NESDIS and its users in a demonstration mode to complement the HIRS and AMSU-based soundings. Additional applications for the IASI may include sea surface temperature, clouds, Earth radiation budget, and land measurements.

Data streams from all core instruments, regardless of platform, plus the SBUV/2, will continue to be available at NESDIS in order to continue to meet current and planned Level 1 data and Level 2 product generation, distribution and archive requirements. In addition, access to the data and/or products of the four new MetOp instruments will be supported in order to enhance fulfillment of NESDIS requirements.

4. POLAR PRODUCT PROCESSING

NESDIS produces more than 140 products from NOAA's polar-orbiting satellites in several atmospheric, earth radiation, land, and ocean disciplines. Products are generated on a variety of temporal and geographic scales in support of NOAA's weather forecasting and ocean observation requirements and other domestic and international users.

Products in the IJPS era will become operational with a phased approach after the MetOp launch. Products will be classified as baseline or Day-1 if they are necessary for an operational transition from an older spacecraft (i.e. the NOAA-KLM series). Enhancements, or Day-2 products, are those that require further science validation, system verification development, and/or user evaluation before being deemed operational. In addition, some products will initially be classified as demonstration products while others will be used for research purposes as new applications are developed. NOAA's initial operational, demonstration, and research applications for the IJPS instruments are contained in Table 1.

4.1 *Day-1 Baseline/Operational Products*

Operational products are those that are supported by the NESDIS Office of Satellite Data Processing and Distribution 24 hours per day, 7 days per week in accordance with user product formatting, accuracy, and timeliness requirements. Processing systems will need to be able to process data from the new HIRS/4 and MHS instruments on NOAA-N for continuity of the afternoon mission. In order for the MetOp-1 satellite to replace NOAA-M as the operational morning satellite, keeping the continuity of the morning mission, the products currently generated from the core instruments are required to be generated, distributed, and archived on an operational basis. These include Level 1 and 2 products from AMSU-A, AVHRR/3, HIRS/4, and MHS, and Level 1 products from SEM.

4.2 *Day-2 Enhancements/Operational Products*

These products are generally from the new data streams aboard MetOp due to new instrumentation and enhanced recording capability. While they are not required for operational transition from an older spacecraft, they will be deemed operational on an individual basis as each meets operational status criteria. These products include the global full resolution 1-km AVHRR Level 1 datasets, Level 1 and 2 ASCAT data, IASI Level 1C data, and GOME Level 2 data.

4.3 *Day-2 Enhancements/Demonstration Products*

These products are also from new data streams aboard MetOp but are not required for operational transition. Demonstration products will provide global coverage in a timely manner to selected users for evaluation but will not have support 24 hours per day, 7 days per week nor will be archived. These products include Level 2 products from IASI and Level 2 products based on full resolution 1-km AVHRR data.

4.4 *Day-2 Enhancements/Research Products*

These products are under development and will initially have a research status. They are as a result of new data streams aboard MetOp and include Level 1 and 2 products from GRAS and direct application of Level 1 GOME datasets.

4.5 *Additional Product System Modifications*

In the IJPS era due to data volume and transmission capabilities, MetOp data will arrive at the NESDIS ingestor in granules, or small subsets, of the orbit versus full orbital transmissions from the traditional

NOAA satellites. Level 1 data will be produced in "pipeline" format to allow for the near simultaneous processing of each granule to meet dataset timeliness requirements. The polar product processing systems will also need to process the Level 1 data into Level 2 products via a pipeline format in order to meet user timeliness requirements. Enhanced formatting and distribution capabilities at this suborbital level are being investigated with users to further improve product timeliness while continued orbital formatting may be need for archive continuity.

Table 1. NOAA's Initial Applications for IJPS Instruments

	AMSU-A	AVHRR/3	HIRS/4	MHS	SBUV/2	SEM/2	IASI	ASCAT	GOME-2	GRAS
Aerosols		D1-O								
Atmospheric Moisture				D1-O						R
Atmospheric Temperature	D1-O		D1-O				D			R
Cloud Imagery		D1-O								
Ocean Winds								D2-O		
Ozone			D1-O		D1-O				D2-O	
Precipitation	D1-O	D1-O		D1-O						
Radiation Budget		D1-O	D1-O							
Sea Ice	D1-O	D1-O								
Sea Surface Temperature		D1-O								
Significant Event Imagery		D1-O								
Solar Environment Monitoring						D1-O				
Snow and Ice Cover	D1-O	D1-O								
Vegetation Index		D1-O								

D1-O: Day-1 Operational D2-O: Day-2 Operational D: Demonstration R: Research

5.0 CONCLUSION

Plans are in place to continue generating and distributing operational products, from both morning and afternoon environmental polar-orbiting satellites, with a core set of imagery and sounding instruments. In addition, new instrumentation on the MetOp satellites will give NESDIS users and scientists the opportunity to apply additional datasets to and develop new products for numerous atmospheric, ocean, and land applications.

The NESDIS SATellite PRoducts Overview Display (SATPROD) contains information on the current suite of NESDIS products, satellites and instruments that are involved in creating operational, experimental, and developmental products. SATPROD is available at the following web site:

http://osdacces.nesdis.noaa.gov:8081/satprod/

6.0 REFERENCES

Bunin, S. L., T. B. Passin, P. M. Taylor, and D. G. Gray, 2000: *The NESDIS Satellite Product Overview Display.* Preprints, 16th IIPS, Long Beach, CA, Amer. Meteor. Soc., 447-450.

Holmes, D., S. L. Bunin, and H. J. Silva, 2002: *An Overview of the Initial Joint Polar-orbiting System (IJPS) and its Impact on the NOAA/NESDIS POES Program*, Preprints, 18th IIPS, Orlando, FL, Amer. Meteor. Soc., paper 2.1.

IJPS Web Site: http://discovery.osd.noaa.gov/ijps/

Mignogno, M. and J. Silva, 2001: *POES Program Status and NOAA Participation in the Initial Joint Polar Satellite System,* MAXI Review.

Silva, J. and L. A. Deem, 1998: *Transitioning the Polar-orbiting Operational Satellite Program to the New Millennium with Participation in the Initial Joint Polar-orbiting Operational Satellite System*, Preprints, 14th IIPS, Phoenix, AZ, Amer. Meteor. Soc., 142-145.

Taylor, P. M., and B. A. Banks, 1998: *An Overview of the NOAA/NESDIS Data Processing Systems and Derived Products for NOAA-KLM*, Preprints, 14th IIPS, Phoenix, AZ, Amer. Meteor. Soc., 113-118.

2.3 NOAA'S GOES SATELLITE PROGRAM - STATUS AND PLANS

Gerald J. Dittberner[1]
National Oceanic and Atmospheric Administration (NOAA)
National Environmental Satellite, Data, and Information Service (NESDIS)
Suitland, Maryland

1. INTRODUCTION

The GOES mission is to maintain a continuous stream of data from two Geostationary environmental operational satellites. To satisfy this mission, the National Oceanic and Atmospheric Administration (NOAA) maintains operational satellites at the GOES-West position (GOES-10 at 135°W) and at the GOES-East position (GOES-8 at 75°W). Because the GOES Program competes in the United States' commercial launch services market, positions in the launch queue must be secured with typical lead times of 12 to 15 months. To reduce the risk of a break in service, NOAA uses the on-orbit spare concept. For example, NOAA launched GOES-10 as an on-orbit spare and on July 21, 1998, GOES-10 replaced GOES-9 as the operational GOES-West satellite when GOES-9 showed signs of imminent failure.

2. THE CURRENT SERIES: GOES-8, GOES-9, GOES-10, GOES-11, and GOES-M

The present GOES constellation consists of two operational satellites, GOES-8(I) and GOES-10(K); a fully capable on-orbit spare, GOES-11(L); and a limited-capability on-orbit spare, GOES-9(J). GOES-12(M) was launched July 23, 2001 and will complete checkout in December 2001. The five satellites in the GOES I through M series were produced by Space Systems/Loral. NOAA describes each satellite with a letter (e.g., I, J, etc.). Once it is successfully inserted into geostationary orbit, it is redesignated with a number (e.g., 8, 9, etc.).

2.1 *NOAA GOES-8*

GOES-8 was launched from Cape Canaveral April 13, 1994, is the operational satellite over the Americas and the Atlantic Ocean at 75°W, and continues to provide data more than two years beyond its nominal five year design life. It is the first GOES satellite stabilized in a three-axis pointing mode rather than as a spinner. It was designed this way to allow nearly instantaneous, properly navigated and registered data to track rapidly developing severe weather and so that the atmospheric Sounder instrument could stare long enough at one spot to provide a high signal to noise ratio. Instrumentation on GOES-8 consists of an Imager, a Sounder, and a Space Environmental Monitor (SEM) suite; along with a Data Collection System (DCS), weather facsimile (WEFAX) transponders, and Search and Rescue (SAR) receivers.

The Imager is a five channel imaging radiometer. Images are formed by scanning an array of detector footprints across the Earth from East to West, then back from West to East, from the top of the image to the bottom. An excellent description of both the Imager and Sounder can be found in Menzel and Purdom (1994). The visible channel consists of eight detectors mounted in a north-south line, each having a horizontal resolution of one km at nadir. Each scan covers an eight km swath. There are four infrared channels centered at 3.9, 6.7, 10.7, and 12.0 micrometers. Three of the IR channels consist of two four km detectors also mounted in a north-south line. The two detectors cover eight km each scan. One detector, the 6.7 micrometer channel, has one detector at eight km resolution. Thus, each scan produces eight lines of visible, two lines of IR in three channels and one line at 6.7 micrometers.

The Sounder instrument is a 19 channel discrete-filter radiometer that senses emitted radiances to measure the vertical distribution of temperature, moisture, cloud top temperatures, and ozone in the atmosphere. In addition to the one visible channel, there are seven longwave, five midwave, and six shortwave IR channels, all with horizontal resolution of 8.6 km at nadir. The Sounder stares at each field of view on the Earth for 0.1 to 0.4 seconds (commandable) and measures radiances in all 19 channels.

The Imager and Sounder each use a single scan mirror for East-West and North-South motion. Two motors are provided for each direction in the Imager design, one to move the mirror and one as backup. The Sounder has the same system design. On GOES-8, one of the Sounder East-West mirror motor windings failed in August 1994. Since that time, the backup motor has continued to provide data and no significant break in service has occurred.

Charged particles have rendered some of the memory in the Attitude and Orbit Control Electronics inoperable, although the backup electronics and remaining memory have allowed GOES-8 to continue to provide continuous operational data. Attitude and three-axis pointing are nominally controlled by two momentum wheels and one reaction wheel. Two of the three are required for operational control.

2.2 *NOAA GOES-9*

[1] *Corresponding author address:* Gerald J. Dittberner, NOAA/NESDIS/OSD1, 5200 Auth Road, FB4, Room 3010, Suitland, MD 20746, e-mail: Gerald.Dittberner@noaa.gov

GOES-9, launched May 23, 1995 was the operational satellite over the Pacific Ocean at 135°W until July 21, 1998. At that time, both momentum wheels were exhibiting signs consistent with lubrication starvation in patterns similar to those seen in other momentum wheels just before failure. GOES-9 is believed to have only a few weeks of usable life left. It is presently in an on-orbit storage mode near 105°W, and serves as a limited-life spare if needed.

GOES-9 has the same instruments as GOES-8. In April 1996, the Imager mirror motor suffered the same problem with one of its East-West scan motors as the GOES-8 Sounder, but the GOES-9 Imager remains capable of providing data using its backup motor. Motors on subsequent Imagers and Sounders have been redesigned to eliminate this failure mode.

2.3 *NOAA GOES-10*

GOES-10 was launched April 25, 1997 as an on-orbit backup and was activated on July 21, 1998 to replace GOES-9 as GOES-West. GOES-10 has the redesigned East-West motors to eliminate the mirror motor problems faced on GOES-8 and GOES-9.

In May 1997, the solar array, which is designed to rotate once each day to keep itself pointed at the sun, slowed down and eventually stopped. However, innovative work by NOAA and NASA engineers led to turning the spacecraft into an upside down orientation (a yaw-flip maneuver) in which the solar array rotates backwards (Williams, 1998). This maneuver was highly successful in saving the spacecraft. Thanks to careful planning and preparation by the product production offices, data from GOES-10 were flowing within one day of activation and continues nominally as of this writing. Software was changed so that data from the instruments are provided to users as if the spacecraft were in the normal upright orientation. Users require no adjustments, and notice no difference in the GVAR data stream.

2.4 NOAA GOES-11

GOES-11, launched May 3, 2000, successfully completed its checkout phase and is now in place near 105° W as the fully capable on-orbit spare. Instrumentation on GOES-11 is the same as on the pervious three satellites.

2.5 *NOAA GOES 12*

GOES-12 was launched July 23, 2001 and is expected to complete its checkout about the time of this conference. GOES-12 has the redesigned instrument motors and carry the same instrument complement as GOES-8, 9, 10, and 11, with two exceptions. The Imager on GOES-12 has its 12.0 micrometer channel replaced by a 13.3 micrometer channel to better determine the heights of mid-level steering winds and more accurately measure atmospheric and cloud optical properties. Also, the 6.7 micrometer channel resolution was be increased from eight km to four km .

GOES-12 carries the first Solar X-Ray Imager (SXI) instrument, designed to provide images of the Sun in four X-Ray energy bands at intervals as frequently as once every few minutes. SXI data will provide the first continuous operational series of Solar X-Ray images and is expected to provide extremely valuable data during the Solar Maximum, expected to peak in 2000 or 2001.

3. NEXT: THE GOES-N SERIES

For the next series, instruments and spacecraft are being manufactured under separate contracts, each structured for two firm orders with two separate options for a third and a fourth, i.e., as a 2+1+1 procurement. Imager and Sounder instruments are under development by ITT Aerospace/Communications. Solar X-Ray Imagers are being produced by Lockheed-Martin Advanced Technology Laboratories and the spacecraft are being manufactured by Hughes Space and Communications. GOES-N will be launched in early 2003. The current launch schedule is provided in Table 1.

Imagers and Sounders will be essentially the same as for the GOES I-M series. Imager channels remain the same as those on GOES-12, with a reduction in horizontal resolution from eight km to four km in the 13.3 micrometer channel on GOES-O, P, and Q. Sounder instruments will be the same filter-wheel based sounders. For SXI, current plans are to fly one on every other satellite so that there is always one operational unit in orbit.

Shortly before GOES-N is launched, analog WEFAX signals will be replaced by the digital Low Rate Information Transmission (LRIT) system. More information can be found in McClinton and Dittberner, 2001.

Satellites in the GOES-N series also have additional space, power, and data capacity for experimental sensors. Current candidates under consideration are instruments such as a Special Events Imager and a Volcanic Ash Mapper.

4. FUTURE: THE GOES-R SERIES

A number of studies are underway to help design the follow-on series of GOES sensors and satellites. A top level Program Development Plan (NESDIS, 1999) provides guidance for the next series. An important review of user requirements along with an analysis of potential benefits has been underway for more than two year. The first of a sequence of User Workshops was held in Boulder in September 2000. A description of this "Initial GOES-R+ User Workshop" 2000 can be found in Gurka and Dittberner, 2001a. A larger open user workshop was held in May, 2001 in Boulder. See the companion paper at this conference: Gurka and Dittberner, 2001b.

Much has been learned about how these data enhance meteorological forecasting in the Weather Forecast Offices and increase forecast skill in numerical models. In fall 1997, Sounder data were first operationally

assimilated into numerical models along with high spatial density wind information. GOES data make this an exciting time for meteorology.

An Advanced Baseline Imager (ABI) and Advanced Baseline Sounder (ABS) are planned for the GOES-R series. Engineering requirements were developed based on the 1999 National Weather Service needs (NWS Office of Meteorology, 1999), and passed to NOAA's System Acquisition Office and NASA for procurement activities. The ABI will have 8 to 12 channels, increased horizontal and higher coverage rates and be fully capable of operating through eclipse and keep out zones (Gurka and Dittberner, 2001). The ABS is expected to be an interferometer-type instrument closely modeled after the Geostationary Imaging Fourier Transform Spectrometer (GIFTS) being developed by NASA for its New Millennium Program (NMP). ABS procurement will follow ABI procurements by about six months. Spacecraft for remaining ABI/ABS instruments for GOES R through U will be procured with a new competitive contract.

5. PRODUCTS

In October 1997, GOES Sounder precipitable water started being used in the operational ETA numerical model runs. Starting in December 1997, high spatial density winds, derived from Imager IR and water vapor channels, were being used in the operational ETA model. Also, In 1997, the GOES fog product was distributed in the Advanced Weather Information Processing System (AWIPS). Forecasters in Weather Forecast Offices throughout the United States began using GOES-based winds, temperature and moisture soundings, and Derived Product Imagery (DPI) in daily forecast operations. Both forecasters and numerical models are benefitting from the use of GOES data.

In 2000, four Sounder Derived Product Imagery (DPI) products, one of the highest priority new product sets demanded by field forecasters, were made available operationally to the Advanced Weather Interactive Processing System (AWIPS) input site fro distribution.

6. SUMMARY

NOAA's GOES program continues to maintain the required flow of data from two operational satellites and has taken steps to ensure this continuity with an on-orbit spare philosophy. Instruments continue to evolve as meteorologists, atmospheric scientists, and engineers work with these data and discover new ways to provide better service to users. Emerging technologies are being examined to reduce costs and increase the information content of products provided.

7. REFERENCES

Gurka, J., and G. Dittberner, 2001a: The next generation GOES instruments: status and potential impact, Proceedings, AMS 5th Symposium on Integrated Observing Systems, Albuquerque, NM, January 15 - 19, 2001, 5pp.

Gurka, J., and G. Dittberner, 2001b: Recommendations from the GOES Users' Conference, Preprints, AMS 11th Conference on Satellite Meteorology and Oceanography, Madison, Wisconsin, October 15 - 19, 2001, 4pp.

McClinton, A. Jr., and G. Dittberner, 2001: GOES-N, The first of the next series - user community upgrades, Proceedings, AMS 17th Conference on Interactive Information Systems (IIPS) for Meteorology, Oceanography, and Hydrology, Albuquerque, NM, January 15 - 19, 2001, 2pp.

Menzel, P., and J. Purdom, 1994: Introducing GOES-I: The first of a new generation of Geostationary Operational Environmental Satellites, *Bull. Amer. Meteor. Soc.*, Vol. 75, No. 5, pp. 757-781.

National Weather Service Office of Meteorology, 1999: Operational Requirements Document for the Evolution of Future NOAA Geostationary Imagery, 31pp.

NESDIS, 1999: GOES-2010, Program Development Plan, April, 1999, 25 pp.

Williams, J.: Ingenuity turns eye back to the weather, *USA Today*, February 17, 1998, p. 10B.

GOES Launch Planning Schedule

Table 1. GOES Launch Schedule

Spacecraft	Spacecraft Availability	Planning Launch Date
GOES-N	Jan 2003	Jan 2003
GOES-O	Apr 2004	Apr 2005
GOES-P	Apr 2006	Apr 2007
GOES-R	Apr 2010	Apr 2012

2.4 NOAA POLAR INSTRUMENT DATA GENERATION FOR LEVEL 1B USERS

Arlington R. Morgan
Computer Sciences Corporation, Suitland, MD

Emily D. Harrod
NOAA/NESDIS, Suitland, MD

INTRODUCTION

The National Oceanic and Atmospheric Administration (NOAA)/National Environment Satellite Data and Information Service (NESDIS)/Office of Satellite Data Processing and Distribution (OSDPD)/Information Processing Division (IPD) receives and formats raw spacecraft instrument data from the TIROS series of polar-orbiting operational environmental satellites (POES) into user-friendly Level One-B-Star (1B*) (unpacked) and One-B (1B) (packed) formats for distribution to the NOAA polar data user community. Level 1B* data is used internally and Level 1B is distributed to users nationally and internationally. Throughout this paper, these data sets will be collectively referred to as Level 1B. The Pre-Product Processing (PPP) system is used to create and monitor the quality of the 1B data sets produced from ingested raw polar satellite data. The PPP subsystems that process the ingested polar spacecraft data perform the following functions:

(i) Calibration—maintains a spacecraft-specific database for each POES

(ii) Earth Location—provides POES spacecraft geolocation information included in the 1B data

(iii) Polar Data Preprocessing (PDP)—executes the algorithms for calibrating, Earth locating, quality checking, and formatting the ingested polar satellite data

(iv) Quality Control (QC) Monitoring System—performs quality checks, produces trending plots, and is used to analyze and evaluate the Level 1B data

In this paper, we describe the NOAA PDP of Level 1B data with particular emphasis on the user utilization of this data to generate various products.

NOAA POLAR INSTRUMENT DATA 1B PROCESSING

2.1 Polar Instruments Data Types

The PDP processors create Level 1B formats from the ingested POES raw satellite Level 1A data sets. These processors generate and distribute the following thirteen 1B data types:

AMSU-A — Advanced Microwave Sounding Unit – A[1]
AMSU-B — Advanced Microwave Sounding Unit – B[1]
DCS — Data Collection System
GAC — Global Area Coverage Advanced Very High Resolution Radiometer (AVHRR)
HIRS — High-Resolution Infrared Radiation Sounder
HRPT — High-Resolution Picture Transmission AVHRR
LAC — Local Area Coverage AVHRR (recorded)
MSU — Microwave Sounding Unit[1]
SAR — Search and Rescue
SBUV — Solar Backscatter Ultraviolet Radiometer
SEM — Space Environment Monitor
SSU — Stratospheric Sounding Unit
TIP — TIROS Information Processor

2.2 Ingest and Preprocessing

Operation of the various NOAA polar satellite Level 1B data processing systems is principally the responsibility of IPD. IPD receives data from the Satellite Operations and Control Center (SOCC) and processes it into Level 1A and 1B data in the Central Environmental Satellite Computer System (CEMSCS). The CEMSCS has ingest and preprocessing systems for NOAA polar, NOAA geostationary, and some non-NOAA satellites. The system described in this document is most relevant to the NOAA PDP system. The PDP operation consists of components such as prelaunch activities, ingest 1A processing, 1B processing, calibration, navigation, product generation, and archive. The software systems that are implemented, operated, and maintained are in the following functional categories: Ingest (Level 1A), satellite dataset processing (Preprocessing Level 1B), product processing, archiving, QC monitoring, navigation and Earth-location, data communications, calibration (pre- and post-launch), and shared processing.

Ingest

The ingestor transforms the satellite Level 0 (raw data) into a more processing friendly Level 1A data set as follows:

1. Accepts and synchronizes frames of Level 0 satellite data.
2. Performs first-level quality control of data stream, filling data gaps as necessary.
3. Extracts instrument and spacecraft data from Level 0 data and reformats it into the Level 1A file format.
4. These Level 1A data sets are made available for Level 1B generation under a unique data set name

* *Corresponding author address:* Arlington R. Morgan, NOAA/NESDIS, FB#4, Rm. 0303, E/SP13; 4401 Auth Road; Suitland, MD 20746-4303; e-mail: Arlington.Morgan@noaa.gov

[1] MSU and SSU sounding instruments were replaced with AMSU-A and B instruments on the NOAA KLM series (NOAA-15, NOAA-16, ...).

that includes orbit number identifiers and time duration for the pass.

Preprocessing

The primary function of the data preprocessing is to create the Level 1B datasets. The software formats, error checks, calibrates, Earth locates, and otherwise manages the ingested data. Raw spacecraft data is received via the Polar Acquisition and Control Subsystems (PACS) operated in SOCC and is made available to the Preprocessing operation from the Ingest System as Level 1A data sets. The transformation from the Level 1A format to Level 1B format primarily consists of the addition of instrument calibration coefficients, Earth location information, quality control information to the raw data stream, and supplemental data about the spacecraft and the instruments onboard the satellite. Data in the Level 1B format is made accessible for internal product processing, archival, and file transfer for use by the meteorological, oceanographic, and climatological communities.

Calibration

As part of normal operations, the data preprocessing software performs online instrument data calibration and monitors instrument telemetry to detect anomalies. Instrument channel calibration coefficients are derived from the Instrument's observations of a warm internal target and a cold external target (space). The software appends these coefficients to the scan line for later product processing. When anomalies are detected, the data is flagged as suspect for the product systems.

Earth Location

The Advanced Earth Location Data System (AELDS) produces the Earth location data contained in the Level 1B. An online Earth location system, AELDS, uses scan line time codes to produce latitude and longitude Earth location parameters. The AELDS process provides more than just latitude and longitude information. Given the satellite position and velocity vector, the Greenwich hour angle (GHA), scan time, stepping time, stepping angle, and number of positions desired, AELDS will provide the following for the requested scan point of a specific instrument:

Satellite height	Solar zenith angles
Satellite zenith angle	Solar azimuth angles
Satellite azimuth angles	Relative azimuth angles
Latitude angles	Longitude angles
Northbound/southbound indicators	

Monitoring and Quality Assurance

Monitoring software examines the real-time operation of the software system or performance of an instrument and generates operator error messages, statistics, and reports. Comparison with appropriate "truth" data is required in the monitoring system. Printouts and/or interactive data displays are examined for credibility. To ensure that the Earth location and navigation information provided by IPD lies within acceptable accuracy limits, QC operations are performed before, during, and after generation of the data. At present, four types of checks are used:

Navigation: When the user ephemeris file (UEF) containing predicted satellite position and velocity data is generated, the radius vector is compared to that generated using the elements for the previous 7 days (delta-R). Generally, these differences remain less than 1 kilometer for at least 7 to 10 days.

Online Earth location: An Earth location tolerance check of the satellite subpoint (nadir) location has been integrated into the AELDS process. An independent method calculates the subpoint position and compares it to the AELDS generated position. The acceptable value of the difference can be reset and checking can be turned on or off. This tolerance check gives the reassurance that the Earth location algorithm is behaving correctly.

Post-processing Earth location: An image QC system is used to verify the accuracy of the Earth location data embedded in the AVHRR instrument Level 1B files. Generally, the Earth location error seen in the image data around the satellite subpoint remains within 0 to 2 kilometers (specifications for AVHRR are 4 to 5 kilometers). The error near the limb is expected to be larger and is often near 5 kilometers. The current exception is an anomaly seen in the Northern Hemisphere ascending passes and the Southern Hemisphere descending passes, which displays an additional 4- to 5-kilometer error along track. Using the above-image QC techniques provides greater insight into the magnitude and source of Earth location errors.

Trending: Daily monitoring is also performed using the quality control and instrument trending system providing graphical statistics on the Level 1B data for each instrument. More than 3,400 instrument parameters are analyzed using this system. The PPP website address cited in the summary section of this paper provides access to a subset of this system. (Click on **Instrument and Calibration Trending**).

CUSTOMER UTILIZATION OF LEVEL 1B DATA

The following products are generated from the NOAA/NESDIS Level 1B data. For details on these products, go to the Products Systems Branch (PSB) website provided in the summary.

1. **Sea Surface Temperature (SST) Products:** NOAA/NESDIS produces and archives two types of SST products, gridded products and geographically organized retrievals. The sea surface temperature products include SST anomalies, contour charts, and analyzed fields. Also provided are maps of current SSTs, ocean surface winds, hot spots, and degree heating weeks, which are useful for monitoring coral bleaching at various sites around the globe.

2. **Mapped GAC Products:** The mapped GAC products comprise mapped mosaics displayed on polar stereo graphic and Mercator map projections with both forms available on digital media. The mapped mosaics consist of daytime visible (VIS) and infrared (IR), and nighttime IR imagery. NESDIS/IPD also produces an

operational mapped GAC product, which is known as the *Global Vegetation Index Product*. This product provides a means of monitoring the density and vigor of green vegetation over the growing areas of the Earth.

3. **Radiation Budget Products:** The Radiation Budget products include daily and monthly mean global maps of outgoing longwave (infrared) radiation and absorbed and available incoming shortwave (solar) radiation. This data is frequently used to study global climate change.

4. **Sounding Products:** A sounding is a vertical atmospheric temperature or moisture profile derived from radiance measurements. NESDIS currently has the capability of producing a maximum of 3,175,000 soundings every 24 hours from three operational spacecraft. ATOVS from NOAA-15 or 16 generates retrievals with a 60 km resolution (40 km at nadir). AMSU-B from NOAA-15 or 16 generates retrievals with a 15 km resolution and 15 km spacing between retrievals; the data are sampled to reduce the data volume by half.

5. **Coast Watch Product:** The Coast Watch program provides high-resolution (1km/4km) satellite data and derived products (including sea surface temperature) for coastal regions. The data is frequently used by fisherman.

6. **Snow and Ice Products:** Meteorologists and climatologists are interested in short-term and long-term observations of snow and ice cover because of its affect on weather forecasting and climatic processes. Snow and ice analysts in the NOAA NESDIS have been creating weekly maps showing the extent of snow cover for the Northern Hemisphere since 1966.

7. **Ozone (SBUV/2) Products:** The Ozone products are generated from the SBUV/2 (Solar Backscattered Ultraviolet Radiometer/Version 2). The SBUV/2 is a non-scanning, nadir-viewing instrument designed to measure scene radiance in the spectral region from 160 to 400 nm. SBUV data is used to determine the vertical distribution of and total ozone in the atmosphere and solar spectral irradiance.

   The SBUV/2 sensor data consists of radiance and irradiance measurements taken in both the discrete mode (12 wavelengths) and the sweep mode (1680 wavelengths) at approximately 2 Angstrom intervals.

8. **Aerosol/Optical Thickness Products:** The aerosol products are produced from NOAA-16 AVHRR data on a weekly basis. The primary products are a global 1-degree map of aerosol optical thickness (AOT) based on a composite of 1 week's worth of data and the monthly mean product. Also, there are contour plots of weekly composites and monthly means.

Summary

The IPD is making every effort to provide quality Level 1B data to the user community in fulfillment of the NOAA/NESDIS mission "to provide and ensure timely access to global environmental data from satellites...." Enhancements to improve the efficiency and accuracy of the Level 1B generation process and the product itself are planned to support future missions (such as NOAA-M, NOAA-N, and MetOp). Users interested in getting more information on the Level 1B process, products, and updates should check the following websites:

http://www.osdpd.noaa.gov/ — general information on the IPD

http://www.osdpd.noaa.gov/PSB/PSB.html — information on the products from PSB

http://www.osdpd.noaa.gov/PSB/PPP/PPP.html — information on the Level 1B calibration, Earth location, QC, and instrument trending.

Those users interested in archived Level 1B data may consult the NOAA Satellite Active Archive (SAA) website, http://www.saa.noaa.gov/. The mission of the SAA is to provide electronic distribution of data and derived data products from U.S. POES.

References

NOAA/NESDIS/OSDPD website, http://www.osdpd.noaa.gov/. *NOAA KLM User's Guide*, May 1999 version, http://www2.ncdc.noaa.gov/docs/klm/index.htm

2.5 RECENT DEVELOPMENTS IN QUIKSCAT NEAR-REAL-TIME PROCESSING AT NOAA/NESDIS

Jeffrey M. Augenbaum* and Raymond W. Luczak
Computer Sciences Corporation, Suitland, MD

Gene Legg
NOAA/NESDIS, Suitland, MD

1 INTRODUCTION

The QuikSCAT near-real-time (NRT) processing at NOAA/NESDIS has been operational since February 2000 and continues to be enhanced and maintained under Computer Sciences Corporation's (CSC) Central Satellite Data Processing (CSDP) contract. In addition to the originally planned ocean winds products, several new products have been added to the processing stream on an experimental basis. In this paper we describe additional QuikSCAT products such as the high resolution (12.5 km) wind product as well as Ice and Ocean image products that have been added to the processing stream and their impact on production. In addition, we describe forthcoming changes to be incorporated to accommodate the ADEOS-II mission which will be launched early next year.

2 NOAA/NESDIS QUIKSCAT NRT PROCESSING SYSTEM

2.1 NRT Data Processing

The QuikSCAT NRT processing system at NOAA/NESDIS continues to be enhanced in collaboration with JPL and NOAA/NESDIS. Details of the NRT processing system's data flow are contained in Augenbaum, et. al. (2001) and summarized in Figure 1. The main operational mission is to produce wind retrievals in 25 km resolution Wind Vector Cells (WVC) on an orbit by orbit basis within three hours of observation and to make them available in BUFR format. This product contains both the wind retrievals along with the sigma-0 values for each wind vector cell. An additional, winds only, solution is also produced and made available in a binary format.

Monthly latency and processing statistics have been tracked at NOAA since QuikSCAT went operational. Analyzing the monthly data for the last year shows that on average NOAA has received the data within 150 minutes of observation 85% of the time which meets the requirement. The end-to-end (observation to product available) processing times have been less than 190 minutes, 88% of the time. The NOAA only processing times have averaged less than 45 minutes 94% of the time.

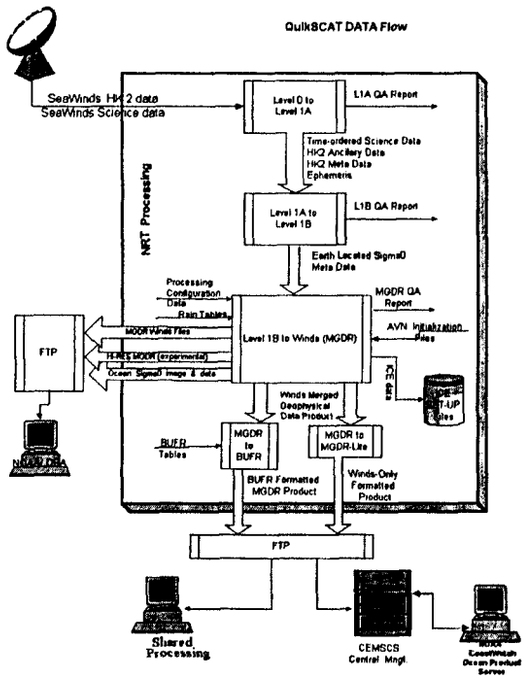

FIGURE 1. QuikSCAT Data Flow Diagram

2.2 New Products

Although some tradeoffs in resolution versus processing speed are made to the NRT processing of wind retrievals in order to meet the NRT operational requirements, the Level 1B (L1B) intermediate product can still be used to produce other high resolution products. After the operational requirements are met, the L1B intermediate product is used to generate high resolution wind retrievals, ice edge detection and ocean surface images.

* Corresponding author's address:
Dr. Jeffrey Augenbaum, NOAA/NESDIS, 4401 Suitland Dr., FB#4, Suitland, MD 20746;
e-mail Jeffrey.Augenbaum@noaa.gov

2.2.1 Ocean Sigma-0 image

The most recent product added to the processing stream is an Ocean Sigma-0 image, based on image processing algorithms developed by Dr. David Long of the BYU Microwave Earth Remote Sensing (MERS) Laboratory (www.mers.byu.edu/Seawinds-1.html). The NRT processing system produces high resolution (on a 2.5 km swath based grid) Normalized Radar Cross Section (NRCS) or Sigma-0 images using AVE resolution enhancement and also gif formatted images on an orbit by orbit basis. Dr. Paul Chang (NOAA/ORA) has set up a QuikSCAT Storms web page at http://manati.wwb.noaa.gov/cgi-bin/qscat_storm.pl to make the Sigma-0 images available over areas of storm activity. A sample image of storm GABRIELLE, off the coast of Florida, is displayed in Figure 2. Currently, only the vertically polarized, forward look measurement from QuikSCAT is produced. The idea here is that looking at the scatterometer data in this way, rather than the calculated, wind retrievals, might provide additional uses for QuikSCAT data. For comparison purposes, the QuikSCAT wind retrievals for Storm GABRIELLE are displayed in Figure 3.

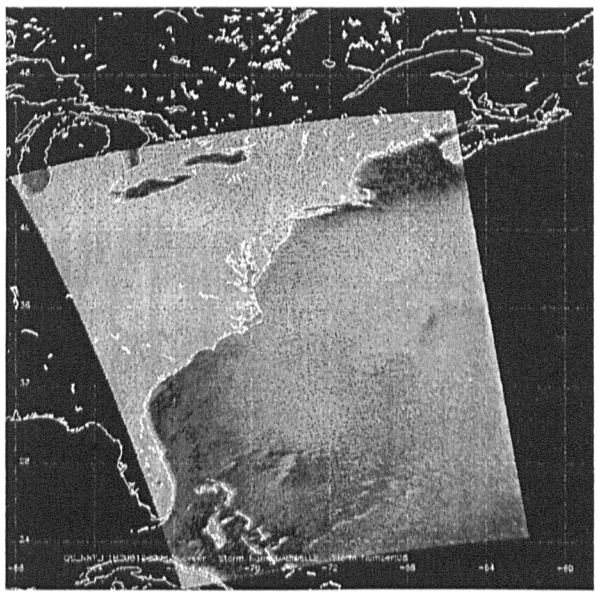

FIGURE 2. Sample Sigma-0 image of Storm GABRIELLE off of Florida Coast

2.2.2 Ice Images

The Ice image products are also based on algorithms developed by Dr. David Long (BYU) and have been produced operationally since June 2000. The NRT image processing software generates a set of "AVE" enhanced resolution images from the L1B data files. Recently, the Scatterometer Image Reconstruction (SIR) processing routines that produce the .ave and .sir images have been updated to produce sharper images. The large polar images use the AVE method while the special regions, which are smaller, use the full SIR resolution enhancement. We are currently producing daily ice image products for the Alaska, Antarctic, Arctic, North Pacific, Ross Ice Shelf and Weddel Sea regions. These products are available on a daily basis at http://manati.wwb.noaa.gov/cgi-bin/qscat_ice.pl. Further documentation is available at ftp://www.osdpd.noaa.gov/pub/seawinds/Ice_doc.txt

In addition, the National Ice Center produces their own images from the .sir data. They are currently distributing near-real-time ICE images of the northern and southern hemisphere. Their products are available at www.natice.noaa.gov/science/products/qs.html

2.2.3 High-resolution wind retrievals

In addition to the above products, the L1B product is also used to produce high resolution wind retrievals with a 12.5 km resolution. This product is currently considered experimental, and it has not yet been validated.

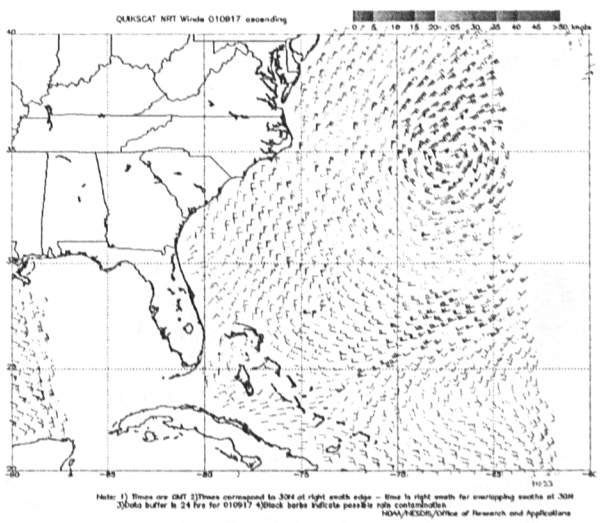

Figure 3. Wind retrievals for Storm GABRIELLE

3 ADEOS-II PROCESSING

One of the most anticipated changes for the QuikSCAT processing system is the launch of a second Seawinds instrument on the Adeos-II spacecraft, scheduled for February 2002. The result of this will be a second QuikSCAT data stream to be processed in near-real-time.

At present the NOAA/NESDIS QuikSCAT NRT processing system consists of dual, four-processor

SUN Enterprise 4500 Servers each equipped with 2.5 GB ram and 45 GB of disk storage. One machine functions as the primary processing server, and the other is used as a backup processing server. Failure of a successful push from CSAFS to the primary server automatically results in a push to the backup server. It is anticipated that the processing system configuration will be modified so that a separate SUN Enterprise machine will be available as the primary processing server for each data stream. One for Seawinds on QuikSCAT and one for Seawinds on ADEOS-II. There will be another machine to serve as a secondary, backup, processing server for both QuikSCAT and ADEOS-II. The current machines are also being upgraded to six-processors each to handle the additional processing that the new products have imposed.

The core processing software is being developed at JPL. The ADEOS-II processing will be similar to the QuikSCAT processing, with raw science files processed through to wind products. The main difference is that the ADEOS-II data stream will come directly from the ADEOSFS in Japan as opposed to the CSAFS at NASA/Goddard and it will not contain the HK bookkeeping files where we get the time data. HEOC (Hatoyama Earth Observing Center) time difference files will only be sent once per day. The time difference files will then be processed to produce the necessary time files.

The rest of the processing will follow that of QuikSCAT, as displayed in Figure 1. The file and directory structure of both processing systems is being reworked to provide clear identification and separation between QuikSCAT and ADEOS-II components. A conversion routine has been written to convert QuikSCAT telemetry data to ADEOS-II so that testing of the ADEOS-II processing software can begin in the near future. Both QuikSCAT and ADEOS-II processing software are being updated to incorporate improved algorithms developed over the past two years since QuikSCAT has been operational.

4 CONCLUSIONS

QuikSCAT near-real-time processing has been operational since February 2000 and continues to meet NOAA's mission requirements of near-real-time data processing within 180 minutes of observation 85% of the time. Over the past year, the system has been enhanced to include additional products that our customers have found to be useful. While requiring additional processing resources, these additional products do not detract from the core operational mission in any significant way. Plans are in place for major upgrades in the processing system in both hardware and software to accommodate the forthcoming ADEOS-II data stream.

5 REFERENCES

Augenbaum, J. M., Luczak, R.W. and Legg, G., 2001 "Quikscat Near-Real-Time Data Processing and Product Generation at NOAA/NESDIS", Proceedings of the 17th International Conference on Interactive Information and Processing Systems (IIPS) for Meteorology, Oceanography, and Hydrology, Albuquerque, New Mexico pp. 324-328

Hoffman, R.N., and Dunbar, R.S., 2000: NASA SeaWinds Scatterometer Real-Time Merged Geophysical Data Product (SWS_Met) User's Guide. Version 2.3.0, Jet Propulsion Laboratory, Pasadena, CA 45 pages.

Leidner, S.M, Hoffman, R.N. and Augenbaum, J., 2000: SeaWinds Scatterometer Real-Time BUFR Geophysical Data Product User's Guide Version 2.3.0, NOAA, Washington, DC 34 pages.

Remund, Q.P. and Long, D.G. 1998 "Sea Ice Mapping Algorithm for QuikSCAT and Seawinds,"Proceedings of the International Geoscience and Remote Sensing Symposium, Seattle, Washington, pp.1686-1688

2.6 EVOLUTION OF NANOOK, THE NOAA/NESDIS NEAR-REAL-TIME MODIS PROCESSING SYSTEM

Paul Haggerty, Science and Technology Corporation, Suitland, Maryland *
Kristina Sprietzer, Science and Technology Corporation, Suitland, Maryland
Gene Legg, National Oceanic and Atmospheric Administration, Suitland, Maryland
Ray Luczak, Computer Sciences Corporation, Suitland, Maryland

1. INTRODUCTION

NANOOK is a combined scheduler and processing system for MODIS (Moderate Resolution Imaging Spectroradiometer) data. NANOOK is a hybrid system containing both a task scheduler and processing control system developed under the CSC Central Satellite Data Processing Center (CSDPC) contract, and a suite of NASA-built product generation software.

NANOOK accepts Rate Buffered Data from EDOS (Earth Observing System Data Operations System) and converts it to the Level 0 data format required by MODAPS (MODIS Adaptive Processing System) science software packages. The scheduler, as written by NOAA, is then in charge of managing all incoming and ancillary data, passing the data through the various modules of the science code (and additional NOAA produced production code), and proper distribution of all output products.

In the year since the NANOOK went on-line there have been a great number of changes to the system, both in capabilities, and in requirements. There are also a number of problems that still need to be overcome to effectively utilize the system.

2. THE OLD NANOOK

When NANOOK originally went on line in December of 2000, it was tasked with producing a limited set of products over the continental United States, plus Alaska and Hawaii. It was developed on an SGI ORIGIN 2000 computer attached to a Clarion RAID unit with 550GB of storage, 275GB of which were allocated to NANOOK, the remainder being allocated to AIRS (Atmospheric Infrared Sounder), a related NOAA project which is also engaged in proof-of-concept and operational demonstration.

The RAID held two copies of all original data, intermediate data, ancillary data, final products, and processing code. Storage requirements were then doubled by the implementation of two separate but parallel development and production processing systems. The developmental system allowed for new software to be tested without disrupting the flow of data.

Paul D. Haggerty, NOAA/NESDIS/IPD Federal Center FB-4, RM 0303, 4401 Suitland Road, Suitland, MD 20746; e-mail: Paul.Haggerty@noaa.gov

Twelve CPUs (from a total of 32) running at 250MHz were made available to process data for the designated area of coverage. The remainder of the CPUs were allocated to AIRS.

In order to allow for parallel processing, MODIS data was broken up into granules that consist of five minutes of contiguous data. Image 1 below shows the coverage of a typical granule. The limited daily coverage requirement resulted in approximately 18-20 of these granules for the continental US, 6-10 granules for Hawaii, and 6-10 granules for Alaska. Fortunately, since TERRA is a polar orbiting spacecraft, the incoming data load was limited to approximately 3-4 granules per orbit, which allowed for the small number of CPUs to keep up with the data flow.

IMAGE 1. RGB composite
Sept. 15th, 2001 : 1635 UTC
Southeastern United States

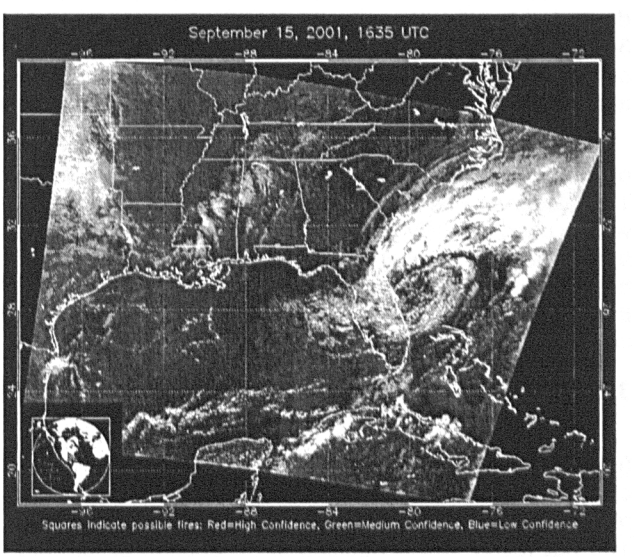

On a typical day, this data load averaged approximately thirty-five granules. Since each granule generated two gigabytes of products in each of the development and production systems, the storage system very quickly filled to capacity. This necessitated purging the data and the products immediately after being processed. Unfortunately, this left little to no opportunity to study the data in depth or to go back and reprocess specific areas for more detailed information.

Since this was a pilot project for processing near-real-time data using data ported from its original design environment, the primary concern was installing the software and acquiring ancillary data. The initial investment provided an environment in which data could be processed, but at a limited trial capacity. Although storage capacity concerns were envisioned and expected at the start of this project, there were sufficient resources allocated to show that the project could be successfully tested. And thanks to assistance from NASA, the system has now been expanded not only to fulfill it's original designs, but to assist another NOAA project, and to provide risk reduction for the upcoming NPOESS (National Polar-orbiting Operational Environmental Satellite System) project, and it's precursor NPP (NPOESS Preparatory Project) which will test three of the four major new instruments.

3. THE NEW NANOOK

3.1 Physical Growth of the System

The original physical components of NANOOK consisted of three full sized cabinets, one of which held the RAID, and the other two holding thirty-two CPUs and associated electronics.

Despite using SGIs newly modularized system to reduce space, the expansion to the new system has tripled the floor space and power requirements. The new NANOOK uses an ORIGIN 3800, which has two full sized cabinets for the sixty-four 400MHz CPUs dedicated to MODIS, and a third cabinet for the ORIGIN 3400 with thirty-two CPUs now dedicated to AIRS. Both projects now share a fourth cabinet housing a five-terabyte RAID storage system.

To reduce the volume of bandwidth for data distribution, a new ORIGIN 3200 system was added. This fileserver has five terabytes of RAID storage which will be used for daily data storage and distribution. This brings the total number of cabinets for the entire system to six which, in addition to the original hardware, triples the floor space and power requirements for the new configuration.

3.2 The AQUA Satellite

Early in 2002, NASA is scheduled to launch AQUA (previously known as EOS-PM1), the second satellite to carry the MODIS instrument. NANOOK is already being reconfigured to be able to support this second sensor. The net result of this addition is a doubling of all data requirements, including processing, storage, and distribution.

3.3 The AIRS Project

The AQUA satellite carries several different sensors, one of which is the new AIRS sensor. The NOAA AIRS project is also interested in processing near-real-time data, and will require the global cloud mask produced by NANOOK from the MODIS data. While this is not the full product suite of NANOOK, it will require global processing to the level 1B stage. This by itself will increase CPU needs from four CPUs per hour to 48 CPUs per hour, and increase data storage requirements from 35GB per day (just for Level1B) to 576GB per day.

3.4 Additional Products

The fire detection product, which was to be part of the Land Surface Reflectance product, has been re-written as a stand-alone product. On a global scale, this produces 15MB of data per granule, or an additional eight gigabytes of products. Due to interest from many parties, this product has been added to the NANOOK requirements. An example is shown below in Image 2. This image shows an early version of the product labeling possible locations of fires on the southeastern coast of Africa, and the island of Madagascar.

Other products created by NOAA include regional mosaics covering the Continental U.S, Alaska, and Hawaii. Images covering the current month, and the previous month are available at the NANOOK website: *http://www.osdpd.noaa.gov/MODIS*

Image 2: Fire Product Image.
31 August 2001.
Southeast African Coast, Island of Madagascar.

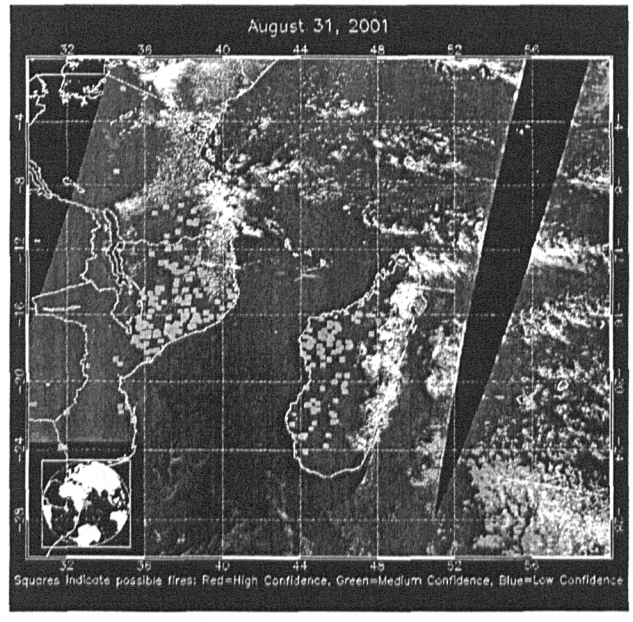

3.5 File Server for customer access

The original design for data distribution was for NANOOK to transmit all output products to NOAA's Central Environment Satellite Computer System (CEMSCS). However, this server is rapidly becoming saturated in bandwidth and storage due to the large variety of products from many other NOAA programs. Rather than overload the CEMSCS distribution server further, it was decided to procure a file server system that will allow all the products generated by NANOOK to be made available to the users without further burdening

CEMSCS. It was decided to have a file server as a separate machine from the processing system for two reasons. The first reason is that it will not compromise the security of the production servers by allowing public access. The second, that it will not overwhelm the network resources of the production server by shipping multiple copies of the products to multiple customers.

The Origin 3200, which serves as the fileserver, has an attached five terabyte RAID storage system which allows approximately one weeks worth of data to be kept.

4. Risk Reduction for NPOESS

In 2004, the NPOESS Preparatory Project Satellite will be launched as a test bed to validate the new sensors that will be launched as part of the NPOESS (National Polar-orbiting Operational Environmental Satellite System) constellation beginning in 2009. NPOESS combines NASA (National Aeronautics and Space Administration), NOAA (National Oceanic and Atmospheric Administration), and Department of Defense meteorological programs in to a single program for the entire nation. Among the instruments carried aboard NPP and NPOESS will be VIRS (Visible Infrared Imaging Radiometer Suite), and CrIS (Cross-track Infrared Sounder), the follow-on instruments to MODIS and AIRS respectively. These sensors will gather larger datasets than any before.

NANOOK has therefore been tasked as a risk reduction system in preparation for these new sensors. NANOOKs purpose in this regard is to identify the hardware, software, and network configurations that will allow NOAA to handle these extremely large datasets in near-real-time.

NOAA will use MODIS and AIRS data to simulate these high volumes and multi-spectral instruments. NANOOK will then provide real benchmarks for processor performance, data communications, and storage, thus allowing NOAA to generate findings and recommendations for NPP and NPOES planning. These findings will then allow NPP and NPOES to use real-world experiences when making decisions for ground system and instrument science designs.

5. SUMMARY

The NANOOK system has evolved from a basic proof of concept processing system to an operational products processing system for MODIS. Furthermore, not only has the processing increased, but also the physical system: more CPUs, increased storage, and a higher volume communications system. Because of the success of the proof of concept system, the requirements of the system have also grown and the system will be used in risk reduction for the NPP project which is scheduled of launch in 2004.

6. REFERENCES:

Images were created using Granule_Imager version 1.0, developed by Mark Gray (mag@climate.gsfc.nasa.gov) of the MODIS Atmospheres Group at the Goddard Space Flight Center. Modified for Fire Product overlay by Paul Haggerty (Paul.Haggerty@noaa.gov)

AWIPS for Satellite-Derived Hydrometeorological Applications

Roderick A. Scofield and Robert J. Kuligowski
NESDIS/Office of Research & Applications/Hydrology Team
Shuang Qiu
QSSGroup, Inc.
Clay Davenport
I. M. Systems Group, Inc.

Discussion and Outlook

This paper briefly discusses the status and future outlook of satellite - derived products for hydrometeorological applications with an emphasis on heavy precipitation watches and warnings. Due to the presence of Mesoscale Convective Systems (MCS) Data from geostationary (GOES = Geostationary Operational Environmental Satellite) and polar orbiters (microwave data from the Defense Meteorological Satellite Program (DMSP) Special Sensor Microwave/Imager (SSM/I), NOAA/Advanced Microwave Sounding Unit (AMSU), and Tropical Rainfall Measuring Mission (TRMM)) are among the primary sources of information for the diagnosis and prediction of flash floods. GOES has the unique ability to observe the atmosphere and its cloud cover from the global scale down to the storm scale, frequently and at high resolution. Microwave radiances are available on only an intermittent basis, but are strongly related to cloud and atmospheric properties. This places the geostationary satellite and polar microwave derived products at the very heart of weather analysis and forecasting. Thus this suite of satellite products is ideally suited for diagnosing the concatenation of meteorological scales and processes from the global scale to the synoptic scale to the mesoscale and finally to the storm scale. Many heavy precipitation and flash flood events are produced from such an interaction between the various meteorological scales. A conceptual model of a Hydrometeorological Forecast Funnel for satellite products is displayed in Figure 1 (Scofield and Achutuni, 1996). On the global to synoptic scale, GOES derived products such as winds, precipitable water (PW), relative humidity, and stability indices (Hayden et al. 1996) are available to assess the precipitation efficiency of the environment; microwave-derived PW is one of the most accurate and reliable sources of moisture information over the oceans (Ferraro et al. 1998). Synoptic to mesoscale products include the 6.7 mm water vapor imagery and the above mentioned GOES- and microwave-based ones for detecting lifting mechanisms and local area trends in moisture, stability, and boundaries that will initiate, focus, maintain, or dissipate flash flood producing storms (Scofield et al. 2000). On the storm scale, satellite algorithms for estimating precipitation are already in operations and new ones will soon be implemented (Scofield, 1987, Vicente et al. 1998 and Ferraro et al. 1998),. In addition for the storm scale, the following conceptual models and algorithms are being developed: satellite-based conceptual models for determining storm propagation (Corfidi et al. 1996 and Shi Jiang and Scofield, 1987) and soil wetness (Achutuni et al. 1996). This storm scale (especially MCS) can produce energy feedback to the larger scales by altering the circulation, temperature and moisture fields over distances of hundreds of miles (160 km or more) (Maddox et al. 1981). Manifestations of this feedback process from the storm scale to the other scales are: outflow boundaries produced by cold domes of air and mesohighs at low levels, a vortex produced at mid-levels and anticyclonic outflows aloft that can produce jet streaks to the north of the MCS. The future is extremely exciting. The biggest challenges are how to best integrate the various GOES and polar microwave data sets with each other. More accurate and robust algorithms will become operational in the near future as these integrated satellite data sets are combined with other ancillary data platforms.

Acknowledgments

The authors would like to thank Ralph Ferraro of the NESDIS/ORA/Hydrology Team for his review of this paper and Mike Hodges a member of the same team for preparation of the illustration. Finally, we appreciate the efforts of Joan Reed for helping to layout and finalize the manuscript.

References

Achutuni, R., R.A. Scofield, N. Grody, and C. Tsai, 1996: Global monitoring of large area flooding using the DMSP SSM/I soil wetness index. *Proc. Eighth Conf. on Satellite Meteorology and Oceanography*, Atlanta, GA, Amer. Meteor. Soc., 455 - 459.

Corfidi, S.F., J.H. Merritt, and J.M. Fritsch, 1996: Predicting the movement of Mesoscale Convective Complexes. Wea. and Fore., **11**, 41 - 46.

Ferraro, R.R., S.J. Kusselson, and M. Colton, 1998: An introduction to passive microwave remote sensing and

its applications to meteorological analysis and forecasting. *Nat. Wea Dig*, **22**, 11 - 23.

Hayden, C.M., G. S. Wade, and T. J. Schmit, 1996: Derived product imagery from GOES-8. *J. Appl. Meteor.*, **35**, 153 - 162.

Maddox, R.A., D.J. Perkey, and J. M. Fritsch, 1981: Evolution of upper tropospheric features during the development of Mesoscale Convective Complexes. *J. Atmos. Sci*, **38**, 1664 - 1674.

Scofield, R.A., G. Vicente, and M. Hodges, 2000: The use of water vapor for detecting environments that lead to convectively produced heavy precipitation and flash floods. *NOAA Tech. Rept,. NESDIS 99*, U. S. Dept of Commerce, Washington, DC, 64 pp.

Scofield, R.A. and R. Achutuni, 1996: The satellite forecasting funnel approach for predicting flash floods, *Remote Sens. Rev.*, **14**, 251-282.

Scofield, R.A., 1987: The NESDIS operational convective precipitation estimation technique. *Mon. Wea. Rev.*, **115**, 1773-1792.

Shi, Jiang., and R. A. Scofield, 1987: Satellite observed convective system (MCS) propagation characteristics and a 3-12 hour heavy precipitation forecast index. *NOAA Tech. Memor. NESDIS 20*, U.S. Dept. of Commerce, Washington, DC, 43 pp.

Vicente, G., R.A. Scofield, W.P. Menzel, 1998: The operational GOES infrared rainfall estimation technique: *Bull. Amer. Meteor. Soc., Amer. Meteor. Soc.*, **79**, 1883 - 1898.

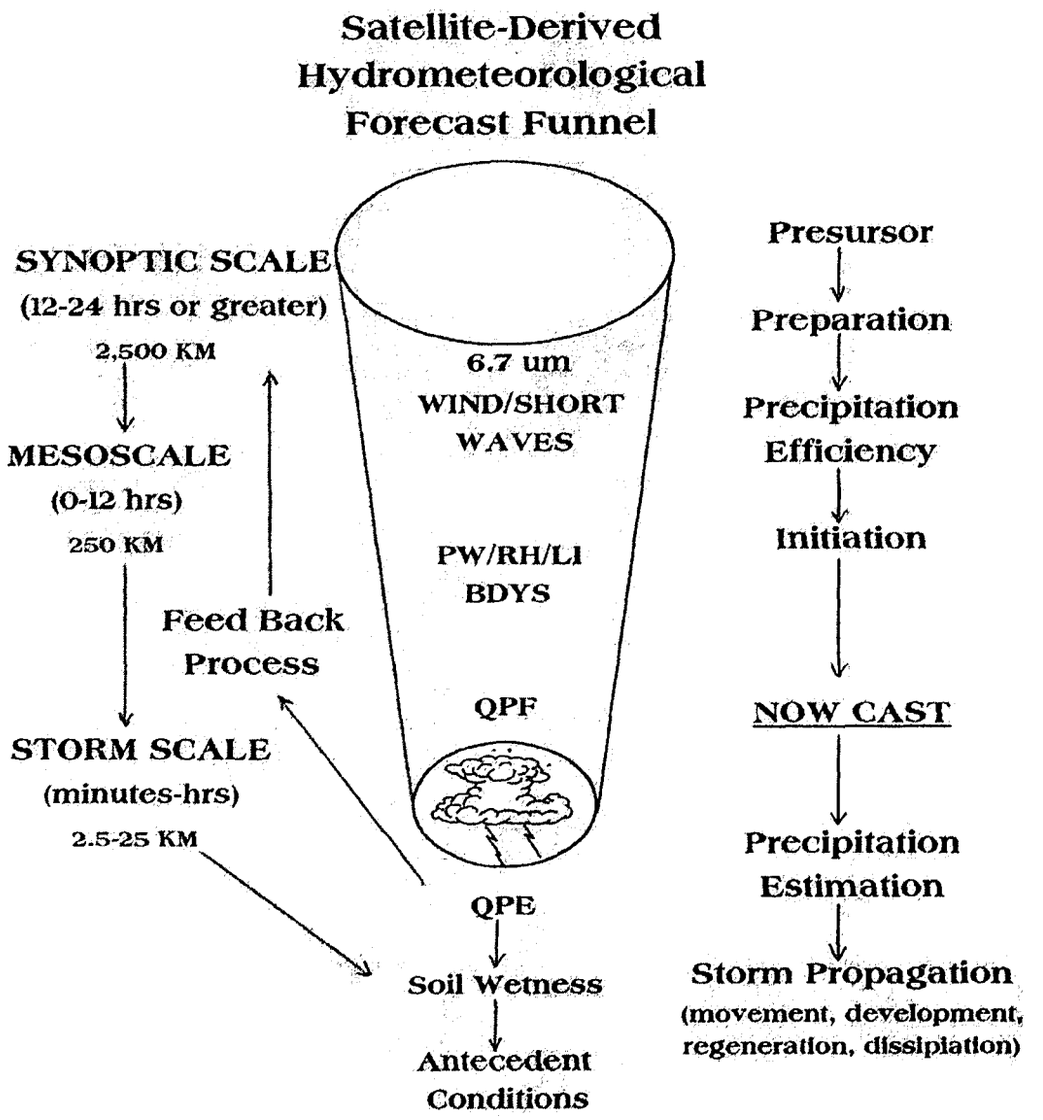

PW = Precipitable Water
RH = Relative Humidity
QPE = Quantitative
Precipitation Estimation

LI = Lifted Index
BDYS = Boundaries
QPF = Quantitative
Precipitation Forecast

Figure 1. Satellite - derived Hydrometeorological Forecast Funnel for applications to AWIPS

NESDIS IPD Model for Developing Production Monitoring Software

AMSU-B, an example

New system developed

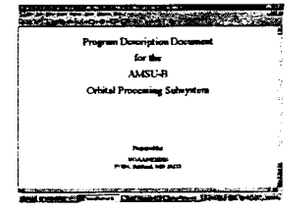

Work with developers on manual monitoring

Test and document manual monitoring

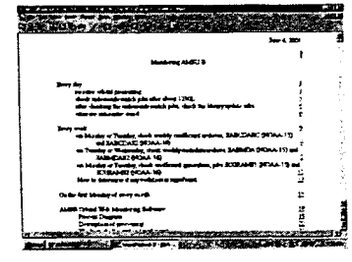

Automate manual monitoring in perl

Automated monitoring graphically

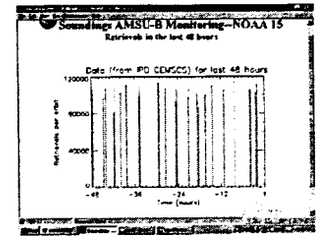

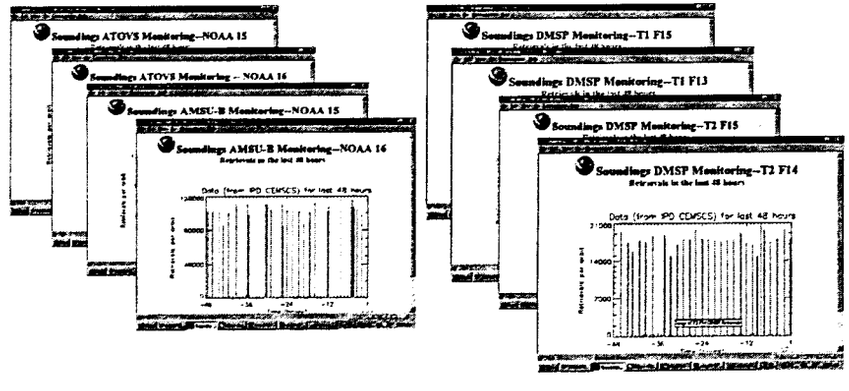

Add to production suite

P1.16 APPLICATIONS OF NOAA MODIS NEAR-REAL-TIME DATA

Kristina Sprietzer, Science and Technology Corporation, Suitland, Maryland *
Paul Haggerty, Science and Technology Corporation, Suitland, Maryland
Gene Legg, National Oceanic and Atmospheric Administration, Suitland, Maryland
Ray Luczak, Computer Sciences Corporation, Suitland, Maryland

1. INTRODUCTION

This poster session will display sample products, example applications, and performance analysis of NANOOK, NOAA's near-real-time processor.

NANOOK is a combined scheduler and processing system for MODIS (Moderate Resolution Imagine Spectrometer) data. NANOOK is a hybrid system containing both a task scheduler and processing control system developed under the CSC Central Satellite Data Processing Center (CSDPC) contract, and a suite of NASA-built product generation software.

NANOOK accepts Rate Buffered Data from EDOS (Earth Observing System Data Operations System) and converts it to the Level 0 data format required by MODAPS (MODIS Adaptive Processing System) science software packages. The scheduler, as written by NOAA is then in charge of managing all incoming and ancillary data, passing the data through various modules of the science code (and additional NOAA produced production code), and proper distribution of all output products.

In order to facilitate accurate forecasting, NOAA has set an objective to provide near-real-time products to various customers using the MODIS instrument. While the products produced by NANOOK are not much different from those produced by NASA, some care must be used in evaluating this near-real-time data. NASA uses more complete and sophisticated data checking and actual (not predicted) ancillary data to produce the most accurate data products for long-term research. However, this delays the final products for periods of time from 3 days to 2 weeks, preventing its use for real-time analysis.

2. APPLICATIONS

MODIS products have been shown to be applicable to the average US citizen by being instrumental in helping save lives and property during a national disaster. During the weeks around Labor Day 2000, forest fires in Montana and Idaho prevented normal reconnaissance flights due to heavy smoke and fire. The National Fire Service turned to NOAA for access to the developmental Level 1B data products being produced by NANOOK. Using the infrared scanners the National Fire Service was able to track the movement and extent of the fires even through the thick smoke. Today, a newly developed fire detection product is being tested which will allow hot spots and potential fires to be detected and identified.

Other MODIS products that will be displayed include more traditional visual images of hurricanes, snow and ice, ocean color, and sea surface temperature products. See the back cover of the 17th International conference IIPS for Meteorology, Oceanography, and Hydrology proceedings for an example of Hurricane Keith.

A web calendar has been created as a means to quickly display thumbnail and low-resolution granule imagery of CONUS and selected regions. This is useful for development purposes to quickly evaluate coverage and data availability. Selected NOAA staff involved in validation of the products can use these pages to determine which data sets to request, thus saving time and bandwidth in large download transfers. Some of this data is available to the public via the OSDPD web server at: *http://www.osdpd.noaa.gov/MODIS*

3. PERFORMANCE OF NANOOK

The problems associated with NANOOK as a near-real-time processing system generally center around the transferring and processing of voluminous data sets. Statistics have been gathered and analyzed to illustrate the problem with latency in retrieving both raw data through the NASA network, and ancillary data which is necessary for improving the quality of the data products.

Lastly, data files are unusually large, thus consuming vast amounts of storage and network bandwidth. Although NOAA has accommodated this problem by acquiring Terabyte RAID storage systems and building Gigabit Ethernet networks to hand the full data flow, the problems will still need to be resolved by NOAA's potential customers, who will need to make sure that adequate storage and network bandwidth are allocated at their local sites to handle whatever products and regions of interest are desired.

Kristina Sprietzer, NOAA/NESDIS/IPD Federal Center FB-4, RM 0303, 4401 Suitland Road, Suitland, MD 20746; e-mail: Kristina.Sprietzer@noaa.gov

3.11 GOES USERS' CONFERENCE RECOMMENDATIONS FOR THE ADVANCED BASELINE IMAGER AND SOUNDER

James J. Gurka*, Gerald J. Dittberner, and Timothy J. Schmit
National Environmental Satellite, Data and Information Service (NESDIS)

1. INTRODUCTION

The GOES Users' conference was held from May 22 through 24, 2001 in Boulder Colorado, with close to 200 participants from government, the private sector, academia and the international community. It was organized by the National Oceanic and Atmospheric Administration (NOAA) with cooperation of the National Aeronautics and Space Administration (NASA), the American Meteorological Society (AMS), the National Weather Association, the World Meteorological Organization, and the National Institute of Standards and Technology.

The goals of the conference were: (1) to inform GOES users of plans for the next generation (GOES R Series) capabilities; (2) to provide information on the potential applications; (3) to determine user needs for new products, data distribution, and data archiving; (4) to assess potential user and societal benefits of GOES capabilities; and (5) to develop methods to improve communication between the National Environmental Satellite, Data, and Information Service (NESDIS) and the GOES user community. Sessions included: Planned and Potential Sensors for U.S. Geostationary Satellites; User Requirements, Applications, and Potential Benefits from Future GOES; Future International Geostationary Satellites; and Communications, Ancillary Services and Training Issues. The third day of the conference consisted of facilitated breakout sessions in which the user community was asked to provide input to ten questions on their future needs for products, services, data distribution, archiving, training and potential benefits of the next generation GOES to their operations and to society.

This paper will provide a summary of the recommendations provided by the GOES user community, focusing on the Advanced Baseline Imager (ABI) and Sounder (ABS).

2. POTENTIAL BENEFITS

During the breakout sessions on the third day, the first question dealt with potential benefits of the GOES program. Specifically: "Considering the information presented during this conference regarding the potential benefits and service improvements of GOES, can you foresee additional savings in terms of life, injury avoidance or protection of property? Please indicate the three most important benefits to your program or to society."

Respondents indicated that planned improvements for the next generation GOES would lead to significant improvements in detection of atmospheric moisture and improved quality of satellite derived winds, leading to improved numerical model performance. This together with subjective use of the improved satellite data and products by forecasters, will result in more timely and accurate weather forecasts, including: improvements in tornado warnings; forecasts of hurricane landfall; forecasts of flooding; and forecasts that provide much more detail.

The improved forecasts in general will lead to preservation of life and property; improved quality of life due to better recreational planning; improved safety and economic benefits to commercial, military and general aviation; improved management of energy resources; improved planning and management of ground and marine based transportation; improved fisheries management; improved guidance for State Emergency Managers; cost savings for agricultural applications from better planning of watering, and application of pesticides, herbicides and fertilizers; improved management of water resources and flood control; and improved military operations due to improved forecasts for trafficability, weapons trajectories, ship and plane sorties for storm avoidance, and aircraft carrier operations.

To ensure the realization of these benefits, the conference participants provided numerous recommendations regarding the ABI and ABS. Their recommendations are in the following sections.

3. ADVANCED BASELINE IMAGER

One of the strongest messages coming out of the Conference was that a minimum of twelve spectral channels on the imager will be required to meet the needs of a wide cross section of the user community. These channels should include the following: a) 0.64μ for daytime detection of clouds; b) 0.86μ for daytime detection of clouds, aerosols, vegetation and ocean properties; c) 1.375μ for daytime detection of thin cirrus; d) 1.6μ for distinguishing clouds from snow and water cloud from ice cloud (daytime only) e) 3.9μ for detection of fires, and nighttime detection of low clouds and fog; f) 6.15μ for detecting upper tropospheric moisture and determining upper level flow; g) 7.0μ for detecting mid tropospheric moisture and determining mid level flow; h) 8.5μ determining cloud phase, detecting sulfuric acid aerosols and determining surface properties; i) 10.35μ for determination of cloud particle size and surface properties; j) 11.2μ for detection of clouds, generating

* Corresponding author address: James J. Gurka, NOAA/NESDIS, FB-4, room 3010B , 5200 Auth RD., Suitland, MD 20746-4304;
email: james.gurka@noaa.gov

cloud drift winds, and determination of low level water vapor. k) 12.3μ for detection of volcanic ash, low level water vapor, and sea surface temperatures; and l) 13.3μ for determining cloud-top parameters and determining cloud heights for improved quality cloud drift winds.

In addition to these channels, which are considered absolutely essential, there was a strong recommendation for at least two additional channels: the 0.47μ and the 9.6μ. The 0.47μ channel would be valuable for generating true color images, and for detecting aerosols and haze in determining slant range visibility for aircraft operations. The 9.6μ channel would be important for detecting ozone and for the detection and forecasting of clear air turbulence. Beyond these channels, providing they would not result in major additional sensor complexity or expense, a 4.57μ channel would be useful for improved determination of precipitable water and a 14.2μ channel would be valuable for more accurate cloud top heights. However, these products will also be generated by the hyperspectral sounder on the GOES-R series.

The participants strongly endorsed plans for improved spatial and temporal resolution. Current plans call for 0.5 km spatial resolution (at satellite subpoint) for the 0.64μ channel and 2 km resolution for all other channels. Since there will be more quantitative applications for both the visible and IR channels, there was a recommendation that the resolution of the .86μ channel match the 0.5k resolution of the 0.64μ channel. Also, the visible channels should be calibrated on-board.

Participants voiced the need for improved temporal resolution to meet the need for simultaneous global, synoptic and mesoscale imaging needs. The ABI should be capable of providing full disk images every 5 minutes and a 1000km X 1000km area every 30 seconds.

4. ADVANCED BASELINE SOUNDER

For geostationary soundings to provide a truly useful complement to other observing systems, they must yield continuous, reliable, high spectral resolution data in the following locations: (1) areas not observed by other data sources (e.g., over the coastal waters and open oceans), (2) near gradients of data when these gradients occur between observations derived from other sources of data, and (3) between temporal gaps of polar-orbiting satellite observations, providing complete observations of the diurnal cycle. This is true for the radiances, the soundings themselves, and the derived sounding product images. Future GOES sounders must be capable of covering much larger areas every hour to satisfy the observational needs over both the continental U.S. and the data-sparse ocean areas.

While NWS forecasters find the products from the present GOES Sounder to be valuable observational tools in the forecast process (Schmit et al. 2001), and continue to develop more operational uses for the data, the relatively coarse vertical resolution of the filter wheel sounder limits its value for some applications. The present generation of GOES sounder is limited to a 2-3°C accuracy over a 3 to 5 km layer. Broderick et al. (1981) illustrates how soundings from radiometers with poor vertical resolution can easily miss meteorologically important features such as temperature inversions and dry/moist layers. The availability of GOES-derived soundings with improved vertical and temporal resolution would greatly enhance the ability to initialize numerical models with more realistic observational assessments of temperature, water vapor and wind (Aune et al. 2000).

The recurrent message from the conference participants, was that while the current filter wheel sounder provides valuable information for both numerical models and for subjective use in the forecast offices, future applications will require a much faster coverage rate for the sounder with much improved spectral and spatial resolution. For numerical applications in the 2010 time frame, models with much improved physics and a spatial resolution of 1 to 2 km, will demand detailed information on clouds, moisture and surface specifications as well as tendencies. In the seamless suite of products from the National Centers for Environmental Prediction (NCEP), with its essential climate, weather and water linkages, all model applications are essentially driven by the global model system, which in turn is driven by global observations, including observations from both polar and geostationary satellites. Improved spectral and spatial coverage of future GOES Sounders will be critical to meeting the National Weather Service's (NWS) future goals for numerical weather prediction, objective nowcasting and real time forecaster products.

The specific user recommendations for the ABS follow:

1) Coverage rate should be much faster than the current sounder to eliminate the conflict between global and mesoscale observations. It should be able to scan an area close to full disk within one hour.
2) It should be capable of operating in a rapid scan mode, sacrificing areal coverage for greater temporal resolution over a limited area when needed.
3) It should have a field of view no larger than 4 km, to allow for more observations between clouds.
4) It should be able to detect temperature inversions, which are critical for severe weather forecasting.
5) Calibration information and algorithms to generate products should be made available to the user community.
6) Soundings are needed in cloudy areas. Conventional GOES clear air soundings should be supplemented either by a microwave sounder in geostationary orbit, or with GOES IR soundings above the clouds and polar microwave soundings.
7) Funding for research and development of new satellite products should be part of the satellite acquisition budget.
8) For developing new satellite products there should be improved collaboration between research and operations.
9) In operations there is a need for a blend of data and products from operational and research satellites.

If their recommendations are met, the user community expects that the ABS will: 1) depict water vapor as never before by identifying small scale features

of moisture vertically and horizontally in the atmosphere; 2) track atmospheric motions much better by discriminating more levels of motion and assigning heights more accurately; 3) characterize the life cycle of clouds and distinguish between ice and water cloud, and identify cloud particle sizes; 4) accurately measure surface temperatures (both land and sea) by accounting for emissivity effects; and 5) distinguish atmospheric constituents with improved certainty, including volcanic ash, ozone, methane and other trace gases.

5. NEW IMAGER AND SOUNDER PRODUCTS

With the expected improvements for the ABI and ABS, the user community suggested the following new or improved products be developed for operational use: a) atmospheric aerosols; b) cloud phase; c) cloud particle size; d) surface properties; e) improved satellite derived winds; f) moisture flux; g) improved quantitative precipitation estimates; h) improved volcanic ash product; i) clear air turbulence threat areas; j) cloud emissivity; j) improved low cloud and fog product; k) cloud layers; l) probability of rainfall for each pixel; m) improved sea surface temperature product; n) true color product; o) cloud optical depth; p) sulfur dioxide concentration (precursor to volcanic eruption); q) aircraft icing threat; r) ocean color; s) under (ocean) surface features (i.e. coral reefs); t) improved sea ice products; u) improved vegetation index; v) ozone layers; and w) surface emissivity.

6. DATA DISTRIBUTION

The current GOES transmits data with a rate of 2.1 Mbits per second. The GOES-R series, with thousands of bands on the sounder, as well as more channels on the imager with higher spatial and temporal resolution, the data rates will increase to 20 to 80 Mbits per second, depending on the amount of data compression used. Options include land line distribution, commercial satellite distribution, or rebroadcast from the GOES. The current L band broadcast may have to be changed to an X band transmission (which has problems with rain fade and low angle reception). This would require completely new reception equipment. The current L band is also the only approved method of transmission while the satellite is moving into position from a storage location. The conference participants were asked to convey their needs for data distribution and provide suggestions for optimum methods of distribution.

Some recurring themes among the user responses include: 1) There is a wide spectrum of user needs with different tiers of data access. There should be a full range of methods of reception to accompany the broad range of data requirements. 2) Data distribution should be timely and have low cost and low data rate options available. 3) Data distribution options that should be considered include: a) commercial satellite broadcast; b) direct broadcast from GOES; c) Internet; d) dedicated land lines. e) data acquisition by users from a central location; and f) some combination of "a" through "e". 4) Re-use existing ground station assets and broadcast a subset of the ABI/ABS data streams from decommissioned GOES satellites.

7. DATA AND PRODUCT ARCHIVE NEEDS

The breakout groups recommended that a full spectrum of GOES products, ranging from raw data to highly processed products be available in an archive for applications ranging from the nowcasting scale to the climate scale. The products should be stored in a user friendly format, allowing for easy remote access at minimal cost to the user. The user must also have access to metadata, including information on data and product quality trends due to variations in instrument or satellite performance. Users should be able to browse, select and submit requests for products via the internet. Potential options for product distribution to the users include: File Transfer Protocol (FTP) for electronic transfer, CD-ROMs, and DVDs. Turnaround for most data requests should be less than 1 day, while one week should be allowed for extremely large requests (i.e. years worth of data).

8. NEW DATA INTEGRATION

Participants of the workshop provided several recommendations on ways to minimize the time required for integrations of the GOES-R data stream into operations: 1) leverage data from relevant instruments on other satellites to better understand GOES-R capabilities (i.e. use the Atmospheric Infrared Sounder (AIRS) and the Geostationary Imaging Fourier Transform Spectrometer (GIFTS) data to prepare for ABS; use the Moderate Resolution Imaging Spectroradiometer (MODIS) to simulate ABI data); 2) provide correctly formatted sample data sets to the user community at least one year prior to the GOES-R launch; 3) requirements for operational algorithms should be identified by the spring of 2002; 4) operational algorithms should be developed 3 to 5 years prior to launch; 5) establish a working group to develop plans to provide sample data sets and for development of new operational algorithms; 6) NOAA should invest in education, training, research, and product development to ensure optimal use of GOES-R products shortly after launch; 7) provide an extended scientific checkout period following the GOES-R launch to allow use of current data and to ease the transition to new data sets. 8) NOAA should have in place a fully operational infrastructure for reception, distribution, processing, and archiving, ready for use with test data sets prior to the GOES-R launch.

9. EDUCATION OF USER COMMUNITY

To ensure maximum return on the investment in the next generation GOES, the breakout groups recommended a comprehensive education program for all levels of GOES users, including: forecasters, emergency managers, recreational users, academia, the media, industrial users, and commercial users. Education programs should be funded as part of the end-to-end GOES program budget.

Methods of education should include: 1) conferences and workshops; 2) web-based training; 3) teletraining; 4) CD-ROM or DVD based training; 5) brief segments on the Weather Channel; 6) educational packages appropriate for Congress, upper level management, and business leaders.

10. SUMMARY AND CONCLUSIONS

The GOES Users' Conference was a good initial step for improving communication between NESDIS and the GOES User Community. Participants strongly supported a continuation of the process promoting a two way dialogue between GOES users and those planning the development of the next generation GOES.

The participants strongly voiced the requirement for improvements in spectral, spatial, and temporal resolution in both the future Imager and Sounder. Observations should be relevant for all spatial scales, from the global to the mesoscale, for multi-discipline applications in meteorology, climatology, hydrology and oceanography. In order to meet the needs of a wide cross section of the user community, at least 12 imager channels will be required with .5 km resolution in the visible channels and 2 km resolution in the IR channels.

The Sounder should provide observations approaching radiosonde quality. It should: 1) provide an accurate three-dimensional picture of atmospheric water vapor; 2) determine atmospheric motions much better by discriminating more levels of motion and assigning heights more accurately; 3) distinguish between ice and water cloud and identify cloud particle size; 4) provide a field of view no greater than 4 km to provide better viewing between clouds and near cloud edges; 5) provide accurate land and sea surface temperatures and characteristics by accounting for emissivity effects; 6) distinguish atmospheric constituents with improved certainty, including volcanic ash, ozone, and methane; and 7) detect atmospheric inversions.

These improvements in the imager and sounder should lead to improved service to the user community, including: 1) improved quantitative precipitation forecasts; 2) reduced size of geographic areas affected by watches; 3) improved early detection of severe weather and flash floods; 4) improved forecasts of hail and hail size; 5) improved prediction of fog formation and dissipation; 6) improved forecasts of microburst potential; 7) improved forecasts of mesoscale convective systems; and 8) improved forecasts of hurricane intensity and motion.

11. ACKNOWLEDGMENTS

The authors would like to thank all the participants of the GOES Users' Conference, especially the Program Committee, the speakers, participants of the breakout sessions, NIST personnel for logistic support, and all those who provided valuable suggestions for improving the future GOES program. The authors would also like to thank Dick Reynolds and Anthony Mostek for reviewing the manuscript.

12. REFERENCES

Aune,R.M., W.P. Menzel, J. Thom, G.M. Bayler, A. Huang, and P. Antonelli, 2000: Preliminary findings from the geostationary interferometer observing system simulation experiments (OSSE). NOAA/NESDIS Tech. Rep. 95, 18 pp.

Broderick H.,C . Watkins and A. Gruber, 1981: Statistical and synoptic evaluations of TIROS-N and NOAA-6 retrievals. NOAA Tech. Report NESS 86, Washinton, D.C.

Li, J., T.J. Schmit, H.L.. Huang, and H.M. Woolf, 2001: Retrieval of atmospheric inversions using geostationary high-spectral-resolution sounder radiance information. 11th Conference on Satellite Meteorology and Oceanography, 15-18 October, Madison, WI.

Schmit, T.J., W.F. Feltz, W.P. Menzel, J. Jung, A.P. Noel, J.N. Heil, J.P. Nelson III, G.S. Wade, 2001: Validation and use of GOES sounder moisture information, Submitted to Wea Forecasting.

4.3 A COMPARISON OF GOES AND AMSU BASED TOTAL PRECIPITABLE WATER RETRIEVALS

[1]Jaime Daniels* and [1]Ralph Ferraro

[1]NOAA/NESDIS/Office of Research & Applications/Atmospheric Research & Applications Division
Camp Springs, MD

1. INTRODUCTION

Satellite-derived total precipitable water (TPW) products from both infrared (IR) and microwave (MW) sensors provide an invaluable source of information on atmospheric moisture for use by weather forecasters and numerical weather prediction (NWP) models. This is particularly true over the oceanic regions where little other observational moisture data is available (Ferraro, et al, 1998). Forecasters on the west coast of the United States, for example, rely heavily on satellite-derived moisture products to depict expansive moisture plumes emanating from the Pacific Ocean. These moisture plumes significantly impact the duration and intensity of rainfall events on the west coast. Satellite-derived estimates of TPW also provide critical initialization input to NWP assimilation systems.

A number of viable satellite TPW products are available from both the GOES and polar orbiting DMSP and NOAA satellites. The purpose of this study is to compare the operational GOES sounder TPW and the NOAA-15 Advanced Microwave Sounding Unit (AMSU) TPW products and to characterize observed similarities and differences.

An eventual goal of this study would be to yield insight as to under what conditions each of these products work best, and determine random and systematic errors for each technique that can lead to a formal "blending" mechanism for improved AWIPS products and NWP model assimilation.

2. ALGORITHMS

The GOES sounder TPW product is derived using a simultaneous physical retrieval algorithm (Ma et al., 1999). The products are generated using clear radiance observations from the GOES sounder (channels 1-8 and 10-16), a space and time interpolated first guess temperature and moisture profile from a short-term Aviation (AVN) model forecast, an objective analysis of hourly surface observations, and an estimate of surface skin temperature and emissivity. The experimental GOES TPW retrievals used in this study are computed at each sounder field-of-view (FOV) having a horizontal resolution of 10 km. GOES soundings are computed from GOES-8 and GOES-10 measurements every hour over the continental United States and adjacent waters.

*Corresponding author address:
Jaime M. Daniels, E/RA2
NOAA/NESDIS/Office of Research & Applications
5200 Auth Road, Room 601
Camp Springs, MD 20746

The NOAA-15 AMSU derived TPW was initially based on a scheme developed by Grody et al (2000) and utilizes measurements at 23.8 and 31.4 GHz. It is valid over ocean only. The spatial resolution is 45 km at nadir. The AMSU TPW algorithm was recently revised and implemented into operations during August 2001 for both NOAA-15 and NOAA-16. Two changes were made from the original algorithm. The first and most important is a physically consistent retrieval scheme (Weng et al, 2000) that simultaneously retrieves TPW, cloud liquid water and rain rate. The second change over the original algorithm is the use of ocean surface wind speeds from the Aviation (AVN) NWP model from the National Center for Environmental Prediction (NCEP). Use of the AVN surface wind speeds have a second order effect on the AMSU TPW retrievals.

The GOES and AMSU products are complimentary in nature. The GOES is generated hourly, but is limited to clear regions, while the AMSU is available only twice a day from NOAA-15, but is retrieved under all weather conditions (except heavy rain) over ocean.

3. METHODOLOGY

GOES-8, GOES-10 and NOAA-15 AMSU TPW products were collected and co-located in time (within 15 minutes) and space (within 10km). AMSU TPW retrievals closest to the GOES TPW retrievals were saved to a database. Some quality control was applied to the matchup process including removal of AMSU retrievals that were contaminated by coastlines and/or rain measurements (based on the AMSU retrieved rain rate). Because of the overpass time of the NOAA-15 (730 and 1930 local time), the GOES-8 matchups were restricted to 0-2 GMT and 12-14 GMT, and the GOES-10 were between 2-5 GMT and 15-19 GMT. Variations in the number of matchups each day were found as a result of the amount of cloudiness which prevents the calculation of GOES retrievals.

4. RESULTS

Results from an earlier comparison of GOES and AMSU TPW retrievals from June 2000 showed excellent agreement. Slightly different versions of the GOES and AMSU retrieval algorithms were used in these early comparisons and are described in Ferraro and Daniels, 2000. Figure 1 shows a scatter diagram of GOES-10 TPW versus NOAA-15 AMSU TPW. The mean GOES-10 and NOAA-15 AMSU TPW values were within 1mm and the correlation coefficient between the two datasets was 0.92. The comparison between GOES-8 and NOAA-15 AMSU TPW retrievals showed a similar result. Figure 2 shows GOES-10 TPW retrievals plotted over GOES-10 infrared

window imagery at 17Z on June 18, 2000. NOAA-15 AMSU retrievals are contoured overtop of this image. One first observes that the GOES retrievals are available only in cloud-free regimes. Excellent agreement is observed between the GOES and AMSU TPW retrievals and both datasets successfully capture existing moisture gradients.

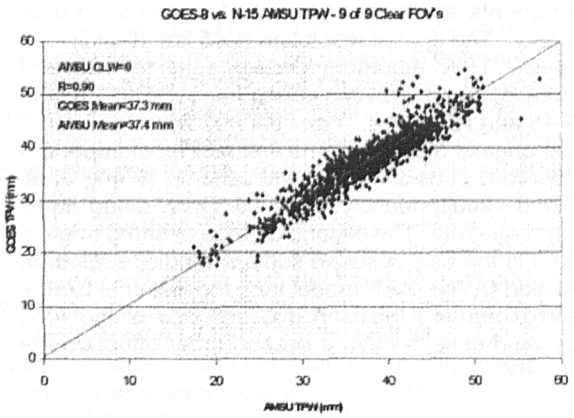

Figure 1. GOES-10 TPW retrievals (in mm) on the y-axis versus NOAA-15 AMSU TPW retrievals (in mm) on the x-axis.

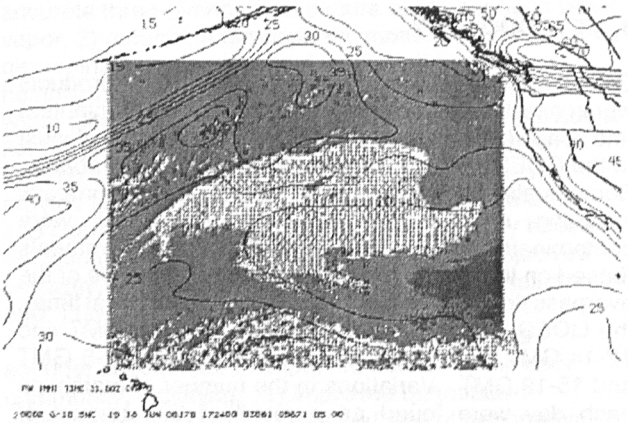

Figure 2. GOES-10 TPW retrievals plotted over infrared window imagery. NOAA-15 AMSU TPW retrievals are contoured.

A similar comparison of retrieved GOES and AMSU TPW products was done for July-August 2001, but with the updated algorithms described in Section 2 above. The GOES TPW retrievals used in this updated analysis are at the full resolution of the GOES sounder and offer improved spatial coverage. For example, retrievals are available closer to cloud edges and in clear areas between scattered cloud cover. Improvements in the AMSU TPW algorithm result in better TPW products. Preliminary comparisons for a three day period in July 2001 show that the GOES and AMSU TPW values agree within 0.1mm. At the time of this writing, the analysis of these datasets was ongoing. Results of this analysis will be presented at the conference.

5. SUMMARY

Comparison between GOES and AMSU retrieved TPW show excellent agreement. An earlier assessment of these dataset was done on data collected from June 2000. More recent changes to both the GOES and AMSU retrieval algorithms has been done. As a result, another comparison of the retrieval products is underway for data collected in July-August 2001. The analysis of these data is currently underway and will be presented at the conference.

6. REFERENCES

Ferraro, R.R. and J. Daniels, 2000: A Comparison of GOES and AMSU Based Total Precipitable Water Retrievals. *Fifth Sympsium on Integrated Observing Systems, Albuquerque, NM, Amer. Meteor. Soc, 130-131.*

Ferraro, R.R., S.J. Kusselson, and M. Colton, 1998: An introduction to passive microwave remote sensing and its applications to meteorological applications to meteorological analysis and forecasting. *Nat. Wea. Dig.*, **22 (3)**, 11-23

Grody, N., J. Zhao, R. Ferraro, F. Weng, 2000: Determination of precipitable water and cloud liquid water over oceans from the NOAA-15 AMSU. *In Press, J. Geophys. Res.*

Ma, X.L., T.J. Schmit, and W.L. Smith, 1999: A nonlinear physical retrieval algorithm-Its application ot the GOES-8/9 Sounder. *J. Appl. Met.*, **38**, 501-513.

2.2 STATUS AND OUTLOOK OF OPERATIONAL SATELLITE PRECIPITATION ALGORITHMS FOR EXTREME PRECIPITATION EVENTS

Roderick A. Scofield and Robert J. Kuligowski
NOAA/NESDIS/ORA/Hydrology Team
Camp Springs, MD

1. INTRODUCTION

This paper briefly describes the status and outlook of operational satellite precipitation algorithms for extreme precipitation events. From 1978 through 2000, Satellite Precipitation Estimates (SPE's) for flash floods were produced by a combination of manual effort and computer algorithms via the Interactive Flash Flood Analyzer (IFFA), and their primary application was to alert forecasters and hydrologists of the potential for heavy precipitation and flash floods. For the past several years, efforts have been focused on automating SPE's in order to increase both their timeliness and their applicability. In addition to their present status as an "alert tool", SPE's will one day be directly incorporated into a number of prediction estimation and forecasting products, including:

- the Stage III multi-sensor analysis (Fulton et al. 1998),
- hydrologic models that are run at local River Forecast Centers (RFC's),
- numerical weather prediction models—to improve quantitative precipitation forecasts (QPF),
- cloud models that in turn will provide precipitation estimates.

2. INTERACTIVE FLASH FLOOD ANALYZER (IFFA)

The NOAA/NESDIS Satellite Analysis Branch (SAB) produces quantitative precipitation estimates (QPE) (Borneman 1988; Kuligowski 1997) and outlooks for field forecasters using the Interactive Flash Flood Analyzer (IFFA) technique (Scofield and Oliver 1977; Scofield 1987). The IFFA, which was designed for highly intense precipitation events, uses GOES-based satellite data because of their high spatial and temporal resolution. SAB forecasters determine which portions of convective clouds are active based on changes between consecutive GOES infrared (IR) and visible (VIS) images, and then apply the IFFA technique as a basis for drawing isohyets of estimated rainfall from the active clouds. The resulting estimates are adjusted for overshooting cloud tops, cloud mergers, available moisture, low-level inflow, and the speed of the storm. A rain burst factor helps to account for extremely heavy rainfall that can occur in the incipient stages of a Mesoscale Convective Systems (MCS). Also, since the original IFFA algorithm was designed for cold-top convection (colder than -58 °C), the equilibrium level temperature is used to adjust for warm tops (Scofield and Oliver 1987).

These QPE's are also extrapolated to produce 3-h precipitation forecasts (outlooks) (Spayd and Scofield 1984), taking into account the growth, decay, and movement of individual convective systems (Shi and Scofield 1987; Juying and Scofield 1989). SAB's SPE's and outlooks are sent out via AWIPS (Advanced Weather Interactive Processing System); graphics of the estimates are also available on the Satellite Services Division home page (http://www.ssd.noaa.gov/PS/prodnsvcs.html). However, due to the manual/interactive nature of the IFFA methodology, these SPE's cover limited areas over limited periods of time and can take a significant amount of time to produce.

3. THE AUTO-ESTIMATOR (A-E) AND THE HYDRO-ESTIMATOR (H-E)

In order to improve the spatial and temporal coverage of SPE's and increase their timeliness, NESDIS/ORA has developed an automatic SPE algorithm for high-intensity rainfall called the Auto-Estimator (A-E). The original A-E developed by Vicente et al. (1998) uses 10.7-μm brightness temperatures and their spatial gradients and time changes at 30-min intervals, plus a precipitable water (PW)/relative humidity (RH) adjustment using data from the Eta model. During 1998 and 1999, a number of enhancements were added to this algorithm:

- using 15-min imagery instead of 30-min (note that IFFA still uses 30-min imagery because production of the estimates is quite labor-intensive);
- using 15-minute WSR-88D data to screen out nonraining cold cloud;
- an equilibrium level temperature adjustment (from the Eta model) for warm-top convection modeled on Scofield and Oliver (1987);
- parallax and orography adjustments (Vicente et al. (2001).

The A-E is used to produce real-time estimates of both instantaneous rainfall rates and accumulations over 1, 3, 6, and 24 h. These estimates can be accessed via the NOAA NESDIS Flash Flood Home Page (http://orbit35i.nesdis.noaa.gov/arad/ht/ff).

Another version of the A-E, called the Hydro-Estimator (H-E), has been developed with two significant new features:

1. a new screening technique that separates raining and non-raining pixels according to the difference between the pixel 10.7-μm brightness temperature and the mean value of the surrounding pixels, and also uses this difference to adjust the relationship between brightness temperature and rainfall rate in the raining pixels;
2. Separate adjustments for PW and RH that improve the handling of stratiform events with embedded convection.

In June 2001, the A-E became operational and began to replace some of the functions of the IFFA, especially for convective events. SAB meteorologists

*Corresponding author address: Roderick Scofield, 5200 Auth Road WWB/601, Camp Springs, MD 20746-4304; e-mail: Roderick.Scofield@noaa.gov

have indicated that the A-E has significantly increased their productivity: they can monitor a greater number of heavy rainfall systems than before and disseminate a greater number of satellite precipitation estimation messages (called SPENES) in a more timely fashion than before. In some cases SPENES's were issued prior to the actual onset of flooding, allowing National Weather Service (NWS) Forecast Offices to issue appropriate warnings in a timely fashion. Though the performance of the A-E is slightly superior to that of the H-E by some measures (see below), the H-E was recently chosen for implementation on AWIPS. This is in part because the NWS Office of Hydrologic Development (OHD) has a requirement for SPE's that are outside the area of coverage, making the A-E with its dependence on radar inappropriate for their applications.

4. THE GOES MULTI-SPECTRAL RAINFALL ALGORITHM (GMSRA)

In addition to the A-E and H-E, NESDIS has been developing and testing the GMSRA (Ba and Gruber 2001), which uses all five GOES channels in an effort to improve the screening of anvil debris cirrus and to improve precipitation estimation from stratiform events:

- A threshold albedo value from the visible channel to screen out thin cirrus;
- Difference between the 6.9-μm and 10.7-μm brightness temperature to distinguish overshooting tops from anvil cirrus;
- A 3.9-μm reflectance derived from 3.9-, 10.7-, and 12.0-μm radiance data that is related to cloud particle size and used to screen out clouds with small particles (effective radius of less than 15 μm);
- Changes in 10.7-μm brightness temperature to infer cloud growth rate.

Once the cloud screening is performed, both the probability of precipitation and the conditional rain rate are computed from the 10.7-μm brightness temperaturewith different calibrations for different regions. An adjustment for subcloud evaporation similar to that used in the A-E is also made.

A nighttime cloud screening is used in a second version of the GMSRA. At night, clouds are considered to be raining only if the difference between the 10.7 mm and 12.0 mm is below a certain threshold value and the difference between the 3.9 mm and 10.7 mm exceeds a certain threshold.

5. PRECIPITATION ESTIMATES FROM POLAR ORBITAL SATELLITES (POES)

Microwave radiances are more directly related to precipitation than VIS and IR radiances (Ferraro, et. al., 1996, 1997, 2000)–while the latter reflect the properties of the cloud tops, the former are a function of the distribution of water and ice within the cloud itself. However, at this point microwave instruments are limited to polar-orbiting platforms such as the Defense Meteorological Satellite Program (DMSP) satellites that carry the Special Sensor Microwave Imager (SSM/I), and the NOAA polar orbiters that carry the Advanced Microwave Sounding Unit (AMSU).

Scattering-based estimation techniques, which can be used over land and water, rely on the fact that ice particles in clouds cause backward scattering of upwelling terresrial radiation, and thus decrease the brightness temperature over a radiometrically warm background. A more direct estimate of rainfall rate can be obtained using emission-based techniques: liquid precipitation causes brightness temperature increases over a radiometrically cold background. However, this approach is useful only over ocean surfaces, since the emissions from radiometrically warm land surfaces are virtually indistinguishable from the radiation signature of the liquid precipitation.

SAB meteorologists are currently using POES-microwave derived precipitation estimates to compute rainfall potentials from tropical cyclones prior to landfall (Kidder et al. 2001; Scofield et al. 2001; WMO 1999), and from heavy precipitation-producing cloud bands entering the west coast during the winter season.

6. GOES + POES PRECIPITATION ALGORITHMS

Precipitation estimates from GOES- and POES-based instruments possess a number of complementary strengths and weaknesses. While IR/VIS-based estimates from GOES are indirect, in that the characteristics of the cloud tops are used to infer the rate of rainfall, microwave-based estimates from POES are based on the concentration of water and ice within the cloud. However, these POES-derived estimates are much less frequent and have lower spatial resolution than the GOES data, making the GOES data necessary for analyzing heavy precipitation associated with mesoscale structures embedded within Mesoscale Convective Systems (MCSs), tropical cyclones, and extratropical cyclones.

Consequently, the next step is to combine the GOES with the POES in developing precipitation algorithms applicable to heavy precipitation and flash flood producing systems. Previous POES-GOES algorithms have been developed for global (e.g. Adler et al. 1994) and regional (e.g. Vicente 1994; Turk et al. 1998; Sorooshian et al. 2000) usage. Plans are underway to develop a methodology similar to one of these regional algorithms. The first (Vicente 1994) uses linear regression to find the relationship between GOES 10-7-μm brightness temperatures and microwave rain rate estimates when they are coincident in time and space. This relationship can be maintained until the next POES pass, or adjusted according to the time since the most recent pass. The second approach (Turk et al.1998) matches the cumulative distribution functions of the brightness temperatures and microwave rain rates to update the relationship between the two. NESDIS is currently testing and evaluating a form of this algorithm that has incorporated some of the A-E enhancements such the PW/RH adjustment, the radar-based screening of nonraining cloud pixels, and the parallax adjustment. This algorithm uses microwave estimates from SSM/I, AMSU, and the Tropical Rainfall Measuring Mission (TRMM) Microwave Imager (TMI) (Kummerow et al. 1998) for calibration. The third algorithm (Sorooshian et al. 2000) is called PERSIANN (Precipitation Estimation from

Remotely Sensed Information using Artificial Neural Networks) and uses neural networks to relate characteristics of the 10.7-μm brightness temperature field to TMI rain rate estimates. NESDIS scientists are working with the PERSIANN developers to validate and improve this algorithm.

NESDIS/ORA is also developing the Self-Calibrating Multivariate Precipitation Retrieval (SCaMPR) (Kuligowski 2001) technique that combines the strengths of both GOES and microwave. Unlike the aforementioned GOES-POES techniques that rely on data from a single GOES channel, the SCaMPR algorithm considers data from a number of GOES channels and derived parameters to both distinguish raining from non-raining pixels and to estimate rainfall rate for raining pixels. Both the selection of input parameters and their calibration are performed using statistical techniques.

As additional polar satellites with microwave sensors are launched the relationships between GOES data and microwave-based rain rate estimates will be able to be updated more frequently–perhaps every 2-3 hours. A challenge will be to fine-tune these multi-channel, multi-sensor algorithms for application to the mesoscale in order to provide realistic precipitation estimates for flood and flash flood analysis and prediction.

7. TWO EXAMPLES OF EXTREME RAINFALL EVENTS

7.1 Tropical Storm Allison (5-6 June 2001)

Tropical Storm Allison produced extremely heavy rainfall from eastern Texas across the Gulf States and along the Mid-Atlantic Coast, resulting in the most extensive flooding ever associated with a tropical storm. In the Houston, Texas metropolitan area, more than 30 inches (750 mm) of rain were reported at several locations with at least 22 fatalities and nearly $2 billion in damage estimates.

Table 1 is an example of ongoing validation being performed at NESDIS for a number of GOES and GOES-POES precipitation algorithms (Kuligowski et al. 2001). The NESDIS verification program has initially compared six variations of four satellite precipitation algorithms: the A-E, H-E, H-E (R) (a version of the H-E that uses a radar to screen out nonraining cloud pixels), "blended" (the modified Turk GOES/microwave algorithm), GMSRA #1 (the original version) and GMSRA #2 (the version with the additional nighttime rain/no rain screen). Table 1 displays 24-h validation statistics, using rain gauges from the cooperative observer network as "ground truth". In this example, the A-E had the lowest RMSE and highest correlation with observed amounts, with the H-E performing somewhat less well by these measures but outperforming the remaining four algorithms. The H-E and the two versions of the GMSRA had the least bias, however.

7.2 Meoscale Convective System producing devastating floods over West Virginia (8-9 July 2001).

Devastating flash floods occurred in southern West Virginia and eastern Kentucky on 8-9 July 2001. As many as 3,000 homes were damaged or destroyed by flooding and mud slides and three people were killed in the most costly flood in West Virginia history.

Table 1. Satellite-estimated rainfall compared to raingauge observations for Tropical Storm Allison during the 24 h ending 1200 UTC 6 June 2001, centered in the Houston, TX metropolitan area.

Algorithm	Additive Bias (mm)	Adjusted RMSE (mm)	Correlation Coefficient
A-E	-18.3	25.8	0.69
H-E	-11.7	27.0	0.64
H-E (R)	-17.9	27.6	0.62
Blended	-20.7	28.2	0.59
GMSRA #1	-9.5	28.2	0.59
GMSRA #2	-10.8	28.1	0.59

For flash floods, validating algorithms over shorter time periods (less than 24 hours) is extremely important. Table 2 is an example is an example of NESDIS' validation using 6-h totals from Stage III radar-raingauge data as ground truth (Kuligowski et al. 2001). As with Allison, the A-E had the highest correlation with observations, but a strong wet bias also gave it the highest RMSE of the group. The H-E and the blended algorithms had the lowest biases and correlations that were only slightly below that of the A-E, resulting in significantly lower RMSE values than the A-E. The GMSRA estimates had significantly poorer correlations with observations than the other four estimates.

Table 2. Satellite-estimated rainfall compared to the Stage III product for an MCS over West Virginia during the 6 h ending 1800 UTC 8 July 2001.

Algorithm	Additive Bias (mm)	Adjusted RMSE (mm)	Correlation Coefficient
A-E	7.6	15.8	0.79
H-E	1.4	12.2	0.71
H-E (R)	1.1	12.2	0.72
Blended	-0.8	10.2	0.73
GMSRA #1	4.0	12.8	0.53
GMSRA #2	3.9	12.8	0.54

8. SUMMARY, OUTLOOK AND DISCUSSION

A readily available avenue for improving satellite algorithms is in calibration, especially for those algorithms with fixed calibrations (the A-E, H-E, and GMSRA). Significant additional investment in calibration and validation for different types of precipitation systems will be needed in order to make these algorithms more robust. This work would be well-served by improvements in the availability, reliability, and timeliness of presently existing ground-truth data sets, such as the Oklahoma mesonet. Improving the reliability of the real-time dissemination of TRMM data would also improve their usefulness in the heavy precipitation/flash flood forecasting process.

The next generation of satellite algorithms for heavy precipitation and flash floods will make greater use of all of the GOES imager channels; GOES and POES sounding channels also need to be exploited as potential contributors for estimating precipitation. The next-generation algorithms will also use calibrated microwave precipitation estimates (which are more physically robust than IR-based estimates) to continuously adjust GOES precipitation measurements both with respect to intensity and location. Many challenges and questions must be resolved in the development of satellite precipitation algorithms for heavy precipitation and flash floods:

1. improving the physical understanding of the relationship between precipitation and the signals observed in the visible, IR, and microwave frequencies, and how to best integrate this multi-frequency information;
2. developing a comprehensive precipitation algorithm that uses all available information, including radar and in situ raingauge measurements.
3. determining the best approach for algorithm development: statistical/mathematical techniques (e.g. regression, neural networks (e.g. Zhang et al. 1999)), versus physically-based approaches (e.g. cloud models);
4. discerning the best way to display the estimates: as exact values, or in term of probability (similar to the probabilistic QPF approach that the NWS has undertaken).

Of course, improvements in the constellation of available satellites also have the potential to significantly improve the state of satellite QPE. Hardware improvements include the launch of additional microwave instruments onboard POES platforms in order to increase the number of microwave passes per day. The launch of the Advanced Microwave Sounding Radiometer (AMSR) in 2002 will help toward this end, and a Global Precipitation Mission (GPM) is planned to further expand the polar microwave instrument constellation and improve coordination. In addition to increasing the quantity of instruments, improvements in quality are also sought, in terms of increase in sensor resolution and scanning speed.

Reiterating what was said in the introduction, the motivation for improved automated SPE algorithms for heavy precipitation/flash flood applications is to produce a product that is more timely than the manually-intensive IFFA and that is also suitable for direct incorporation into multisensor precipitation analyses, hydrologic models, and numeric models.

With regard to multisensor precipitation analyses, the ultimate goal is to integrate the GOES IR-based estimates with microwave-based estimates, radar-based analyses, and in-situ rain gauge measurements to produce a multi-spectral/multi-sensor algorithm for estimating precipitation form all types of precipitation systems. QPE-SUMS (Gourley 2000) is a good example of integrating real-time radar rainfall estimates with GOES IR-based precipitation estimates in real time. These integrated precipitation data sets can then be combined with the use of geographic information systems (GIS) data to improve the prediction of streamflows and crests.

The future of satellite rainfall algorithms for extreme precipitation events is quite exciting. More accurate and robust precipitation algorithms for extreme precipitation events will become operational in the near future. Furthermore, as the coverage of routine satellite precipitation estimates becomes worldwide (e.g. Alfaro and Scofield 2001), the potential benefits to the user community will be immense.

9. ACKNOWLEDGMENTS

The authors would like to thank Arnold Gruber and Ralph Ferraro of the NESDIS/ORA/Hydrology Team for their critical review of this paper and Joan Reed of NESDIS for help in laying out the manuscript.

10. REFERENCES

Adler, R. F., G.J. Huffman, and P.R. Keehn, 1994: Global rain estimation from microwave-adjusted geosyncgronous IR data. *Remote Sens. Rev.*, **11**, 125-152.

Alfaro, R., and R. A. Scofield, 2001: Validation of GOES precipitation estimates over Central America. Preprints, *11th Conf. on Satellite Meteorology and Oceanography*, Madison, WI.

Ba, M.B. and A. Gruber, 2001: GOES multi-spectral rainfall algorithm (GMSRA). *J.Appl. Meteor.*, **40**, 1500-1514.

Borneman, R., 1988: Satellite rainfall estimating program of the NOAA/NESDIS Satellite Analysis Branch. *Natl. Wea. Dig.*, **13**, 7-15.

Ferraro, R., F. Weng, N. Grody, and L. Zhao, 2000: Precipitation characteristics overland from the NOAA-15 AMSU sensor. *Geophys. Res. Lett.*, **27**, 2669-2672.

Ferraro, R. R., 1997: SSM/I derived global rainfall estimates for climatological applications. *J. Geophys. Res.*, **102**, 16,715-16,736.

Ferraro, R.R., Weng, F., Grody, N.C., and A. Basist, 1996: An eight-year (1987-1994) climatology of rainfall, clouds, water vapor, snowcover,, and sea-ice derived from SSM/I measurements. *Bull. Amer. Meteor. Soc.*, **77**, 891 - 905.

Fulton, R. A., J. P. Breidenbach, D. J. Seo, and D. A. Miller, 1998: The WSR-88D rainfall algorithm. *Wea. Forecasting*, **13**, 377-395.

Gourley, J.J. 2000: QPE SUMS and QIWI. Available at http://www.nssl.noaa.gov/teams/western/qpe/overview/index.htm.

Juying, X. and R.A. Scofield, 1989: Satellite-derived rainfall estimates and propagation characteristics associated with mesoscale convective systems (MCS). *NOAA Tech. Memo. NESDIS 25*, U.S. Dept. of Commerce, Washington, D.C. 49 pp.

Kidder, S.Q., M.D. Goldberg, R.M. Zehr, R.M. DeMaria, J.F.W. Purdom, C.S. Velden, N.C. Grody, and S.J. Kusselson: Satellite analysis of tropical cyclones using the Advanced Microwave Sounding Unit (AMSU). *Bull. Amer. Meteor. Soc.*, **81**, 1241-1259.

Kuligowski, R.J., 1997: An overview of National Weather Service Quantitative Precipitation Estimates (QPE): *Techniques Development Laboratory Office Note 97-*

4, U.S. Dept. of Commerce, Washington, D.C., 27 pp.

-----, 2001: A self-calibrating GOES rainfall algorithm for short-term rainfall estimates. Accepted by the *Journal of Hydrometorology*.

-----, S. Qiu, R.A. Scofield, A. Gruber, 2001: The NESDIS QPE verification program. Preprints, *11th Conference on Satellite Meteorology and Oceanography*, Madison, WI.

Kummerow, C., W. Barnes, T. Kozu, J. Shiue, and J. Simpson, 1998: The tropical rainfall measuring mission (TRMM) sensor package. *J. Atmos. Ocean. Tech.*, **15**, 809-817.

Scofield, R.A., 1987: The NESDIS operational convective precipitation estimation technique. *Mon. Wea. Rev.* **115**, 1773-1792.

-----, 2001: Comments on "A quantitative assessment of the NESDIS Auto-Estimator". *Wea. Forecasting*, **16**, 277 - 278.

-----, M. DeMaria, and R. Alfaro, 2001:Space-based rainfall capabilities in hurricanes offshore and inland. Preprints, *Symposium on Precipitation Extremes: Prediction, Impacts, and Response*, Albuquerque, 297 - 301.

-----, and V.J. Oliver, 1977: A scheme for estimating convective rainfall from satellite imagery. *NOAA Tech. Memo. NESS 86*, U.S. Dept. of Commerce, Washington, DC, 47 pp.

Shi, J. and R.A. Scofield, 1987: Satellite observed mesoscale convective system (MCS) propagation characteristics and a 3-12 hour heavy precipitation forecast index. *NOAA Tech. Memo., NESDIS 20*, U.S. Dept. of Commerce, Washington, D.C., 43 pp.

Sorooshian, S., K-L Hsu, X. Gao, H.V. Gupta, B. Imam, and D. Braithwaite, 2000: An evaluation of PERSIANN system satellite-based estimates of tropical rainfall. *Bull. Amer. Meteor. Soc.*, **81**, 2035-2046.

Spayd, L. E., Jr., and Scofield, R.A., 1984: A tropical cyclone precipitation estimation technique using geostationary satellite data. *NOAA Tech. Memo. NESDIS 5*, U.S. Dept. of Commerce, Washington, D.C., 36 pp.

Turk, F.J., F.S. Marzano, and E.A. Smith, 1998: Combining geostationary and SSM/I data for rapid rain rate estimation and accumulation. Preprints, *9th Conference on Satellite Meteorology and Oceanography*, Paris, 462-465.

Vicente, G., 1994: Hourly retrieval of precipitation rate from the combination of passive microwave and IR satellite radiometric measurements, Ph.D. Thesis. Dept. of Atmospheric and Oceanic Sciences, U. of Wisconsin, 127 pp.

-----, and R.A. Scofield, 1998: The operational GOES infrared rainfall estimation technique. *Bull. Amer. Meteor. Soc.*, **79**, 1883-1898.

-----, J.C. Davenport, and R.A. Scofield, 2001: The role of orographic and parallax corrections on real time high resolution satellite rainfall rate distribution. *Int. J. Remote Sens.*, in press .

World Meteorological Organization Technical document, 1999: *Estimating the amount of rainfall associated with tropical cyclones using satellite techniques*, Eric Barrett, editor, Rpt. No. TCP-42, 294 pp.

Zhang, M. and R.A. Scofield, 1994: Artificial neural network techniques for estimating convective rainfall and recognizing cloud mergers from satellite data. *Int. J. Remote Sens.*, **15**, 3241 - 3261.

2.4 SATELLITE RAINFALL ESTIMATION OVER SOUTH AMERICA: EVALUATION OF TWO MAJOR EVENTS

Daniel A. Vila *
Sistema de Alerta Hidrológico - Instituto Nacional del Agua
Buenos Aires, Argentina

Roderick A. Scofield
NOAA/NESDIS/ORA/Hydrology Team
Camp Springs, MD

J. Clay Davenport
I .M. Systems Group, Inc.
Kensington, MD

1. INTRODUCTION

Remote estimation of rainfall, especially using satellite and radar data, has been a valuable source of information for flood forecasting and numerous other applications in the hydrometeorological sciences. In South America, the scarcity of real-time rain gauge data and the existence of large unpopulated regions make satellite estimates an excellent tool for representing the spatial distribution of precipitation at smaller scales.

Vicente et al. (1998) derived a fully automated method called the Auto-Estimator (AE) that generates rainfall rates (mm/h) based on GOES (Geostationary Operational Environmental Satellite) 10.7-μm brightness temperatures. Numerous improvements have been made from the original version to the current operational version. Section 2 of this paper briefly describes some of these improvements for South America, while in Section 3 the data used in this evaluation (including satellite data, model output and rain gauge stations) are presented. The evaluation method and the results are presented in Section 4; the results and conclusions are discussed in Section 5.

2. METHODOLOGY

The principle behind this single-channel satellite-based precipitation estimator is that cold cloud tops produce greater amounts of rainfall than warmer ones (Scofield 1977). Based on this assumption, Vicente et al. (1998) derived a fully automated method using an empirical power-law function that generates rainfall rates based on GOES 10.7-μm brightness temperatures. Since a single curve cannot represent all processes associated with rain generation, the algorithm uses a moisture correction factor defined as the precipitable water in the layer from surface to 500 hPa (in inches) times the mean relative humidity (RH) between the surface and 500 hPa expressed as a percentage. The PWRH factor (which is scaled form 0.0 to 2.0) reduces rainfall rates in dry environments and increases them in moist ones. The idea was first suggested by Scofield (1987). A new methodology is used operationally to screen out non raining pixels (e.g. cirrus anvils). This technique assumes that raining pixels are colder than the mean of the surrounding pixels. The average brightness temperature and the standard deviation for a circle centered on each pixel is computed for the whole image. The standardized temperature is defined as:

$$T_\sigma = \frac{T - T_{avg}}{\sigma} \qquad (1)$$

where T is the pixel temperature, and T_{avg} is the average temperature and σ the standard deviation for a circular region centered on the pixel.

Two precipitation types are defined: *Convective precipitation*, defined by the empirical power-law function corrected by PWRH and *Stratiform precipitation*, whose maximum value cannot exceed 12mm h^{-1} and must be less than 20% of the convective rain rate that would be associated with the 10.7-μm brightness temperature of the pixel of interest. If T_σ is less than or equal to -1.5, the precipitation is entirely convective, while if T_σ is equal to zero (i.e. the temperature of a given pixel is equal to the average of the surroundings for a given radii), the precipitation is entirely stratiform. When the brightness temperature of a pixel is above the average, the precipitation rate is set to zero. The characteristics of the rainfall when the standardized temperature of a given pixel is between -1.5 and 0 is shown schematically in Fig. 1.

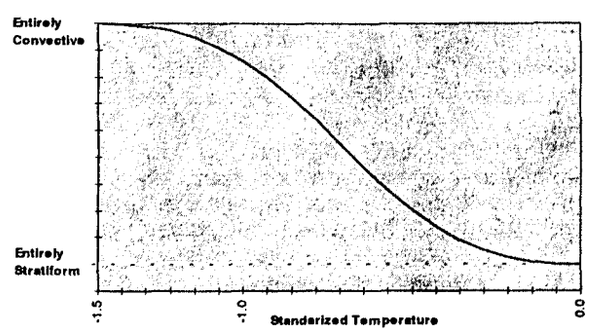

Figure 1. *Proportion of convective and stratiform rainfall for different values of negative standardized temperature. If T_σ is greater than 1, the precipitation rate is set to zero.*

When determining the intensity of precipitation in a convective system, it is important consider whether a

*Corresponding author address: Daniel Alejandro Vila - Instituto Nactional del Agua - Bs. As. - Argentina - email:dvila@ina.gov.ar

region of cold cloud is the coldest in the entire system or merely represents a local minimum. Since a single radius cannot identify both (a small radius will identify local minima but perhaps miss the global minimum temperature, while a large radius will do the opposite), precipitation estimates are computed using radii of 10 and 23 pixels, and the final rainfall estimate is the square root of the product of the two.

Another important variation from the original AE is the method of rainfall accumulation. In the original AE, if no images are available for more than an hour, the estimate during period is zero; this criterion was eliminated for South America. Many times in the day, the time gap is greater than one hour and the dry bias obtained for some cases suggests that the rain continues during the period without available images. The time integration, in this case is carried out between successive images (3 hours maximum) to avoid no-rainfall outputs during these periods. If three successive images in times t_1, t_2 and t_3 are available, the rain rate for a given pixel in the second image will remain constant between $(t_1+t_2)/2$ and $(t_2+t_3)/2$.

Figure 2 shows the availability of GOES-8 10.7-μm data for the Southern Hemisphere between 1200 UTC 20 May and 1200 UTC 22 May 2001 and the time difference between consecutive images. Full-disk images were included in this data set. The maximum gap is up to 3 hours during the evening and night (local time). Velasco and Fritsch (1987), among others, show that this is a preferred time for the onset of convection in this region, so the errors involved in the original estimation process (assuming no precipitation between images that are more than 1 hour apart) may be important.

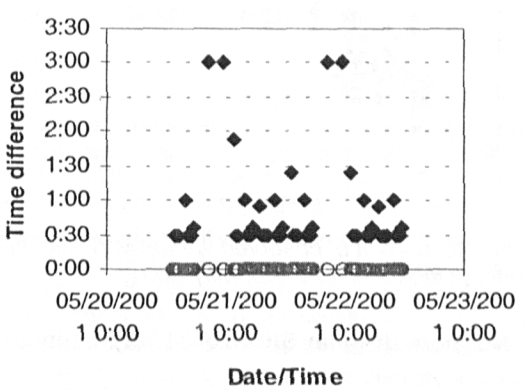

Figure 2. GOES-8 10.7-μm image availability for the Southern Hemisphere from 1200 UTC 20 May to 1200 UTC 22 May 2001. The open circles are the times when images are available; the diamonds are the elapsed time (in hours) between consecutive images.

3. DATA SET

Two major events over the southeastern Del Plata basin in the Uruguay catchment near Salto Grande Dam (approximate area 50,000 km^2, Fig. 3) during May and June 2001 were considered in this study. Data from approximately 50 rain gauges over the target area were

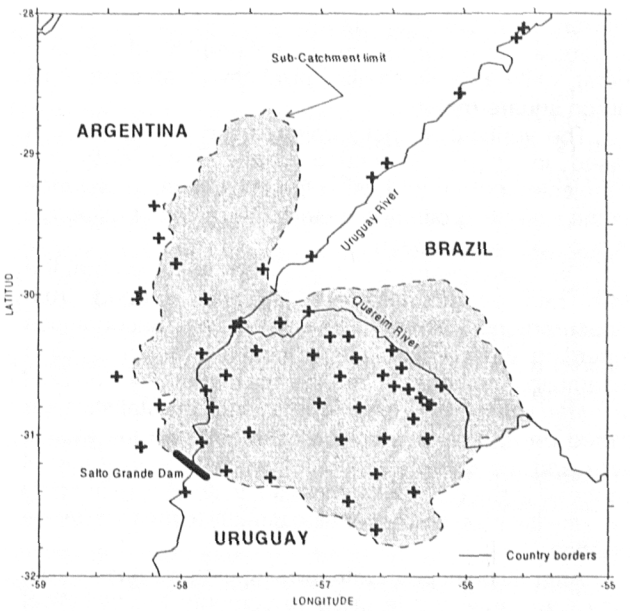

Figure 3. Locations of rain gauges used in this study.

obtained from the Salto Grande Mixed Technical Commission (CTMSG) and the National Meteorology Direction (DNM) of Uruguay. Forecasts from the Aviation (AVN) model were used to estimate the PWRH factor, while satellite imagery were obtained from NESDIS.

The first case, a rapidly-moving cold front that affected the region during 21 May, produced moderate 24-h rainfall amounts of 25 to 100 mm. The availability of satellite images for the surrounding 48-h period can be seen schematically in Fig. 2. There were 25 images for each day, with a maximum time gap of 3 hours.

The second event occurred during 31 May and 1 June 2001 where the core of the storm was located in northern Uruguay and southern Brazil. 24-h rainfall accumulations were as great as 300 mm along the Uruguayan-Brazilian border; 5000 people were evacuated from Artigas county in the north of Uruguay due to flooding along the Quareim river. 29 GOES images were available during the 24-h period of interest, but between 2209 UTC 31 May and 0139 UTC 1 June only 3 images were available.

4. VERIFICATION METHODS

4.1. Statistical Definitions

It is assumed that satellite estimates are independent of the gauges. The statistical measures and definitions used to compare the satellite estimates with the gauges were taken from the results of the 3rd Algorithm Intercomparision Project of the Global Precipitation Climatology Project (GPCP) (see Ebert 1996).

4.2. Intercomparison of Satellite and Gauge Rainfall

Many approaches are available for comparing rain gauge measurements with remotely sensed measurements of rainfall at the same location. There is an inconsistency in the volume of water being measured by

different sensors: the gauge samples a few cubic centimeters of water over an area of one-fifth of a square meter, while a single satellite pixel covers an area of 16 million square meters.

The verification methodology used in this study is based in 24-h rain gauge data. These data are reprojected onto a grid using the cubic inverse distance as the weighting criterion method. A radius of influence of one pixel was chosen.

The intercomparison in this study assumes that the 24-h rain gauge data are the best ground truth measurements. Nevertheless, there are uncertainties regarding the precise gauge location and in satellite resampling methods. To reduce this uncertainty, the *best adjusted value* (MVE) technique is used: the statistics are based on the minimum difference between the rainfall data and the satellite estimates within a 9-pixel kernel centered in the rain gauge location, instead of using only the satellite pixel corresponding directly to the rain gauge location.

After all point pairs with missing data were removed, they were analyzed in order to compute the statistical parameters for different intervals. These intervals (expressed in millimeters) are 0-7 mm, 7-26 mm, 26-52 mm and over 52 mm. The overall statistics for each event is performed as a weighted average. The weight factor for each interval is 1, 2, 4 and 8 respectively (higher amounts have more influence than the lower ones).

4.3. Case Evaluation

4.3.1. Rapidly-moving Cold Front of 21 May 2001

A fairly rapidly-moving frontal produced moderate amounts of rainfall (25-100 mm) during 21 May 2001 in the middle Uruguay catchment. The system began to develop at 0600 UTC 21 May in northwestern Uruguay and then propagated toward the northeast, where the maximum rainfall amounts were observed.

Table1 shows the statistical information for this event. In all cases the bias is negative. Since this is the definition of bias in Ebert (1996), it means that the satellite underestimated the average amount of rainfall. The weighted averaged RMSE is 14.6 mm and the skill score is 0.80, where skill score is defined as

$$SKILL = \frac{1}{n}\sum_{i=1}^{n}\left[\frac{|O_i - E_i|}{O_i + E_i}\right] \qquad (2)$$

where O_i and E_i are matched observation-estimate pairs, of which n are available.

The increase in bias with observed amount combined with high correlation coefficients for all four categories suggests that the relationship between the estimates and observations fits a linear equation very well but has a slope of less than 1 (Fig. 4). In other words, the underestimation increases with the amount of observed rainfall, but the ratio between the satellite estimates and the corresponding observations remains unchanged. Note that the highest last rainfall accumulation interval in Table 1 contains very few validation points, so the statistics have less significance than for the other intervals.

***Table 1**: Statistics for the storm of 21 May 2001 in the Salto Grande Dam region. D is the interval of observed amounts in mm; WTAVG is the weighted average described in Section 4.2. NUM is the number of pixels in each interval, BIAS the additive bias, CORR the correlation coefficient, RMSE the root-mean-squared error, POD the probability of detecton, FAR the false alarm rate, and SKILL is defined in Eq. (2).*

D (mm)	NUM	BIAS (mm)	CORR	RMSE (mm)	POD	FAR	SKILL
0-7	375	-6.60	0.82	12.00	0.95	0	0.77
7-26	338	-7.24	0.77	12.63	0.85	0.01	0.79
26-52	204	-8.48	0.59	14.57	0.55	0.12	0.83
52+	30	-21.53	0.80	24.55	0.33	0	0.76
WTAVG	2107	-9.33	0.71	14.63	0.69	0.05	0.80

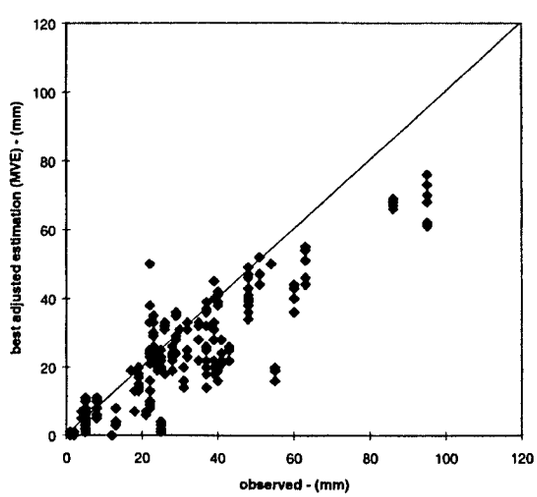

***Figure 4**. Scatterplot of observed versus MVE-estimated 24-h rainfall amounts for 21-22 May 2001.*

4.3.2. Northern Uruguay Storm of 31 May-1 June 2001

The statistical results are shown in Table 2. The weighted averaged bias underestimate the rainfall by approximately 14 mm, and the RMSE is roughly 30 mm during this event. Compared with the area-averaged rainfall (around 100 mm for whole area) the relative bias represents only 15% underestimation and the RMSE is around 30%. The scatterplot of estimated vs. observed values (Fig. 5) confirms that the dry bias becomes stronger as the observed amount increases. As mentioned previously, only 3 images are available between 2209 UTC 31 May and 0139 UTC 1 June, during which the convection was in its initial stages. Undetected rapid decreases in cloud-top temperature during this stage may be responsible for this dry bias.

Table 2. Same as Table 1, but for 31 May-1 June 2001.

D (mm)	NUM	BIAS (mm)	CORR	RMSE (mm)	POD	FAR	SKILL
0-7	321	-9.21	0.93	24.1	1.00	0.03	0.84
7-26	313	-9.49	0.92	24.4	0.92	0.06	0.86
26-52	210	-14.38	0.87	29.64	0.89	0.06	0.86
52+	145	-17.25	0.76	34.47	0.93	0.08	0.88
WTAVG	2947	-13.91	0.85	29.82	0.93	0.07	0.86

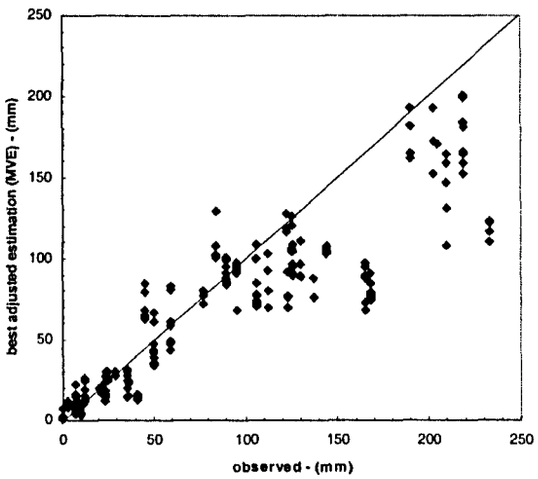

Figure 5. Same as Fig. 4 , but for 31 May-1 June.

5. DISCUSSION AND CONCLUSIONS

Rainfall data are widely used in river discharge forecasts, where the amount, spatial and temporal distribution of precipitation are very important. Infrared techniques using geostationary satellite data with 4-km spatial resolution and half an hour between successive images may help hydrologists link discharge forecast models and rainfall patterns at the appropriate scale. In many regions of South America, the gauge network is very scarce and is not available in real time, so rainfall patterns obtained through traditional interpolation methods are unrealistic and not useful in an operational setting. Satellite techniques can thus offer an alternative source of data to the hydrometeorological community in South America. In addition, the knowledge of flash flood behavior in South America would be very useful to Government emergency management agencies.

In light of these potential applications, it is important to evaluate the errors involved in satellite techniques. The main purpose of this work is to present recent improvements to the Auto-Estimator algorithm and the application of this technique in two flash flood events in the middle Uruguay basin in South America.

The main difference between applying the AE to North America and South America is image availability. While images are available every 15 minutes in North America, in South America this gap may be as long as three hours (Fig. 2). This is a very important factor in the accuracy of the estimates. In both cases (Tables 1 and 2), a dry bias suggests that a lack of images during the first stages of the storm causes an underestimation of rainfall. Nevertheless, if 24-hour accumulated rainfall is integrated in the selected region (the shaded area in Fig. 2) the difference between the observed mean rainfall (interpolated by traditional methods) and the mean estimated precipitation (AE) is less than 10% of the observed average. A detailed analysis of additional cases is planned for different regions of the Del Plata basin during different seasons of the year.

An additional improvement in the technique is in an implementation and testing phase: combining a Digital Elevation Model (at the GOES scale) for South America with low-level winds in produce an orographic correction to satellite rainfall rate distribution (Vicente 2001).

The possibility of using a temperature threshold to classify precipitating systems discrimination would allow analysis of the statistical parameters (average temperature and standard deviation) of each particular system. This approach could produce more realistic patterns of rain, especially for small-scale convection.

6. ACKNOWLEDGMENTS

The first author would like to recognize the NOAA/NESDIS Hydrology Team and Gilberto Vicente for their important contributions to this research, and to thank Bob Kuligowski for his critical review of this manuscript. Thanks to Salto Grande Mixed Technical Commission (CTMSG) and the National Meteorology Direction (DNM) of Uruguay for the rain gauge data used in this paper. The first author is supported by Instituto Nacional del Agua - Argentina and partially financed by UBACyT grant X-149.

7. REFERENCES

Ebert, E. E.,1996: Result of the 3rd Algorithm Intercomparison Project (AIP-3) of the Global Precipitation Climatology Project (GPCP). *Bureau of Meteorology Centre, Report Nº 55*, Melbourne, Australia.

Scofield, R. A., 1987, The NESDIS operational convective precipitation estimation technique. *Mon. Wea. Rev.*, **115**, 1773-1792.

-----, and V. Oliver, 1977: An Scheme for Estimating Convective Rainfall from Satellite Imagery. *NOAA Tech. Memo. NESS 86,* US Department of Commerce, Washington, D.C.

Velasco, I. and J. M. Fritsch, 1987: Mesoscale covective complexes in the Americas. *J. Geophys. Res.*, **92**, 9591-9613.

Vicente G. A., R. A. Scofield, and W. P. Menzel, 1998: The operational GOES infrared rainfall estimation technique. *Bull. Amer. Meteor. Soc.*, **79**, 1883-1898.

-----, J. C. Davenport, and R. A. Scofield, 2001: The role of orographic and parallax corrections on real time high resolution satellite rainfall distribution. *Int. J. Remote Sens.*, in press.

3.10 ERROR ANALYSIS OF MICROWAVE LAND RAINFALL ESTIMATION ALGORITHMS

Jeffrey R. McCollum[1,2] and Ralph R. Ferraro [2]
[1] Cooperative Institute for Climate Studies, University of Maryland, College Park, MD, USA
[2] NOAA/NESDIS Office of Research and Applications, Camp Springs, MD, USA

1. INTRODUCTION

There are now multiple sources of information for global, microwave rainfall estimates in addition to the Special Sensor Microwave/Imager (SSM/I). The other important microwave instruments for rainfall estimation are the Tropical Rainfall Measuring Mission (TRMM) Microwave Imager (TMI), launched in late 1997, the Advanced Microwave Sounding Unit (AMSU) launched in 1998, and the upcoming Advanced Microwave Sounding Radiometer (AMSR), which has an expected December, 2001 launch date on board the Aqua satellite. The sampling error for global estimates from the combination of sensors is reduced with more observations, so algorithm error becomes the main concern. But so far it has been difficult to quantify this error. Here we will review different approaches to validation and give examples of these approaches applied to our microwave satellite land rainfall algorithm

2. APPROACHES TO VALIDATION

Traditionally, satellite rainfall algorithms over land have been compared with ground-based estimates from radar, rain gauges, or a combination of the two. This is usually not possible over ocean, so there it may be more useful to use a physical validation approach, which involves identifying the uncertainty sources in terms of more measurable physical quantities used in the algorithm, for example, the height of the freezing level. The contribution of the sources to the overall uncertainty is often expressed in the form of an analytical model. This approach may also provide some insight over land. In addition to these two approaches, the launch of the first space-borne precipitation radar (PR) on the TRMM satellite in 1997 gives us a third means for validation. Quantitative comparisons between satellite and radar estimates can be made for the inner 1/3 of the TMI swath covered by the PR, so quantitative validation can be done over many tropical ocean and land areas with neither gauges nor radar. The planned Global Precipitation Mission (GPM) will use a core satellite containing a dual-polarization radar, which will provide even more accurate quantitative rainfall estimates for future validation, and will build upon the tropical observation area of TRMM to also cover non-tropical higher latitudes .

The first objective of validation is to identify whether the algorithm has an overall bias. The bias is identified by comparing estimates averaged over long time periods, i.e., monthly or longer. If a bias is found, the algorithm is adjusted to eliminate the bias. Assuming we have an unbiased algorithm, the next step of validation is to estimate the second order (i.e. estimation variance) errors. The second order errors are a function of averaging scale; the errors are less for longer averaging periods (and larger areas). In this study we will look at methods of evaluating second order errors for the near instantaneous scale; if these errors are known along with temporal rainfall correlation, the second order errors for longer averaging periods can be calculated.

2.1 *Ground validation*

In general, these comparisons have yielded only qualitative conclusions, because in most cases the accuracy of the land-based estimates has been neither low enough nor modeled well enough to be used for quantitative evaluations. This has been the case for the large intercomparison projects (i.e., Algorithm Intercomparison Projects (AIP's) 1-3 and Precipitation Intercomparison Projects (PIP's) 1-3), which have used radar estimates as ground reference. However, extensive theoretical work, including some comparisons with satellite estimates, has been done to study the use of rain gauge only estimates for validation. Statistical techniques are applied to estimate the uncertainty of the spatially-averaged estimates from rain gauges (Krajewski et al. (2000), Lebel and Amani (1999), Morrissey et al. (1995), among others), so that the difference between satellite and gauge estimates due to the satellite error can be estimated.

We are proposing to build a ground validation site consisting of a dense rain gauge network in Iowa encompassing an area large enough (~25 km on a side) to contain several satellite fields-of-view (FOV's), which are on the order of several kilometers.

Krajewski et al. (2000) used the theoretical equation of Morrissey et al. (1995) to determine the uncertainty of rain gauge means over 2.5° boxes for validation of satellite estimates. The same equation can be applied to this site and we have done some preliminary calculations as an illustration.

* *Corresponding author address:* Jeffrey R. McCollum, Univ. of Maryland, Dept. of Meteorology, College Park, MD, 20742; email: Jeff.McCollum@ noaa.gov

Figure 1 shows the results of application of the Morrissey et al. (1995) equation to the Iowa grid box for different numbers of uniformly-spaced gauges. The uncertainty of the gauge mean is expressed as a fraction of the uncertainty if one gauge was used to estimate a spatial average for an area with spatially-uncorrelated rainfall; the standard deviation of the estimate would simply be the standard deviation of the gauge accumulation about the long-term mean rainfall rate, which can be calculated from the gauge data. However, as more gauges are used for the mean and as spatial correlation is considered, this standard deviation is reduced.

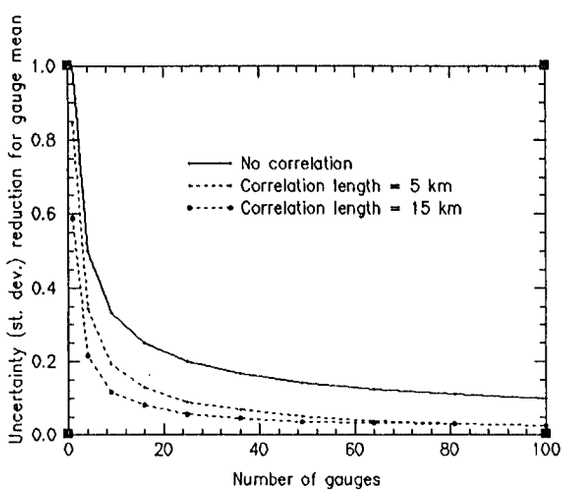

Figure 1. Results from application of the theoretical Morrissey et al. (1995) equation to the 0.25° Iowa site, assuming exponential correlation functions with the given correlation lengths for 15-minute rainfall. The y-axes shows the reduction in the uncertainty, expressed as standard deviation, about the gauge mean based on the sampling of the grid box from the given gauges.

For example, the point corresponding to four gauges for non-correlated rainfall is 0.5, because the variance of a random sample is reduced by n, where n is the number of random samples. In this case, the number of random samples is 4, reducing the variance by 4 and the standard deviation by 2. With correlated rainfall, the standard devation is reduced further. The correlation length of 15-minute rain gauge accumulations has been calculated as around 5 km with data from Brazil. In Iowa, this correlation length may be up to 15 km. The results of both possibilities are shown in Figure 1.

For both possible cases, the uncertainty drops rapidly as the first several gauges are added. The standard deviation of the spatial mean can still be cut in half by going from 10 to 25 gauges, so 25 appears to be a good number for our site. The further reduction in accuracy from adding more gauges may not be worth the cost and effort at this time.

2.2 *Error modeling/Physical Validation*

Microwave satellite land rainfall algorithms rely on the ice scattering observed at higher frequencies for rainfall estimation, as heavier rainfall produces more ice and correspondingly lower brightness temperatures. Defining the brightness temperature depression at the 85 GHz channel as Δ85V, the rainfall rate RR can be estimated as

$$RR(85V)_{est} = C85V(\Delta 85V) \quad (1)$$

where C85V is a multiplicative coefficient.

Assuming an unbiased algorithm, we are interested in second order errors, or

$$Var(RR(85V)_{est} - RR(85V)_{true})$$

$$= Var(C85V_{est}(\Delta 85V) - C85V_{true}(\Delta 85V))$$

$$= (\Delta 85V)^2\, Var(C85V_{est} - C85V_{true}) \quad (2)$$

Thus for this simple approach, the error depends on the accuracy of the multiplicative coefficient. Bennartz and Petty (2001) used observations and models of the ice processes to estimate this coefficient and found that it is highly dependent upon the rainfall type. For example, they found values of 0.12 (mm/h)/K for convective rainfall, 0.062 (mm/h)/K for frontal rainfall, and 0.017 (mm/h)/K for rainfall from clouds containing significant graupel. The coefficient can vary by almost an order of magnitude, which results in high uncertainty in the rainfall estimates when just one coefficient is applied globally.

To reduce this uncertainty, algorithms often attempt to estimate the type of rainfall (i.e., convective vs. stratiform) first, and then use an estimation coefficient depending upon rainfall type. This was done in McCollum and Ferraro (2001) for the land portions of the official TMI and Aqua AMSR algorithms.

The estimation equation of McCollum and Ferraro (2001) is:

$$RR(85V) = (P(C)C85V_{conv} + P(S)C85V_{strat})\, \Delta 85V \quad (3)$$

The coefficient is the weighted average of the higher convective rainfall coefficient and lower stratiform coefficient. The probabilities of convective and stratiform rainfall, P(C) and P(S), are estimated based on many physical principles relating brightness temperatures to the convective/stratiform nature of the rainfall. In the error formulation above, the estimation variance becomes

$$Var((RR(85V)_{est} - RR(85V)_{true}))$$

$$= (\Delta 85V)^2\, Var(C85V_{est}(\Delta 85V) - C85V_{true}(\Delta 85V))$$

$$= (\Delta 85V)^2\, (Var((P(C)C85V_{conv}+P(S)C85V_{strat})_{est} - (P(C)C85V_{conv}+P(S)C85V_{strat})_{true})) \quad (4)$$

Unfortunately, it is even more difficult to estimate the variance of this quantity, as it depends on many complicated covariances. Thus for this algorithm,

comparisons with other rainfall estimates may be more useful.

2.3 *Comparisons with PR*

Although the accuracy of the quantitative precipitation estimates from the PR is unknown, we assume they must be more accurate than microwave-based estimates, as the PR can detect raindrops while microwave basically only detects cloud ice. So comparisons with PR should be useful to give a rough estimate of satellite algorithm estimation errors. The TMI estimates from the McCollum and Ferraro (2001) algorithm are compared with coincident PR estimates on the 0.1°, instantaneous scale in Figure 2.

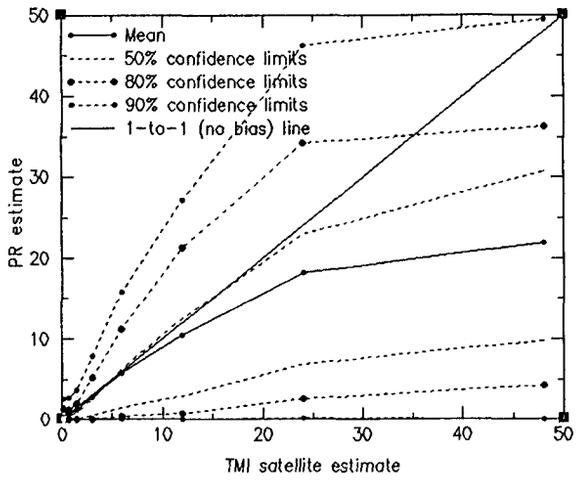

Figure 2. Results from comparison of 0.1° instantaneous rainfall estimates from collocated TMI and PR data over Africa for December, 2000. The observed spreads of PR estimates for different ranges of TMI estimates are shown.

Fig. 2 shows that the spread is indeed quite high. The algorithm is unbiased overall, although it might seem that the satellite estimates are higher than the gauge estimates. Rainfall rate distributions are highly skewed toward the lower rain rate end, so although it's not visible in the plot, the satellite estimates are higher than gauges at the frequently-occurring lowest values. The plot would look the same if the gauge estimates were on the x-axis.

3. SUMMARY

A brief overview and examples of approaches towards land rainfall validation have been given. The rain gauge only method is the most robust; the difficulties are (1) having sites with sufficient data quality, and (2) knowing the statistical properties of the rainfall field so that the rain gauge errors can be estimated. This is why we are proposing a site where we can satisfy these requirements. The analytical error model method will require further study to build a model that incorporates the complicated uncertainty sources of our algorithm. The comparisons with PR give a good preliminary idea of the range of estimation errors and the expected bias for a particular estimate rainfall rate. Quantitative algorithm error estimates can be used in more comprehensive error models to estimate the total (including temporal sampling) error over longer time scales, larger areas, and using multiple satellites.

4. REFERENCES

Krajewski, W. F., G.J. Ciach, J.R. McCollum, and C. Bacotiu, 2000: Initial validation of the Global Precipitation Climatology Project monthly rainfall over the United States. *J. Appl. Meteor.*, **39**, 1071-1086.

Lebel, T., and A. Amani, 1999: Rainfall estimation in the Sahel: what is the ground truth? *J. Appl. Meteor.*, **38**, 555-568.

McCollum J.R., and R.R. Ferraro, 2001: The Next Generation of NOAA/NESDIS SSM/I, TMI, and AMSR-E Official Microwave Land Rainfall Algorithms. Submitted to *J. Geophys. Res.*

Morrissey, M.L. J. A. Maliekal, J. S. Greene, and J. Wang, 1995: The uncertainty of simple spatial averages using rain gauge networks. *Water Resour. Res.*, **31**, 2011-2017.

3.11 A COMPARISON OF TOTAL PRECIPITABLE WATER OBSERVATIONS FROM SATELLITE AND REANALYSIS CLIMATOLOGIES

[1]Ralph Ferraro* and [1]Arnold Gruber

[1]NOAA/NESDIS/Office of Research & Applications/Atmospheric Research & Applications Division
Camp Springs, MD

1. INTRODUCTION

There are several long term global climatologies of total precipitable water (TPW) that are available to the scientific community. These are based on satellite measurements, ground observations and NWP model analysis fields. When performing comparisons of these various time series, one will find that the large scale features, say over a monthly or seasonal time scale, will be very similar. However, in order to determine how well these data sets describe annual and interannual variability, a much more detailed evaluation is needed, which is the purpose of this study. In particular, it is important to evaluate the similarities and differences of each of spatial patterns and features associated with known events such as warm and cold SST events in the tropics.

2. DATA SETS

This investigation will focus on several data sets which are summarized in Table 1.

Table 1. TPW Climatological Data Sets

Source	Years	Type	Comments
SSM/I	1987-2000	Satellite	Ocean Only Ferraro et al, 1996
NVAP	1988-1999	Blended	Land/Ocean Randell, 1996
NCEP	1953-2000	Model & In-situ	Land/Ocean Kalnay et al, 1996
ECMWF	1978-1994	Model & In-situ	Land/Ocean Gibson et al, 1999

3. METHODOLOGY & PRELIMINARY RESULTS

A powerful tool to determine dominant temporal modes in a time series is the Empirical Orthogonal Function (EOF) analysis. For example, Kondragunta and Gruber (1994) used an EOF analysis to investigate diurnal modes in ISCCP daily cloud cover. As an initial study, an EOF analysis was performed on the SSM/I time series for 13-years (1988-2000) for data between 40S and 40N latitude. The mean monthly value for the 13 years was removed from each month of the time series, and the resulting anomalies were normalized by the standard deviation at each grid point. The results are shown in Figure 1.

EOF-2 and EOF-3, explaining 12.5% and 5.5% of the variance, respectively, appear to show a predominant response to the warm and cold SST phases associated with El Nino/La Nina (as noted in the top panels of Figure 1). The most dominant warm phase in the 13-year period occurred during late 1997 and early 1998 (near month 120) while the most dominant cold phase occurred soon after that and lasts to the end of the time series. Examination of the spatial patterns of EOF-2 and EOF-3 show features related to changes in the TPW associated with both surface SST changes and circulation changes linked to both the Walker and Hadley cells, which intensify and weaken during the warm and cold phases. These circulation changes either intensify or weaken moist and dry zones.

A much more detailed EOF analysis and comparison of the various data sets will be presented at the conference.

*Corresponding author address:
Ralph R. Ferraro, E/RA2
NOAA/NESDIS/Office of Research & Applications
5200 Auth Road, Room 601
Camp Springs, MD 20746

4. REFERENCES

Ferraro, R.R., F. Weng, N.C. Grody, and A. Basist, 1996: An eight year (1987-94) climatology of rainfall, clouds, water vapor, snowcover, and sea-ice derived from SSM/I measurements. *Bull. Amer. Meteor. Soc.*, **77**, 894-905.

Gibson, J., P. Kallberg, S. Uppala, A. Hernandez, A Nomura and E. Serrano, 1999: ERA-15 Descripiton. ECMWF Re-Analysis Project Report Series, 84 pp.

Kalnay E., M. Kanamitsu, R. Kistler, W. Collins, D. Deaven, L. Gandin, M. Iredell, S. Saha, G. White, J. Woollen, Y. Zhu, M. Chelliah, W. Ebisuzaki, W. Higgins, J. Janowiak, K. C. Mo, C. Ropelewski, J. Wang, A. Leetmaa, R. Reynolds, R. Jenne, and D. Joseph, 1996: The NCEP 40-year reanalysis project. *Bull Amer. Meteor. Soc.*, **77**, 437-471.

Kondragunta, C. and A. Gruber, 1994: Diurnal variation of the ISCCP cloudiness. *Geophy. Res. Letters*, **24**, 2015-2018.

Randel, D., T. Vonder Haar, M. Ringerud, G. Stephens, T. Greenwald and C. Combs, 1996: A new global water vapor dataset. *Bull Amer. Meteor. Soc.* ,**77**, 1233-1246.

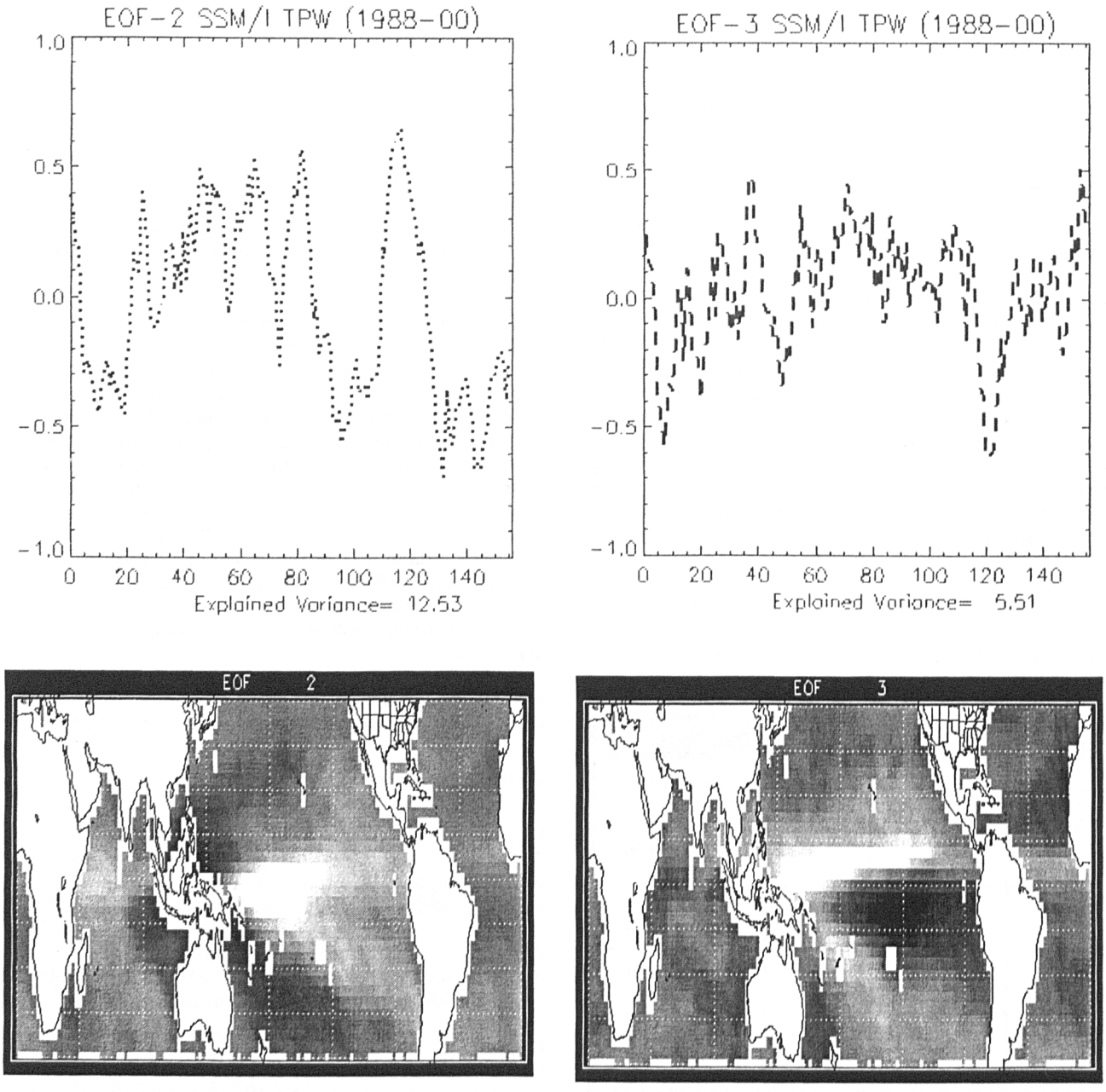

Figure 1 - EOF-2 (left) and EOF-3 (right) for the SSM/I time series (1988 - 2000). The top panels give EOF time coefficients (month 1 is January 1988, month 156 is December 2000) while the bottom panels show the spatial patterns. Gray scale ranges from negative (black) to positive (white).

3.13 INCORPORATING NUMERICAL WEATHER PREDICTION MODEL PARAMETERS INTO THE RETRIEVAL OF PRECIPITATION FROM THE SPECIAL SENSOR MICROWAVE/IMAGER

Robert J. Kuligowski[1]*, Wanchun Chen[2], Ralph R. Ferraro[1], and Russ Treadon[3]
[1]Office of Research and Applications, NOAA/NESDIS, Camp Springs, MD
[2]Caelum Research Corporation, Silver Spring, MD
[3]Environmental Modeling Center, NOAA/NWS/NCEP, Camp Springs, MD

1. INTRODUCTION

A wide variety of algorithms exist for estimating precipitation from radiance values in the microwave portion of the spectrum. These algorithms generally rely on inter-channel comparisons of radiances to infer the presence and rate of precipitation from the radiation emitted by water droplets and ice particles over oceans, or from the backscattering of terrestrial radiation by ice particles over both land and oceans. The resulting estimates tend to be more accurate than estimates produced using radiances from the infrared (IR) portion of the spectrum, at least when comparing instantaneous estimates rather than totals over time when the relatively poor sampling of the polar-orbiting microwave instruments can become problematic (e.g. Adler et al. 1993). However, it is clear that satellite radiances from either the microwave or the infrared alone do not provide all of the information that is relevant to precipitation estimation.

Efforts have been made to incorporate non-satellite information into retrievals that are based on IR and near-IR data from geostationary satellites. For instance, the Auto-Estimator (AE) (Vicente et al. 1998, 2001) uses forecast values of lower-level precipitable water (PW) and relative humidity (RH) from the Eta model to adjust for subcloud evaporation and the availability of moisture in the surrounding environment; a similar procedure is followed in the GOES Multi-Spectral Rainfall Algorithm (GMSRA) of Ba and Gruber (2001). The AE algorithm also computes the convective equilibrium level from Eta temperature and dewpoint fields and used to identify situations where lower (warmer) cloud tops can produce significant precipitation (Vicente et al. 2001).

2. DATA SETS AND METHODOLOGY

Global SSM/I retrievals produced at the Office of Research and Applications (ORA) of the National Environmental Satellite, Data, and Information Service (NESDIS) for August and September 1999 were retrieved from archive, while matching Medium Range Forecast (MRF) model (Kalnay et al. 1998) forecast fields were reproduced for that time period using the current version of the MRF that contains recent changes, including explicit cloud water and ice. The resulting fields are at T126 (approximately 1-degree horizontal resolution).

A number of input variables from the MRF were considered for incorporation into the SSM/I retrieval algorithm, including:

- Precipitable water and relative humidity to account for subcloud evaporation of hydrometeors, as is done in the AE and GMSRA;
- Freezing level to determine the relative proportion of supercooled water and ice (and thus the responsiveness of the microwave radiances to precipitation).

Several sets of validation data were used to develop the appropriate regression relationships and evaluate the results. Raingauge data were obtained from the Oklahoma Mesonet (Brock et al. 1995) and the Comprehensive Pacific Rainfall Database, both of which are maintained by the University of Oklahoma/Environmental Verification and Analysis Center (EVAC). These datasets were supplemented with radar-raingauge rainfall estimates from the Stage III analysis (Fulton et al. 1998) and from the "ground truth" dataset for the Tropical Rainfall Measuring Mission (TRMM) (Simpson et al. 1988).

3. FUTURE WORK

In addition to the work on the SSM/I algorithm, the potential impact of MRF forecast fields on the microwave retrieval algorithm for the Advanced Microwave Sounding Unit (Ferraro et al. 2000) will also be evaluated in the near future. The pursuit of this strategy for future instruments, such as the Advanced Microwave Scanning Radiometer (AMSR) will also be considered.

4. REFERENCES

Adler, R. F., A. J. Negri, P. R. Keehn, and I. M. Hakkarinen, 1993: Estimation of monthly rainfall over Japan and surrounding waters from a combination of low-orbit microwave and geosynchronous IR data. *J. Appl. Meteor.*, **32**, 335-356.

Ba, M., and A. Gruber, 2001: GOES Multispectral Rainfall Algorithm (GMSRA). *J. Appl. Meteor.*, **40**, 1500-1514.

Brock, F. V., K. C. Crawford, R. L. Elliott, G. W. Cuperus, S. J. Stadler, J. L. Johnson, and M. D. Eilts, 1995: The Oklahoma mesonet: a technical overview. *J. Atmos. Ocean Tech.*, **12**, 5-19.

Ferraro, R. R., 1997: SSM/I derived global rainfall estimates for climatological applications. *J. Geophys. Res.*, **102**, 16,715-16,735.

-----, F. Weng, N. C. Grody, and L. Zhao, 2000: Precipitation characteristics over land from the

---

* *Corresponding author address*: Robert J. Kuligowski, 5200 Auth Rd. WWB/601, Camp Springs, MD 20746; e-mail: Bob.Kuligowski@noaa.gov.

NOAA-15 AMSU sensor. *Geophys. Res. Lett.*, **27**, 2669-2672.

Fulton, R. A., J. P. Breidenbach, D. J. Seo, and D. A. Miller, 1998: The WSR-88D rainfall algorithm. *Wea. Forecasting*, **13**, 377-395.

Kalnay, E., S. J. Lord, and R. D. McPherson, 1998: Maturity of operational numerical weather prediction: Medium range. *Bull. Amer. Meteor. Soc.*, **79**, 2753-2769.

Simpson, J., R. F. Adler, and G. R. North, 1988: A proposed Tropical Rainfall Measuring Mission (TRMM) satellite. *Bull. Amer. Meteor. Soc.*, **69**, 278-295.

Vicente, G. A., R. Scofield, and W. P. Menzel, 1998: The operational GOES infrared rainfall estimation technique. *Bull. Amer. Meteor. Soc.*, **79**, 1883-1898.

-----, J. C. Davenport, and R. A. Scofield, 2001: The role of orographic and parallax corrections on real time high resolution satellite rain rate distribution. *Int. J. Remote Sens.*, in press.

P1.4 IMPROVING THE INCOPRORATION OF POLAR SATELLITE PASSIVE MICROWAVE PRECIPITATION ESTIMATES INTO THE NCEP GLOBAL DATA ASSIMILATION SYSTEM

Robert J. Kuligowski[1]*, Russ Treadon[2], Wanchun Chen[3], and Ralph R. Ferraro[1]
[1]Office of Research and Applications, NOAA/NESDIS, Camp Springs, MD
[2]Environmental Modeling Center, NOAA/NWS/NCEP, Camp Springs, MD
[3]Caelum Research Corporation, Silver Spring, MD

1. INTRODUCTION

Previous studies (e.g. Carr and Baldwin 1991; Lin et al. 1997) have demonstrated the value of including observations of precipitation in the initialization of a numerical weather prediction model in order to improve the depiction of the fields of moisture, latent heat flux, cloud cover, and other related parameters in both the initialization fields and in the subsequent model forecasts. The assimilation of estimates of precipitation based on remotely sensed data has also been demonstrated to be beneficial (e.g. Hou et al. 2001; Marecal and Mahfouf 2000), and it has the potential for even greater positive impact than precipitation oservations given the high spatial resolution of the estimates and their availability over oceans

In this vein, the Global Data Assimilation System (GDAS) of the Environmental Modeling Center's (EMC) Medium Range Forecast (MRF) model (Kalnay et al. 1998) has been making limited use of instantaneous rain rate estimates that are derived from radiances from the Defense Meteorological Satellite Program (DSMP) Special Sensor Microwave/Imager (SSM/I) using the algorithms described in Ferraro et al. (1997). Thus far, the impact of the SSM/I rain rate estimates has been largely neutral, except in the case of some tropical storms where greater benefits are found. The predominantly minimal impact is in part because of the lack of a detailed error analysis for determining the appropriate weighting of the estimated rainfall rates. This work represents an effort to produce such an error analysis and to use it to improve the incorporation of the SSM/I rain rate estimates into the GDAS.

2. DATA SETS AND METHODOLOGY

Global SSM/I retrievals produced at the Office of Research and Applications (ORA) of the National Environmental Satellite, Data, and Information Service (NESDIS) for August and September 1999 were retrieved from archive, while matching Medium Range Forecast (MRF) model (Kalnay et al. 1998) forecasts were reproduced for that time period using the current version of the MRF that contains recent changes, including explicit cloud water and ice. The resulting fields are at T126 (approximately 1-degree horizontal resolution).

The relative errors of the SSM/I rain rate estimates and MRF forecasts were compared to several validation data sets. These include raingauge data obtained from the Oklahoma Mesonet (Brock et al. 1995) and the Comprehensive Pacific Rainfall Database, both of which are maintained by the University of Oklahoma/Environmental Verification and Analysis Center (EVAC). These datasets were supplemented with radar-raingauge rainfall estimates from the Stage III analysis (Fulton et al. 1998) and from the "ground truth" dataset for the Tropical Rainfall Measuring Mission (TRMM) (Simpson et al. 1988). All of these datasets, which were aggregated onto the T126 MRF grid, were also used to evaluate the impact of the SSM/I assimilation on the MRF initialization and forecast fields.

3. FUTURE WORK

The inclusion of rain rate estimates from additional microwave sensors should further improve the GDAS by increasing the coverage and frequency of available rain rate data. Consequently, experiments in assimilating rain rate estimates from the Advanced Microwave Sounding Unit (Ferraro et al. 2000) will be conducted in the near future. Future instruments such as the Advanced Microwave Scanning Radiometer (AMSR) will also be considered for investigation.

4. REFERENCES

Brock, F. V., K. C. Crawford, R. L. Elliott, G. W. Cuperus, S. J. Stadler, J. L. Johnson, and M. D. Eilts, 1995: The Oklahoma mesonet: a technical overview. *J. Atmos. Ocean Tech.*, **12**, 5-19.

Carr, F. M., and M. Baldwin, 1991: Assimilation of observed precipitation data using NMC's Eta model. Preprints, *9th Conference on Numerical Weather Prediction*, Boulder, CO, Amer. Meteor. Soc., 422-425.

Ferraro, R. R., 1997: SSM/I derived global rainfall estimates for climatological applications. *J. Geophys. Res.*, **102**, 16,715-16,735.

-----, F. Weng, N. C. Grody, and L. Zhao, 2000: Precipitation characteristics over land from the NOAA-15 AMSU sensor. *Geophys. Res. Lett.*, **27**, 2669-2672.

Fulton, R. A., J. P. Breidenbach, D. J. Seo, and D. A. Miller, 1998: The WSR-88D rainfall algorithm. *Wea. Forecasting*, **13**, 377-395.

Hou, A. Y., S. Zhang, A. da Silva, W. Olson, C. Kummerow, and J. Simpson, 2001: Improving global analysis and short-range forecast using rainfall and observations derived from TRMM and SSM/I passive

---

* *Corresponding author address*: Robert J. Kuligowski, 5200 Auth Rd. WWB/601, Camp Springs, MD 20746; e-mail: Bob.Kuligowski@noaa.gov.

microwave sensors. *Bull. Amer. Meteor. Soc.*, **82**, 659-679.

Kalnay, E., S. J. Lord, and R. D. McPherson, 1998: Maturity of operational numerical weather prediction: Medium range. *Bull. Amer. Meteor. Soc.*, **79**, 2753-2769.

Lin, Y., K. E. Mitchell, E. Rogers, and M. E. Baldwin, 1997: Assimilation of hourly precipitation data to improve the water cycle component of NCEP's Eta model. Preprints, *13th Conference on Hydrology*, Long Beach, CA, Amer. Meteor. Soc., 52-53.

Marecal, V., and J.-F. Mahfouf, 2000: 4D-Var assimilation of TMI rainfall rates. Proceedings, *ECMWF/EuroTRMM Workshop on Assimilation of Clouds and Precipitation*, ECMWF.

Simpson, J., R. F. Adler, and G. R. North, 1988: A proposed Tropical Rainfall Measuring Mission (TRMM) satellite. *Bull. Amer. Meteor. Soc.*, **69**, 278-295.

1.2

AN OVERVIEW OF ACTIVE FIRE DETECTION AND MONITORING USING METEOROLOGICAL SATELLITES

Elaine M. Prins*
NOAA/NESDIS, Office of Research and Applications, Advanced Satellite Products Team (ASPT)
Madison, WI

Joleen M. Feltz, Chris C. Schmidt
Cooperative Institute for Meteorological Satellite Studies (CIMSS), University of Wisconsin
Madison, WI

1. INTRODUCTION

Each year millions of acres of boreal and temperate forests and grasslands are consumed by wildfire resulting in loss of life and property with significant economic costs and environmental impacts. The 2000 fire season in the USA was the worst in nearly 50 years with over 8.4 million acres burned. The estimated cost of fire suppression alone was $1.3 billion. The cost of fire management and suppression is expected to increase, especially along the urban/wildland interface.

Throughout the world, fire also serves as a tool in deforestation, land clearing, grassland management, pest control, and other agricultural applications. Current estimates suggest that globally over 85% of all fires occur in the equatorial and subtropical regions primarily in Africa, South America, and Southeast Asia. Much of this activity is concentrated in developing countries where there are few resources to adequately document the extent of burning.

Biomass burning associated with naturally occurring forest fires, deforestation and other human activities is a distinct biogeochemical process that plays an important role in terrestrial ecosystem processes and regional and global climate change. Fire is a major source of trace gases such as NO, CO_2, CO, O_3, NO_x, N_2O, NH_3, SO_2, CH_3, and other nonmethane hydrocarbons. Preliminary global estimates indicate that biomass burning may be responsible for 38% of ozone in the troposphere, 32% of global carbon monoxide, 39% of the particulate organic carbon, and up to 40% of CO_2. Fire is also a significant source of aerosols (Crutzen et al., 1985; Andreae et al., 1988; Crutzen and Andreae, 1990; Levine, 1991). Studies have shown that the direct and indirect radiative effects of aerosols from biomass burning are a major factor in climate change calculations (Penner et al., 1992). Nationally and within the Framework Convention on Climate Change (FCCC), countries will need to report on their greenhouse gas emissions including those from biomass burning (Justice and Korontzi, 2001). In many countries, remote sensing may be the only economically feasible way to track fire activity.

Over the past twenty years the international scientific research and environmental monitoring communities have recognized the vital role environmental satellites can play in detecting and monitoring active fires both regionally and around the world for hazards applications and to better understand the extent and impact of biomass burning on the global environment. Although the current suite of international polar orbiting and geostationary satellites do not meet all of the needs of the hazards and climate change community, routine generation of real-time fire products would be extremely valuable to both user communities. At the present time, consistent routine global fire products are not available in real time.

Remote sensing of biomass burning is currently the focus of two international efforts that bring together remotes sensing data providers and user communities, including climate change research scientists, resource managers, fire managers, and policy and decision makers. Although the primary focus of each effort is different, they both are dedicated to better utilization of environmental satellite data to detect and monitor active fires regionally and on a global scale. The Global Observation of Forest Cover (GOFC) is a coordinated effort that was originally developed as a pilot project by the Committee on Earth Observation Satellites (CEOS) as part of the Integrated Observing strategy (IGOS), and is now a panel of the Global Terrestrial Observing System (GTOS). Forest fire monitoring and mapping is one of three primary GOFC themes. The fire hazard team of the Disaster Management and Support Group (DMSG) is an ad hoc working group of CEOS focusing on current capabilities and requirements for space-based observations for fire management applications regionally and around the world. Both groups have stated the importance of utilizing operational meteorological satellites for routine fire products and long-term analyses (Dull and Lee, 2001; Gutman, et al.,2001; Justice and Korontzi, 2001).

2. OVERVIEW OF ENVIRONMENTAL SATELLITE FIRE DETECTION

Environmental satellites have been used for fire detection and monitoring for over 20 years. Some of the initial studies were performed using the National Oceanic and Atmospheric Administration (NOAA)-6

* *Corresponding author address:* Elaine M. Prins, NOAA/NESDIS, 1225 W. Dayton St., Madison, WI 53706; email: Elaine.Prins@ssec.wisc.edu.

Advanced Very High Resolution Radiometer (AVHRR) (Matson and Dozier, 1981). This work showed how the different brightness temperature responses between the shortwave infrared (SWIR at 3.74 μm) and the longwave infrared windows (LWIR at 10.8 μm) can be used to locate fires and determine estimates of sub-pixel fire size and temperature. Typically the differences between the SWIR and LWIR bands are on the order of 2 to 4 K due to reflected solar radiation, surface emissivity differences, and water vapor attenuation. Larger differences occur when one part of the pixel is substantially warmer than the rest and in regions with enhanced solar reflection. Since the early 1980s, the AVHRR has been used to monitor fires around the globe using various algorithms ranging from single band image analyses and simple channel differencing to more complex automated contextual algorithms (Muirhead and Cracknell, 1985; Kaufman et al., 1990; Setzer and Pereira, 1991; Justice and Dowty, 1994; Flasse and Ceccato, 1996; Li et al., 2001).

Other polar orbiting sensors have been identified as appropriate for global fire detection including the Advanced Very High Resolution Radiometer (AVHRR), the ERS Along Track Scanning Radiometer (ATSR), the MODerate-resolution Imaging Spectroradiometer (MODIS), the Defense Meteorological Satellite Program (DMSP) Operational Linescan System (OLS), the Tropical Rainfall Measuring Mission (TRMM) Visible and Infrared Scanner (VIRS), and the ADvanced Earth Observing Satellite (ADEOS-II) Global Imager (GLI). In the mid-latitudes these instruments provide several observations of a given region each day. In the near future a suite of geostationary satellites will be available to complement the polar network by providing information on the diurnal timing, spatial distribution, and characteristics of sub-pixel fire activity around the globe. Currently geostationary active fire monitoring using the SWIR band is only feasible in the western hemisphere with the NOAA Geostationary Operational Environmental Satellites (GOES) (Prins et al, 2001). The remainder of this paper will focus on applications of geostationary data for fire detection and monitoring.

3. GOES FIRE MONITORING IN THE WESTERN HEMISPHERE

The current series of GOES satellites provide the unique opportunity to detect and monitor active fires every half hour throughout the western hemisphere. The GOES Imager has five spectral bands (see Table 1) including a broadband visible and 4 infrared bands (Menzel and Purdom, 1994). Several features of the GOES Imager are beneficial for fire monitoring. The oversampling of the instantaneous geometric field of views (IGFOV) in the east/west direction allows for increased opportunities to capture an entire fire within one field of view. The saturation temperature on the shortwave IR window band is significantly higher on GOES-8 (335K) than

Table 1: Geostationary Operational Environmental Satellite (GOES) Characteristics
Current Systems: GOES-8 and GOES-10
Position: GOES-8 at 75 °W and GOES-10 at 135 °W
Design Life: 3-5 years
Operating Agency: National Oceanic and Atmospheric Administration (NOAA)

Band	Wavelength (μm)	Resolution IGFOV (km)	Description
VIS	0.52-0.72	1	Broadband visible
IR 3.9	3.78-4.03	4	SW-R window
IR 6.7	6.47-7.02	8	Water Vapor
IR 10.7	10.2-11.2	4	IR Window
IR 12.0	11.5-12.5	4	Dirty Window

that on AVHRR (320K). If the saturation temperature were near 320K, over 80% of the fire pixels observed in South America would saturate the instrument. A higher saturation temperature allows for easier fire identification in regions with high background temperatures, the ability to monitor diurnal changes in fire size and intensity, and calculations of sub-pixel fire size and temperature estimates. At nadir, the minimum detectable instantaneous fire size burning at an average temperature of 750 K is 0.15ha and increases to 0.32 ha at 50°N (see figure 3 for more details) (Prins et al., 2001).

Throughout the western hemisphere, GOES is used to detect and monitor wildfires in real time for hazard applications and to document fires associated with deforestation and agricultural management (Prins et al, 1998; 2001; Alfaro et al., 1999; Molenar et al. 2000). At the University of Hawaii and the Colorado State University Cooperative Institute for Research in the Atmosphere (CIRA) image processing techniques, such as multispectral band differencing and multi-band image combinations, are used to create derived imagery that highlight regions of possible fire activities (Weaver et al., 1995; Harris, et al. 2000). These derived composite imagery products provide a valuable tool for near real-time fire identification for the trained user. At the University of Wisconsin Cooperative Institute for Meteorological Satellite Studies (CIMSS), multispectral imagery, ancillary data, and statistical and numerical techniques are incorporated in a complex algorithm that automatically locates hot spot pixels and provides estimates of sub-pixel fire characteristics. These products are used in real time for fire identification and monitoring and fire trend analysis activities and can be assimilated into climate change and pollutant transport models in real-time (Prins, et al., 2001). The following sections provide examples of GOES fire monitoring applications being conducted at CIMSS.

3.1 GOES Biomass Burning Trend Analysis in South America

The international scientific community has stressed the need for long-term monitoring of biomass burning for land-use/land-cover change analysis and global climate change research. The NOAA/NESDIS/ORA

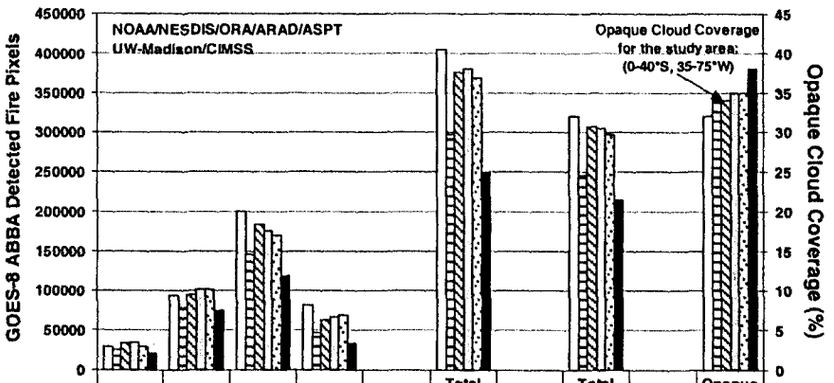

	12 UTC	15 UTC	18 UTC	21 UTC	Total (all times)	Total (daily unique)	Opaque Clouds (%)
1995: # of Fire Pixels	29460	93681	199696	81558	404394	320652	
1996	25865	78854	145674	46291	296684	245029	
1997	33509	95247	184081	62940	375777	307069	
1998	35597	102060	175435	66364	379455	305296	
1999	28781	101658	169160	68401	368000	296418	
2000	21198	74723	119504	33638	249063	215218	
1995: Opaque clouds (%)							32
1996							34
1997							34
1998							35
1999							35
2000							38

Figure 1. Summary of GOES-8 ABBA detected fire pixels in South America for 1995 to 2000.

Advanced Satellite Products Team (ASPT) and the Cooperative Institute for Meteorological Satellites Studies (CIMSS) developed two algorithms to monitor trends in fire, smoke, and clouds in South America using GOES-8 data. The GOES-8 Automated Biomass Burning Algorithm (ABBA) identifies and characterizes sub-pixel burning in GOES imagery (Prins and Menzel, 1994; Prins et al., 1998). It is a dynamic multispectral contextual algorithm which uses the visible, shortwave infrared window (3.9 μm) and longwave infrared window (10.7 μm) bands and ancillary data to locate fires in GOES imagery. Once a fire is found, numerical techniques are used to estimate sub-pixel fire size and temperature. The Merged Automated Cloud/Aerosol Detection Algorithm (MACADA) distinguishes smoke from various cloud types and catalogues smoke and cloud extent. The MACADA is a merged spectral/textural algorithm which uses multispectral GOES data (visible, 3.9, 10.7, 12.0 mm) to map smoke, aerosols, and clouds.

The 1995 fire season represented the first opportunity to quantitatively monitor diurnal fire activity from the GOES-8. It serves as the benchmark year in characterizing diurnal, spatial, seasonal and interannual trends in fire activity, clouds, and aerosols throughout South America. The GOES ABBA and MACADA were applied to 3-hourly (11:45, 14:45, 17:45, and 20:45 UTC) multispectral data collected from June through October in each year from 1995 to 2000. The study area extended from 0 to 40°S and from 35 to 75°W including portions of Brazil, Peru, Bolivia, Paraguay, Uruguay, and northern Argentina. Figure 1 provides an overview of the number of fire pixels detected at each time period and total burning for each year, along with the percent opaque cloud coverage. The opaque cloud coverage gives an indication if the interannual variability in the number of detected fire pixels is due to cloud coverage issues. From 1995 to 1999 the interannual differences in opaque cloud cover were less than 2% on average throughout the fire study area. Opaque cloud cover in the year 2000 was approximately 6% higher than in 1995.

The diurnal cycle is observed in all years with peak burning at 17:45 UTC. The sum of all fire pixels detected at all time periods for each year shows that 1995 was the peak year with over 400,000 fire pixels. The total number of fire pixels detected in 1996 at all time periods was 27% less than in 1995 with only a

slight increase in cloud coverage. In 1997 there was increased fire activity in north-central and northeastern Brazil primarily due to drought conditions associated with El Nino, although the total number of detected fire pixels was 7% less than in 1995. In 1998 the ABBA detected elevated burning in eastern Brazil with approximately 6% less fire pixels than in 1995. In 1999 enhanced fire activity was observed in southwestern Brazil, Paraguay, and Bolivia where wildfires raged out of control, although the number of fire pixels detected was 9% less than in 1995. The 2000 fire season showed a significant decrease in fire activity, nearly 38% less than in 1995. This change was accompanied by a 6% greater occurrence of opaque clouds in the study area.

Most fires in South America can be detected from satellite for only a few hours. The daily unique column shows that on average 82% of the fire pixels observed at a given time period were not observed at the other times in a day. In the year 2000, over 86% of the fires were observed in only one of the four time periods, possibly due to cloud obscuration in other time periods. This emphasizes the importance of high temporal observing systems to capture the short-lived fires and to have more opportunities for cloud-free viewing. Comparisons with the INPE AVHRR fire product for the 1995-2000 time period show that although both instruments detect similar patterns in burning, diurnal monitoring is necessary to monitor fires as they occur (Feltz, et al., 2001).

3.2 Applications of the Wildfire ABBA Throughout the Western Hemisphere

A new version of the GOES-8 ABBA was developed for fire detection and monitoring throughout the western hemisphere. The Wildfire ABBA enables fire monitoring in most ecosystems and was streamlined to allow for rapid processing of half-hourly GOES data. GOES-8 Wildfire ABBA composite fire products are created and posted on the Web in real time at the following web site: http://cimss.ssec.wisc.edu/goes/burn/wfabba.html. Initial evaluation of the Wildfire ABBA in Canada, Southeastern U.S., Mexico, and South America indicates improvements in identifying wildfires, distinguishing between fires and highly reflective surfaces and cloud edges, and a reduction in false alarms. In Canada preliminary studies have demonstrated the utility of high-temporal GOES data for early detection of large rapidly growing fires in remote regions of Quebec (Moreau, Personal Communication, 1999). In addition to applications in fire management, the Wildfire ABBA products are also being assimilated into the Navy Aerosol Analysis and Prediction System (NAAPS) as part of the Fire Locating and Modeling of Burning Emissions (FLAMBE) project (Prins et al., 2001).

Composites of the half-hourly Wildfire ABBA fire products provide a unique perspective regarding the prevalence and distribution of fire in the western hemisphere. Figure 2 is a composite of all fires detected in half-hourly GOES-8 imagery from 1 September 2000 through 28 February 2001. The most obvious feature of the 6-month composite is the that the vast majority of fires are located in South America, reflecting the extensive use of fire in deforestation and agricultural management. Although it is important to note that the study period did not include spring agricultural burning in Central America and the Southeast U.S.

Several areas of enhanced fire activity are outlined in North America. Clusters of fire pixels were detected in the plains of central Canada and North Dakota (location a). These fires were located in both cropland and forested regions. Although the major conflagrations in the western U.S. occurred in August of 2000, this composite shows wildfires burning in the western U.S. (location b) beyond August. Numerous fire pixels are identified along the Mississippi Delta region (location c) and are predominantly associated with agricultural activity. Fires in the southeastern U.S. (location d) are located in both cropland and forested areas. We have not been able to verify the cluster of fires in southern Florida (location e), but smoke plumes were observed in this region on a number of occasions. The fire pixels in Cuba (location f) and Central America (location g) are probably associated with agricultural burning.

The fires in the northwestern portion of South America, in the countries of Venezuela and Colombia (location h), are predominantly located in cattle ranching regions, although crops are grown here as well. Some of this fire activity is also located in forested regions. Numerous fire pixels were detected in the Guiana Highlands region of Venezuela, Guyana, and northern Brazil (location i). Thousands of fire pixels were located along the arc of deforestation in Brazil. The burning pattern is similar to what has been documented by the South American GOES-8 ABBA (Prins et al., 1998; 2001). The majority of these fires are associated with agricultural applications and deforestation activities. The composite shows distinct burning patterns along rivers and in areas with recent road construction (linear features) as observed at locations j, k, and l. The fires observed at location l represent a new region of expanding deforestation in western Amazonia associated with a new road being constructed over the Andes to link Brazil with Peruvian ports on the Pacific Coast. Fires in eastern Brazil and central Bolivia are primarily associated with ongoing agricultural management. The cluster of saturated fire pixels in south-central Argentina (location m) represents extensive fires that burned throughout December and January along the grassland/desert boundary. They produced large smoke palls that extended to the Atlantic Ocean. These fires were also observed in NOAA AVHRR imagery and were documented on the NOAA Operational Significant Events Imagery (OSEI) web site.

4. FUTURE GLOBAL GEOSTATIONARY FIRE CAPABILITIES

One of the goals of the international GOFC fire monitoring and mapping efforts is to promote and

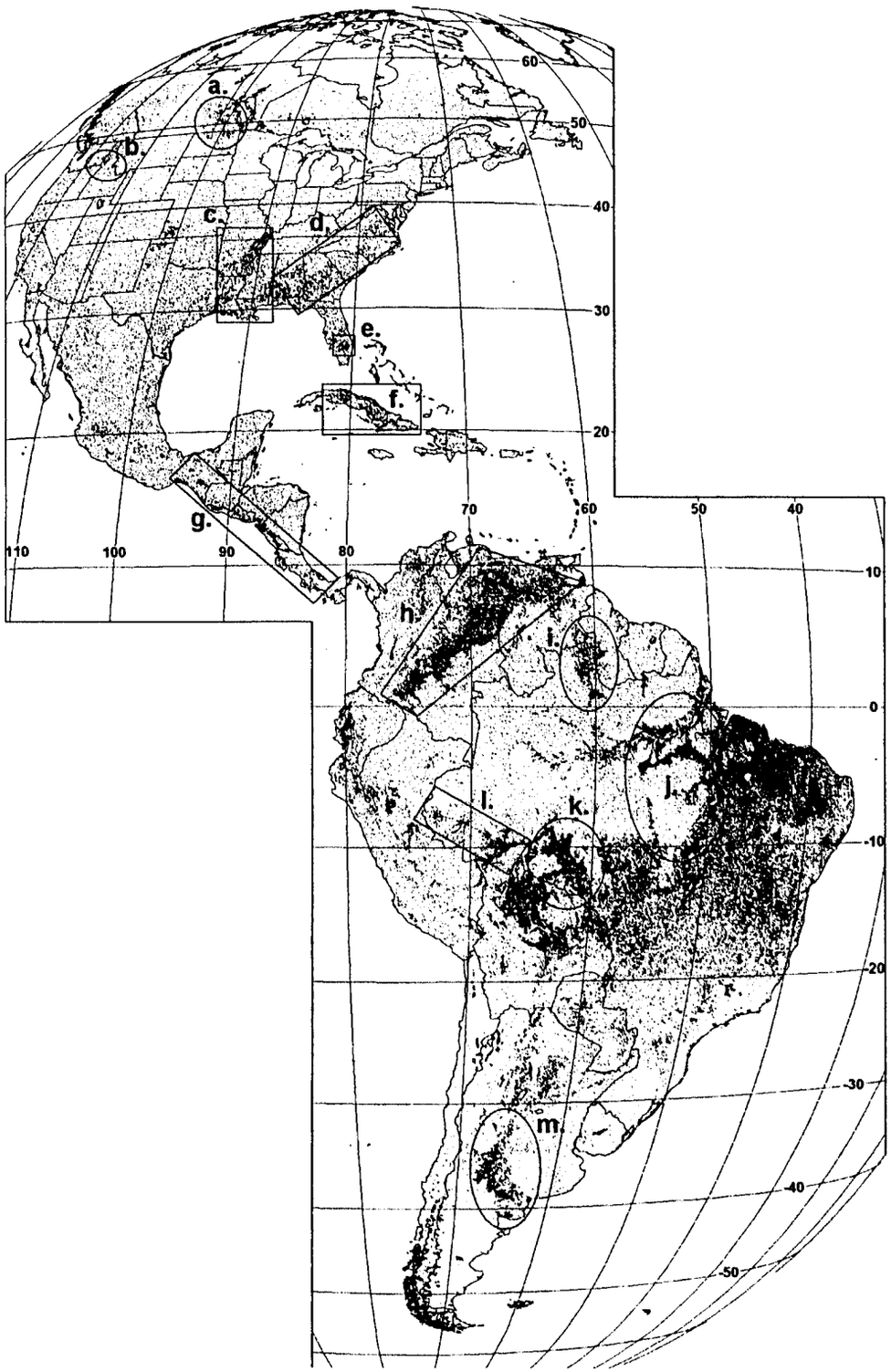

Figure 2. GOES-8 Wildfire ABBA composite of all half-hourly detected fire pixels for the time period 1 September 2000 through 28 February 2001.

support the development of a network of global geostationary satellites providing operational standard active fire products in near-real time and creating a long-term archive of fire data. A global geostationary fire network will be possible with the launch of the European Meteosat Second Generation(MSG) satellite in 2002 and the replacement Japanese Multi-functional Transport Satellite (MTSAT-1R) in 2003.

The MSG is a spin-stabilized satellite and will serve as the successor to the European Meteorological Satellite (Meteosat) series. The primary instrument on the MSG is the Spinning Enhanced Visible and Infrared Imager (SEVIRI) containing 3 visible bands (broadband centered at 0.75 μm, and bands at 0.63 and 0.81 μm), 1 near-infrared (NIR at 1.6 μm) and 8 infrared bands (3.9, 6.2, 7.3, 8.7, 9.7, 10.8, 12.0, and 13.4 μm) (see Table 2). Full disk imagery will be available every 15 minutes. The 3.9 μm band will enable sub-pixel fire monitoring in Europe and Africa with excellent coverage of the African forests. In addition, nighttime measured 1.6 μm radiance will provide quantitative observations of hot spots in the absence of reflected solar radiation contamination during the day, as demonstrated with the ATSR (Wooster and Rothery, 1997). The IGFOV at nadir will be approximately 1.6 km in the broadband visible and 4.8 km in the remaining bands, although all bands will be oversampled with a sampled resolution of 1 km in the broadband visible (HRV) and 3 km in all other bands. This oversampling can be used to enhance the spatial resolution and increases the opportunity to capture an entire fire within one field of view.

The elevated saturated temperature (>335 K) in the 3.9 μm band will minimize the impact of saturation and allow for sub-pixel fire characterization. Minimum detectable fire size estimates, presented in figure 3, indicate that MSG will be able to detect a 0.22 ha fire burning at 750 K at the equator and a 0.46 ha fire at 50°N.

MTSAT is a multi-functional three-axis stabilized satellite that is being produced by the Japan Meteorological Agency (JMA) and the Japan Civil Aviation Bureau (JCAB) to serve both a meteorological mission as the successor to the Geostationary Meteorological Satellite (GMS) series and an aeronautical mission (JMA, 1997). The initial MTSAT was lost during launch in the fall of 1999. Preliminary indications are that Japan will try to launch a replacement satellite MTSAT-1R in 2003.

The MTSAT-1R will include the Japanese Advanced Meteorological Imager (JAMI) which is similar to the GOES in terms of spectral coverage (Kigawa, 2000). This overview is based on current preliminary design specifications for the JAMI. The JAMI includes one visible band (broadband centered at 0.72 μm) and 4 infrared bands (3.75, 6.75, 10.8, and 12.0 μm). The current JAMI design specifies a spatial resolution at nadir of 0.5 km in the visible and 2 km in the infrared bands, although the data may be disseminated to the user community with the reduced resolution of 1 km in the visible and 4 km in the IR. The increased spatial resolution of MTSAT over GMS-5 and the addition of the 3.75 μm band will make geostationary diurnal fire monitoring in the western Pacific possible for the first time, with increased temporal resolution, providing coverage of the full disk region every 18 minutes.

Table 2: Meteosat Second Generation (MSG)
Launch Date: 2002
Position: Greenwich Meridian
Design Life: 7 years
Operating Agency: EUMETSAT

Band	Wavelength (μm)	Resolution IGFOV (km)	Description
HRV 0.75	0.60-0.90	1.6	Broadband visible
VIS 0.6	0.56-.71	4.8	Visible and Near IR
VIS 0.8	0.74-0.88	4.8	
IR 1.6	1.50-1.78	4.8	
IR 3.9	3.48-4.36	4.8	IR windows
IR 8.7	8.30-9.10	4.8	
IR 10.8	9.80-11.80	4.8	
IR 12.0	11.00-13.00	4.8	
IR 6.2	5.35-7.15	4.8	Water Vapor
IR 7.3	6.85-7.85	4.8	
IR 9.7	9.38-9.94	4.8	Ozone
IR 13.4	12.40-14.40	4.8	Carbon Dioxide

Table 3. Multi-functional Transport Satellite (MTSAT)
Launch Date: ~2003
Position: 140°E
Design Life: 5 years
Operating Agency: Japan Meteorological Agency (JMA) and the Japan Civil Aviation Bureau (JCAB)

Band	Wavelength (μm)	Resolution IGFOV (km)	Description
VIS 0.72	0.55-0.80	0.5	Broadband visible
IR 3.7	3.5-4.0	2	SWIR window
IR 6.7	6.5-7.0	2	Water Vapor IR
IR 10.8	10.3-11.3	2	IR Window
IR 12.0	11.5-12.5	2	Dirty Window

*Japan Meteorological Agency, 1997

The MTSAT-2, which is scheduled for launch in 2004, will be similar to the imager on the original MTSAT platform with a spatial resolution of 1 km in the visible and 4 km in the infrared bands. The infrared bands will have the same spectral configuration as the JAMI with half-hourly observations available for the entire full disk region. The saturation temperature in the 3.75 μm band on both MTSAT-1R and MTSAT-2 is expected to be near 320 K which will hinder sub-pixel fire characterization due to saturation, but saturation will still be less of an issue than with the current AVHRR 1 km Local Area Coverage (LAC) data.

The JAMI offers a unique opportunity to provide early warning in the detection of smaller fires which are not detectable by other geostationary platforms. Minimum detectable fire size estimates shown in figure 3 suggest that the spectral configuration and 2

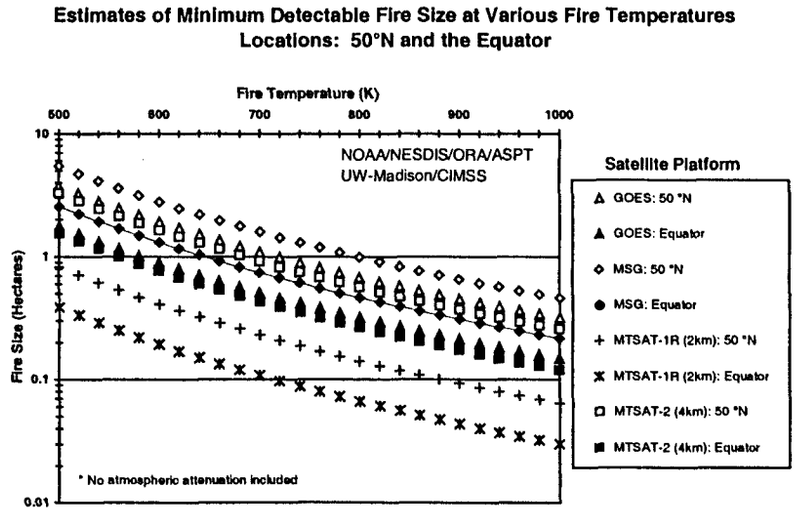

Figure 3. Minimum detectable fire size estimates for GOES, MSG, and MTSAT

km spatial resolution of the SWIR band on MTSAT-1R will allow it to detect significantly smaller fires than GOES-8. The MTSAT-1R will be able to detect a 0.03 ha fire burning at 750 K at the equator. The minimum detectable fire size at 50°N is 0.06 ha. This is 5 times smaller than the GOES minimum detectable fire size. The infrared spatial resolution of 4 km on MTSAT-2 will increase the minimum detectable fire size to 0.12 ha at the equator and 0.26 ha at 50°N for a fire burning at 750K.

5. CONCLUSIONS

Current international environmental meteorological satellites were not specifically designed for the purpose of fire monitoring and have limitations in this application. In spite of the limitations, studies have shown that they are a valuable resource for near real-time detection and monitoring of active fires. To date these satellites have been underutilized. International efforts are underway to better utilize environmental satellite data for detecting and monitoring active fires regionally and on a global scale for the wildfire management and climate change communities. In particular, operational satellites such as the NOAA POES, GOES, and DMSP platforms can provide consistent fire products from similar platforms over many years. Furthermore operational satellite data archives can be analyzed to study long-term trends in fire activity around the globe for climate applications. Within the next few years, an international suite of geostationary satellites will be able to monitor diurnal fire activity around the globe. Together with current and future meteorological/environmental polar-orbiting satellites, this suite of geostationary sensors will be able to detect and monitor fires as they occur and provide information on spatial, diurnal, seasonal, and interannual trends in biomass burning around the globe.

6. REFERENCES

Alfaro, R., W. Fernandez, and B. Connell, 1999: Detection of the forest fires of April 1997 in Guanacaste, Costa Rica, using GOES-8 images. *International Journal of Remote Sensing.* **20**(6), 1189-1195.

Andreae, M. O., E. V. Browell, M. Garstang, G. L. Gregory, R. C. Harriss, G. F. Hill,D. J. Jacob, M. C. Pereira, G. W. Sachse, A. W. Setzer, P. L. Silva Dias, R. W. Talbot, A. L. Torres and S. C. Wofsy, 1988: Biomass burning emissions and associated haze layers over Amazonia. *J. Geophys. Res.*, **93**, 1509-1527.

Crutzen, P.J., A. C. Delany, J. Greenburg, P. Haagensen, L. Heidt, R. Lueb, W. Pollock, W. Seilor, A. Wartburg, and P. Zimmerman, 1985: Tropospheric chemical composition measurements in Brazil during the dry season. *J. of Atmos. Chemistry*, **2**, 233-256.

Crutzen, P. J. and M. O. Andreae, 1990: Biomass burning in the tropics: impact on atmospheric chemistry and biogeochemical cycles. *Science*, **250**, 1669-1678.

Dull, C. W., and B. S. Lee, 2001: Satellite earth observation information requirements of the wildland fire management community. In Global and Regional Wildfire Monitoring: Current Status and Future Plans (F. J. Ahern, J. G. Goldammer, C. O. Justice, Eds.), SPB Academic Publishing , The Hague, Netherlands, pp. 19 - 33.

Feltz, J. M. and E. M. Prins, 2001: A comparison of the GOES-8 ABBA and INPE AVHRR fire products for South America from 1995 – 2000. Proceedings of the 11th Conference on Satellite Meteorology and Oceanography, Madison, WI, October 15-18, 2001, pp. TBD.

Flasse, S. P., and P. Ceccato, 1996: A contextual algorithm for AVHRR fire detection. *Int. J. Remote Sens.* **17**(2), 419-424.

Gutman, G., C. Elvidge, I. Csiszar, and P. Romanov, 2001: NOAA archives of data from meteorological satellites useful for fire products. In Global and Regional Wildfire Monitoring: Current Status and Future Plans (F. J. Ahern, J. G. Goldammer, C. O. Justice, Eds.), SPB Academic Publishing , The Hague, Netherlands, pp. 257-265.

Harris, A. J. L., L. P. Flynn, K. Dean, E. Pilger, M. Wooster, C. Okubo, P. Mouginis-Mark, H. Garbeil, C. Thornber, D. Rothery, and R. Wright, 2000: Real-time monitoring of volcanic hot spots with satellites. In *Remote Sensing Volcanism, AGU Monograph Series.* (P. Mouginis-Mark, J. Fink, J. Crisp, Eds.), pp. 139-159.

Japan Meteorological Agency (JMA), 1997: Meteorological observation with the Multi-functional Transport Satellite (MTSAT). Report produced by the Office of Meteorological Satellite Planning Administration Division, Observations Department, Japan Meteorological Agency, 4 pp.

Justice, C. O., and P. R. Dowty, 1994: Technical Report of the IGBP-DIS Satellite Fire Detection Algorithm Workshop. February, 1993, NASA/GSFC, Greenbelt, MD, Technical Report, IGBP-DIS Working Paper No. 9, IGBP, Paris.

Justice, C., and S. Korontzi, 2001: A review of satellite fire monitoring and requirements for global environmental change research. In Global and Regional Wildfire Monitoring: Current Status and Future Plans (F. J. Ahern, J. G. Goldammer, C. O. Justice, Eds.), SPB Academic Publishing , The Hague, Netherlands, pp. 1-18.

Kigawa, S., 2000: Overview of MTSAT-1R Imager. Japan Meteorological Satellite Center Technical Note No. 39, Japan Meteorological Agency, in press.

Kaufman, Y. J., C. J. Tucker, and I. Fung, 1990: Remote sensing of biomass burning in the tropics. *Jour. of Geophys. Res.,* **95**, 9,927-9,939.

Levine, J.S., 1991: Biomass burning: combustion emissions, satellite imagery, and biogenic emissions. In *Global Biomass Burning: Atmospheric,Climatic, and Biospheric Implications*, edited by J. S. Levine, The MIT Press, Cambridge, MA, pp. 264-271.

Li, Z., Y. J. Kaufman, C. Ichoku, R. Fraser, A. Trishchenko, L. Giglio, J-Z. Jin, and X. Yu, 2001: A review of AVHRR-based active fire detection algorithms: principles, limitations, and recommendations. In Global and Regional Wildfire Monitoring: Current Status and Future Plans (F. J. Ahern, J. G. Goldammer, C. O. Justice, Eds.), SPB Academic Publishing , The Hague, Netherlands, pp. 199 - 225.

Matson, M., and J. Dozier, 1981: Identification of subresolution high temperature sources using a thermal IR sensor. *Photo. Engr. and Rem. Sens.* **47**,1311-1318.

Menzel, W. P., and J. F. W. Purdom, 1994: Introducing GOES-I: the first of a new generation of geostationary operational environmental satellites. *Bull. Amer. Met. Soc.* **75**(5):757-781.

Molenar, D. A., K. J. Schrab, and J. F. W. Purdom, 2000: RAMSDIS contributions to NOAA satellite data utilization. *Bull. Amer. Met. Soc.* **81**(5), 1019-1030.

Moreau, M. , 1999: Personal Communication. Environment Canada/Meteorological Services/Quebec region. Ste-Foy, Quebec, Canada.

Muirhead, K, and A. Cracknell, 1985: Straw burning over Great Britain detected by AVHRR. *Intl. Jour. of Remote Sensing*, **8**, 827-833.

Penner, J. E., R. E. Dickinson, C. A. O'Neill, 1992: Effects of aerosol from biomass burning on the global radiation budget. *Science*, **256**, 1,432-1,433, 1992.

Prins, E. M., and W. P. Menzel, 1994: Trends in South American biomass burning detected with the GOES VAS from 1983-1991. *J. Geophys. Res.* **99**(D8), 16,719-16,735.

Prins, E. M., J. M. Feltz, W. P. Menzel, and D. E. Ward, 1998: An overview of GOES-8 diurnal fire and smoke results for SCAR-B and the 1995 fire season in South America. *Jour. of Geo. Res.* **103**(D24), 31,821-31,836.

Prins, E., J. Schmetz, L. Flynn, D. Hillger, J. Feltz, 2001: Overview of current and future diurnal active fire monitoring using a suite of international geostationary satellites. In Global and Regional Wildfire Monitoring: Current Status and Future Plans (F. J. Ahern, J. G. Goldammer, C. O. Justice, Eds.), SPB Academic Publishing , The Hague, Netherlands, pp. 145 - 170.

Schmetz, J., H. Woick, S. Tjemkes, and J. Rattenborg, 1998: From Meteosat to Meteosat Second Generation. Proceedings of the *Ninth Conference on Satellite Meteorology and Oceanography.* Paris, France, May 25-29, pp. 335-338.

Setzer, A. W. and M. C. Pereira, 1991: Amazonian biomass burnings in 1987 and an estimate of their tropospheric emission, *Ambio*, **20**, 19-22.

Weaver, J., J. Purdom, and T. Schneider, 1995: Observing forest fires with the GOES-8 3.9 μm imaging channel. *Weather and Forecasting.* **10**(4), 803-808.

Woick, H., J. Schmetz, and S. Tjemkes, 1997: An introduction to Meteosat Second Generation imagery and products. Presented at the 1997 Meteorological Data Users' Conference, Brussels, Belgium, Sep. 29- Oct. 3.

Wooster, M. J., and D. A. Rothery, 1997: Thermal monitoring of Lascar Volcano, Chile, using infrared data from the along-track scanning radiometer: a 1992-1995 time series. *Bull. Volcanol.* **58**, 566-579.

P1.13

A COMPARISON OF THE GOES-8 ABBA AND INPE AVHRR FIRE PRODUCTS FOR SOUTH AMERICA FROM 1995-2000

Joleen M. Feltz*
Cooperative Institute for Meteorological Satellite Studies, University of Wisconsin, Madison, Wisconsin

Elaine M. Prins
NOAA/NESDIS/ORA Advanced Satellite Products Team, University of Wisconsin, Madison, Wisconsin

Alberto W. Setzer
Instituto Nacional de Pesquisas Espaciais, Sao Paulo, Brazil

1. INTRODUCTION

Since 1995 the Cooperative Institute for Meteorological Satellite Studies (CIMSS) at the University of Wisconsin - Madison has been using the Geostationary Operational Environmental Satellite (GOES)-8 Automated Biomass Burning Algorithm (ABBA) to monitor diurnal biomass burning activity throughout South America during the height of the fire season (June - October). The Brazil Instituto Nacional de Pesquisas Espaciais (INPE) has monitored fire activity in Brazil using the Advanced Very High Resolution Radiometer (AVHRR) sensor on board the NOAA-12 polar orbiting satellite since 1987. This paper presents a comparison of these two fire products during each fire season from 1995 to 2000. It will include an overview of the spatial and temporal observing characteristics of both the GOES and AVHRR instruments and discuss advantages of each system for fire identification in the region. This comparison will show that the higher temporal resolution of the GOES and the higher spatial resolution of the NOAA AVHRR provide complementary information about fire activity in South America.

2. THE GOES-8 ABBA AND NOAA AVHRR INPE FIRE PRODUCTS

The GOES-8 ABBA is a fully automatic fire detection algorithm which uses the visible (near 0.65 micron), short-wave infrared window (near 4 micron), and the long-wave infrared window (near 11 micron) data, along with moisture information from other data sets, to identify and characterize sub-pixel fire activity. The GOES-8 spatial resolution is 4 km at the sub-satellite point, but studies have shown that GOES-8 can accurately identify fires a few acres in size (Menzel and Prins, 1996a; 1996b; Prins and Menzel, 1996a; 1996b). The geostationary orbit of GOES-8 provides the opportunity to view and estimate fire activity over portions of South America every half-hour, with complete continental coverage at three-hour intervals. These data can then be studied individually or combined in a daily unique fire composite. Fire pixels from four different time periods (1145, 1445, 1745, and 2045 UTC) are combined in the daily unique fire composite. If a fire pixel is observed in more than one time period, only one occurrence of the fire pixel is selected for the daily unique fire pixel composite. Typically, over 80% of the fire pixels observed in one time period are not observed at any of the other three observation periods (Prins et al., 1998; 2000; 2001).

The AVHRR sensors on the NOAA polar orbiting series of satellites have a spatial resolution of 1 km at the sub-satellite point. Generally, INPE reports fire pixels from the NOAA-12 sensor with the exception of 1-14 August 1995, when the NOAA-14 sensor was used to report the fire pixels. The fire detection method employed by INPE is a digital nonsupervised clustering algorithm which selects pixels as burning if the AVHRR radiometric temperature exceeds 46°C (Setzer and Pereira, 1991). Data from the afternoon overpass are used to identify fire pixels. Fire counts from INPE are provided in a weekly email in grid format. They consist of a 7-day sum at 0.5-degree increments from 7°N to 40°S and 75°W to 34.5°W. A second receiving station, added in 1999, increased the observation region. However, the smaller region is used in this study for consistency between years.

Previous studies have characterized the GOES-8 observed diurnal, spatial, seasonal, and interannual trends in fire activity, clouds, and aerosols throughout South America for each fire season (June –October) from 1995 to 1999 (Prins et al., 1998; 2000). This study will focus on the combined spatial and temporal distribution of fires provided by GOES and AVHRR for the months of August-October 1995-2000. This captures the peak of the burning season and minimizes the number of missing days.

* *Corresponding author address:* Joleen M. Feltz, University of Wisconsin-Madison, Cooperative Institute for Meteorological Satellite Studies, 1225 W. Dayton, Madison, WI 53706; email: joleen.feltz@ssec.wisc.edu.

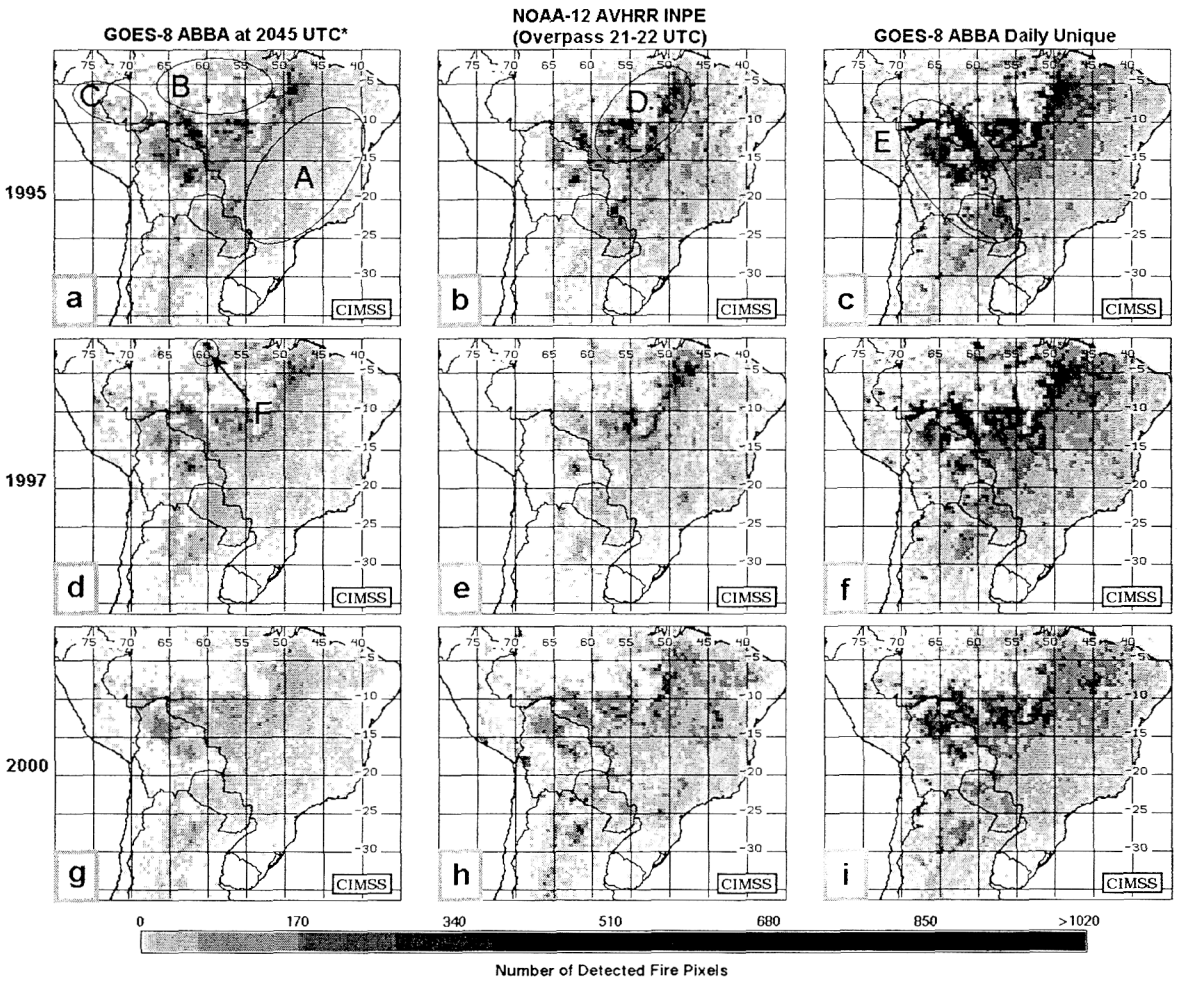

*August 1-14, 1995: GOES-8 1745 UTC data used to correspond to the NOAA-14 overpass (17-18 UTC) used for the INPE fire product

Figure 1: A comparison between the GOES-8 ABBA and NOAA-12 AVHRR INPE detected fire pixels for the months of August-October 1995, 1997, and 2000. The grid spacing is 0.5 degrees.

3. FIRE DISTRIBUTIONS IN SOUTH AMERICA AS OBSERVED BY GOES and NOAA AVHRR IN 1995, 1997, AND 2000

Fire distributions for all the years from 1995-2000 were plotted, and three representative years are shown in figure 1. The GOES-8 ABBA fire product at 2045 UTC (fig 1a, 1d, 1g), the NOAA-12 AVHRR INPE detected fire pixels from the afternoon overpass (fig 1b, 1e, 1h), and the GOES-8 ABBA daily unique fire product (fig 1c, 1f, 1i) are shown for comparison. The most active year was 1995 followed by 1997. The 1997 season was also selected to show the effect of drought in northern Amazonia. Both sensors observed less burning in 2000, providing an opportunity to compare a year with lower activity to the peak years. Examples from these three years show that satellite regional coverage, view angle, time of observation, and sensor spatial resolution all affect fire detection.

Overall, the NOAA-12 AVHRR INPE algorithm detects more fire pixels in a single time period than the GOES-8 ABBA at that same time period. This pattern is especially pronounced in the cerrado regions (region A) where narrow flame fronts are difficult to detect with GOES-8 due to its reduced spatial resolution. It is sometimes possible for GOES-8 to detect cerrado fires in the initial flaming stage, and the GOES-8 ABBA daily unique fire product shows many fires in the cerrado region which were missed in the 2045 UTC GOES-8 ABBA, but reported in the NOAA-12 AVHRR INPE fire pixel product. The two instruments tend to show the same patterns in regions where the view angle for both sensors is low and the coverage for AVHRR is good.

Burning along roads and the Amazon river (region B) is observed in all of the images, but the single time period distributions neither capture the extent nor the intensity of activity. Every year fires along the road being constructed west from Rondonia

(region C) to the Pacific coast appear in the GOES-8 ABBA fire composites. However, the road is not well defined in the NOAA-12 AVHRR INPE fire pixel product except in year 2000. The detection of burning along the road in 2000 by the AVHRR sensor resulted from the addition of a western receiving station providing more consistent information in western South America. The sensors also consistently show that most fire activity is concentrated in the "arc of deforestation" (region D). The GOES-8 ABBA also indicates that the borders between Bolivia and Rondonia, and Acre and Paraquay (region E) are places of more persistent activity. In peak years the GOES-8 ABBA 2045 UTC fire pixel product compares well with the NOAA-12 AVHRR INPE fire pixel product. However, the single time period quantities underestimate the number of fires reported throughout the day. In addition, the NOAA-12 AVHRR INPE product underestimates burning along the border regions as compared to the GOES-8 ABBA daily unique and in 1997 and 2000, the GOES-8 ABBA 2045 UTC data. It is near these border regions, close to the GOES-8 sub-satellite point of 0°N and 75°W, where the view angle for GOES-8 is optimal. The 1997 drought in Northern Amazonia caused a lake north of Manaus to dry (region F). The exposed timber on the bottom of the lakebed subsequently caught fire. Both sensors captured this event, but the AVHRR did not observe as many instances of that fire. The fire burned for days, but the AVHRR observed the Manaus region less than 2% of the time from August-October 1997.

4. COMPARISONS OF FIRE QUANTITIES DERIVED FROM GOES AND NOAA AVHRR FROM 1995-2000

The number of fires reported by both GOES and AVHRR are displayed in table 1. Since each year covers a different date range, the 1995 totals are a combination of two different time periods, and a second AVHRR receiving station was added in 1999, interannual comparisons of the totals are not possible. Two of these caveats produce results that are easily distinguished in the data shown in table 1. First, the contribution of the 1745 UTC period to the GOES-8 ABBA daily unique composite is significant. Therefore, the fire pixel totals for both GOES-8 ABBA at a single time period and the NOAA-12 AVHRR INPE are closer to the total fire pixel estimates of the ABBA daily unique algorithm in 1995 than in other years. Secondly, the 1999 and 2000 INPE totals are closer to the GOES-8 ABBA daily unique totals in the respective years, reflecting the extended coverage of the AVHRR.

The GOES-8 ABBA daily fire pixel counts range from 1.5 to 4.5 higher than the single time period NOAA-12 INPE AVHRR observations between 21-22 UTC. The ratio of ABBA daily unique fire pixels to the single time period ABBA estimates is even higher, ranging from 3 to 5. Grid subsets were used to allow a comparison between the GOES-8 ABBA daily unique and the NOAA-12 AVHRR INPE fire pixel products where the NOAA-12 AVHRR has better coverage (table 2).

Table 1

Year	Julian Day (NOAA Overpass)	INPE	GOES Single Time Period	GOES Daily Unique
1995	209-226 (17-18 UTC) 227-303 (19-22 UTC)	134417	86827	267584
1996	208-305 (19-22 UTC)	45137	42393	205293
1997	213-304 (19-22 UTC)	66097	56449	260696
1998	213-309 (19-22 UTC)	110675	60326	248018
1999	213-304 (19-22 UTC)	141516	62340	247583
2000	214-305 (19-22 UTC)	103272	29107	169095

Table 2

	Fire Pixel Counts (Ratio of GOES/INPE)		
	Entire Grid	60% Coverage	80% Coverage
1995	2.0	1.3	1.1
1996	4.5	3.0	2.5
1997	3.9	2.5	2.2
1998	2.2	1.6	1.4
1999	1.7	1.7	1.8
2000	1.6	1.6	1.6

When the NOAA-12 AVHRR views a region at least 60% of the time, the ratio of GOES-8 ABBA daily unique fire pixel observations to NOAA-12 AVHRR INPE fire pixels decreases to a ratio ranging from 1.3 to 3. At 80% coverage, the ratio is between 1.1 and 2.5. The lack of variability in the ratios for 1999 and 2000 are a result of the increased AVHRR coverage following the addition of the second receiving station. Prior to 1999, less than 30% of the study area had 60% or greater overpass coverage. This value increased to 50% in 1999 and to 91% in 2000.

The 1 km resolution of the NOAA-12 AVHRR generally provides the capability to detect more fires at a single time period, and provides enhanced information where the overpass coverage is high. However, the ability to capture fires as they burn throughout the day is also extremely important since previous studies have shown that many fire signatures are often only intense enough to be detected by satellite for a short time period (Prins et al, 1998; 2000).

5. CONCLUSIONS

Comparisons of the NOAA-12 AVHRR INPE and the GOES-8 ABBA fire pixel products show similar features in the spatial distribution of fires in South America. The higher spatial resolution of the NOAA-12 AVHRR results in more fire pixel observations at an instantaneous point in time and allows for the identification of fires with smaller flaming fronts. Since GOES-8 is in geostationary orbit, it can capture

the diurnal cycle of anthropogenic fires for better definition of regions with strong temporal signatures. It is also able to capture some fires in the flaming stages that are below the threshold of detection in later time periods. The consistent and complete continental coverage of GOES-8 allows it to observe fires in regions not adequately covered by a single overpass of the NOAA-12 satellite. The addition of the second NOAA polar orbiting satellite receiving station in 1999 made a significant impact on regional coverage. GOES-8 and AVHRR provide distinct and complementary capabilities for monitoring fire activity in South America.

6. REFERENCES

Menzel, W.P., and E.M. Prins, 1996a: Monitoring biomass burning and aerosol loading and transport utilizing multispectral GOES-8 data. 1996 International Symposium on Optical Science, Engineering, and Instrumentation, SPIE, Denver, Colo, August 4-9, 1996, pp. 50-59.

Menzel, W.P., and E.M. Prins, 1996b: Monitoring biomass burning with the new generation of geostationary satellites. In Biomass Burning and Global Change, edited by J.S. Levine, MIT press, Cambridge, MA, pp. 56-64,

Prins, E.M., and W.P. Menzel, 1996a: Monitoring biomass burning and aerosol loading and transport from a geostationary satellite perspective. Seventh Symposium on Global Change Studies, Am. Meteorol. Soc., Atlanta, Ga., Jan. 28 – Feb. 2, 1996, pp. 160-166.

Prins, E.M., and W.P. Menzel, 1996b: Investigation of biomass burning and aerosol loading and transport utilizing geostationary satellite data. In Biomass Burning and Global Change, edited by J.S. Levine, MIT press, Cambridge, MA, pp. 65-72.

Prins, E.M., W.P. Menzel, and J.M. Feltz, 1998: Characterizing spatial and temporal distributions of biomass burning using multi-spectral geostationary satellite data. Ninth Conference on Satellite Meteorology and Oceanography, Paris, France, May 25-29, 1998, pp. 94-98.

Prins, E.M., J. M. Feltz, R. A. Frey, C. C. Schmidt, W. P. Menzel, D. Wylie, 2000: A five-year trend analysis of biomass burning in South America Using GOES, Presented at the American Geophysical Union Spring Meeting, May 30 – June 2, 2000, Washington D.C.

Prins, E.M, J.M, Feltz, C.C. Schmidt, 2001: An overview of active fire detection and monitoring using meteorological satellites, Proceedings of the 11th Conference on Satellite Meteorology and Oceanography, Madison, WI, October 15-18, 2001, pp TBD.

Setzer, A.W., and M.C. Pereira, 1991: Amazonia biomass burnings in 1987 and an estimate of their tropospheric emissions. Ambio, 20, 19–22.

P1.14

Principal Component Image Analysis of MODIS for Volcanic Ash

Donald W. Hillger*
NOAA/NESDIS/ORA/RAMMT
CIRA / Colorado State University
Fort Collins CO

James Clark
NOAA/NESDIS/OSDPD/SSD
Satellite Analysis Branch
Camp Springs MD

1. Introduction

Current volcanic ash detection techniques rely heavily on split window differencing of the thermal longwave infrared bands (11 and 12 ?m) on current operational satellites (Prata 1989). However this technique is not uniformly effective in properly classifying volcanic ash pixels in the satellite scene, often falsely interpreting meteorological cloud as volcanic ash clouds and conversely (Simpson et al 2000). A recommendation of that study is that new research-grade satellite remote sensing instruments employing multi-spectral observations of volcanic plumes in the thermal infrared be used to better characterize eruptive events and that the information be used to design improved volcanic ash cloud detection sensors. This will lead eventually to wider operational exploitation of these powerful and increasingly accessible technologies (Oppenheimer 1998).

One of the new satellite research sensors currently available is the Moderate Resolution Imaging Spectroradiometer (MODIS). MODIS imagery offers a multi-spectral advantage over Geostationary Operational Environmental Satellite (GOES) imagery for viewing volcanic ash plumes. The advantage is due to the larger number of spectral bands on MODIS (36 bands: 19 bands in the visible and near-infrared, and 17 bands in the longer-wavelength infrared). In comparison there are five bands in the GOES Imager. All of the thermal infrared bands of MODIS are available at 1 km spatial resolution (at nadir). This is a horizontal resolution advantage over 4 km GOES infrared data, but that is not the focus of this study. In addition, some of the MODIS bands are in portions of the spectrum not sensed by GOES. This spectral advantage however is offset by the lack of sufficient temporal resolution and continuity to follow rapidly-changing phenomena as is customary from geostationary orbit.

2. Principal Component Imagery

In their study of volcanic plumes, Dean et al (1994) found that satellite images analyzed using principal component techniques clearly distinguished the plume from the surrounding terrain. Their preferred analysis technique utilized three-color composites of principal component and spectral band images to show the extent of the plume as well as its opaque and transparent properties. While typically applied to remote sensing of earth resources, principal component analysis has been applied to GOES Imager and Sounder data to create Principal Component Images (PCIs) for the detection of atmospheric and surface features in multi-band imagery (Hillger* 1996, Hillger and Ellrod, 2000). In addition, the use of principal component analysis becomes increasingly important as the number of spectral bands increases.

Half-hourly GOES imagery is used by the Washington Volcanic Ash Advisory Center (VAAC) to routinely produce analyses of ash plumes. One of the image products used to generate the ash advisories is PCI analysis of GOES multi-spectral imagery, in use operationally since December 1999. The basic PCI product is based on the three infrared bands (bands 2, 4, and 5) of the GOES Imager. Each of the three component images is a linear combination of the input bands with weights applied based on the transformation of the original bands using eigenvector/eigenvalue analysis of the original imagery. For the GOES Imager, PCI-2 and PCI-3 have proven to be the most useful for volcanic hot spot and ash plume detection respectively. This is because the common or correlated information in the three GOES infrared bands is relegated to PCI-1. PCIs 2 and 3 contain band difference information that highlights features not seen in single-band imagery. PCI-2 is primarily a band 2/4 (shortwave/longwave difference) image, and PCI-3 is primarily a band 4/5

* Corresponding author address: Dr. Donald W. Hillger, NOAA/NESDIS/RAMMT, CIRA/Colorado State University, Fort Collins CO 80523-1375. E-mail: hillger@cira.colostate.edu

(longwave split window difference) image, with small contributions from the remaining band in each case.

3. Analysis of Volcanic Ash

The case analyzed for this study was a large eruption of ash from the Popocatepetl volcano (hereafter abbreviated Popo, 19.02°N, 98.62°W) at 5426 m elevation near Mexico City. One of the days with widespread ash was 20 December 2000. Figure 1 shows an analysis issued by the Washington VAAC (Operations 1999) giving the extent of the ash plume based on GOES multi-spectral imagery for 1715 UTC. This analysis time matches the time of the MODIS imagery that was analyzed using PCIs. The ash extends mainly south and east of the volcanic source, to as far away as the Yucatan Peninsula. In the ash analysis the plume is given in two parts, at different flight levels (FL250 [7600 m] and FL320 [9800 m]). These levels were estimated by effectively matching the derived vector motion of the ash as seen in GOES imagery to the appropriate height levels from the Mexico City upper-air sounding and a model sounding.

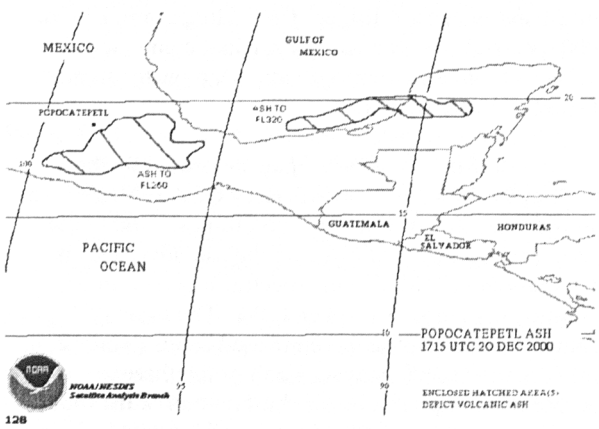

Figure 1: Volcanic ash analysis at 1715 UTC on 20 December 2000 for Popocatepetl volcano near Mexico City. Analysis based on GOES multi-spectral imagery by the Satellite Analysis Branch (SAB) Washington VAAC.

PCI-3 in Figure 2 is one of the GOES products used to generate the ash analysis in Figure 1. This product shows the ash cloud with good contrast to the image background, but with somewhat limited contrast to some of the other image features. The ash is mainly concentrated to the east and southeast of Popo. Ash extends east to a secondary maximum over Yucatan. The extent of the ash in both the ash analysis and PCI-3 serve as guides for the MODIS analysis to follow.

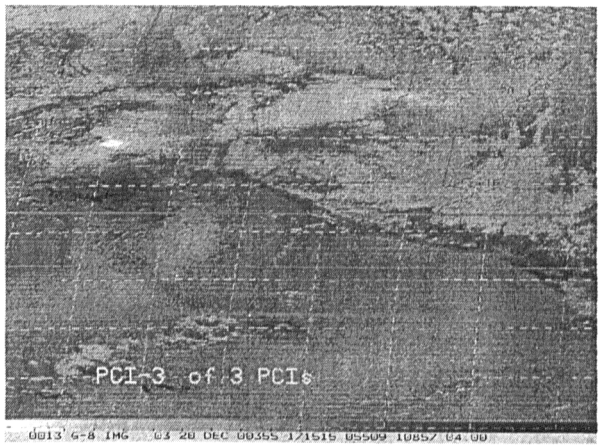

Figure 2: PCI-3 of 3 PCIs that were generated from the three thermal infrared bands (2, 4, and 5) of GOES for 1715 UTC on 20 December 2000. PCI-3 is one of the products used to generate the ash analysis in Figure 1. This product shows the ash cloud with significant contrast to the image background. This PCI is inverted black-to-white to make the ash plume white.

MODIS data for this volcanic ash case were available at 1715 UTC. None of the MODIS bands showed the relatively diffuse ash for this case when viewed alone. This is expected when the ash signal is subtle, appearing in contrast to the image background much more readily in multiple-image combinations. Ash that is associated with meteorological cloud can more easily be seen, but the ash content may be unknown. PCI analysis of the 17 MODIS thermal infrared bands provided several views of the ash plume. Table 1 shows the bandwidths and primary uses of MODIS thermal infrared bands used in the analysis.

The PCI analysis of the 17 thermal infrared bands of MODIS resulted in 17 PCIs. This paper will discuss only those PCIs that qualitatively show significant evidence of ash in contrast to the image background and other image features. This will lead into an analysis of the MODIS bands that contributed to those PCIs. The PCIs for this case are remapped from the MODIS polar-orbit projection into the GOES projection, to be more easily compared and contrasted with the ash analysis in Figure 1 and the GOES image in Figure 2.

Figure 3, showing the first PCI (PCI-1), which contains the majority (76%) of the information content (explained variance) in the 17 MODIS bands that went into the 17 PCIs, information common to all the thermal infrared bands. As such it gives an idea of the overall cloud conditions at the time of the event, the main features available in most of the thermal infrared bands.

The whitest areas are the highest clouds, low clouds are medium gray, and land surfaces are dark. Land surfaces vary in temperature from the blackest (hottest) to lighter gray (cooler). The area around but mainly to the north of Popo (which is marked by a label and an arrow pointing to the location of the volcano) contains some middle to higher-level clouds. Some of the white cloud mass nearest the volcano, appearing in PCI-1 as a result of appearing in most of the infrared bands, must be meteorological cloud. No ash plume is apparent in this image. Rather, the ash appears in higher-ordered PCIs where it becomes detectable by combining images from various portions of the spectrum.

Table 1: MODIS thermal infrared bands and bandwidths

Primary Use	MODIS Band	Bandwidth (□m)
Surface/Cloud Temperature (shortwave CO_2)	20	3.66-3.84
	21	3.929-3.989
	22	3.929-3.989
	23	4.02-4.08
Atmospheric Temperature (shortwave CO_2)	24	4.433-4.498
	25	4.482-4.549
Cirrus Clouds	26	1.36-1.39
Water Vapor	27	6.535-6.895
	28	7.175-7.475
	29	8.4-8.7
Ozone (O_3)	30	9.58-9.88
Surface/Cloud Temperature (split window)	31	10.78-11.28
	32	11.77-12.27
Cloud Top Altitude (longwave CO_2)	33	13.185-13.485
	34	13.485-13.785
	35	13.785-14.085
	36	14.085-14.385

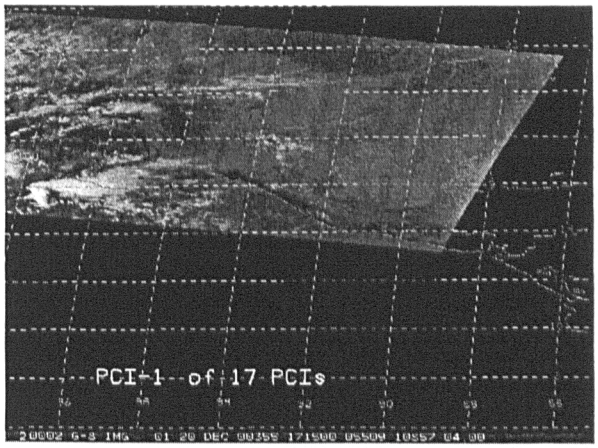

Figure 3: PCI-1 of 17 PCIs that were generated from the 17 thermal infrared bands of MODIS for 1715 UTC on 20 December 2000. PCI-1 shows the main cloud features common to all of the MODIS infrared bands.

3.1 Analysis of the PCIs That Show Ash

Of the remaining higher-ordered PCIs, only those in which the ash was detected with significant contrast to the image background and other image features will be discussed. The discussion will focus on where the ash was detected in each PCI, some of the relative qualities of those images for ash detection, and on the MODIS bands that contributed to those PCIs.

Table 2 summarizes details of the nine (of seventeen) PCIs that contained identifiable ash signal. The PCIs are listed in order of decreasing ash signal or contrast to the background and other features of the image. In the first three PCIs listed in the table the ash has much more contrast to surrounding regions than in the next three, and even more contrast than in the last three PCIs, which are of limited value for ash detection. The relative qualities of each PCI are given in the second column of Table 2. Detection problems, such as low contrast, noise, and confusion between ash cloud and non-ash features, are noted. Because of the decreasing ability to detect ash compared to the image background and other image features, it is increasingly hard to use more than the first six of these PCIs to determine the presence of ash for this case. Of those six PCIs, only the first three will be shown.

Each PCI consists of combinations of all input bands, but only a few of the original bands contribute heavily to the PCIs, as indicated by their much larger weight in the creation of the PCIs. After a discussion of the first three PCIs, in the order listed in Table 2, details summarizing the MODIS bands contributing to those PCIs will follow. In the last two columns of the table

are the percentage of the explained variance and the signal-to-noise ratio for each PCI. The signal-to-noise ratios were determined using spatial structure analysis (Hillger and Vonder Haar, 1988). A signal-to-noise ratio greater than 1.0 represents sufficient signal in the image to view features. (The top value in the last column, 1.70, means there is 70% more signal than noise in PCI-9). These two columns show that the information content of the PCIs is a very small fraction of the total signal in the MODIS bands, and that the signal in some of the PCIs is marginally above the noise level of the image. From these numbers it is clear that the best ash signal does not necessarily come from PCIs with larger explained variances or highest signal-to-noise ratios.

Table 2: PCIs in descending order of qualitative value for ash plume detection

PCI number (in descending qualitative value)	Qualitative assessment of ash contrast to the image background and features	PCI Explained Variance (%)	PCI Signal-to-Noise Ratio
9	Good ash concentration and extent	0.12	1.70
8	Good ash concentration and extent, noisy	0.18	1.26
16	Good ash concentration and extent, but cloud	0.002	3.30
14	Densest ash only, low contrast	0.012	1.48
4	Densest ash only, significant cloud contamination	2.7	6.55
10	Densest ash only, low contrast, noisy	0.07	1.26
13	Very weak, low contrast	0.027	1.20
15	Very weak, contaminated	0.003	1.70
7	Questionable value	0.39	3.71

PCI-9 in Figure 4a shows the volcanic ash as light gray in contrast to the image background. The ash also appears in PCI-8 in Figure 4b but with more noise than PCI-9. Table 2 gives a signal-to-noise ratio of 1.70 for PCI-9 and 1.26 for PCI-8. The signal-to-noise ratio is quite small for both PCIs, but there is sufficient signal above noise and contrast to the image background, so that the extent of the ash in both of these PCIs agrees well with the ash analysis in Figure 1. However, the increased signal-to-noise for PCI-9 gives the image a smoother-looking background, as opposed to the more apparent noise and line-to-line striping (due to multiple detectors in the MODIS instrument) in PCI-8. There is also one bad half-line of data near the middle of the MODIS band 30 image that was transferred into most of the PCIs as a dashed line similar to the latitude and longitude lines.

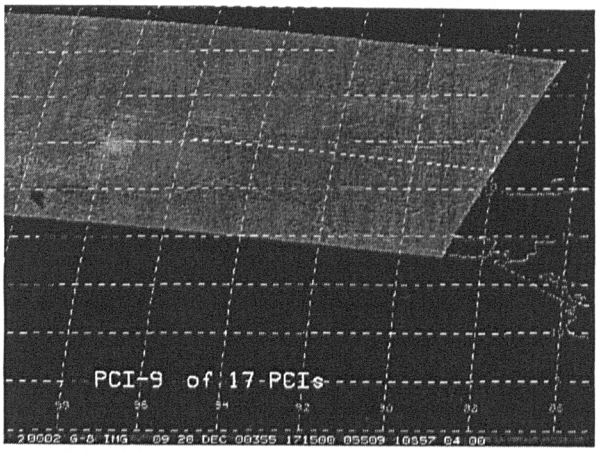

Figure 4a: PCI-9 of 17 PCIs that were generated from the 17 thermal infrared bands of MODIS for 1715 UTC on 20 December 2000. PCI-9 shows the ash plume as light gray, with good contrast to the image background and low noise.

In PCI-8 the portion of the ash plume not obscured by the clouds, as identified in PCI-1 in Figure 3, is denser to the east and southeast of the volcano. The ash also extends quite far east over the Yucatan Peninsula where there is a secondary maximum, due to an earlier exhalation of ash. The elongated west-east area of ash extending to the Yucatan may be slightly easier to identify in PCI-8, but there is increased chance of confusion between ash and low clouds to the south as seen in PCI-1. Also, another difference between the two PCIs is that the maximum ash concentration is east of Popo in PCI-8 and more southeast of Popo in PCI-9, probably due to variations in the height of the ash as noted in the analysis.

Figure 4c shows PCI-16, the next PCI in Table 2, with somewhat reduced ability to detect ash. The extent of the ash in PCI-16 is quite similar to that of GOES PCI-3 in Figure 2. PCI-16 is interesting because there is more connection between the primary ash maximum near Popo and the secondary ash maximum over Yucatan, highlighting this portion of the ash cloud. The secondary maximum also appears more intense

than in either PCI-9 or PCI-8. The variations are likely due to changes in the ash particle concentration and height of the ash in various parts of the plume. PCI-16 also contains more false ash-like signal. In particular, the thin line of ash-like signal just north of Popo, stretching from the western edge of the image eastward to 95°W, is identifiable as cirrus in PCI-1. Otherwise non-ash contamination in the signal can cause misidentification and either over- or under-estimation of the extent of the ash plume. This non-ash signal is probably the source of the increased signal-to-noise (3.3 from Table 2) for PCI-16, not the ash signal.

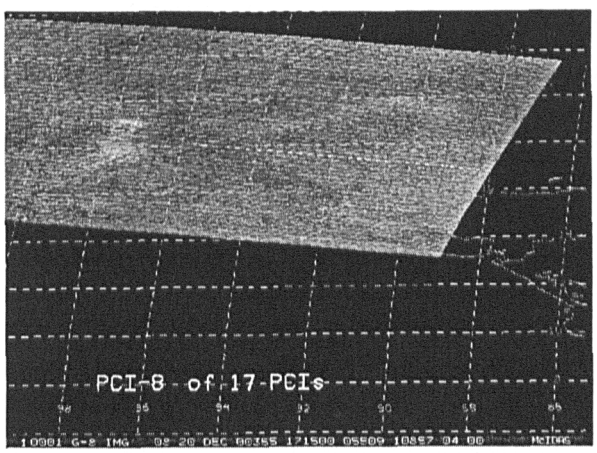

Figure 4b: Same as Figure 4a except PCI-8. PCI-8 shows the ash as white but contains significant image striping and noise from the MODIS instrument compared to PCI-9.

Table 3 gives information on the six MODIS bands that contributed the most to PCIs that were best at detecting the ash plume. Only the nine MODIS bands that contributed significantly to the first six PCIs are listed. For each of those bands the explained variance and sign are given for their contribution to each of the six PCIs. The explained variance is a measure of the magnitude of the contribution of each band and the sign is given to indicate whether the band contributed positively or negatively to a particular PCI. Whether the sign of a particular band is positive or negative is only important relative to the signs of the other bands, otherwise any PCI can be inverted along with the signs of all of the bands that contributed to it.

In Table 3 the two bands, one with the most positive and the other with the most negative explained variance, are bolded for each PCI. After the third PCI, the following row contains the sums of the explained variances for each band to the first three PCIs, regardless of the sign of the contribution. The bands that are considered most important for volcanic ash detection, with variances above 30%, are bolded. In this case the most important bands for overall ash detection are 25 (marginally), 30, 31, and 36. Likewise, the final row in the table gives the sums of the explained variances for each band to all six PCIs indicated as adequate for ash detection. This time the most important bands, with total explained variance over 50%, are bands 29 through 32, 34, and 36, leaving out band 25. The additional bands are important for locating more subtle variations in the ash plume density, such as seen in PCI-14. Thus these bands should not be excluded from ash analysis.

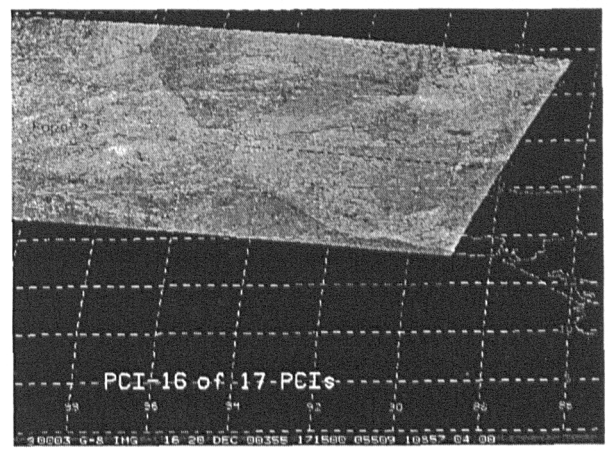

Figure 4c: Same as Figure 4a except PCI-16. PCI-16 shows the ash plume as lighter gray, but suffers from possible false ash signal due to cloud contamination.

The bands determined to be most important are combined in various ways to reveal the ash: PCI-9 is the difference between the ozone and longwave CO_2 bands at 9.7 ?m and 14.2 ?m respectively; PCI-8 is mainly the difference between shortwave and longwave CO_2 bands at 4.52 ?m and 14.2 ?m respectively; PCI-16 is the difference between a longwave window band and a nearby "dirty" window band at 11.0 ?m and 12.0 ?m respectively; and PCI-14 is primarily the difference between a water vapor band and a "dirty" window band at 8.6 ?m and 12.0 ?m respectively.

There is an emissivity minimum between 8.0 and 9.7 ?m due to silicate rock, which is probably why the combination of bands in PCI-9 is the most important. Also, the 8.6 ?m band is near the peak absorption for sulphate aerosols around 8.4 ?m (Prata 1989), which is probably why the combination of bands in PCI-14 is important, in addition to the minimum in emissivity due to silicate in that portion of the spectrum.

Table 3: MODIS bands contributing heavily to the first six PCIs in Table 2 (in descending order of ash plume contrast to the image background and other image features)

PCI	Explained Variance (%) and Sign (negatives in parentheses) of MODIS Band Contributions								
	20	25	29	30	31	32	33	34	36
	3.75 □m	4.52 □m	8.6 □m	9.7 □m	11.0 □m	12.0 □m	13.3 □m	13.6 □m	14.2 □m
9	3	(11)	(~0)	51	~0	(~0)	1	1	(16)
8	4	(19)	2	9	1	~0	(2)	(6)	54
16	~0	~0	(7)	(~0)	63	(17)	(~0)	~0	~0
Sum of above	7	30	9	60	64	17	3	7	70
14	1	(2)	48	(4)	(2)	(36)	1	~0	(~0)
4	24	1	(17)	(1)	(6)	(6)	~0	6	12
10	(1)	(1)	1	~0	~0	(1)	(36)	43	(1)
Sum of all above	33	34	75	65	72	60	40	56	84

4. Summary and Conclusions

The abundance of bands available on MODIS requires sophisticated band-combination techniques such as PCIs to determine the bands that are most suitable for detection of volcanic ash. Even though the explained variance of most of the PCIs is generally small, several of these image products provided sufficient signal above noise to see the ash plume with good contrast to the image background and other image features. While many of the MODIS bands contribute to ash detection, various combinations of these bands, in the form of various PCIs, highlight variations in the ash plume height and/or density, where the ash occurs at different levels or has different particle concentrations. These applications of the PCI technique isolate MODIS band combinations that are the most useful and significant for qualitatively detecting both the extent and the concentration of the ash.

The multitude of MODIS bands gives much more flexibility for ash detection than the limited number of bands on the GOES Imager. The results of this study indicate that several of the MODIS bands are useful for volcanic ash detection, in particular, bands 29 through 32, in the water vapor and longwave portions of the spectrum. This includes the 7.0 to 9.7 □m portion of the spectrum known for volcanic ash signature. However, band 30 at 9.7 □m is neither available on the current GOES Imager nor planned for future GOES Imagers. Regardless, better ash plume detection will be available with the increased number of bands and good temporal resolution available from the Imagers planned for the GOES series.

Acknowledgements

The MODIS data for this study were provided by Chris Moeller of the CIMSS at the University of Wisconsin in Madison. Funding for this study is made available through NOAA Grant NA67RJ0152.

5. References

Dean, K., S.A. Bowling, G. Shaw, and H. Tanaka, 1994: Satellite analyses of movement and characteristics of the Redoubt volcano plume, January 8, 1990. *Journal of Volcanology and Geothermal Research*, 62, 339-352.

Hillger, D.W., and T.H. Vonder Haar, 1988: Estimating noise levels of remotely-sensed measurements from satellites using spatial structure analysis. *J. Atmos. Ocean. Tech., 5(2),* April, 206-214.

Hillger, D.W., 1996: Meteorological analysis using principal component image transformation of GOES imagery. *International Radiation Symposium - IRS'96: Current Problems in Atmospheric Radiation,* (W.L. Smith and K. Stamnes, Editors; A. Deepak Publishing), 19-24 August, Fairbanks AK, 480-483.

Hillger, D.W., and G.P. Ellrod, 2000: Detection of unusual atmospheric and surface features by employing Principal Component Image transformation of GOES imagery, *Tenth Conference on Satellite Meteorology and Oceanography*, AMS, 9-14 January, Long Beach CA, 461-464.

Operations of the Washington Volcanic Ash Advisory Center, 1999: *Third Caribbean/South American Regional Air Navigation Meeting,* International Civil Aviation Organization, October 05-15, 5-p.

Oppenheimer, C., 1998: Volcanological applications of meteorological satellites, *International Journal of Remote Sensing*, 19, 2829-2864.

Prata, A.J., 1989: Observations of volcanic ash clouds in the 10-12 □m window using AVHRR/2 data, *International Journal of Remote Sensing*, 10, 751-761.

Simpson, J.J., G. Hufford, D. Pieri, and J. Berg, 2000: Failures in detecting volcanic ash from a satellite-based technique, *Remote Sensing of Environment*, 72, 191-217.

P 1.15

Loss of the 12.0 μm "Split Window" Band on GOES-M: Impacts on Volcanic Ash Detection

Gary P. Ellrod
Office of Research and Applications (NOAA/NESDIS)
Camp Springs, Maryland 20746

1. INTRODUCTION

Beginning with the Geostationary Operational Environmental Satellite (GOES)-M spacecraft (successfully launched on 23 July 2001) through GOES-Q (scheduled launch in 2007), a 12.0 μm "Split Window" InfraRed (SWIR) band (4 km resolution) on the Imager will be replaced by a 13.3 μm CO_2 absorption band (8 km resolution). Table 1 summarizes the changes planned for the reconfigured GOES Imagers. A more detailed description of GOES-M, with an assessment of effects on many environmental parameters, is available in Schmit et al, (2001).

Brightness temperature differences (BTD) between the IR window bands at 10.7 μm (Band 4 on GOES) and 12.0 μm (Band 5) have been successfully used in tracking hazardous volcanic ash clouds since they first became available on GOES-8 in 1994. Negative values of the Band 4 minus Band 5 BTD are typical of volcanic ash, while positive values denote meteorological clouds (e.g. Prata, 1989). This Two-Band Split Window (TBSW) product from GOES-8 is relied upon heavily at the Washington Volcanic Ash Advisory Center (VAAC), which is responsible for operational hazard monitoring of a large, volcanically-active portion of the Caribbean, and Central and South America. Other North American VAACs (Anchorage, Montreal) also employ the TBSW from GOES, but to a lesser extent.

The purpose of this paper is to describe the possible impact of the loss of this IR channel on volcanic ash detection within the GOES field-of-view, and discuss alternative strategies to mitigate this loss. The latter comprise: (1) maximum utilization of all remaining GOES channels, and (2) exploitation of the global constellation of polar orbiting meteorological satellites, including the operational National Oceanic and Atmospheric Administration (NOAA) series, and research satellites launched by the National Aeronautics and Space Administration (NASA).

2. DATA AND PROCEDURES

In order to assess the effect of the GOES-M+ Imager channel reconfiguration on volcanic ash detection, GOES-8 Imager or Sounder data from several prior eruptions were analyzed to see how volcanic ash coverage would look with and without the use of the 12.0 μm IR band. The GOES-8 Sounder (see Menzel et al, 1998) has all IR bands currently on the Imager, plus the 13.3 μm band, although at a lower resolution (10 km). The analysis was completed using principle component image software developed by Hillger (1996) which displays unique information available from the input IR wavelengths. The best principle component depiction of the ash cloud for each event was compared to a subjective best estimate of the actual ash cloud coverage based on: (1) analysis of all available GOES data, including visible images, (2) the evolution of the volcanic cloud from its eruption to image time, and (3) VAAC advisories. In one case (26 December 1997) a concurrent Total Ozone Mapping Spectrometer (TOMS) Aerosol Index image was obtained as a source of independent ash coverage.

In addition to qualitative comparisons, a quantitative parameter, termed "false pixel rate" (FPR) was determined. The FPR describes the percentage of the total image area (expressed in pixels) comprised of "false ash" (based on the subjective "true" ash plume described above). This can be described as:

$$FPR = (T - A) / N \qquad (1)$$

where T is the total of ash plus false pixels, A is the number of "true" ash pixels, and N is the total number of pixels in the image scene.

The six cases analyzed are summarized in Table 2, which contains information on the volcano name, date, time(s), type of data evaluated (Imager versus Sounder) and relative strength of the eruption. Analysis of the 26 December 1997 Soufriere Hills eruption is not complete. Two cases (Lascar, 20 July 2000 and Guagua Pichincha, 5 October 1999) were evaluated at hourly intervals for several hours. For some events that utilized only Sounder data, only single time periods are available due to the relatively infrequent Sounder scanning of volcanically active regions (once every six hours for the Caribbean, one to three hours for the Gulf of Mexico, none over South America).

3. RESULTS

Preliminary results indicate that the loss of the SWIR band will result in an increase of mis-identified ("false") ash pixels which seem to vary diurnally. During the

Corresponding author address: Gary P. Ellrod, Room 601, E/RA2, WWB, 5200 Auth Road, Camp Springs, MD 20746 Email: gary.ellrod@noaa.gov

daytime, the increase in false pixel rate without SWIR will be minimal (~1-2%) due to the positive contribution of reflectance in the 3.9 μm shortwave IR band. At night, the false pixel rate increases by a factor of ~ 4, likely due to the loss of shortwave reflectance.

A representative daytime example is shown by the histogram in Figure 1 for the Guagua Pichincha eruption. At 2015 UTC (~1.5 hr after eruption), the FPR is >5 times larger using the SWIR than without its use. Use of the SWIR is less effective shortly after the eruption, due to the opacity of the volcanic cloud caused by large ash particles and considerable condensed water droplets and/or ice. At the later times (2115 and 2215 UTC) the FPR is ~3%, comparable to that obtained from the best image with no SWIR contribution. The increase in the latter to ~5% by 2215 UTC is due to less contribution from solar reflectance as sunset approaches. The role of reflectance at shortwave IR wavelengths has been described by Schneider and Rose (1994) for analysis of Spurr volcano ash samples in Alaska. An image comparison at 2215 UTC is shown in Figure 2.

A nighttime example from the GOES Sounder was obtained for an ash cloud from Popocatepetl volcano in Mexico that drifted across eastern Mexico on the night of 23 January 2001. The FPR values for the image that all four IR bands (including SWIR) are ~5 times less than for one that uses only the other IR bands. The latter were determined using the Sounder equivalents to Imager bands 2, 3, 4 and 2, 3, 4, and 6, respectively (Band 6 will be the new 13.3 μm IR). Inclusion of data from the 13.3 μm band appears to provide a slight positive impact, allowing for better discrimination of ash from thin cirrus clouds. A scatter plot of the Sounder data at this time for equivalent Bands 4 minus 6 vs Band 4 temperature (Figure 3) indicated a significantly higher BTD for cirrus clouds than for ash.

Subjective evaluation indicated that most of the mis-identified ash is not contiguous with the "true" ash plume or cloud, however, suggesting that a human analyst can successfully track an ash plume or cloud, and provide a reasonably good estimate of its area. The capability to animate GOES imagery at 15 to 30 min intervals provides valuable continuity in this analysis. Any gain achieved from the 13.3 μm IR data will be offset somewhat by its lower resolution (8 km), until GOES-O in 2005 when it will improve to 4 km.

4. ALTERNATIVE DATA SOURCES

In addition to the GOES Imager, the GOES Sounder provides 18 IR bands at 10 km resolution. The Sounder has limited spatial and temporal coverage however (current GOES operational scanning areas and schedules may be viewed at: http://www.ssd.noaa.gov). Nevertheless, if dedicated to view volcanic regions more often, the Sounder can provide useful TBSW-based image products (Ellrod, 1998).

The 12 μm IR channel will continue to be available at 1 km resolution from the Advanced Very High Resolution Radiometer (AVHRR) on the NOAA polar spacecraft The Moderate Resolution Infrared Spectrometer (MODIS) on the NASA Earth Observation Satellites (Aqua and Terra) will also have this spectral band , along with 35 others, also at 1 km. The Chinese Fun Yueng (FY)-1C has also recently become available to the Anchorage VAAC to fill some data gaps at high latitudes. The polar satellite data can provide better quality images to supplement (or calibrate) ash products generated from GOES. Merging of concurrent GOES and POES images is also a possibility.

5. SUMMARY AND CONCLUSIONS

GOES Imager and Sounder data were evaluated to determine the possible effects of losing the 12 μm Split Window IR band, on GOES-M (12) through Q (a period of at least 6 years). Principle component images with and without the SWIR were compared subjectively, and objectively using a false alarm rate parameter. GOES Sounder data were also evaluated in a few instances to assess any potential contributions from the new 13.3 μm Imager band. During periods of daylight, there was little difference in the quality of IR detection without the SWIR, likely due to the reflectance peak of ash near 3.9 μm. At night, the ash detection capability appeared to be somewhat worse, due to more interference from non-ash features, such as clouds or surface features. The effects of this performance on aviation operations could be an occasional increase in the area of analyzed ash coverage to err on the side of safety, resulting in somewhat longer enroute diversions. The 13.3 μm IR band should be useful in distinguishing ash from cirrus clouds, but not from low level water droplet cloud systems. In summary, we will still be able to observe and track significant volcanic ash clouds in the GOES-M through Q era (2002-2008+), but with some degradation that will be most significant at night.

6. REFERENCES

Ellrod, G. P., 1998: The use of GOES Sounder imagery for the detection of hazardous volcanic ash plumes. *National Weather Digest*, **22**, 3-9.

Hillger, D. W., 1996: Meteorological features from principle component image transformation of GOES imagery. Proceedings, Soc. of Photo-Optical Instr. Eng., 7-9 August 1996, Denver, Colorado, 111-121.

Menzel, W. P., F. C. Holt, T. J. Schmit, R. M. Aune, A. J. Schreiner, G. S. Wade, and D. G. Gray, 1998: Application of GOES-8/9 Soundings to Weather Forecasting and Nowcasting. *Bull. Amer. Meteor. Soc.*, **79**, 2059-2077.

Prata, A. J., 1989: Observations of volcanic ash clouds in the 10-12 μm window using AVHRR/2 data. *Int. J. Remote Sensing*, **10**, 751-761.-

Schneider, D. J. and W. I. Rose, 1991: Observations of the 1989-90 Redoubt Volcano Eruption Clouds Using AVHRR Satellite Imagery. *U. S. Geological Survey Bulletin 2047*, Proceedings of the First International Symposium on Volcanic Ash Detection and Aviation Safety, USGS, Reston, Virginia, 405-418.

Schmit, T. J., E. M. Prins, A. J. Schreiner, and J. J. Gurka, 2001: Introducing the GOES-M Imager. *National Weather Digest*, in press.

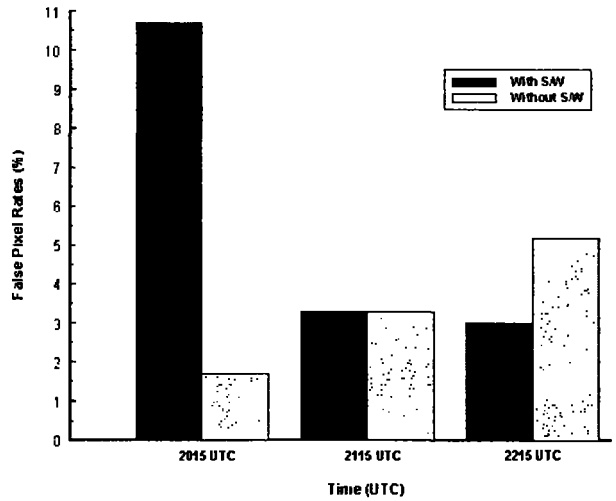

Figure 1. Histogram of False Pixel Rates (%) for Lascar eruption on 20 July 2000 with (black fill) and without (gray fill) the 12.0 μm IR band on the GOES Imager.

Table 1.
Imager Channel Configuration of GOES: Current vs GOES M-Q

	Current GOES (8-11)		GOES M-Q (2002-2008)		
Imager Band	**Wavelength (μm)**	**Resolution (km)**	**Wavelength (μm)**	**Resolution (km)**	**Description**
1	0.6	1	0.6	1	Daytime visible
2	3.9	4	3.9	4	Shortwave IR
3	6.7	8	6.7	**4**	Water Vapor
4	10.7	4	10.7	4	Window IR
5	12.0	4	-	-	Split Window
6	-	-	**13.3**	**8**	CO2 absorption

Table 2.
Volcanic Eruption Cases Evaluated for GOES Ash Detection Capability

VOLCANO	DATE	TIMES	TYPE	INTENSITY
Soufriere Hills, Montserrat	29 Sep 97	1620 UTC	Sounder	Weak
Soufriere Hills, Montserrat	23 Sep 97	1520 UTC	Sounder	Weak
Popocatepetl, Mexico	23 Jan 01	0420 UTC	Sounder	Moderate
Guagua Pichincha, Ecuador	5 Oct 99	2015-2215 UTC	Imager	Moderate
Lascar, Chile	20 Jul 00	1539-1739 UTC	Imager	Moderate
Soufriere Hills, Montserrat	26 Dec 97	1520 UTC	Sounder	Strong

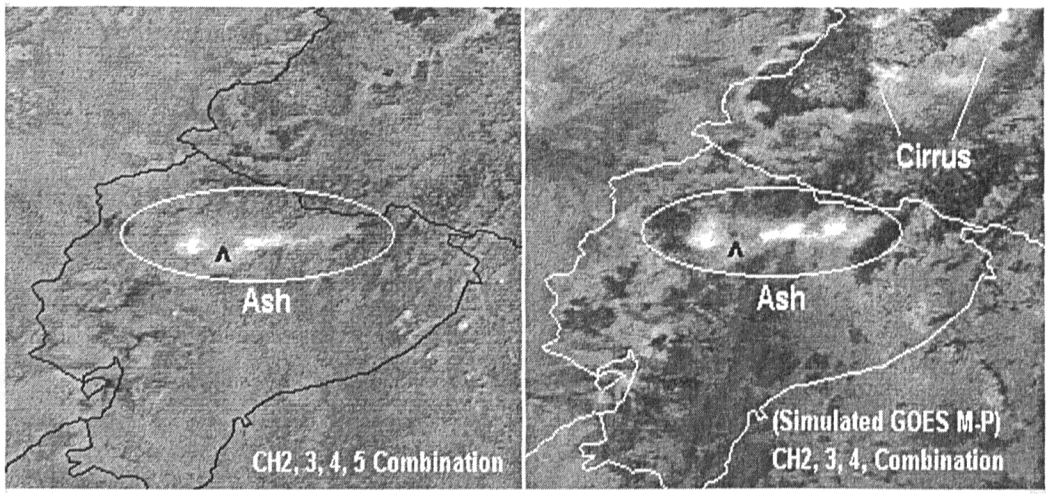

Figure 2. Comparison of ash cloud depiction from the GOES Imager on 5 October 1999 at 2215 UTC using all five IR bands, including 12 µm (left) versus only bands 2, 3, and 4 (right). The ash was produced by a moderate eruption of Guagua Pichincha volcano near Quito, Ecuador (shown by the ^) near 1945 UTC.

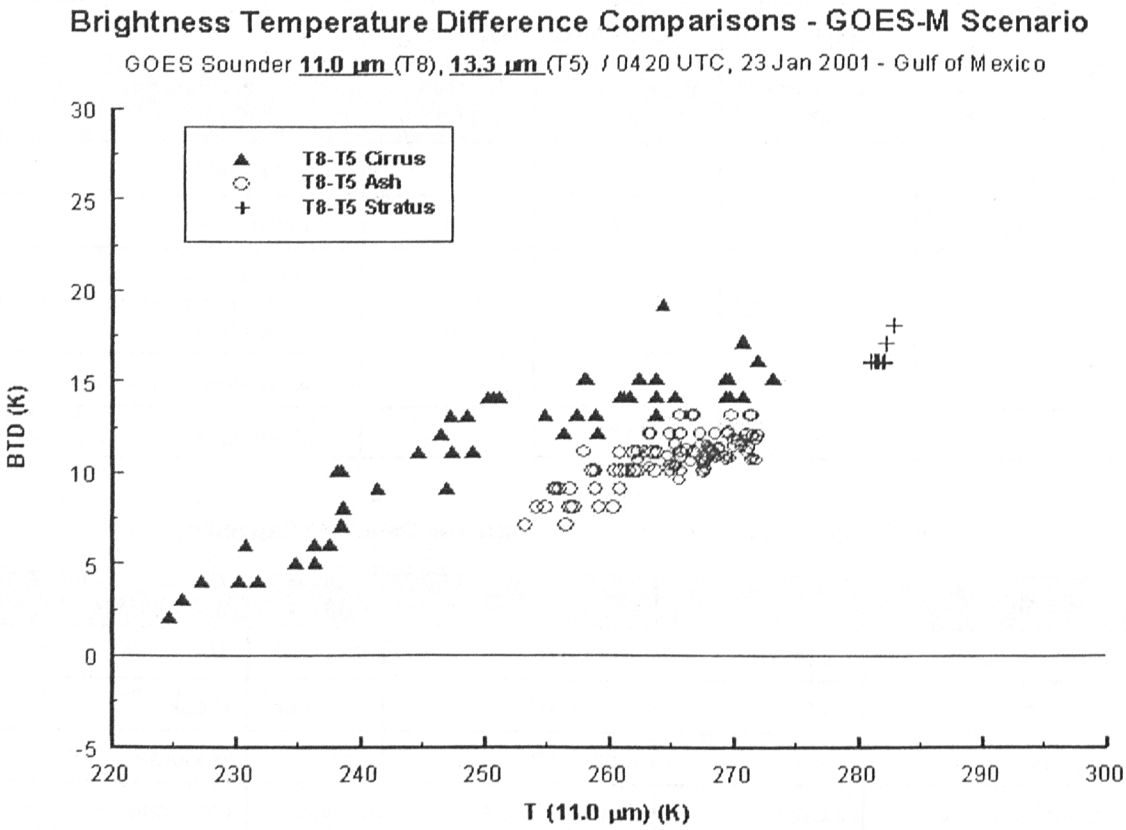

Figure 3. Scatter plot of GOES Sounder IR bands 8 - 5 BTD (equivalent to GOES-M Imager bands 4-6) versus Band 8 temperature (K) for volcanic ash (circles) and cirrus clouds (triangles) at 0420 UTC on 23 January 2001. Sounder bands 8 and 5 will be equivalent to GOES-M Imager bands 4 and 6, respectively.

P3.10

ASSIMILATION OF GOES SOUNDER CLOUD TOP PRESSURE IN NCEP'S 48KM ETA MESOSCALE MODEL

James A. Jung
Cooperative Institute for Meteorological Satellite Studies (CIMSS)
University of Wisconsin-Madison

Robert M. Aune
NOAA/NESDIS, Office of Research and Applications, Advanced Satellite Products Team (ASPT)

Timothy J. Schmit
NOAA/NESDIS, Office of Research and Applications, Advanced Satellite Products Team (ASPT)

Tom H. Zapotocny
Cooperative Institute for Meteorological Satellite Studies (CIMSS)
University of Wisconsin-Madison

Madison, WI

1. INTRODUCTION

As numerical models move to higher resolution and become more sophisticated a greater emphasis will be put on cloud prediction schemes. In the past modelers have used a wide spectrum of cloud prediction algorithms. Zivkovic and Louis (1992) and Arakawa and Schubert (1974) used diagnostic relationships of model dependent moisture variables. Lin et al. (1983) used bulk parameterizations of condensation and precipitation. Cotton et al. (1982) used comprehensive physical cloud algorithms that incorporated predictive equations for numerous particle shapes, size distributions and growth rates.

More mesoscale models are incorporating cloud prediction schemes that represent cloud water explicitly. Zhao and Carr (1997) developed the cloud prediction scheme for the Eta Model (Rogers et al. 1996), Brown et al. (1998) developed the cloud prediction scheme presently used in the Rapid Update Cycle (Benjamin et al. 1998). These cloud schemes are playing an ever increasing role in the models through their interactions with radiation, moisture transport and precipitation forecasts.

Corresponding author address: James A. Jung, NOAA Science Center, 5200 Auth Road, Camp Springs, MD, 20746;
email: Jim.Jung@noaa.gov.

Attempts have been made to initialize moisture and clouds in models using various types of satellite observations. Various degrees of success, using different methods, have been obtained by Wright and Hand (1994), Aune (2000), Kim and Benjamin (2000), and Bayler et al. (2000). In this paper we describe our initial attempt to modify or nudge the Eta cloud water mass field toward current satellite cloud observations. Our goal is to produce an improved cloud and moisture field for the analysis and subsequent forecast.

2. CLOUD OBSERVATIONS

The cloud top pressure product used is derived from the Geostationary Operational Environmental Satellites (GOES) infrared sounder (Menzel et al. 1998). The sounder covers about half of the operational Eta domain (using both GOES-east and GOES-west) with a pixel resolution of about 10km. The cloud top pressure is determined by the CO_2 absorption and a "split window" technique (Menzel et al. 1992). These data are produced hourly by NOAA/NESDIS and are available to NCEP.

3. MODEL BACKGROUND

For this experiment we used the November 1999 version of NCEP's operational Eta Data Assimilation/ Forecast

System (EDAS) (Black 1994; Rogers et al. 1996). Our experiment was conducted at 48km resolution with 45 vertical layers and is the same size as the operational Eta. The observations, including radiances, used during the 12-hour data assimilation cycle were obtained from NCEP and are equivalent to the operational Eta.

4. TECHNIQUE DESCRIPTION

The latitude/longitude of each cloud observation is mapped onto the corresponding Eta line/element. In the case of the 48km Eta, it is possible to have more than one observation at a grid point. Where more than one cloud observation is present the lowest pressure (highest cloud) observation is used. The cloud top pressure is then converted to the corresponding model layer. In an attempt to reduce some of the temporal variability, the relative humidity is checked one layer above and below the observation and is adjusted to that layer with the highest relative humidity.

Starting from the top of the model downward, cloud water mass is set to the minimum model threshold down to the cloud layer. If the cloud water mass is greater than the model's minimum threshold at the cloud layer, the cloud water mass is not changed. If the cloud water mass is equal to the model's minimum threshold, cloud water mass is added. The amount of cloud water mass added varies with respect to the model's threshold to initiate precipitation. Presently one-fourth of the precipitation threshold is added. Cloud water mass is not adjusted below this point. If no cloud is detected in the model grid box, cloud water mass is set to the minimum threshold down to the surface of the model.

The cloud water mass is adjusted after each cloud physics timestep (every 4th model timestep or 480 seconds) with the cloud top pressure data valid during that hour. The cloud nudging technique is done during the entire 12 hour data assimilation cycle with the T-0 analysis being used for the forecast and the next data assimilation cycle.

5. RESULTS

The impact of initializing the cloud water field is determined by comparing forecasts with the initialized clouds to a parallel control forecast which is as close as possible to the operational Eta model. The control forecast typically has an excess of high cirrus clouds. Most of the adjustment the cloud nudging does during the 12 hour EDAS is to remove cirrus. A comparison of a cloud-adjusted analysis with the control analysis is shown in Fig.1. Once the forecast cycle starts the Eta model begins to generate excess cirrus. There is generally good agreement out to about 6 hours at which time the cirrus becomes excessive as shown in Fig. 2.

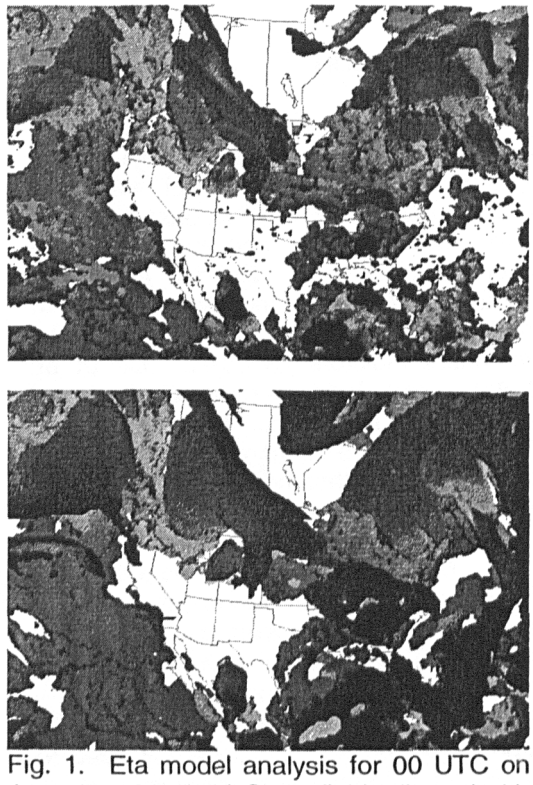

Fig. 1. Eta model analysis for 00 UTC on June 4, 2001. (top) Cloud field adjusted with GOES Sounder clouds. (bottom) Cloud field from control analysis.

The authors have looked at other statistics to determine impact of the cloud adjustment. We have presently completed winter and spring cases. The relative humidity shows a small improvement in the upper level wet bias associated with the

removal of the excess cirrus. The precipitation threat scores showed small mixed results. This result was expected since the cloud adjustment only has an impact out to about 6 hours where the threat scores are for a 24-hour time period. Results that were not expected are the lack of impact on the temperature. No differences were found in the temperature comparisons between the cloud adjusted and control forecasts. It has since been found that the radiation physics do not take into account changes in the grid scale cloud water mass.

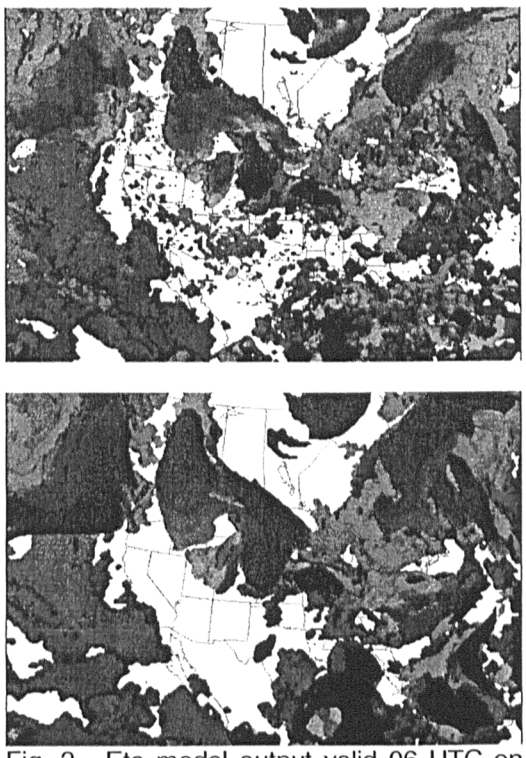

Fig. 2. Eta model output valid 06 UTC on June 4, 2001. (top) Analysis of the cloud field adjusted with GOES Sounder clouds. (bottom) Cloud field from 6 hour forecast using the 00 UTC cloud adjusted analysis.

Some problems were also found in the cloud product. At times there can be considerable temporal variability in the assigned cloud top pressure. To remove some of this, the layers above and below the assigned layer are checked for the highest relative humidity. If one of these layers has a higher relative humidity, the cloud top is reassigned to that layer.

6. REMARKS

The scheme described above will be tested during the summer and fall to get a more complete picture of the cloud assimilation effects. Efforts are presently underway at NCEP and NESDIS to address some of the deficiencies identified in the cloud product and the Eta's cloud physics.

7. REFERENCES

Arakawa A., and W.H. Schubert, 1974: Interaction of a cumulus cloud ensemble with the large-scale environment. Part I, *J. Atmos. Sci.* **31**, 674-701.

Aune, Robert M., 1996: Initializing cloud predictions using the GOES-8 sounder. 8th Conf. On Satellite Meteorology and Oceanography, Atlanta, GA, Amer. Meteor. Soc., 408-412.

Bayler, G.M., R.M. Aune, and W.H. Raymond, 2000: NWP cloud initialization Using GOES sounder data and improved modeling of nonprecipiataing clouds. *Mon. Wea. Rev.*, **128**, 3911-3920.

Benjamin, S.G., J.M. Brown, K.J. Brundage, B.E. Schwartz, T.G. Smirnova, T.L. Smith, L.L. Morone, and G.J. DiMego, 1998: The operational RUC-2. 16th Conference on Weather Analysis and Forecasting, Phoenix, AZ, Amer. Meteor. Soc., 249-252.

Black, T.L., 1994: The new NMC mesoscale Eta model: Description and forecast examples. *Wea. Forecasting*, **9**, 265-278.

Brown, J.M., T.G. Smirnova, and S.G. Benjamin, 1998: Introduction to MM5 level-4 microphysics into the RUC-2. Preprints, 12th Conf. On Numerical Weather Prediction, Phoenix, AZ, Amer. Meteor. Soc., 113-115.

Cotton W. R., M.A. Stephens, and G.J. Tripoli 1982: The Colorado State University three-dimensional cloud/mesoscale model – 1981. Part II: An ice phase parameterization. *J. Rech. Atmos.*, **16**, 295-320.

Kim, D., S.G. Benjamin, 2000: Assimilation of cloud-top pressure derived from GOES sounder. Preprints, 10th Conf. On Satellite Meteorology and Oceanography, Long Beach, CA. Amer. Meteor. Soc., 110-113.

Lin, Y-L., R.D. Farley, and H.D. Orville, 1983: Bulk Parameterization of the snow field in a cloud model. *J. Clim. Appl. Meteor.*, **22**, 1065-1092.

Menzel, W.P., F.C. Holt, T.J. Schmit, R.M.Aune, A.J. Schreiner, G.S. Wade, and D.G. Gray, 1998: Application of GOES-8/9 soundings to weather forecasting and nowcasting. *Bull. Amer. Meteor. Soc.*, **79**, 2059-2077.

Menzel, W.P. D.P. Wylie and K.I. Strabala, 1992: Seasonal and diurnal changes in cirrus clouds as seen in four years of observations with the VAS. *J. Appl. Meteor.*, **31**, 370-385.

Rogers, E., T.L. Black, D.G. Deaven, G.J. DiMego, Q. Zhao, M. Baldwin, N.W. Junker, and Y. Lin, 1996: Changes to the operational "early" Eta analysis/forecast system at the National Centers for Environmental Prediction. *Wea. Forecasting*, **11**, 391-413.

Wright, B.J., and W. Hand, 1994: An operational cloud analysis for the UK Met Office mesoscale model. Preprints, 10th Conf. On Numerical Weather Prediction, Portland, Amer. Meteor. Soc., 321-323.

Zhao, Q., and F.H. Carr 1997: A prognostic cloud scheme for operational NWP models. *Mon. Wea. Rev.*, **125**, 1931-1953.

Zivkovic, M. and J-F. Louis, 1992: A new method for developing cloud specification schemes in a general circulation model. *Mon. Wea. Rev.*, **120**, 2928-2941.

P3.29 CLOUD-DRIFT AND WATER VAPOR WINDS IN THE POLAR REGIONS FROM MODIS

Jeffrey R. Key[1*], David Santek[2], Christopher S. Velden[2], and W. Paul Menzel[1]
[1]Office of Research and Applications, National Environmental Satellite, Data, and Information Service, NOAA
1225 West Dayton Street, Madison, WI, 53706
[2]Cooperative Institute for Meteorological Satellite Studies, University of Wisconsin-Madison
1225 West Dayton Street, Madison, WI, 53706

1. INTRODUCTION

In the early 1960s Tetsuya Fujita developed analysis techniques to use cloud pictures from the first TIROS polar orbiting satellite for estimating the velocity of tropospheric winds (Menzel, 2001). Throughout the 1970s and early 1980s cloud motion winds were produced from satellite data using a combination of automated and manual techniques. In 1992, the National Oceanic and Atmospheric Administration (NOAA) began using an automated winds software package that made it possible to produce a full-disk wind set without manual intervention. The carbon dioxide (CO_2) slicing algorithm (Menzel et al., 1983) made it possible to assign accurate cloud heights to the motion vectors. Fully automated cloud-drift wind production from the Geostationary Operational Environmental Satellites (GOES) became operational in 1996, and now wind vectors are routinely used in operational numerical models of the National Centers for Environmental Prediction (NCEP).

Satellite-derived wind fields are most valuable for the oceanic regions where few observations exist and numerical weather prediction model forecasts are less accurate as a result. Like the oceans at lower latitudes, the polar regions also suffer from a lack of observational data. While there are land-based meteorological stations in the Arctic, and a small number of stations around the coast of Antarctica, there are no routine observations of winds over the Arctic Ocean and most of the Antarctic continent. Unfortunately, geostationary satellites are of little use at high latitudes due to the large view angles and poor spatial resolution, resulting in large uncertainties in the derived wind vectors.

Can polar-orbiting satellites be used to obtain wind information at high latitudes? Difficulties arise from the irregular temporal sampling and viewing geometry, but the idea has been explored before with promising results. The Advanced Very High Resolution Radiometer (AVHRR) was used by Herman (1993) to estimate cloud-drift winds for a few Arctic scenes. When compared to rawinsonde winds, the AVHRR winds were found to have a root-mean-square error of 6 m s^{-1}. Herman and Nagle (1994) compared cloud-drift winds from the AVHRR using two different methods of obtaining cloud height to gradient winds computed with the HIRS sounder. The AVHRR cloud-drift winds that incorporated the CO_2 slicing method (using HIRS channels) were found to be comparable to the HIRS gradient winds, with root-mean-square errors less than 5 m s^{-1}. Turner and Warren (1989) obtained useful cloud track wind information from AVHRR Global Area Coverage (GAC) data in the Weddell Sea, Antarctica.

In this paper we discuss a new effort to obtain estimates of high-latitude tropospheric winds using the MODerate Resolution Imaging Spectroradiometer (MODIS) on-board the National Aeronautics and Space Administration's (NASA) polar orbiting Terra satellite. Sampling issues are discussed, and results from a case study are presented.

2. TEMPORAL SAMPLING

Statistical analyses of visible, infrared, and water vapor wind data sets from geostationary satellites versus rawinsonde verification data have shown that the optimal processing intervals are 5 minutes for visible imagery of 1 km resolution, 10 minutes for infrared imagery of 4 km resolution, and 30 minutes for water vapor imagery of 8 km resolution. How often can we obtain wind vectors from a polar-orbiting satellite? Not surprisingly, the answer depends on the latitude and the number of satellites. Figure 1a shows the frequency of time differences between successive overpasses at a given latitude-longitude point on a single day with only one satellite. At 60° latitude there are two overpasses separated by about 10 hours. Obviously, no useful wind information can be obtained at this latitude with only a single satellite. At 80° there are many views separated by 100 minutes (the orbital period), but there is still a 13 hour gap each day. Even with large gaps at a single location, however, wind vectors can be obtained during part of every day for the entire Arctic and Antarctic regions.

Figure 1b shows the coverage with multiple satellites: the current NOAA-15, NOAA-16, Terra, and Chinese FY-1C satellites and NASA's future Aqua platform. Orbital characteristics based on current plans for Aqua were used in the simulation. Temporal gaps of a few hours still exist at the lower latitudes of the polar regions but at the higher latitudes the temporal coverage is very good. Given that geostationary satellites provide wind information equatorward of about 60 degrees latitude, global coverage can be obtained by using polar-orbiting satel-

* *Corresponding author address:* Jeff Key, NOAA/NESDIS, 1225 West Dayton Street, Madison, WI 53706; e-mail: jkey@ssec.wisc.edu.

lites for the high-latitudes, though two or more will be required to satisfy temporal sampling requirements.

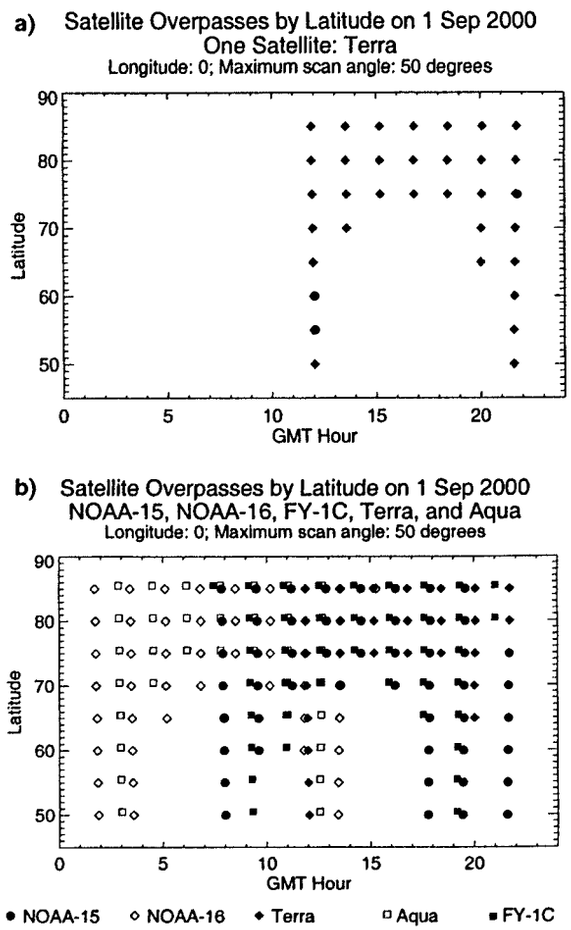

Fig. 1. (a) Time differences between successive overpasses of a single satellite (Terra) as a function of latitude over the course of a day at the Prime Meridian. Only overpasses with view angles less than 50 degrees are considered. (b) Time differences between successive overpasses of five satellites.

3. METHODS

Cloud and water vapor tracking with MODIS data is based on the established procedure used for GOES, which is essentially that described in Merrill (1989), Nieman et al. (1997), and Velden et al. (1997). With MODIS, cloud features are tracked in the infrared window band at 11 μm; water vapor features are tracked in the 6.7 μm band.

After remapping the orbital data to a polar stereographic projection, potential tracking features are identified. The lowest brightness temperature in the infrared window band (generally indicating cloud) within a target box is isolated and local gradients are computed. The size of the target area controls the density of derived vectors. Gradients that exceed a specified threshold are classified as targets for tracking. For water vapor target selection, local gradients are computed for the area surrounding every pixel rather than the single pixel with the minimum brightness temperature in a box. Water vapor targets are selected in both cloudy and cloud-free regions.

The tracking method employs a simple search for the minimum of the sum of squared radiance differences between the target and the search boxes in two subsequent images. A model forecast of the upper level wind is used to choose the appropriate search areas. Displacement vectors are derived for each of the two subsequent images. They are then subject to consistency checks to eliminate accelerations that exceed empirically determined tolerances. A final step in the tracking process is an adjustment to the vector speed for a well-documented slow bias in the upper-tropospheric cloud-tracked winds.

Height assignments can made with any of three methods. The infrared window method assumes that the mean of the coldest values in a sample is the temperature at the cloud top. The temperature is compared to a numerical forecast of the vertical temperature profile to determine the cloud height. This method is reasonably accurate for opaque clouds, but inaccurate for semi-transparent clouds.

The CO_2 slicing method works well for both opaque and semitransparent clouds. Cloudy and clear radiance differences in the CO_2 (13.3 μm) and infrared window bands are ratioed and compared to the theoretical ratio of the same quantities, calculated for a range of cloud pressures. The cloud pressure that gives the best match between the observed and theoretical ratios is chosen (Menzel et al., 1983; Frey et al., 1999).

The H_2O-intercept method of height determination can be used as an additional metric or, in the case of some other polar-orbiting imagers, in the absence of a CO_2 band. This method examines the linear trend between clusters of clear and cloudy pixel values in water vapor-infrared window brightness temperature space, predicated on the fact that radiances from a single cloud deck for two spectral bands vary linearly with cloud amount. The line connecting the clusters is compared to theoretical calculations of the radiances for different cloud pressures. The intersection of the two gives the cloud height (Schmetz et al., 1993).

We are investigating cloud height assignment where the results of the MODIS cloud product algorithm (Menzel and Strabala, 1997) are incorporated into the processing stream. Cloud top pressure is derived from a multi-channel CO_2 slicing technique and the cloud mask.

After wind vectors are determined and heights are assigned, the resulting data set is subject to a postprocessing, quality-control step. The purposes of this step are to determine the tropospheric level that best represents the motion vector being traced, to edit out vectors

that are in obvious error, and to provide end users with vector quality information (Velden et al., 1998).

4. APPLICATION

Figure 2 illustrates the application of the method to MODIS data. The figure shows wind vectors derived from both cloud and water vapor tracking in three consecutive overpasses on 6 September 2000 over the western Arctic Ocean. Portions of the underlying infrared image are devoid of wind vectors because those areas were not observed in subsequent overpasses. The three overpasses were separated by approximately 100 minutes for a total time span of 3.3 hours.

Vector heights, which represent the height of the cloud or water vapor feature that was tracked, are given in three broad categories: low (white), middle (grey), and high (black). Lower tropospheric wind estimates occur within the cyclonic system north of Siberia and also just east of 120 E longitude; mid-level, high velocity winds were measured in and around the frontal structure extending from the lower center portion of the image through the New Siberian Islands and also northeast of Wrangel Island in the bottom left portion of the image. Vectors for upper-level winds, primarily from the water vapor band, occur throughout the field.

5. CONCLUSIONS

This study has demonstrated the feasibility of deriving tropospheric wind information at high latitudes from polar-orbiting satellites. The methodology employed is based on the algorithms currently used with geostationary satellites, modified for use with the polar-orbiting MODIS instrument.

The project presents some unique challenges, including the irregularity of temporal sampling, different viewing geometries from one image to the next, large uncertainties in the model forecast profiles used in height assignment and quality control, and the complexity of surface features, including their motion. These and other issues will be investigated in the future, as part of an extensive processing and validation campaign. Model impact studies are also planned.

Acknowledgments. This work was supported by NOAA contract NA07EC0676.

6. REFERENCES

Frey, R., B. A. Baum, W. P. Menzel, S.A. Ackerman, C.C. Moeller, and J. D. Spinhirne, 1999: A comparison of cloud top heights computed from airborne LIDAR and MAS radiance data using CO2-slicing. *J. Geophys. Res.*, 104(D20), 24,547-24,555.

Herman, L.D., 1993: High frequency satellite cloud motion at high latitudes. *Proceedings of the 8th Symposium on Meteorological Observations and Instrumentation*, Amer. Meteorol. Soc., Anaheim, CA, 17-22 January, 465-468.

Herman, L.D. And F.W. Nagle, 1994: A comparison of POES satellite derived winds techniques in the Arctic at CIMSS. *Proceedings of the 7th Conference on Satellite Meteorology and Oceanography*, Amer. Meteorol. Soc., Monterey, CA, June 6-10, 444-447.

Menzel, W.P., 2001: Cloud tracking with satellite imagery: From the pioneering work of Ted Fujita to the present. *Bull. Amer. Meteorol. Soc.*, 82(1), 33-47.

Menzel, W.P. and K. Strabala, 1997: Cloud top properties and cloud phase algorithm theoretical basis document. Unpublished report, Cooperative Institute for Meteorological Satellite Studies, University of Wisconsin, 1225 W. Dayton Street, Madison, WI, 53706, 55 pp.

Menzel, W.P., W.L. Smith, and T.R. Stewart, 1983: Improved cloud motion vector and altitude assignment using VAS. *J. Climate Appl. Meteorol.*, 22, 377-384.

Merrill, R., 1989: Advances in the automated production of wind estimates from geostationary satellite imageing. *Proc. Fourth Conf. Satellite Meteorol.*, San Diego, CA, Amer. Meteorol. Soc., 246-249.

Nieman, S.J., W.P. Menzel, C.M. Hayden, D. Gray, S.T. Wanzong, C.S. Velden, and J. Daniels, 1997: Fully automated cloud-drift winds in NESDIS operations. *Bull. Amer. Meteorol. Soc.*, 78(6), 1121-1133.

Schmetz, J., K. Holmlund, J. Hoffman, B. Strauss, B. Mason, V. Gaertner, A. Koch, and L. van de Berg, 1993: Operational cloud motion winds from METEOSAT infrared images. *J. Appl. Meteorol.*, 32, 1206-1225.

Turner, J. and D.E. Warren, 1989: Cloud track winds in the polar regions from sequences of AVHRR images. *Int. J. Remote Sensing*, 10(4), 695-703.

Velden, C.S., C.M. Hayden, S.J. Nieman, W.P. Menzel, S. Wanzong, and J.S. Goerss, 1997: Upper-tropospheric winds derived from geostationary satellite water vapor observations. *Bull. Amer. Meteorol. Soc.*, 78(2), 173-196.

Velden, C.S., T.L. Olander and S. Wanzong, 1998: The impact of multispectral GOES-8 wind information on Atlantic tropical cyclone track forecasts in 1995. Part 1: Dataset methodology, description and case analysis. *Mon. Wea. Rev.*, 126, 1202-1218.

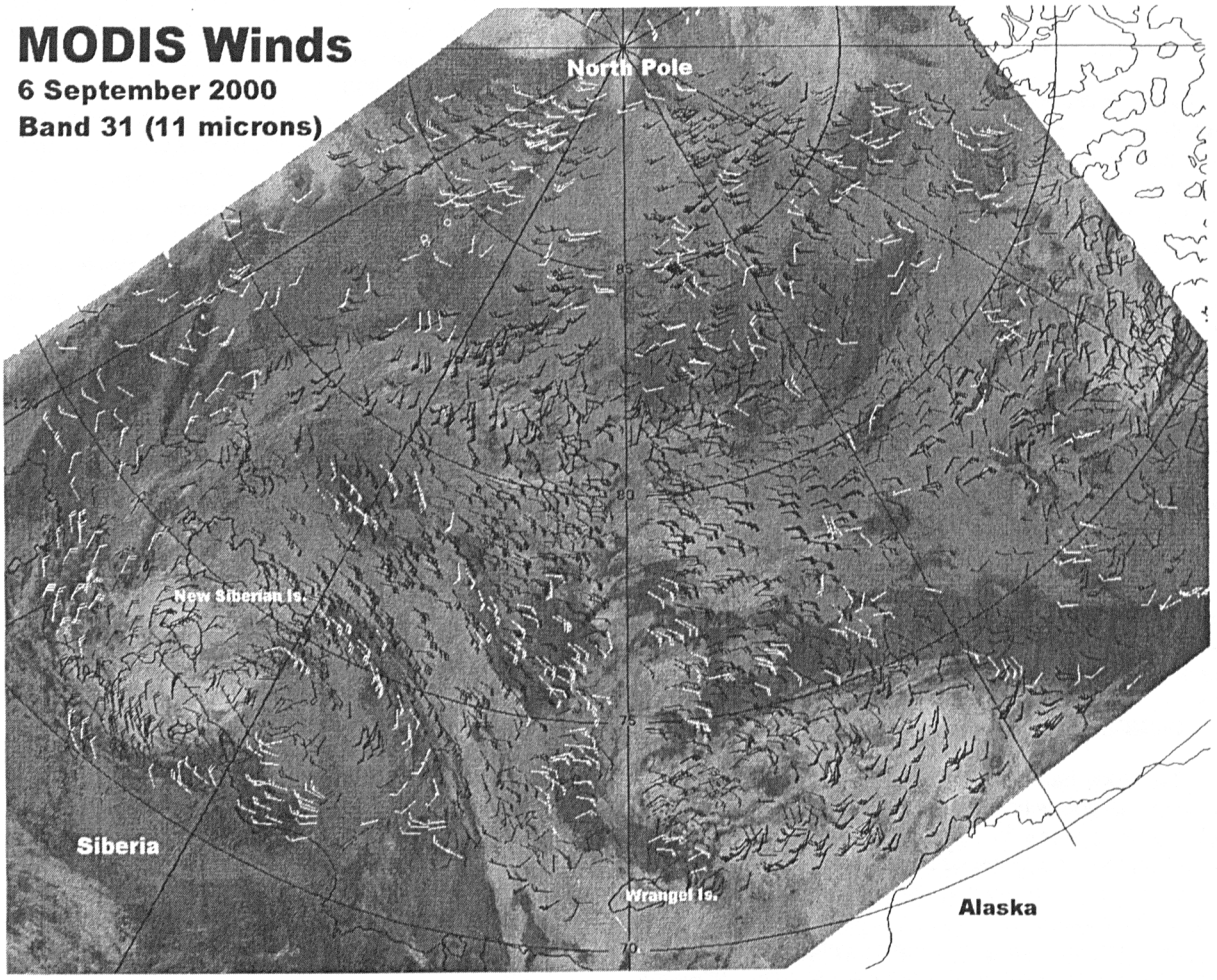

Fig. 2. Wind vectors determined with the automated cloud and water vapor tracking algorithm for 6 September 2000. Vectors are plotted on a MODIS 11 μm image, the first in the sequence of three overpasses spanning a time period of approximately 4.5 hours. Vector heights are given in three broad categories: low (white), middle (grey), and high (black).

P3.37

A Validation Study of the GOES Sounder Cloud Top Pressure Product

James A Hawkinson*, Wayne Feltz, Timothy J. Schmit#, Anthony J. Schreiner, Steven A. Ackerman

Cooperative Institute for Meteorological Satellite Studies (CIMSS)
Space Science and Engineering Center UW-Madison
Madison, Wisconsin

NOAA/NESDIS/ORA Advanced Satellite Products Team

1. INTRODUCTION

One of the derived operational products from the Geostationary Operational Environmental Satellite (GOES-8) Sounder is the Cloud Top Pressure measurement. This product is available for the GOES-8 domain in real-time at hourly time resolution. The sounder outputs the average cloud top pressure reading from a 3X3 (nine pixels approximately 35x45 km) Field of View (FOV), and the single FOV, as well as the maximum and minimum values from the 3X3 FOV. The data used for validation purposes comes from the March 2000 Intensive Operational Period (IOP) from the Department of Energy's (DOE) Atmospheric Radiation Measurement (ARM) program Cloud and Radiation Testbed (CART) site near Lamont, OK. This includes cloud top height derived from a ground-based combination Micropulse Lidar/Millimeter Cloud Radar (MPL/MMCR), which uses an algorithm developed by Eugene Clothaiux (Clothiaux et al. 2000). MPL/MMCR output is every ten seconds during the IOP. GOES cloud top data range from 7 March 2000 to 31 March 2000, giving 600 possible observation times. Data were filtered to give only observation times that contain one cloud layer to provide an accurate comparison between the ground-based and space-based observation locations.

2. Method

In order to prepare the two data sets for an objective comparison, the GOES cloud top pressure observations were converted into altitude in meters. This was achieved by using radiosonde data from the CART site. A pressure-height profile was constructed from the closest radiosonde to the time of observation. Radiosondes were launched every six hours during the IOP from the CART site. Once this conversion was done, the two data sets could be compared using a time series plot (Fig. 1).

* Corresponding author address: James Hawkinson, 1225 West Dayton Street Room 238, Madison, WI, 53706; e-mail: jahawkin@students.wisc.edu.

Since the MPL/MMCR is subject to attenuation effects and local cloud top height deviations at the single observation point over the CART site, the data needed to be desensitized. This was achieved by using a range binning process which entailed placing every MPL/MMCR observation surrounding the GOES sounder observation time (five minutes before and after the GOES observation time was used) into a range bins of 250m. Each range bin must have a given amount of observations in it to be considered valid (a threshold of observation). Those range bins that do not meet the threshold value are discarded, while the temporal average cloud top height is used from the valid range bins. Noticeable improvement in the results was seen after this range binning tool place. This is demonstrated in scatter plots within figures 2 and 3. Notice the considerable improvement in agreement when the binning methodology is used.

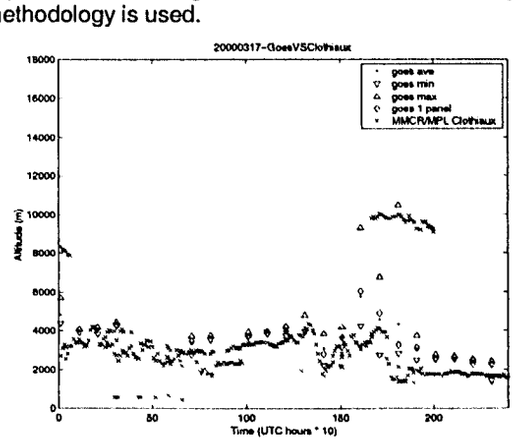

Figure 1: An example of GOES and MPL/MMCR cloud top height time series. This is for 17 Mar 2000.

To further filter the data for a direct comparison, measures were taken to eliminate observation times where multiple cloud layers were present. Although the GOES sounder product cannot explicitly detect multiple cloud layers, use of the 3X3 FOV maximum and minimum cloud top height values can give a reasonable estimate of the existence of multiple cloud layers. The

determination of multiple cloud layers was done by specifying a maximum variance in the 3X3 FOV maximum and minimum cloud top height. Any observation time that had a variance greater than 2000 meters would be deemed to be a multiple cloud layer situation. Through the use of two different methods of filtering, the ground-based data was desensitized and multiple cloud layers were eliminated, allowing for an objective comparison between the two independent observations.

3. Results

The first direct comparison made between the GOES and MPL/MMPL was detection of clouds. This is a yes/no comparison, either the instrument is reporting a cloud top height or it is not. For this comparison, the temporal threshold for the MPL/MMCR data set was set to a very low value 16% of observations needed for a valid cloud. The value was set so low in order to minimize attenuation effects of the instruments. The GOES sounder and MPL/MMCR agree on the existence or lack there of a cloud 75% of the time (345/460). It should be noted that for 140 of 600 possible observation times, the sounder was in eclipse mode.

To further compare the two measurements, scatter plots with both GOES sounder and MPL/MMCR cloud top height values were produced. To demonstrate the importance of data filtering, the progression of filtering techniques is shown with their respective scatter plots.

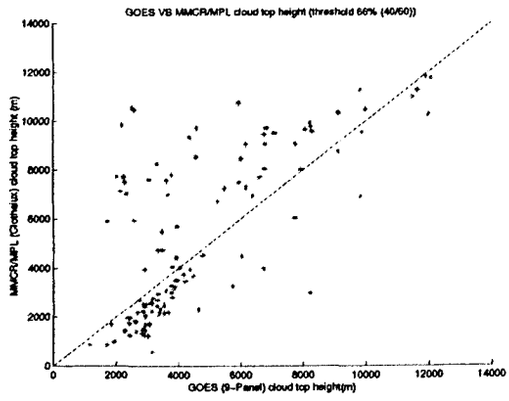

Figure 2: A scatter plot comparing GOES and MPL/MMCR cloud top height with no data filtering. Little correlation is seen.

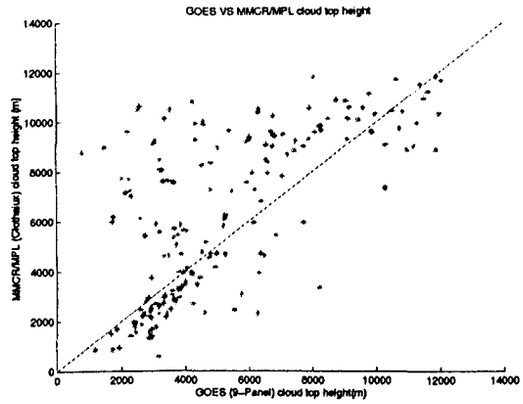

Figure 3: Scatter plot using binning process for MPL/MMCR.

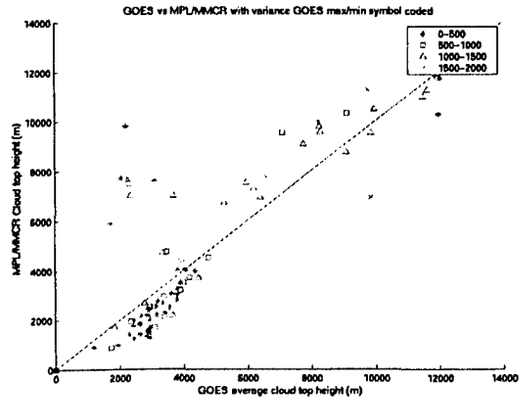

Figure 4: Scatter plot using binning process for MPL/MMCR and filtering out multiple cloud layers. Amount of variance between sounder 3X3 FOV maximum and minimum cloud top height is symbol coded.

At this point after using the two different filtering techniques, significant correlation was seen in the scatter plot. But there still were eight outliers (seen in a cluster in Figure 4 in the upper-left corner) where the GOES sounder were placing the cloud top height around 2000 meters, and the MPL/MMCR cloud top height around 6000 meters-10000 meters. This group of outliers can be seen in Figure 4. Such large variance between the two sources is alarming, so each individual outlier was examined to determine why the discrepancy exists. Six of the eight outliers could be explained by examining the data close up. This was done by going back to the time series plots as seen in Figure 1.

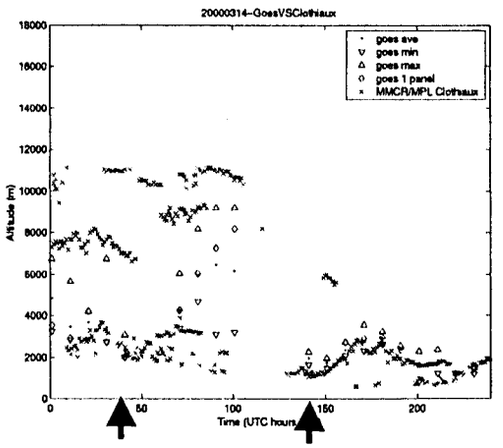

Figure 5: Two instances of outliers that can be explained by examining the time series. Attenuation effects and multiple cloud layers led to the outliers.

After six of the eight outliers were accounted for, they were discarded from the scatter plot. Eliminating these outliers led to an increase in correlation as seen in Figure 6. Of the two remaining outliers that could not be accounted for by manual inspection, both were found to be high cirrus cloud tops.

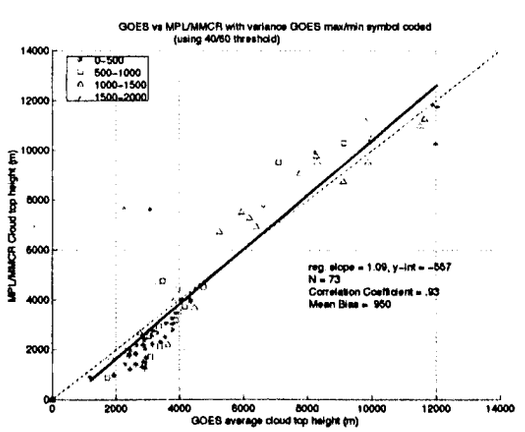

Figure 6: A correlation coefficient of .93 and a mean bias of 950m is seen after application of filtering techniques and removal of outliers.

4. Conclusions

In order to ensure a direct comparison between GOES sounder cloud top height and ground-based MPL/MMCR cloud top height, measures were taken filter out instances of multiple cloud layers. Once this was achieved, high correlation was seen between the two sets of observations. With a mean bias of 950m between the two data sets, the GOES sounder cloud top pressure product can be seen as an accurate instrument. Both of the instances where the GOES sounder had significant error (> 2500m), cirrus clouds were present. The error in the GOES sounder measurement can be attributed to the low optical depth and emmitance of the clouds. This exposes the limits of the current GOES sounder instrument, and demonstrates the need for development of a higher resolution sounder instrumentation.

2. ACKNOWLEDGEMENTS

This research was supported by the Department of Energy Atmospheric Radiation Measurement Program Grant DE-FG-02-92ER61365 and NOAA Grant NA67EC0100.

6. REFERENCES

Clothiaux, E. E., T. P. Ackerman, G. G. Mace, K. P. Moran, R. T. Marchand, M. A. Miller, B. E. Martner, 2000: Objective Determination of Cloud Heights and Radar Reflectivities Using a Combination of Active Remote Sensors at the ARM CART Sites. J. Appl. Meteor: 39, No. 5, pp. 645-665.

McClesse, D. J. and L. S. Wilson, 1976: Cloud top heights from temperature sounding instruments. Quart. J. Royal Meteor. Soc., 102, 781-790.

Ma, Xia L., T. J. Schmit, W. L. Smith, 1999: A nonlinear physical retrieval algorithm'its application to the GOES-8/9 sounder. J. Appl. Meteor. 38, No. 5, 501-513.

Menzel, W. P., F. C. Holt, T. J. Schmit, R. M. Aune, G. S. Wade, D. G. Gray, A. J. Schreiner, 1998: Application of GOES- 8/9 Soundings to weather forecasting and nowcasting. Bull. Amer. Meteor. Soc. 79, 2059R 2078.

Schreiner, A. J., T. J. Schmit, and W. P. Menzel, 2001: Observations and Trends of Clouds Based on GOES Sounder Data. J. Geophys. Res. Accepted for publication 2001.

P3.38 IS THE RESOLUTION OF GOES SOUNDER DATA SUFFICIENT TO SUPPORT SINGLE FIELD OF VIEW RETRIEVALS AND DERIVED PRODUCTS?

Gail M. Bayler*, Suzanne Wetzel Seemann, Jun Li and Timothy J. Schmit**
Cooperative Institute for Meteorological Satellite Studies, University of Wisconsin-Madison
**NOAA/NESDIS/ORA/ARAD/ASPT
Madison, Wisconsin

1. INTRODUCTION

Atmospheric profiles of temperature and moisture, and subsequent derived product imagery of precipitable water, lifted index and skin temperature, are calculated from Geostationary Operational Environmental Satellite (GOES) sounder radiances (Ma et al., 1999) in clear-sky Fields of View (FOV). In cloudy areas, cloud-top parameters are generated from sounder radiances. The sounder instrument FOV varies from approximately a 10 km by 10 km square at nadir to about a 11 km (east-west) by 16 km (north-south) rectangle in the mid-latitudes. Operationally, the data are spatially averaged over a field of regard (FOR) of 5x5 pixels. Hence temperature and moisture retrievals (at 40 pressure levels) have a spatial resolution of, at best, about 50 km. The signal-to-noise ratio of the GOES-9 sounder (launched in May 1995) improved from that of GOES-8 (launched in April 1993) (Menzel et al., 1998) and the trend has continued through GOES-11 (launched in May 2000), Daniels and Schmit, 2001.

At the Cooperative Institute for Meteorological Satellite Studies (CIMSS), retrievals and derived product images (DPI) are produced routinely with a 3x3 FOR. Sounder DPI consist of 3-layer precipitable water (PW1, PW2, PW3), total precipitable water (TPW), lifted index (LI), and skin temperature (SKN T). TPW (surface to 300 hPa) is the product considered in this paper since it is an integrated value.

The improved spatial resolution of approximately 30 km from 50 km allows more precise depiction of cloudy/clear regions, profiles of temperature and dew point temperature, and DPI. Since FOV averaging is done to reduce instrument noise and the signal-to-noise ratios have improved, the question then arises whether single FOV (SFOV), i.e. each individual pixel (1x1) retrievals and DPI depict true meteorological signal or whether the instrument noise remains too large. Ferraro and Daniels, 2001, found the similarity between GOES-8 and –10 and AMSU TPW retrievals to decrease for SFOV. Comparisons of 5x5, 3x3 and 1x1 TPW are presented. MODIS (MODerate resolution Imaging Spectroradiometer) data (Ackerman et al. 1998) are used as a source of validation.

* *Corresponding author address:* Gail M. Bayler, Cooperative Institute for Meteorological Satellite Studies, University of Wisconsin-Madison, 1225 W. Dayton St., Madison, WI 53706; e-mail: gail.bayler@ssec.wisc.edu.

2. GOES SOUNDER RETRIEVAL AND DERIVED PRODUCT IMAGERY ALGORITHM

Retrievals and DPI may be produced only in clear skies; therefore, the first step in the retrieval process determines the location of cloud (Schreiner et al. 2001), sometimes referred to as the cloud mask. For each FOV, a flag is set that indicates clear, cloudy, or unknown conditions.

To produce 5x5 or 3x3 FOR retrievals and DPI, there must be a minimum number of clear FOVs. For example, a 3x3 FOR is flagged cloudy if 5 or more FOV are cloudy and a 5x5 FOR is flagged cloudy for 9 or more cloudy FOV. Retrievals that otherwise might have been made in the clear SFOV are not made (a drawback of spatial averaging). Next, the algorithm attempts to achieve convergence for the retrieval within three iterations. If convergence is not reached, the retrieval is abandoned and the next 3x3 FOR is

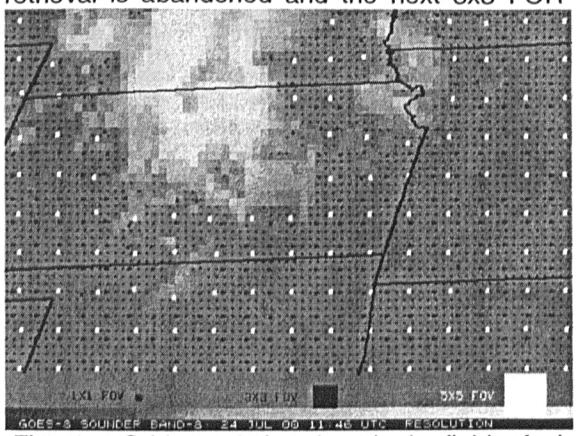

Fig. 1. Grid resolution for single field of view (SFOV), 3x3 field of regard (FOR) and 5x5 FOR. Image shown is 12:00 UTC on 24 Jul 2000 centered on Kansas. The three boxes at the bottom show spatial coverage for 1x1, 3x3 and 5x5 FOR, respectively.

examined. DPI are calculated from the temperature/moisture retrievals. Everywhere that 3x3 FOR retrievals are made, DPI are calculated for the clear-flagged SFOV within the 3x3 FOR. If a 3x3 retrieval is not made, SFOV DPI are not attempted since it was not possible to update the model guess.

SFOV retrievals and DPI do not use a 3x3 FOR guess and so both are made at each clear-flagged FOV.

3. COMPARISON OF SPATIAL AVERAGING

A case study is presented for 24 July 2000 with data from both GOES-8 and GOES-11. Figure 1 illustrates the retrieval locations of the three spatial resolutions considered. GOES-8 TPW calculated as SFOVs exhibit some striping compared to 3x3 FOR and 5x5 FOR. In Fig. 2a, this striping, variation in TPW values in rows of pixels, is exhibited in central Oklahoma parallel to the axis of instability in the 20-30 mm range. Most likely, this is an artifact of the instrument since atmospheric TPW variations are typically more continuous and because averaging into 3x3 or 5x5 FOR generally removes striping, Fig. 2b. Detail is lost with 3x3 processing, however, as Fig. 2b depicts a less continuous axis of instability.

a)

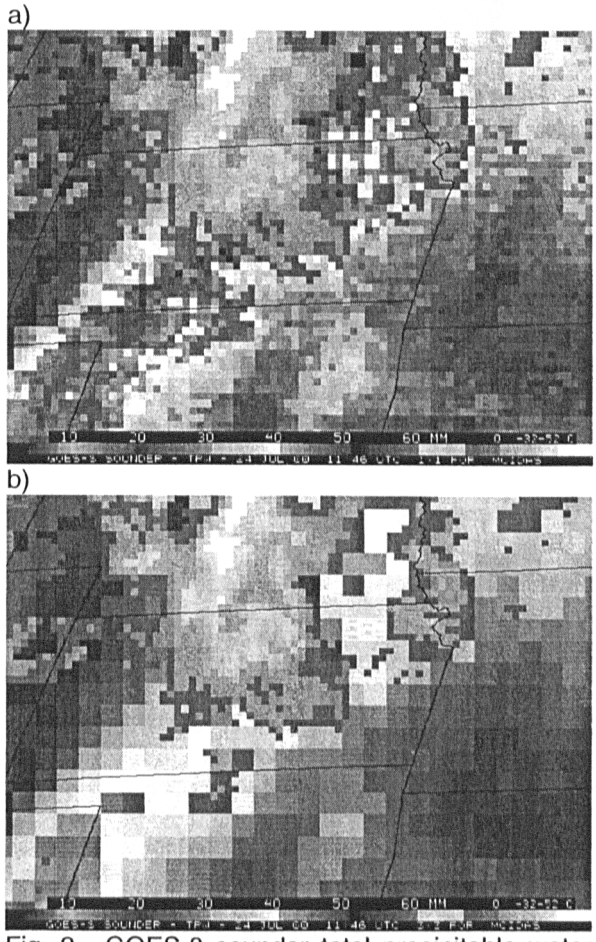

Fig. 2. GOES-8 sounder total precipitable water (mm) at 11:46 UTC on 24 Jul 2000. Cloud edges are black. a) single field of view (1x1) with evidence of striping over central Oklahoma. b) 3x3 field of regard. where spatial averaging minimizes striping.

a)

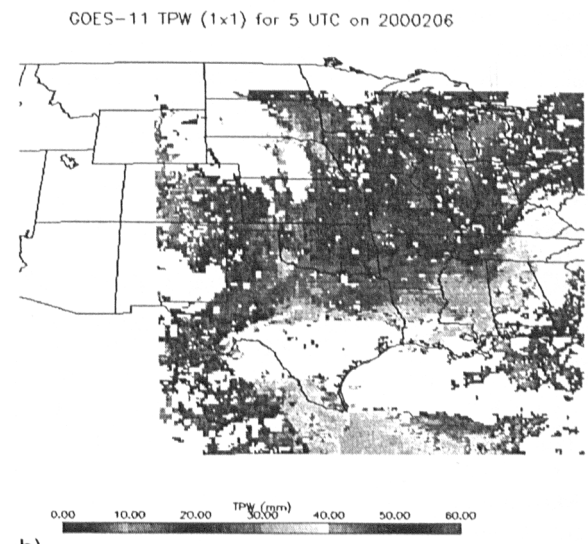

b)

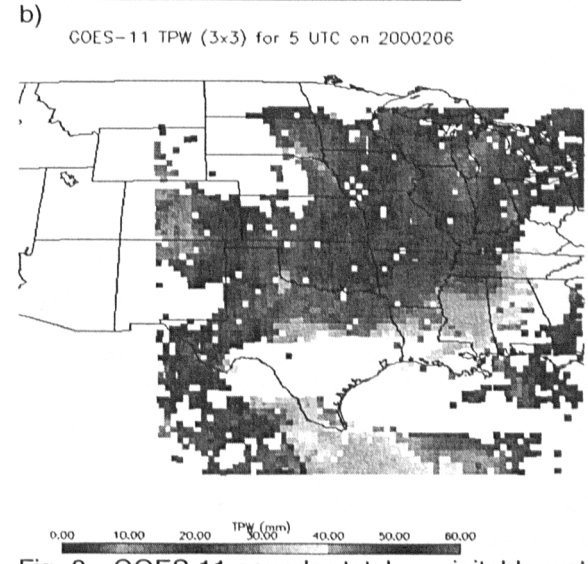

Fig. 3. GOES-11 sounder total precipitable water (mm) at 05:00 UTC on 24 Jul 2000 for a) single field of view (1x1) and b) 3x3 field of regard.

Figures 3a and 3b depict GOES-11 1x1 and 3x3 FOR respectively, at 05:00 UTC for the same day. The GOES-11 data came from the 6-week NOAA science test during the satellite check-out phase. Striping is not manifested in Fig. 3a. Thus instrument improvements may mean SFOV DPI are feasible.

GOES-8 TPW is verified against radiosonde data at 12:00 UTC for 24 Jul 2000 (Table 1). For each spatial resolution, retrievals within 55 km (half a degree) of the radiosonde were verified. Differing resolution retrievals within 5 km of each other were then extracted for final statistics. This colocation was done so comparisons were between spatially close retrievals and the compared retrievals were verified with the same radiosonde data. Although the sample size is small, the statistics indicate that both 3x3 and 5x5 spatial averaging for GOES-8 produce retrievals that more closely agree with radiosonde TPW.

Table 1. Radiosonde verification of GOES-8 sounder total precipitable water at 12:00 UTC on 24 Jul 2000.

RAOB vs. Retrieval	1x1 vs. 3x3	1x1 vs. 5x5
Bias*	2.75/2.04	2.92/2.30
standard deviation	3.22/2.26	2.60/2.27
RMSE**	4.24/3.04	3.91/3.23
Number of matches	23	13
Max. match distance between retrievals	5 km	5 km
Avg. match distance between RAOB and retrievals	34/34 km	39/38 km

*Bias=RAOB-retrieval

**RMSE=SQRT((bias)^2+(standard deviation)^2)

High spatial resolution MODIS TPW data, an independent source of verification, is shown in Fig. 4. MODIS data are collected in 5 minute granules; therefore, this is a two granule image, from 04:50 and 04:55 UTC. The southern Gulf States exhibit TPW values (mm) in the high 20s, with the tip of Texas and southward in the 30s. The large, dark area in the northwest corner represents TPW values of 15 mm. The MODIS and GOES-11 TPW data qualitatively agree.

4. SUMMARY

Improvements in sounder technology over the succession of the GOES-8-11 have yielded improved signal-to-noise ratios. To minimize striping, spatial averaging (3x3 or 5x5 FOR) was a necessity for GOES-8. The striping is not seen with a case comparing GOES-11 sounder total precipitable water data. Additionally, values compare well with higher resolution MODIS data. Thus for this case, single field of view TPW DPI are feasible with GOES-11 sounder data. New case studies will be examined and further radiosonde comparisons will be made.

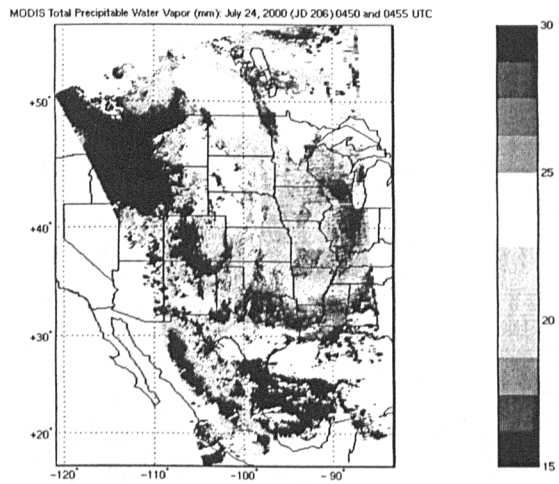

Fig. 4. MODIS total precipitable water (mm) at 4:50 and 4:55 UTC on 24 Jul 2000.

5. REFERENCES

Ackerman, S. A., K. I. Strabala, W. P. Menzel, R. A. Frey, C. C. Moeller, and L. E. Gumley, 1998: Discriminating clear sky from clouds with MODIS. J. Geophys. Res., **103**, 32141-32157.

Daniels, J. M. and T. J. Schmit, 2001: GOES-11 Imager and Sounder Radiance and Product Validations. NOAA Tech. Memo., in press.

Ferraro, R. and J. Daniels, 2001: A comparison of GOES and AMSU based total precipitable water retrievals. Preprints, *Fifth Symposium on Integrated Observing Systems*, Albuquerque, NM, Amer. Meteor. Soc., 130-131.

Ma, X. L., T. J. Schmit, and W. L. Smith, 1999: A nonlinear physical retrieval algorithm-Its application to the GOES-8/9 sounder. J. Appl. Meteor., **38**, 501-513.

Menzel, W. P., F.C. Holt, T.J. Schmit, R.M. Aune, A.J. Schreiner, G. S. Wade, and D. G. Gray, 1998: Application of *GOES8/9* soundings to weather forecasting and nowcasting. *Bull. Amer. Meteor. Soc.,* **79**, 2059-2077.

Menzel, W. P., and J. F. W. Purdom, 1994. Introducing GOES-I: The first of a new generation of geostationary operational environmental satellites, *Bull. Amer. Meteor. Soc.*, **75**, 757-781.

Schreiner, A. J., T. J. Schmit, and W. P. Menzel, 2001: Trends and observations of clouds based on GOES sounder data. *J. Geophysical Rev.*, in press.

P3.40 AN EVALUATION OF SEVERAL YEARS OF CIMSS AND NESDIS GOES SOUNDER DATA

James P. Nelson III *,[1], Timothy J. Schmit,[2] and W. Paul Menzel [2]

[1] Cooperative Institute for Meteorological Satellite Studies (CIMSS)
University of Wisconsin-Madison, Madison, WI

[2] NOAA/NESDIS/ORA
Advanced Satellites Products Team (ASPT)
Madison, WI

1. INTRODUCTION

At The Cooperative Institute for Meteorological Satellite Studies (CIMSS), vertical temperature and moisture profiles retrieved from GOES Sounder radiances (retrievals) have been produced and compared to radiosondes since 1995. In addition, National Environmental Satellite, Data, and Information Service (NESDIS) operational retrievals have also been compared with radiosondes. Comparision of these two rich datasets allows for extensive evaluation of past performance, and could lead to ideas for future retrieval improvements.

The main focus of this paper is to compare these two sets of retrievals with collocated, verifying radiosonde data. Due to space limitations, only Total Precipitable Water (TPW) will be examined; however, several temperature and moisture parameters will be examined at the conference. The data will be analyzed by month and season, by time (00UTC vs. 12UTC), by region (north vs. south, etc.), and by sensor (GOES-E vs. GOES-W). Moreover, an evaluation of one of the more important components of the retrieval process, the bias adjustment of the measured GOES radiances, will also be undertaken. The differences between the adjustments used in the CIMSS and NESDIS retrievals will be outlined and compared explicitly for Sounder band 5 (13.4μm) here, but will be expanded to include numerous Sounder bands at the conference.

2. GOES RETRIEVALS OF TEMPERATURE AND MOISTURE

Radiance data from the Sounder instruments aboard the GOES-I/M series of spacecraft have been available since mid-1994 (Menzel and Purdom 1994). This information can be used in a number of different ways; one of its uses is as a major component in deriving vertical profiles of temperature and moisture (satellite retrievals). For the last several years, GOES retrievals at both CIMSS and NESDIS (designated as OPS) have been produced using a nonlinear physical retrieval algorithm (Ma et al. 1999). Briefly, this algorithm uses GOES Sounder cloud-free radiances in a number of spectral bands that have been averaged over 1-N Fields of View (FOV) to adjust initial guess vertical profiles of temperature and moisture. At CIMSS, the averaging is done within a 3 X 3 matrix of FOVs (N<=9), while the NESDIS operational retrievals are produced using a 5 X 5 FOV matrix (N<=25). Since the nominal horizontal resolution of a GOES Sounder FOV is approximately 10km at the sub-satellite point (Menzel and Purdom 1994), the nominal dimensions of the CIMSS and NESDIS retrievals are approximately 30 X 30 and 50 X 50 km, respectively.

As part of the physical retrieval process, an adjustment to the input radiances is necessary to account for errors in both the radiative transfer model and instrument calibration (Ma et al. 1999). This correction is known as the radiance bias adjustment. The adjustment is computed differently for the OPS and CIMSS retrievals. The OPS retrievals use a method known as "shrinkage estimation" (Schmit 1996), a regression approach that involves using 26 predictors to determine an hourly bias adjustment to apply in each Sounder channel.

On the other hand, retrievals produced at CIMSS now employ a somewhat simpler approach to bias adjustment. Not only are the number of predictors reduced from 26 to 5, the regression coefficients need only be computed once every several months. The simpler approach has been made possible because of expanded GOES radiance ground processing that resulted in more accurate calibration of radiance data (Weinreb 1997).

*Corresponding author address: James P. Nelson III, Univ. of Wisconsin-Madison, 1225 W. Dayton St. Madison, WI 53706; email: jimn@ssec.wisc.edu.

3. RETRIEVAL AND BIAS CORRECTION RESULTS

In this work, several years of GOES retrieval results from both CIMSS and NESDIS are examined. The examinations are conducted using two approaches: 1) comparisons of retrieval parameters, such as precipitable water and temperature, with the same from verifying radiosonde data, and 2) comparisons of the radiance bias adjustments made at CIMSS and NESDIS. The overall period of study for GOES-8 ranges from January 1998 through June 2001, while the same for GOES-10 ranges from January 1999 through June 2001. In the interest of brevity, our discussion will focus on comparing retrieval Total Precipitable Water vapor (TPW) with collocated radiosonde data. Previous work has shown that the nonlinear retrieval algorithm makes a larger adjustment to the guess moisture profile than the guess temperature profile (Ma et al. 1999).

3.1. Comparisons of retrieval parameters with radiosondes

Table 1 shows retrieval versus radiosonde bulk statistics for both the CIMSS and OPS retrievals, further subdivided by guess and retrieval, as well as retrieval time. These datasets have been constructed by requiring that each retrieval be collocated within approximately 0.1 degrees latitude/longitude (L/L) with a nearby radiosonde. The number of collocation matches (N) is larger for the CIMSS retrievals than the OPS retrievals because of the different retrieval processing box sizes. Looking first at the GOES-8 bulk statistics, one can see that the bias (GOES minus RAOB) is always negative. Furthermore, the standard deviation (SD) is reduced for all 4 sets of GOES-8 retrievals (00Z CIMSS, 12Z CIMSS, 00Z OPS, 12Z OPS) compared to their respective guesses. The 12Z retrieval SD values tend to be larger than their 00Z counterparts (3.22 versus 3.04 for CIMSS retrieval TPW, 3.29 versus 3.05 for OPS retrieval TPW). Looking at the average TPW data, there is a tendency for the CIMSS guesses and retrievals to contain less moisture than the OPS guesses and retrievals. Perhaps this is related to the different retrieval box sizes.

Turning our attention now to the GOES-10 bulk statistics, note that the number of radiosonde matches is approximately one-quarter of those from GOES-8. This is because less of the GOES-10 data is over CONUS. Also note how both the bias and SD values are reduced compared to the GOES-8 data. This is probably not too surprising, considering the average TPW values for GOES-10 are significantly smaller than the GOES-8 data. However, it is also interesting to note that the change in TPW bias when comparing the guess and retrieval data more often has the proper sign (i.e., the retrieved TPW is closer to the collocated radiosonde TPW than the guess) for GOES-10 when compared to GOES-8.

Table 1. Retrieval versus radiosonde bulk statistics. Collocation distance is approximately 0.1 degrees latitude/longitude. Minimum clear FOVs is 4. BIAS, SD and AVG values are in mm.

DATASET	PERIOD	BIAS	SD	AVG GUESS / RET TPW	AVG RAOB TPW	CC	N
00Z CIMSS G-8 TPW guess	1/98-6/01	-0.62	3.15	16.25	16.88	0.959	2260
00Z CIMSS G-8 TPW retrieval	1/98-6/01	-0.64	3.04	16.23	16.88	0.961	2260
12Z CIMSS G-8 TPW guess	1/98-6/01	-1.10	3.39	16.51	17.61	0.957	1870
12Z CIMSS G-8 TPW retrieval	1/98-6/01	-0.89	3.22	16.72	17.61	0.961	1870
00Z OPS G-8 TPW guess	1/98-6/01	-0.23	3.33	17.68	17.91	0.956	750
00Z OPS G-8 TPW retrieval	1/98-6/01	-0.62	3.05	17.29	17.91	0.963	750
12Z OPS G-8 TPW guess	1/98-6/01	-0.61	3.38	17.65	18.26	0.963	679
12Z OPS G-8 TPW retrieval	1/98-6/01	-1.11	3.29	17.15	18.26	0.965	679
00Z CIMSS G-10 TPW guess	1/99-6/01	-0.40	2.62	10.00	10.40	0.906	630
00Z CIMSS G-10 TPW retrieval	1/99-6/01	-0.35	2.05	10.05	10.40	0.944	630
12Z CIMSS G-10 TPW guess	1/99-6/01	-0.86	2.73	11.06	11.92	0.925	442
12Z CIMSS G-10 TPW retrieval	1/99-6/01	-0.41	2.56	11.51	11.92	0.936	442
00Z OPS G-10 TPW guess	1/99-6/01	-0.11	2.59	12.17	12.29	0.928	143
00Z OPS G-10 TPW retrieval	1/99-6/01	0.12	2.46	12.41	12.29	0.935	143
12Z OPS G-10 TPW guess	1/99-6/01	-0.76	2.66	10.72	11.48	0.900	170
12Z OPS G-10 TPW retrieval	1/99-6/01	-0.49	2.46	10.99	11.48	0.914	170

Finally, the correlation coefficients (CC) are also smaller for GOES-10 than for GOES-8, perhaps showing that the GOES-10 averaged radiances tend to show a little less sensitivity to the first guess than the GOES-8 radiances.

In all subsequent results, the input data to the statistics computations are filtered twice. First, retrievals are only used in the computations if they

are collocated within approximately 0.5 degrees L/L of a nearby radiosonde. This initial filtering procedure produces CIMSS/RAOB and OPS/RAOB collocation files. Then, the CIMSS/RAOB and OPS/RAOB matches are themselves subjected to the same 0.5 degrees L/L collocation procedure, as well as a 1 hour time collocation threshold. This results in one final file of matches, with all retrieval/RAOB matches being collocated within 0.5 degrees L/L, and the CIMSS and OPS retrievals themselves also being collocated within 0.5 degrees L/L. The intent is to compare CIMSS and OPS retrievals at very similar locations, while still maintaining a reasonably large dataset for the statistics.

Figure 1 shows a time series of GOES-8 00UTC and 12UTC combined TPW retrieval versus radiosonde bias for the CIMSS and OPS retrievals. Note the overwhelming tendency for negative biases, in agreement with Table 1 above. This may be demonstrating a weakness of coarse spectral resolution radiometers to detect low-level moisture. Also, the biases for both the CIMSS and OPS retrievals are maximized, in terms of largest dry bias versus the radiosondes, during the warmest and most moist summer months, and minimized during the cooler/dryer months. The same warm/moist and cool/dry seasonal tendencies also exist for GOES-10 (not shown). Furthermore, comparing the CIMSS and OPS biases to each other, one can see an interesting shift that occurred about July 2000. Prior to that time, the CIMSS biases tended to be closer to zero than the OPS retrievals, while after that point the OPS retrieval biases were closer to 0. This may be an indication of needing to update the CIMSS radiance adjustment database.

Figure 2 depicts a geographical distribution of CIMSS GOES-8 and GOES-10 combined 00UTC and 12UTC TPW bias at radiosonde locations. As one might expect, there are more negative than positive bias values. No clear regional bias tendencies are apparent, although pockets of positive bias exist in the Upper Midwest, along the

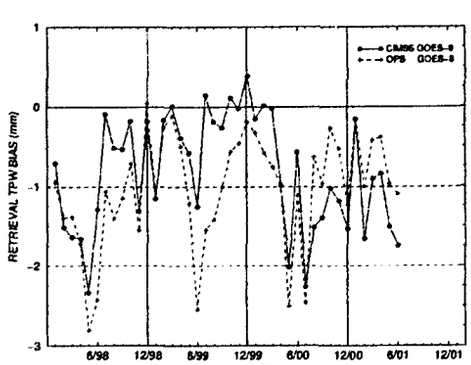

Fig. 1. GOES-8 CIMSS and OPS monthly, combined 00UTC and 12UTC TPW bias. Period is from January 1998 through June 2001.

eastern seaboard, along the Gulf coast, and over Mexico. Note also the large (in magnitude) negative biases in southern Texas. Similar distributions of bias are seen in Fig. 3 for the OPS retrievals, with an additional region of positive bias in the Pacific Northwest, and even larger negative biases in southern Texas (-4.45 mm versus -3.46 mm). More detailed study is required to determine the source of these large negative biases.

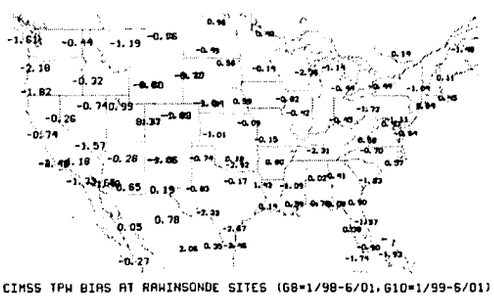

Fig. 2. CIMSS combined 00UTC and 12UTC retrieval TPW bias at radiosonde locations for GOES-8 (January 1998 – June 2001) and GOES-10 (January 1999 – June 2001). The larger numeric fonts (western portion) represent GOES-10 data.

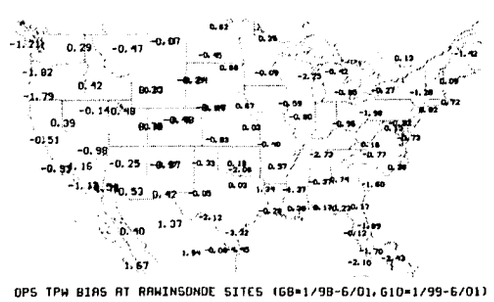

Fig. 3. As in Fig. 2 but for OPS retrievals.

3.2. Comparisons of bias-corrected radiances with radiosondes

As mentioned above, a GOES Sounder radiance bias adjustment in each channel is vital for producing satellite retrievals of temperature and moisture via a physical retrieval algorithm (Ma et al. 1999). To examine the results of the bias adjustment procedures used in the last several years at CIMSS and NESDIS, we have selected band 5 (13.4μm), a channel used in the retrieval of both temperature and moisture. Radiation in this band eminates mainly from the lower troposphere and surface (Menzel et al. 1998).

Figure 4 shows a time series of CIMSS monthly-averaged band 5 retrieval brightness temperatures for the period January 1998 – June

2001. The most obvious feature is the seasonal cycle. In the chart, the lowest average brightness temperatures are always the cloud-cleared, 3 X 3 FOV- averaged values, with the bias-corrected values being slightly warmer. The collocated radiosonde data are the warmest values. It can be seen that the bias adjustment is always towards the collocated radiosonde data. Note that these radiosondes are only shown for comparison and are not the same historical set of radiosondes used in calculating the CIMSS bias adjustment regression coefficients.

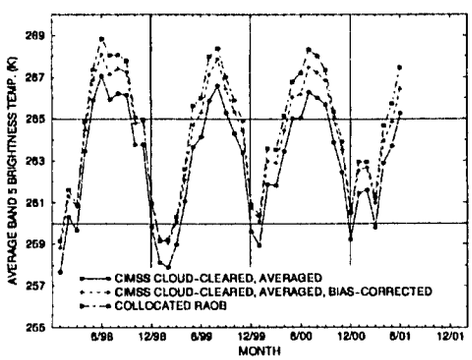

Fig. 4. CIMSS 12UTC GOES-8 monthly, averaged band 5 (13.4μm) retrieval brightness temperatures (measured and bias-corrected), along with average band 5 brightness temperatures computed for collocated radiosondes. Period is from January 1998 through June 2001.

The corresponding time series of OPS retrieval monthly-averaged band 5 brightness temperatures for the same period (not shown) is very similar, although the OPS average values are usually a fraction of a degree warmer than their CIMSS counterparts. Furthermore, and perhaps more significantly, the OPS bias-corrected brightness temperatures tend to be closer to the collocated radiosonde data than the CIMSS bias-corrected brightness temperatures. This may be a reflection of the more frequent updates of the OPS bias adjustment regression coefficients. The CIMSS bias adjustment regression coefficient database is likely in need of an update.

4. SUMMARY AND FUTURE WORK

This paper presents comparisons of satellite retrievals of temperature and moisture produced at CIMSS and NESDIS over the last several years, focussing on the derived product TPW. In terms of bulk statistics, both the CIMSS and NESDIS retrieved TPW exhibit a reduced SD when compared to its guess when compared to collocated radiosondes. In addition, the GOES-10 biases are usually smaller than GOES-8, and the GOES-10 SD values are always smaller than GOES-8.

Both the CIMSS and OPS GOES-8 and GOES-10 retrieval TPW biases tend to be more negative (retrieval drier than collocated radiosonde) in the warmer, more moist months. In terms of regional distributions of TPW bias, negative biases predominate for both the CIMSS and OPS retrievals, although pockets of positive biases also exist.

The radiance bias adjustment in Sounder band 5 (13.4μm) for both the CIMSS and OPS retrievals is such that the final bias-corrected brightness temperatures used in the physical retrieval algorithm agree more closely with nearby collocated radiosonde data than the uncorrected radiances.

By necessity due to space limitations, only retrieved TPW and band 5 bias adjustment data have been explicitly examined in this paper. At the conference, the comparisons will be expanded to include other retrieval parameters and Sounder bands. In particular, the radiance bias adjustment used at CIMSS and NESDIS will be examined more closely in an attempt to determine which is the better approach.

5. REFERENCES

Ma, X. L., T. J. Schmit, and W. L. Smith, 1999: A nonlinear physical retrieval algorithm—its application to the GOES-8/9 Sounder. *J. Appl. Meteor.*, **38**, 501-513.

Menzel, W. P., and J. F. W. Purdom, 1994: Introducing GOES-I: The first of a new generation of geostationary operational environmental satellites. *Bull. Amer. Meteor. Soc.*, **75**, 757-781.

Menzel, W. P., F. C. Holt, T. J. Schmit, R. M. Aune, A. J. Schreiner, G. S. Wade, and D. G. Gray, 1998: Application of GOES-8/9 soundings to weather forecasting and nowcasting. *Bull. Amer. Meteor. Soc.*, **79**, 2059-2077.

Schmit, T. J., 1996: Sounder bias correction of the east-west radiance gradient. *Proc. SPIE*, **2812**, Denver, CO, 630-637.

Weinreb, M. P., M. Jamieson, N. Fulton, Y. Chen, J. X. Johnson, J. Bremer, C. Smith, and J. Baucom, 1997: Operational calibration of Geostationary Operational Environmental Satellite-8 and –9 imagers and sounders. *Appl. Opt.*, **36**, 6895-6904.

P3.47

THE NESDIS SATELLITE QPE VERIFICATION PROGRAM

Robert J. Kuligowski[1]*, Shuang Qiu[2], Roderick Scofield[1], and Arnold Gruber[1]
[1]Office of Research and Applications, NOAA/NESDIS, Camp Springs, MD
[2]QSS Corporation, Lanham, MD

1. INTRODUCTION

Numerous algorithms for quantitative precipitation estimates (QPE) from satellites have been developed or are under development. Systematic validation of these algorithms is crucially important (a) in order to communicate the relative merits and weaknesses of these algorithms to potential users; and (b) to determine which algorithms present the most promising avenues for further development. However, algorithm intercomparison data for short-range applications (i.e. hours to days) is lacking.

In response, on 1 April 2001 personnel at the Office of Research and Applications (ORA) of the National Environmental Satellite, Data, and Information Service (NESDIS) initiated real-time evaluation of several satellite QPE algorithms over portions of the continental United States. The specifics of this evaluation are described in section 2, followed by a brief presentation of results in section 3 and future plans in section 4.

2. VALIDATION PROGRAM SPECIFICS

2.1. Algorithms

Six variations of four satellite rainfall algorithms are being tested. These include the operational Auto-Estimator (AE) (Vicente et al. 1998, 2001) and a variant dubbed the "Hydro-Estimator". The latter adjusts the rain-rate curve according to the difference in brightness temperature between the pixel of interest and its neighbors; it also treats the precipitable water and relative humidity adjustments separately. Versions of the "Hydro-Estimator" with and without the radar-based rain-no rain screen of the operational AE are being tested.

In addition to these three algorithms, two versions of the GOES Multi-Spectral Rainfall Algorithm (GMSRA) (Ba and Gruber 2001) are being tested: the standard version and a version that uses the difference between the 6.9-μm and 10.7-μm brightness temperature to differentiate between raining and nonraining areas at night.

The sixth algorithm being tested is a GOES-microwave blended product (Turk et al. 1998) that uses the AE screens and adjustments but updates the rain rate curves by matching the cumulative distribution functions of microwave rain rate estimates from the Special Sensor Microwave/Imager (Ferraro 1997), the Advanced Microwave Sounding Unit (AMSU) (Ferraro et al. 2000), and the Tropical Rainfall Measuring Mission (TRMM) Microwave Imager (TMI).

2.2. Validation Data and Event Classification

Validation is performed against two data sets. Daily estimates of precipitation from the satellite algorithms are evaluated against raingauges from the cooperative observer network. For shorter time periods, 6-h totals of satellite-estimated precipitation are evaluated against the Stage III radar-raingauge rainfall estimates (Fulton et al. 1998) produced operationally by the River Forecast Centers (RFC's).

At this time validation is being performed over a limited area. During this past spring season (April-May 2001), evaluation was performed in two regions. The first was the West Coast, consisting of the areas of responsibility of the Northwest RFC (NWRFC), and the California-Nevada RFC (CNRFC). The second area was the southern Plains, comprising the areas of the Arkansas-Red Basin RFC (ABRFC), the West Gulf RFC (WGRFC), and the Lower Mississippi RFC (LMRFC). These regions are indicated in Fig. 1. For the summer season (June-August 2001), the Colorado Basin RFC (CBRFC) was substituted for the NWRFC in order to capture the effects of the summertime monsoon in the Southwest.

To facilitate the evaluation of algorithm performance for specific events, the precipitation events were divided into four categories: stratiform, "cold-top" convective

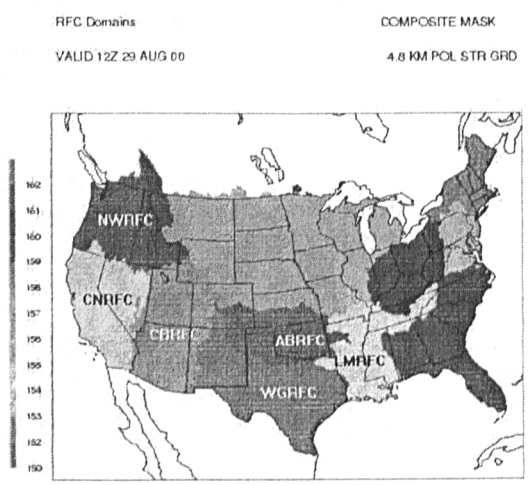

FIGURE 1. River Forecast Center (RFC) areas used in this study. [Figure courtesy of NCEP.]

---

* *Corresponding author address*: Robert J. Kuligowski, 5200 Auth Rd. WWB/601, Camp Springs, MD 20746; e-mail: Bob.Kuligowski@noaa.gov.

(coldest tops below -58°C), "warm-top" convective (no tops colder than -58°C), and tropical.

2.3. Statistics

Algorithm performance is evaluated using the root-mean-squared error (RMSE), the bias ratio (total estimated amount / total observed amount), and the correlation coefficient (CC). The performance of the algorithms is also evaluated as a function of observed rainfall amount using the probability of detection (POD), false alarm rate (FAR), bias ratio, and Heidke Skill Score (HSS).

3. RESULTS

Sample statistics for cold-top convective events are given in Table 1, while Fig. 1 contains a sample plot of the POD, FAR, bias, and HSS as a function of observed 6-h precipitation amount.

TABLE 1. Summary statistics for April-June 2001 cold-top events in the ABRFC, LMRFC, and WGRFC regions.

Algorithm	RMSE (mm)	Bias Ratio	CC
Operational AE	5.3	1.20	0.64
"Hydro-Estimator"	5.1	1.05	0.56
"Hydro-Est." (radar screen)	4.8	0.89	0.59
GMSRA	6.3	1.66	0.47
GMSRA (nighttime screen)	6.5	1.73	0.48
GOES/Microwave blend	6.0	1.15	0.56

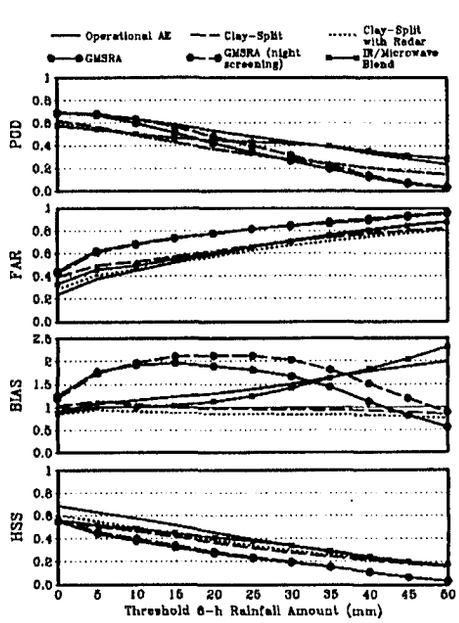

FIGURE 2. POD, FAR, bias, and HSS as a function of observed 6-h precipitation amount for the same data as in Table 1.

During April-June 2001, the operational AE exhibited the best overall correlation between estimates and observations. However, the "Hydro-Estimator" estimates were less biased than the AE and significantly outperformed the AE in some instances, such as for heavy precipitation from warm-top convection (not shown). The radar-based rain/no rain screen had a small effect on the performance of the "Hydro-Estimator", especially compared to the considerable difference (not shown) between the AE with and without the screen. The GOES/Microwave blend performed similarly to the AE; significant improvement in the rain-rate curves was achieved only for heavy warm-top convective events. The GMSRA exhibited the poorest overall performance.

4. FUTURE WORK

In addition to eventually expanding the validation to the entire continental U.S., additional algorithms will be evaluated These include the Microwave-Infrared Rain Rate Algorithm (MIRRA) (Miller et al. 2001), Precipitation Estimation from Remotely Sensed Information using Artificial Neural Networks (PERSIANN) (Sorooshian et al. 2000), and the Self-Calibrating Multivariate Precipitation Retrieval (ScaMPR) algorithm (Kuligowski 2001).

5. REFERENCES

Ba, M., and A. Gruber, 2001: GOES Multispectral Rainfall Algorithm (GMSRA). *J. of Appl. Meteor.*, in press.

Ferraro, R. R., 1997: SSM/I derived global rainfall estimates for climatological applications. *J. Geophys. Res.*, **102**, 16,715-16,735.

-----, F. Weng, N. C. Grody, and L. Zhao, 2000: Precipitation characteristics over land from the NOAA-15 AMSU sensor. *Geophys. Res. Lett.*, **27**, 2669-2672.

Fulton, R. A., J. P. Breidenbach, D. J. Seo, and D. A. Miller, 1998: The WSR-88D rainfall algorithm. *Wea. Forecasting*, **13**, 377-395.

Kuligowski, R. J., 2001: A self-calibrating real-time GOES rainfall algorithm for short-term rainfall estimates. Submitted to *J. Hydrometeor.*

Miller, S. W., P. A. Arkin, and R. Joyce, 2001: A combined microwave/infrared rain rate algorithm. *Int. J. Remote Sens.*, in press.

Sorooshian, S., K.-L. Hsu, X. Gao, H. V. Gupta, B. Imam, and D. Braithwaite, 2000: Evaluation of PERSIANN system satellite-based estimates of tropical rainfall. *Bull. Amer. Meteor. Soc.*, **81**, 2035-2046.

Turk, F. J., F. S. Marzano, and E. A. Smith, 1998: Combining geostationary and SSM/I data for rapid rain rate estimation and accumulation. Preprints, *9th Conf. on Satellite Meteorology and Oceanography*, Paris, Amer. Meteor. Soc., 462-465.

Vicente, G. A., R. Scofield, and W. P. Menzel, 1998: The operational GOES infrared rainfall estimation technique. *Bull. Amer. Meteor. Soc.*, **79**, 1883-1898.

-----, J. C. Davenport, and R. A. Scofield, 2001: The role of orographic and parallax corrections on real time high resolution satellite rain rate distribution. *Int. J. Remote Sens.*, in press.

P3.51

Validation of GOES-11 Data

Xiangqian Wu*
Cooperative Institute for Meteorological Satellite Studies
University of Wisconsin, Madison, WI

Timothy J. Schmit
NOAA/NESDIS, Office of Research and Applications (ORA),
Advanced Satellite Products Team (ASPT), Madison, WI

1. Introduction

After successful launch of the 11'th Geostationary Operational Environmental Satellite (GOES-11, Menzel and Purdom, 1994) and the engineering check-out period, the National Oceanic and Atmospheric Administration (NOAA) National Environmental Satellite, Data, and Information Service (NESDIS) conducted a GOES-11 Science Test from June 30 to August 13, 2000. At the Cooperative Institute for Meteorological Satellite Studies (CIMSS) and Advanced Satellite Products Team (ASPT), there were two goals for the GOES-11 science test. One was to investigate the quality of the GOES-11 data, the results of which are summarized in this poster. The other was to generate GOES-11 products (temperature and moisture profiles, total precipitable water, lifted index, cloud-top pressure, satellite-derived winds, sea surface temperature, and biomass burning) and compare these products to those from other satellites. These results, as well as more details of the first goal, are reported by Daniels and Schmit (2001).

2. Instrument Noise

2.1. Sounder

Special GOES-11 Sounder scans of space allowed the determination of noise values by calculating the scatter of radiance when looking at uniform space. Results for all 18 infrared bands of GOES-11 Sounder, taken at 23:46 UTC of July 8, 2000, is presented in Fig. 1. The noise values are generally within specification and lower than those from GOES-8. These noise values have also been monitored for a 24-hour period (between July 7-8, 2000) to confirm that the noise has little diurnal change.

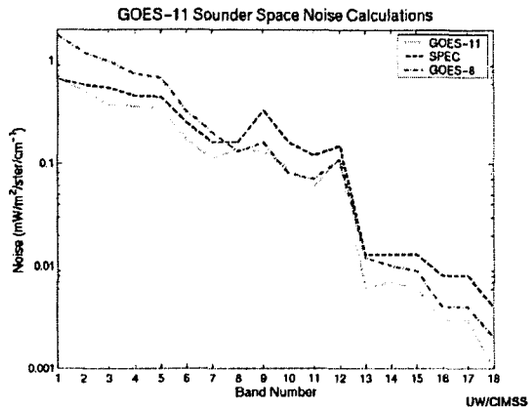

Figure. 1: The noise values of 18 infrared bands of GOES-11 Sounder.

2.2. Imager

Imager noise has been determined in the same way and reported in Table 1. These noise values were once monitored every 15 minutes for a period of 3 hours and were found to vary less than 0.01 to 0.02K. Additionally, they were found to be well within specification and comparable to previous GOES (personal communication, Donald W. Hillger).

Table 1: The noise values of the infrared channels of GOES-11 Imager in terms of brightness temperatures (K). The counterpart values from previous GOES and the specified NEdT values (SPEC) are also listed. The reference temperature is 230K for Band 3 and 300K for other bands.

Band	SPEC	G11	G10	G09	G08
2 (3.9μm)	1.40	0.13	0.17	0.08	0.16
3 (6.7μm)	1.00	0.21	0.09	0.15	0.27
4 (11μm)	0.35	0.07	0.20	0.07	0.12
5 (12μm)	0.35	0.18	0.24	0.14	0.20

• *Corresponding author*: Xiangqian Wu, CIMSS, 1225 W. Dayton St., Madison, WI 53706. fredw@ssec.wisc.edu

3. Imager-to-Imager Comparison

Imager-related comparisons are primarily based on GOES-11 Imager data collected every half hour between 20N-40N, from 00 UTC July 21 to 19 UTC July 24, 2000. The latitude range was chosen to cover both land and sea. To minimize the difference due to view angle, the longitude was limited to 88W-92W and 118W-122W. Corresponding GOES-11 Sounder and GOES-8/10 Imager data were also collected. Weinreb et al. 1997 discusses the calibration methods.

3.1. Visible

Due to the lack of a visible on-board calibration source, visible channels are not absolutely calibrated after launch, hence measurements in these channels are expected to be different. Figure 2 suggests that the sensitivity of GOES-8 (10) visible channel is about 60% (83%) of that of GOES-11.

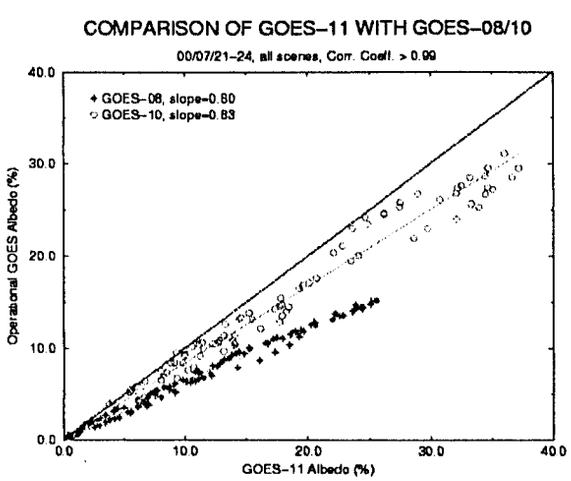

Figure 2: Scatter plot of GOES-8 (*) and GOES-10 (°) albedo as a function of GOES-11 albedo. Albedo is the arithmetic mean of individual pixel albedo within the area of comparison. A diagonal line is shown for reference. The lines of least-squares regression are also shown, whose slopes indicate the sensitivity of the operational GOES relative to GOES-11.

Fig. 2 offers an opportunity to assess the degradation rate of the visible channels of GOES-8/10. In April 1998, a similar comparison revealed that the sensitivity of GOES-8 was about 70% of that of GOES-10 (GOES-K Report). In July 2000, the sensitivity of GOES-8 was about 0.60/0.83=72% of that of GOES-10. This indicates that, in the past two years, the rate of degradation for the two operational satellites have been similar (GOES-10 slightly faster). However, had the degradation rate been constant for each satellite since their launch times, the degradation rate for GOES-8 would be larger:

G08 (6.3 yrs in space): 6.3x=(1-60%) => x=6.3%/yr
G10 (3.3 yrs in space): 3.3x=(1-83%) => x=5.2%/yr

Typically, though, the sensitivity of visible channels experiences a rapid drop shortly after launch, followed by relatively constant degradation. Also note that GOES-10 was in a stowed position for more than a year in space, during which time there probably was little degradation. Taking these into consideration, the rate of degradation can be estimated as following:

G08 (6.3 years in service): x + 6.3y = (1-60%)
G10 (2.1 years in service): x + 2.1y = (1-83%)

which leads to a one-time post-launch drop of x=5.5% and annual degradation of y=5.5%/yr. According to these results, GOES-10 in the past 2.3 years should have lost 5.5+2.1*5.5=17% of its sensitivity (two months in stowed position), whereas GOES-8 should have lost only 2.3*5.5=12.7% of its sensitivity during the same period. This agrees with early observation that GOES-10 has been degrading faster than GOES-8 since April 1998. Also, the sensitivity of GOES-8 in July 2000 would be 70%*(1-12.7%)=61%, close to the 60% obtained by direct comparison.

Knapp and Vonder Haar (2000, referred to as KH hereafter) recently found a 7.6% one-time post-launch drop followed by a 5.6% annual degradation for the visible band of GOES-8 Imager. These results are in reasonable agreement with other studies including ours. Such agreement is remarkable for several reasons. First, their approach of using a radiative transfer model is theoretical in nature, whereas our approach is largely empirical. The consistency of the results from these two very different approaches lends credit to both.

Second, KH restricted their study to the dark ocean scene at local noon. Other studies, for example Greenwald et al (1997), focused on highly reflecting surfaces such as clouds. In our case, scenes for a wide range of illuminations and albedo were examined. Despite of these differences in target selection, the results are similar. In particular, Fig. 2 shows that a linear least-squares regression is a good fit for comparisons of dark and bright scenes. These reconfirm a conclusion by KH that the degradation is relatively uniform throughout the dynamic range of instrument response.

Finally, KH were focused on GOES-8 only, whereas we studied the degradation of both GOES-8/10. Our approach has implicitly assumed that: (1) the sensitivity of the visible channel of GOES-8/10/11 Imagers are the same when first operated on orbit; and (2) the degradation pattern are the same for both GOES-8/10, i.e., a post-launch drop and annual degradation at the same rate. The agreement between the two studies suggests that these assumptions may be valid.

3.2. Infrared

The differences in brightness temperature between GOES-11 and GOES-8/10 for the Imager infrared bands are summarized in Table 2. The infrared bands are expected to be well calibrated without systematic bias among the Imagers, although an absolute calibration difference of 1K is allowed. Table 2 shows that the brightness temperature measured by GOES-11 is about 1K cooler (0.8K warmer) than that by GOES-8/10 for the 3.9 μm (6.7 μm) band. These differences are larger and more persistent than expected. For the split-window bands (11 and 12 μm), the differences are smaller and more variable.

Table 2: Mean difference (K) between GOES-11 Imager and GOES-8/10 Imagers and GOES-11 Sounder for the IR bands.

Band	G11-G08	G11-G10	Img-Snd
2 (3.9μm)	-0.98	-1.43	-1.67
3 (6.7μm)	+0.80	+0.75	+1.33
4 (11μm)	+0.75	+0.45	+0.71
5 (12μm)	-0.01	-0.70	-0.44

In addition to the mean difference, the standard deviations of the differences were analyzed but no significant patterns emerged. The area has also been divided into land and ocean, again the differences are similar to those of the whole. To examine whether the overall difference is caused by a few isolated events, the time series of the differences is studied, which concluded that the differences are fairly steady throughout the 5-day period. The differences do exhibit some diurnal variations, though, which are believed to be caused by a combination of differential heating and viewing geometry of the target and GOES-11 calibration. Finally, to investigate whether the differences are caused by a poor calibration at certain temperatures, for example the very cold/hot scenes, histograms of the differences are examined, which showed that the differences are persistent throughout the range of temperature.

4. Sounder-to-Sounder Comparison

4.1. Visible

On Friday 30 June (14:42 UTC), GOES-11 Sounder normalization software was installed by SOCC, leading to less striping in the Sounder visible imagery (Fig. 3).

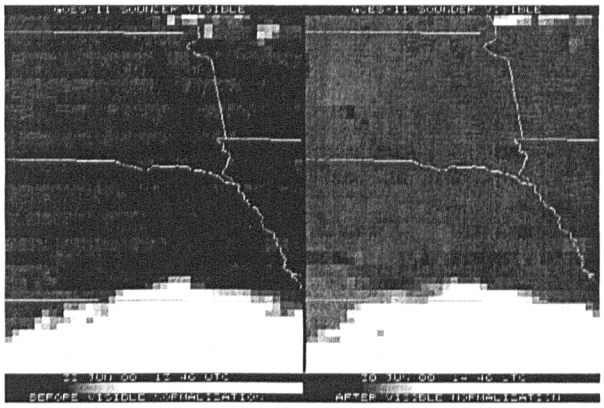

Figure 3: Before (left) and after (right) the application of GOES-11 Sounder visible normalization.

4.2. Infrared

Fig. 4 shows the Sounder brightness temperature differences for all 18 infrared bands between GOES-11 and GOES-8/10 during a nighttime period. Only measurements of similar view angles were compared. The GOES-11 Sounder brightness temperatures are in better agreement with those from GOES-10 than from GOES-8. The operational spectral response functions for both GOES-8 and GOES-10 Sounders were used. The largest differences are for Sounder bands on the edges of absorption features (e.g. 3, 13 and 15).

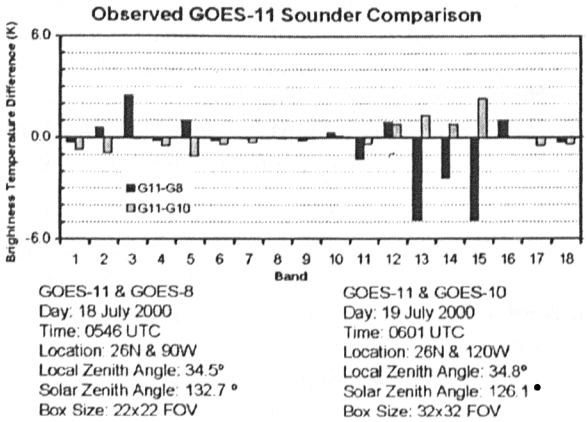

Figure 4: Sounder brightness Temperature differences between GOES-11 and GOES-8/10.

5. Imager-to-Sounder Comparison

Fig. 5 is a comparison of GOES-11 Imager with Sounder. The Imager Band 1 is compared with Sounder band 19; Imager band 4 is compared with Sounder band 8; and Imager band 5 is compared with Sounder band 7. Since there is no Sounder band corresponding closely to the other two Imager bands, Imager band 2 is compared with the mean of Sounder bands 17 and 18 and Imager band 3 is compared with the mean of Sounder bands 11 and 12.

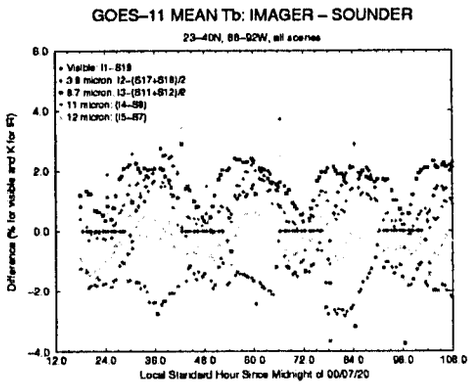

Figure 5: Differences of GOES-11 Imager and Sounder brightness temperatures plotted as a function of time.

The mean differences of Imager-Sounder during this 4-day period have been reported earlier in Table 2. The overall differences for the first three bands could be due to spectral response differences, and the differences for the last two bands are reasonably small. It is interesting, however, that the Imager-Sounder differences are quite similar to the Imager-Imager differences, which could result from a less well calibrated GOES-11 Imager compared with a well-calibrated GOES-11 Sounder and GOES-08/10 Imagers. Fig. 5 also depicts a rather obvious diurnal variation of the differences, particularly for the 6.7 and 11 μm bands. The minima occurred close to the satellite midnight, which is one hour later than the local midnight. This is more likely caused by calibration uncertainties.

6. Summary

The NOAA Science checkout phase of the GOES post-launch testing offers an opportunity to compare various satellite radiances and products. GOES-11 imager and sounder data were taken during the six-week NOAA science test, when the satellite was stationed at 105W. The imager-to-imager radiance comparisons show fair agreement, although the GOES-11 imager shows the greatest differences. The visible sensors of GOES-8/10 were shown to degrade 5.5% shortly after launch, followed by a steady annual rate of degradation of 5.5%. These results are in close agreement with previous studies. Overall, the sounder data from GOES-11 are slightly better than those from GOES-8. The GOES-11 data exhibited less noise and less striping.

7. References

Daniels, J. M., T. J. Schmit, 2001: GOES-11 Science Test: GOES-11 Imager and Sounder Radiance and Product Validations. *NOAA Tech. Rep.* (in press).

Greenwald, T. J., S. A. Christopher, and J. Chou, 1997: Cloud liquid water path comparisons from passive microwave and solar reflectance satellite measurements: Assessment of sub-field-of-view cloud effects in microwave retrievals. *J. Geophys. Res.*, **102**, 19,585-19,596.

Knapp, K. R., T. H. Vonder Haar, 2000: Calibration of the Eighth Geostationary Observational Environmental Satellite (GOES-8) Imager Visible Sensor. *J. Atmos. Oceanic Tech.* **17**, 1,639–1,644.

Menzel, W. P., and J. F. W. Purdom, 1994: Introducing GOES-I: The first of a new generation of Geostationary Operational Environmental Satellites. *Bull. Amer. Meteor. Soc.*, **75**, 757-780.

Weinreb, M. P., M. Jamison, N. Fulton, Y. Chen, J. X. Johnson, J. Bremer, C. Smith, and J. Baucom, 1997: Operational calibration of Geostationary Operational Environmental Satellite-8 and -9 imagers and sounders. *App. Optics*, **36**, 6,895-6,904.

P3.60

DERIVED CLOUD PRODUCTS FROM THE GOES-M IMAGER

Anthony J. Schreiner*
CIMSS/Univ. of Wisconsin, Madison, Wisconsin
Timothy J. Schmit
NOAA/NESDIS/ORA, Advanced Satellite Products Team, Madison, Wisconsin

1. INTRODUCTION

With the launch of the next in the series of geostationary platforms, Geostationary Operational Environmental Satellite (GOES) – M Imager, a modification in the suite of bands has been introduced. The current Imager obtains information from four infrared bands and one visible band (Menzel and Purdom, 1994). GOES-M continues the same number of bands, but initiates several changes. Table 1 summarizes those spectral changes.

Table 1. GOES Imager spectral widths for GOES-8 (similar for GOES-9 through GOES-11) and GOES-M. The units of wavelength are μm; the units for wavenumber are cm^{-1}.

GOES-8 Imager Bandwidths

Ch. No.	Wavelength Range	Central Wave-length	Wavenumber Range
1	0.53-0.72	0.64	13812-19048
2	3.78-4.03	3.91	2482.2-2647.7
3	6.47-7.03	6.75	1421.8-1544.5
4	10.21-11.20	10.69	892.5-979.1
5	11.54-12.47	11.97	802.1-866.2
6	---	---	---

GOES-M Imager Bandwidths

Ch. No.	Wavelength Range	Central Wave-length	Wavenumber Range
1	0.53-0.77	0.65	12970-18939
2	3.76-4.03	3.90	2481.9-2656.4
3	5.77-7.33	6.48	1363.3-1733.4
4	10.23-11.24	10.71	889.7-977.1
5	---	---	---
6	12.96-13.72	13.31	729.0-771.6

The GOES-M Imager includes a band centered at 13.3 μm and improves north-south spatial resolution of a spectrally modified 6.5 μm band. The addition of the 13.3 μm band comes at the expense of eliminating the 12 μm band on the Imagers. GOES-8 and GOES-M Imager spectral response functions are shown in Fig. 1. Note the elimination of the 12 μm band and the addition of the 13.3 μm band, in addition to the modified "water vapor" band.

With the current series of GOES Imagers cloud height or cloud top pressures from the GOES Imager are available using either the IR Window Technique (Schreiner, et al; 1993) or the IR Window-Water Vapor Intercept Technique (Nieman, et al; 1993). By including a "CO_2" band (13.3 μm) among the suite of Imager channels the opportunity for more frequent (than the GOES Sounder) and accurate cloud products (than the GOES Imager) is now possible using the CO_2 Absorption Technique (CAT) (Wylie and Menzel, 1999). The CAT will provide more accurate calculations of Effective Cloud Amount (ECA) than currently available from the GOES Imager, more frequent and timely Satellite Cloud Products (SCP) in support of the Automated Surface Observing System (ASOS), and hemispheric coverage of the CAT for input into numerical prediction models.

The objective of this paper is twofold. First, to briefly describe the changes on the GOES-M Imager. Second, to introduce the cloud product based on the Imager data.

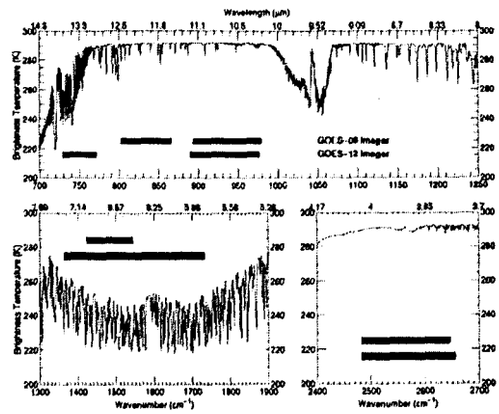

Fig. 1. Spectral ranges for the GOES-8 (top bars) and GOES-M (bottom bars) Imagers. A sample high spectral-resolution earth emitted spectra is also plotted.

* *Corresponding author address:* Anthony J. Schreiner, CIMSS, University of Wisconsin-Madison, 1225 W. Dayton St., Madison, WI 53706;e-mail: tonys@ssec.wisc.edu

2. INSTRUMENT CHANGES

The GOES-M "water vapor" band is spectrally wider than the current 6.7 μm band. The spectral width covers the region from 5.77 to 7.33 μm with a center wavelength of 6.5 μm (Table 1). The water vapor spectral response function was made spectrally wider to improve the signal-to-noise ratio, and thus compensate for the smaller Field Of View (FOV) on GOES-M than previous Imagers. The spectral shift will make it similar to the current European METEOSAT (METEOrological SATellite) "water vapor" band. The current Meteosat bandwidth for the "water vapor" band is 5.7 to 7.1 μm Schmetz et al., 1998). Radiative transfer calculations for a standard atmosphere show that the GOES-M band 3 will be approximately 2 K warmer than the current Imager band 3 onboard GOES-8. This difference is consistent for a variety of atmospheres (not shown) (Schmit et al., 2001).

The GOES-M 6.5 μm band will also have a higher north-south spatial resolution. It will change from approximately 8 km to 4 km at the sub-satellite point. On the GOES Imagers, the IGFOVs are over-sampled in the east/west direction by a factor of 1.75 providing an effective resolution in the east-west direction of 2.3 km (Menzel and Purdom, 1994).

Table 2. GOES-8 (top) and GOES-M (bottom) Imager spatial characteristics. Detector Instantaneous Geometric Field Of View (IGFOV) or footprint is in km at the sub-satellite point. The Sampled Subpoint Resolution (SSR) is also in km and is a finer resolution due to over sampling in the east-west direction. The spatial characteristics are listed as the east-west by north-south dimensions, respectively.

	GOES-8		
Ch.	Descr.	IGFOV	SSR
1	Visible	1.0 x 1.0	0.57 x 1.0
2	SW window	4.0 x 4.0	2.3 x 4.0
3	Water Vapor	8.0 x 8.0	2.3 x 8.0
4	LW window	4.0 x 4.0	2.3 x 4.0
5	Split window	4.0 x 4.0	2.3 x 4.0
6	CO_2	---	---

	GOES-M		
Ch.	Descr.	IGFOV	SSR
1	Visible	1.0 x 1.0	0.57 x 1.0
2	SW window	4.0 x 4.0	2.3 x 4.0
3	Water Vapor	4.0 x 4.0	2.3 x 4.0
4	LW window	4.0 x 4.0	2.3 x 4.0
5	Split window	---	---
6	CO_2	8.0 x 8.0	2.3 x 8.0

The 13.3 μm band, referred to as the GOES Imager band 6, will allow for cloud height determinations. This band is similar, although with a broader spectral response function, to band 5 on the current GOES Sounder (Menzel et al., 1998) (Fig. 2). Forward radiative transfer calculations for a standard atmosphere show the GOES-M Imager 13.3 μm band will have a slightly higher mean brightness temperature than the Sounder band 5 (Fig. 3). This difference of approximately 1.5 K exists for other atmospheres as well (not shown). The GOES-M 13.3 μm spatial resolution will be approximately 8 km in the north-south direction (Table 2).

The addition of the 13.3 μm band results in the elimination of the 12 μm band on the GOES-M/N/O/P Imager. For the GOES cloud product the 12 μm band is used for detecting the presence, or lack of clouds prior to determining the height and amount of cloud (Hayden, et al; 1996 and Schreiner et al; 2001).

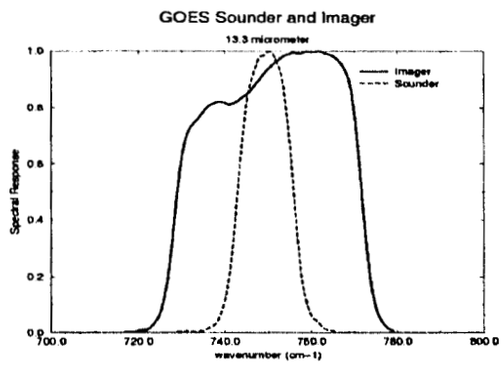

Fig.2. Normalized spectral response function for the GOES-M Imager 13.3 μm band and the corresponding Sounder band.

3. CLOUD PRODUCTS

Cloud products generated via the CO_2 absorption technique have been demonstrated from instruments on both geostationary and polar-orbiting platforms (Wylie and Wang, 1997; Wylie and Menzel, 1999; Schreiner et al., 2001). Cloud products derived from the GOES Sounder have been used to initialize numerical models (Bayler et al., 2001 and Kim et al., 2000). Improved products from the GOES-M Imager will include cloud top pressure, effective cloud amount and cloud top temperature. Fig. 4 shows the Cloud Top Pressure (CTP) derived image using only spectral bands from the GOES Sounder that will be available on the GOES-M Imager. This image has been compared to

one derived from the full set of Sounder bands used for deriving CTP. With a sample size of 3533, the bias (Sounder minus Imager derived CTP) was 20 hPa and the root mean square (rms) was 112 hPa.

With the addition of the 13.3 μm band on the GOES-M Imager, the Satellite Cloud Product (SCP) that complements the ground-based ASOS (Automated Surface Observing System) could be generated from the Imager rather than the Sounder (Schreiner et al., 1993). The SCP, based on GOES-M Imager data, could be available in a more timely fashion since the Imager coverage rate is much faster than the Sounder.

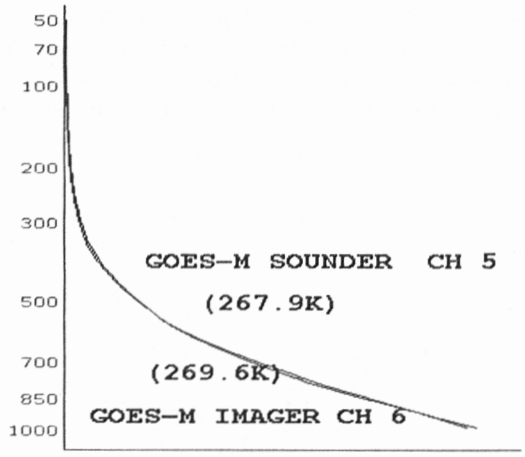

Fig. 3. Weighting function for both the 13.3 μm GOES-M Sounder and Imager bands for a standard atmosphere. The units of the ordinate are pressure (hPa).

An additional product available to the modeling community will be near-hemispheric cloud top information. Assuming the GOES-M schedule is similar to the current GOES-8 a hemispheric view of the earth will occur every three hours. Output from these processed data will provide cloud information in addition to clear, cloudy, and averaged brightness temperatures from 65N to 65S. An example of what such a cloud image may look like will be shown.

The loss of the 12 μm band will negatively impact the detection of low cloud. Currently, 11 minus 12 μm differences are used extensively to flag the presence of clouds at night. Without the 12 μm data, there will be more reliance on visible data during the day and 3.9 μm data during the night for cloud detection. The 13.3 μm data may also help to mitigate the loss of the 12 μm band for cloud detection. Experience with actual GOES-M data during the post-launch checkout will answer this question.

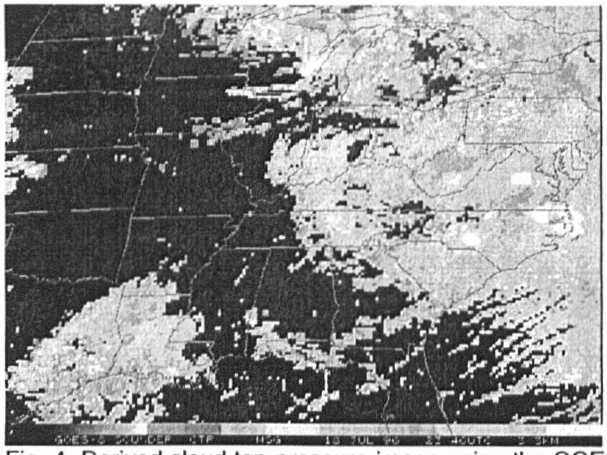

Fig. 4. Derived cloud top pressure image using the GOES Sounder 13.3 μm data and LW infrared window.

4. SUMMARY

Cloud products from the GOES-M Imager will benefit from the inclusion of a band centered at 13.3 μm. Among them are cloud height and effective cloud amount via the CO2 Absorption Technique. Quantitative coverage, both spatially and temporally, will increase. This will benefit the SCP for ASOS and the numerical modeling community.

In order to accommodate the 13.3 μm band, the 12 μm band was eliminated on the GOES-M Imager. This change may affect the ability to detect some clouds, especially low clouds at night. The 12 μm band, along with a host of other bands, will be included on the next generation series of GOES Imagers, beginning with GOES-R in the 2010 era.

5. REFERENCES

Bayler, G. M., R. M. Aune, and W. H. Raymond, 2001: NWP cloud initialization using GOES sounder data and improved modeling of non-precipitating clouds. *Mon. Wea. Rev.*, **128**, 3911-3920.

Hayden, C. M., G. S. Wade, and T. J. Schmit, 1996: Derived product imagery from GOES-8. *J. Appl. Meteor.*, **35**, 153-162.

Kim, D., and S.G. Benjamin, 2000: Assimilation of cloud-top pressure derived from GOES sounder data into MAPS/RUC. Preprints, *10th Conf. On Satellite Meteorology and Oceanography*, Long Beach, CA, Amer. Meteor. Soc., 110-113.

Menzel, W. P., F. C. Holt, T. J. Schmit, R. M. Aune, G. S. Wade, D. G. Gray, and A. J. Schreiner, 1998: Application of GOES-8/9 soundings to

weather forecasting and nowcasting, *Bull. Amer. Meteor. Soc.*, **79**, 2059-2078.

Menzel, W. P., and J. F. W. Purdom, 1994: Introducing GOES-I: The first of a new generation of geostationary operational environmental satellites, *Bull. Amer. Meteor. Soc.*, **75**, 757-781.

Nieman, S.J., J. Schmetz, and W.P. Menzel, 1993: A comparison of several techniques to assign heights to cloud tracers, *J. Appl. Meteor.*, **32**, 1559-1568.

Schmit, T.J., E.M. Prins, A.J. Schreiner, and J.J. Gurka, 2001: Introducing the GOES-M imager. Submitted to *Nat. Wea. Assoc. Digest.*

Schreiner, A. J., D. A. Unger, W. P. Menzel, G. P. Ellrod, K. I. Strabala, and J. L. Pellett, 1993: A comparison of ground and satellite observations of cloud cover. *Bull. Amer. Meteor. Soc.*, **74**, 1851-1861.

Schreiner, A. J., T. J. Schmit, and W. P. Menzel, 2001: Trends and observations of clouds based on GOES sounder data. Accepted by *J. Geophysical Res. --Atmospheres.*

Schmetz, J., H. Woick, S. Tjemkes, and J. Rattenborg, 1998: From Meteosat to Meteosat Second Generation, In Proceedings of the Ninth Conference on Satellite Meteorology and Oceanography, Paris, France, Amer. Meteor. Soc., 335-338.

Wylie, D. P., and P. H. Wang, 1997: Comparison of cloud frequency data for the High Resolution Infrared Radiometer Sounder and the Stratospheric Aerosol and Gas Experiment II. *J. of Geophys. Res.*, **102** (29), 29,893-29,900.

Wylie, D. P., and W. P. Menzel, 1999: Eight years of high cloud statistics using HIRS. *J. Climate*, **12**, 170-184.

P4.2 INTERCALIBRATION OF GEOSTATIONARY AND POLAR-ORBITING INFRARED WINDOW AND WATER VAPOR RADIANCES

Mathew M. Gunshor* [1], Timothy J. Schmit [2], and W. Paul Menzel [3]

[1] Cooperative Institute for Meteorological Satellite Studies
[2] NOAA/NESDIS/ORA/ASPT
[3] NOAA/NESDIS/ORA
Madison, Wisconsin

1. INTRODUCTION

Satellites traditionally used for weather monitoring have proven to be useful in environmental monitoring. Thus, the ability to compare the measured radiances from different instruments has become increasingly important. The Cooperative Institute for Meteorological Satellite Studies (CIMSS) has been intercalibrating five geostationary satellites (GOES-8, -10, METEOSAT-5, -7, GMS-5) with a single polar-orbiting satellite (NOAA-14 HIRS and AVHRR) on a routine, automated basis for over a year using temporally and spatially co-located measurements. The primary focus of this effort has been in comparing the 11-μm infrared window (IRW) channels. Similar efforts are being made for the 6.7-μm water vapor (WV) channels. The numerical methods for conducting the routine intercalibration are being updated. This includes updating the radiative transfer forward model used to estimate the differences in calculated brightness temperatures based on spectral differences between satellite instruments.

2. APPROACH

The technique for intercalibration has been developed at CIMSS over the past several years (Wanzong et al., 1998). Collocation in space and time (within +/- thirty minutes) is required. Data is selected within 10 degrees of nadir for each instrument in order to minimize viewing angle differences. Measured means of brightness temperatures of similar spectral channels from the two sensors are compared. In the IRW channel, data collection is restricted to mostly clear scenes with mean radiances greater than 80 mW/m^2/ster/cm^{-1}, and no additional effort is made to screen out clouds from the collocation area. In the WV channel there is no clear scene restriction applied. Data from each satellite are averaged to an effective 100-km resolution to mitigate the effects of different field of view (fov) sizes and sampling densities; HIRS under-samples with a 17.4 km nadir fov, AVHRR Global Area Coverage (GAC) achieves 4 km resolution by resampling, GOES imager over-samples 4 km in the east-west by 1.7 (Menzel and Purdom, 1994), and METEOSAT-5, METEOSAT-7, and GMS-5 have a nadir 5 km fov. Mean radiances are computed within the collocation area. Clear-sky forward calculations (using a global model for estimation of the atmospheric state) are performed to account for differences in the spectral response functions (Figures 1 and 2). The observed radiance difference minus the forward-calculated clear-sky radiance difference is then attributed to calibration differences.

Thus,

$$\Delta R_{cal} = \Delta R_{mean} - \Delta R_{clear}$$

For comparing a geostationary satellite to HIRS,

$$\Delta R_{cal} = [R^{GEO}_{mean} - R^{GEO}_{clear}] - [R^{HIRS}_{mean} - R^{HIRS}_{clear}]$$

where *GEO* indicates geostationary, *HIRS* indicates the HIRS instrument, *mean* indicates the mean measured radiance, and *clear* indicates the forward calculated clear-sky radiances. Conversion to temperatures for a comparison between a geostationary satellite to HIRS is accomplished by,

$$\Delta T_{HIRS} = [B^{-1}{}^{GEO}_{mean} - B^{-1}{}^{GEO}_{clear}] - [B^{-1}{}^{HIRS}_{mean} - B^{-1}{}^{HIRS}_{clear}]$$

* *Corresponding author address:* Mathew M. Gunshor, Univ. of Wisconsin-Madison, 1225 W. Dayton St., Madison, WI 53706.

where B^{-1} indicates converting radiance to brightness temperature using the inverse Planck Function. An identical method is used for calculating the temperature difference between a geostationary satellite and the AVHRR instrument (ΔT_{AVHRR}).

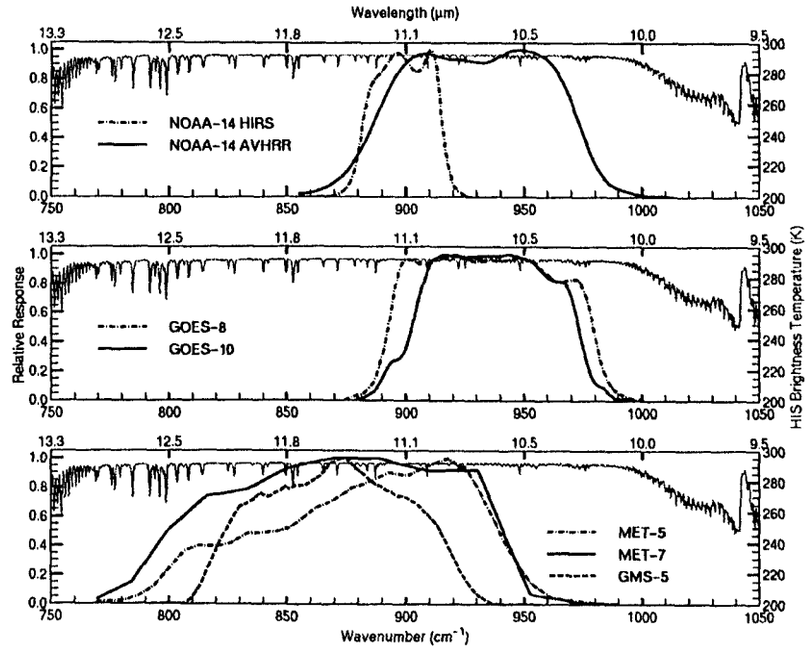

Fig. 1. Infrared Window Channel spectral response functions with a high spectral resolution earth emitted spectrum from a High-resolution Interferometer Sounder.

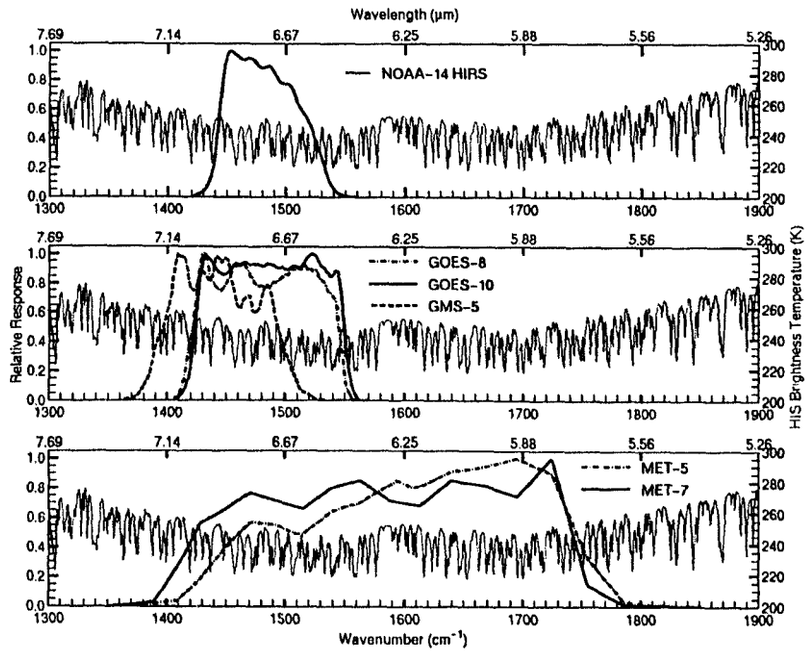

Fig. 2. Water Vapor Channel spectral response functions with a high spectral resolution earth emitted spectrum from a High-resolution Interferometer Sounder.

3. RESULTS

Intercalibration results for all five geostationary satellites covering the time period from January 2000 to July 2001 are shown in Table 1. The mean is the average of all cases for the indicated satellite and a negative sign indicates the measurements from the polar-orbiting instrument (HIRS or AVHRR) are warmer than those from the geostationary instrument. All five geostationary instruments on average are measuring colder temperatures than HIRS and AVHRR in the IRW channel; they measure warmer temperatures on average than HIRS in the WV channel. The standard deviation is the deviation about the mean. In the IRW channel the standard deviations for ΔT_{AVHRR} are lower than they are for ΔT_{HIRS}; the standard deviations for the WV channel comparisons are smaller than those in the IRW channel for ΔT_{HIRS}.

Table 1. January 2000 to July 2001 IRW (top) and WV (bottom) comparison of geostationary satellites and NOAA-14 HIRS and AVHRR.

Delta (geo – leo)		GOES-8 IRW	GOES-10 IRW	MET-5 IRW	MET-7 IRW	GMS-5 IRW
Number of Comparisons	ΔT_{HIRS}	29	227	240	291	119
	ΔT_{AVHRR}	29	227	240	291	119
Mean	ΔT_{HIRS}	-0.55 K	-0.31 K	-0.98 K	-1.12 K	-0.82 K
	ΔT_{AVHRR}	-0.35 K	-0.01 K	-0.34 K	-0.79 K	-0.59 K
Standard Deviation	ΔT_{HIRS}	0.84 K	1.21 K	1.25 K	0.88 K	1.19 K
	ΔT_{AVHRR}	0.32 K	0.43 K	0.64 K	0.65 K	0.73 K

Delta (geo – leo)		GOES-8 WV	GOES-10 WV	MET-5 WV	MET-7 WV	GMS-5 WV
Number of Comparisons	ΔT_{HIRS}	148	272	236	175	139
Mean	ΔT_{HIRS}	1.37 K	2.2 K	4.2 K	3.9 K	1.52 K
Standard Deviation	ΔT_{HIRS}	0.5 K	0.67 K	1.18 K	0.51 K	0.86 K

4. EFFECTS OF THE NEW APPROACH

The approach outlined in this paper is an updated version of the approach used at CIMSS for the past two years and reported at Coordination Group for Meteorological Satellites (CGMS) annual meetings. The first change is in the conversion from radiance to brightness temperature. The old approach used the slope of the Planck Function (dB/dT) while the new approach uses the inverse Planck Function. The second change is updating the forward model to PLOD/PFAAST. Although the results of these two changes are not differentiated here, the updating of the forward model reduced a small amount of error in the results, on the order of a tenth of a degree in some cases. Changing the method of conversion to brightness temperature proved to be a more significant alteration of the approach. For example, ΔT_{HIRS} in the IRW channel was less than 0.5 K for all instruments using the old approach. The results from the new approach do not appear as favorable as the results from the old approach, yet these results more fairly represent the actual differences between satellites and are more consistent with the results of other studies (Tjemkes et al., 2001).

5. CONCLUSIONS

Several conclusions can be drawn from the results in Table 1. The mean difference may suggest comparisons between HIRS and the geostationary

satellites are made difficult by the relatively narrow HIRS spectral response function (Figure 1) and large fov size compared to those of the other instruments. IRW results between AVHRR and all five geostationary instruments show smaller differences. For all geostationary instruments, comparison to HIRS is more favorable in the IRW channel than in the WV channel. This suggests a higher degree of difficulty to compare different instruments for the WV channel. This is possibly due to the widely different spectral responses (Figure 2), a higher degree of uncertainty in the calibration of this channel for some instruments, and the greater inhomogeneity of the atmospheric water vapor structure.

It is not possible, from this study, to determine which satellite is the most accurate or has the best calibration. It is only possible to compare them to each other. The mean differences of all five geostationary instruments appear to be calibrated to within approximately 1 K of each other.

The mean temperature differences in the IRW channel are small compared to those in the WV channel, but the standard deviations follow the opposite trend. Standard deviations in the IRW channel may be larger due to the greater variability in IRW radiances as compared to radiances in the WV channel. The IRW channel will measure surface effects as well as clouds and the range of radiances (and brightness temperatures) will be much greater than that of the water vapor channel, which only measures a small range of radiances (and brightness temperatures) from higher in the atmospheric column.

6. FUTURE WORK

There are two other changes to the technique being discussed. The first would be to use a Sea Surface Temperature (SST) for the surface temperature in the clear-sky forward model calculations. Currently the surface in the model calculations is considered to be the bottom layer of the atmospheric profile. This change is not expected to alter the results greatly, however it would produce slightly more accurate calculated clear-sky brightness temperatures, which may also mean more accurate ΔT calculations.

The second change involves the global atmospheric forecast model used to provide the atmospheric profiles for the forward model calculation. The results of an individual case are sensitive to changes in the moisture profile and this may be the greatest source of error in the intercalibration process. Efforts will be made to see that the most representative atmospheric model data available is used.

In addition to those changes, work has begun to transfer these comparisons from the research side to NESDIS operations. A goal of the CGMS is for all satellite operators to routinely produce similar statistics. There are plans for other polar-orbiting satellites to be compared, such as NOAA-15 or –16.

8. REFERENCES

Menzel, W. P. and J. F. W. Purdom, 1994: Introducing GOES-I: The first of a new generation of geostationary operation environmental satellites. Bull. Amer. Meteor. Soc., **75**, 757-781.

Tjemkes, S.A., M. König, H.-J. Lutz, L. van de Berg, and J. Schmetz, 2001: Calibration of Meteosat water vapor channel observations with independent satellite observations. J. Geophys. Res., **106**, 5,199-5,209.

Wanzong, S. W., W. P. Menzel, and G. Callan, 1998: Intercalibration of GOES, Meteosat, GMS, HIRS, and AVHRR infrared radiances. Report of the 9th Conference on Satellite Meteorology and Oceanography held 25 – 29 May, 1998 in Paris, France. AMS Publication.

P4.20

VALIDATION OF GOES AND MODIS ATMOSPHERIC PRODUCTS AND RADIANCES USING DEPARMENT OF ENERGY ATMOSPHERIC RADIATION (DOE ARM) MEASUREMENT DATA

Wayne F. Feltz*, Timonthy J. Schmit#, Jim Hawkinson, David Tobin, and Suzanne Wetzel-Seeman

Space Science and Engineering Center University of Wisconsin - Madison
Madison, Wisconsin

#NOAA/NESDIS/ORA Advanced Satellite Product Team (ASPT) Madison, Wisconsin, USA

1. INTRODUCTION

The Department of Energy (DOE) Atmospheric Radiation Measurement (ARM) Program (Stokes, 1994) has deployed a suite of ground-based in situ and remote sensing instrumentation to provide a long term (> 10 years) validation data set for General Circulation Models (GCM). The three DOE ARM measurement sites are named Southern Great Plains (SGP Oklahoma/Kansas region), North Slope of Alaska (NSA, near Barrow, Alaska), and Tropical Western Pacific (TWP). The main purpose of the ARM program is to improve knowledge of cloud radiative flux (shortwave and longwave) and to develop new GCM parameterizations to improve climate model forecasts. The ARM data sets have provided a unique high temporal resolution satellite validation source. The University of Wisconsin - Madison Space Science Engineering Center (SSEC) has a real-time direct broadcast downlink capability for the Geostationary Operational Environmental Satellites (GOES) and EOS-Terra data. The NOAA Cooperative Institute for Meteorological Satellite Studies (CIMSS) is producing atmospheric derived products from GOES and MODIS radiances, providing information about atmospheric stability, cloud properties, and moisture. ARM data sets are being used to validate GOES Total Precipitable Water (TPW), cloud tops, and atmospheric soundings derived from the GOES sounder. A best estimate temperature and moisture profile from the DOE ARM SGP site is being used to calculate radiance values for validation of GOES and MODIS radiance measurements. This paper will provide an overview of current DOE ARM measurements used for validation of these satellite products and recent conclusions.

2. GOES MOISTURE PRODUCT VALIDATION

The DOE ARM SGP site offers TPW measurements that allow for more precise validation of GOES retrievals than is possible with radiosondes. An operational microwave radiometer (MWR), located at the SGP central facility near Lamont, has demonstrated an accuracy of 0.7 mm under clear sky conditions (Liljegren 1995). All comparisons reported here are for clear sky cases. The MWR is tuned to the microwave emissions of the water vapor molecules in the atmosphere (Liljegren 1994) and measures TPW vapor every five minutes. The MWR measurements are completely independent of those from the GOES Sounder or radiosondes. These high temporal resolution MWR measurements enable validation of the GOES retrievals at times other than the conventional radiosonde launches (00 and 12 UTC). Of course, the MWR and GOES retrievals still differ in that one is a point measurement (although with an improved accuracy compared to radiosondes) and one a volumetric measurement.

TPW values computed from GOES-8 retrievals (Ma et al. 1999) and their corresponding first guess profiles were compared to the MWR TPW for a 29-day period between 20 March – 17 April 1998. The temporal resolution for GOES-8 was routine hourly profiling. Figure 1 shows a one-day comparison of TPW on 12 April 1998 between the MWR and GOES-8. While the first guess (diamonds), which was interpolated from 6-hourly forecasts, is relatively flat throughout the period, the GOES retrieval algorithm (pluses) produces nearly the same water vapor tendency patterns as measured by the MWR (dashed line). The satellite retrieval uses a 3 x 3 FOV matrix (equating to a 36 km x 45 km box at this geographic location), representing a volumetric profile over a larger horizontal area than the MWR (which represents the atmosphere directly above the instrument). Smooth temporal changes are generated by the GOES physical retrieval algorithm, even when the first guess experiences a discontinuity when switched from using forecasts from the 00 UTC to the 12 UTC model initialization times (e.g. near 18 UTC). These discontinuities could be minimized if the forecasts from the 06 UTC and 18 UTC initialization times were also used to build the first guess profiles for the GOES retrievals. The GOES retrievals follow the water vapor fluctuations between a local minimum of approximately 13 mm at 1130 UTC and a maximum of approximately 24 mm at 14 UTC; the temporally and spatially coarse

* *Corresponding author address*: Wayne F. Feltz, CIMSS/SSEC, 1225 West Dayton Street Room 238, Madison, WI, 53706; e-mail: wayne.feltz@ssec.wisc.edu.

radiosonde network did not capture these changes. Overall, GOES demonstrates skill in resolving the mesoscale water vapor fluctuations on this day.

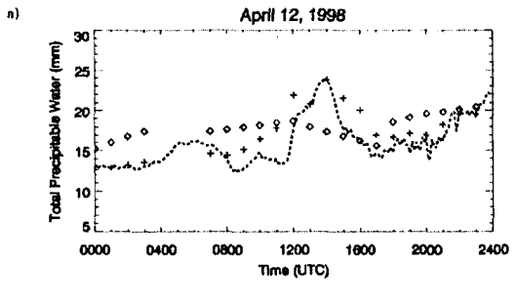

Figure 1: Microwave radiometer (dashed line), Eta model forecast (diamond symbols), and GOES-8 physical retrieval (plus symbols) total precipitable water vapor comparisons near Lamont, Oklahoma on 12 April 1998.

Figure 2 shows the improved agreement of the GOES physical retrieval algorithm (stars) versus the first guess (diamonds) when compared to the MWR measurements during the period 20 March to 17 April 1998. These data were derived by comparing all possible matches between GOES-8 retrievals and the MWR instrument. For the 364 matched values of MWR and GOES-8 shown in Fig. 2, the physical retrieval improves the first guess of TPW RMS from 2.21 to 1.80 mm and the bias from 0.83 to 0.40 mm. Even at greater TPW values, the GOES retrieval values compared better with microwave radiometer values (perfect agreement indicated by the diagonal line).

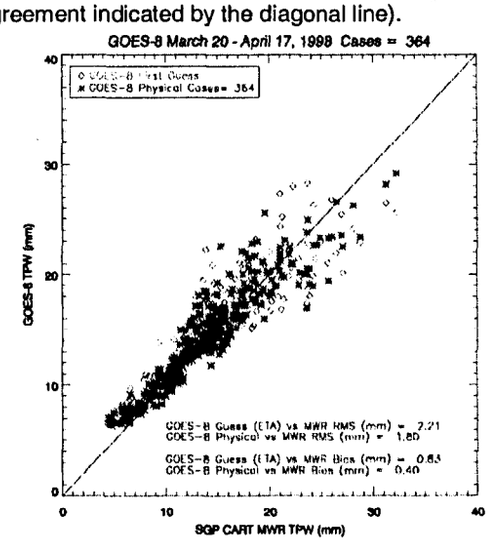

Figure 2: A scatter plot comparing MWR total water vapor values to the Eta model forecast (diamond symbols) and the GOES-8 physical retrieval (star symbols) values. RMS and bias for all matches are quantified in the lower right hand corner.

The DOE ARM microwave radiometer data has provided a valuable stable validation source for space-borne total precipitable water measurements at high temporal resolution. These data are also used to derive the post-launch tests for GOES (Daniels and Schmit 2001). Real-time TPW validation has been implemented at SSEC CIMSS UW-Madison to provide near instantaneous meteorological satellite product evaluation. More information about the evaluation of GOES TPW can be obtained in Schmit et al 2001.

3. GOES CLOUD TOP VALIDATION

A consensus cloud boundary product has been developed for the DOE ARM sites by using combined cloud information from the Microwave Millimeter Cloud Radar (MMCR) and MicroPulse Lidar (MPL). This product was used to validate hourly GOES sounder derived cloud top pressures for March 2000 at the central facility DOE ARM SGP near Lamont, Oklahoma. The DOE ARM cloud boundary data has a time resolution of 10 seconds and is determined over a narrow column of atmosphere over Lamont, Oklahoma. The GOES cloud product is derived from 3x3 FOV and provides an average cloud top pressure as well as minimum and maximum pressures. The technique for determining the GOES cloud top pressure is described in Schreiner et al. 2001. Due to the high temporal and spatial resolution of the DOE ARM cloud boundary product, five minute binning of this product on either side of an hourly GOES determined cloud top was done to minimize resolution discrepancies between the ground-based and space-borne cloud top determination. To simplify the comparison, multiple layered cloud scenes where removed from the samples. This was determined in the GOES 3x3 FOV by analysis of the minimum and maximum cloud top pressure altitude. Cloud top altitude differences of 2 km or less were used within the analysis generally providing uniform cloud top cases.

After accounting for spatial and temporal resolution differences and filtering multiple layer cloud cases, 73 matches between hourly GOES and 10 second MMCR/MPL cloud products were determined for March 2000 near Lamont, Oklahoma (Figure 3). A high correlation of 0.93 with an RMS of 930 meters was calculated. The two outliers in the figure are probably due GOES inability to detect very thin cirrus clouds with low emissivity/optical depth. This study will be expanded to use data for all months in the year 2000 to provide a more robust comparison and provide insight for GOES cloud top pressure altitude algorithm improvement. For more information on this study, view Hawkinson et al. 2001 (presented in these proceedings).

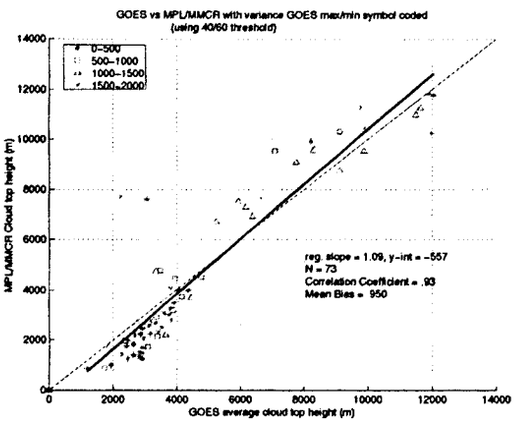

Figure 3: A scatter plot comparing DOE ARM ground-based MPL/MMCR and space-borne GOES derived cloud top altitude after resolution binning and multiple level clouds are removed. A correlation coefficient of 0.93 and a mean bias of 950 m was determined.

4. CONCLUSIONS

DOE ARM data have become an important validation sources for geostationary and polar orbiting satellite platform sounder instrumentation. GOES TPW and cloud top products are being extensively evaluated with the data. GOES cloud top estimates have shown a correlation of 0.93 and RMS differences of approximately one kilometer. The GOES moisture retrieval algorithm improves the precipitable water values from the ETA model first guess by 0.4 millimeters in both an RMS and mean statistical sense as compared the a DOE ARM microwave radiometer. A best estimate product for temperature and moisture derived from DOE SGP site Raman Lidar, AERI, MWR, and radiosonde information is currently providing a way to evaluate EOS Terra (and soon EOS Aqua) overpass radiance calibration (see Wetzel et al. 2001 in these conference proceedings). The DOE ARM NSA and TWP sites will be extensively used to evaluate cloud and thermodynamic retrievals for EOS AIRS and MODIS polar orbiting overpasses in the near future.

5. ACKNOWLEDGEMENTS

This research was supported by the NOAA Grant NA67EC0100. Data were obtained from the Atmospheric Radiation Measurement (ARM) Program sponsored by the U.S. Department of Energy, Office of Science, Office of Biological and Environmental Research, Environmental Sciences Division.

6. REFERENCES

Daniels, J. M., T. J. Schmit, 2001: GOES-11 Science Test: GOES-11 Imager and Sounder Radiance and Product Validations. NOAA Technical Report, In press.

Hawkinson, J., W. F. Feltz, T. Schmit, A. J. Schreiner, S. Ackerman, 2001: A Validation Study of the GOES Sounder Cloud Top Pressure Product Preprints, *Eleventh Conference on Satellite Meteor. And Oceanography,* 15-18 October, 2001, Madison, WI.

Liljegren, J. C., 1994: Two-channel microwave radiometer for observations of total column precipitable water vapor and cloud liquid water path. Preprints, *Fifth Symp. of Global Change Studies,* Nashville, TN.

------, 1995: Observations of total column precipitable water vapor and cloud liquid water using a dual-frequency microwave radiometer. *Microwave Radiometry and Remote Sensing of the Environment*, D. Solimini, Ed., Utrecht, VSP (Vista Science Press), 107-118.

Ma, Xia L., T. J. Schmit, W. L. Smith, 1999: A nonlinear physical retrieval algorithm—its application to the GOES-8/9 sounder. *J. Appl. Meteor.* **38**, No. 5, 501-513.

Menzel, W. P., F. C. Holt, T. J. Schmit, R. M. Aune, G. S. Wade, D. G. Gray, A. J. Schreiner, 1998: Application of GOES-8/9 Soundings to weather forecasting and nowcasting. *Bull. Amer. Meteor. Soc.* **79**, 2059–2078.

Schreiner, A.J., T.J. Schmit, and W.P. Menzel, 2001: Observations and trends of clouds based on GOES sounder data. Journal of Geophysical Research-Atmospheres, Accepted for publication March 2001.

Schmit, T. J., W. F. Feltz, W. P. Menzel, J. Jung, A. P. Noel, J. N. Heil, J. P. Nelson III, Gary S. Wade, 2001: Validation and use of GOES Sounder Moisture Information, Wea. And Fore., In Review.

Stokes, G. M., and S. E. Schwartz, 1994: The Atmospheric Radiation Measurement (ARM) program: Programmatic background and design of the cloud and radiation testbed. *Bull. Amer. Meteor. Soc.*, **75**, 1201-1221.

Wetzel-Seeman S., D. Tobin, L. E. Gumley, C. Moeller, W. P. Menzel, T. J. Schmit, M. Gunshor, 2001: Comparison of MODIS/TERRA radiances with GOES-8, GOES-10, and DOE ARM CART site. Preprints, *Eleventh Conference on Satellite Meteor. And Oceanography,* 15-18 October, 2001, Madison, WI.

P5.5

CHANNEL SELECTION FOR THE NEXT GENERATION GEOSTATIONARY ADVANCED IMAGERS

Timothy J. Schmit
NOAA/NESDIS, Office of Research and Applications, Advanced Satellite Products Team (ASPT)

W. Paul Menzel
NOAA/NESDIS, Office of Research and Applications

Mathew M. Gunshor, James P. Nelson III
Cooperative Institute for Meteorological Satellite Studies (CIMSS)
University of Wisconsin-Madison

Madison, WI

1. INTRODUCTION

To keep pace with the growing need for GOES data and products, NOAA is evolving its geostationary sensor capabilities. The Advanced Baseline Imager (ABI) will be the next generation geostationary imager on GOES-R, beginning in 2010. As with the current GOES Imager, this instrument will be used for a wide range of both qualitative and quantitative applications. The ABI will include a number of improvements over the existing imager besides the additional bands. The ABI will improve the spatial coverage from nominally 4 to 2 km for the infrared bands, as well as almost a five-fold increase of the coverage rate (Gurka and Dittberner 2001). This imager will have a minimum of eight spectral bands and a maximum of twelve spectral bands. The minimum eight bands are similar to the five bands on the current GOES-8/11 Imagers (Menzel and Purdom 1994), plus a snow/cloud-discriminating 1.6 μm band, a mid-tropospheric 7.0 μm water vapor band, and a 13.3 μm band useful for determining cloud heights and amounts. This carbon dioxide-sensitive band is similar to that on the GOES-M and beyond series of Imagers (Schmit et al. 2001). The ABI bands were selected after considering NWS requirements, existing bands on the GOES Imagers and Sounders, bands on other future geostationary satellites, and bands on current and future polar-orbiting satellites. For example, the next generation METEOSAT (METEOrological SATellite) Second Generation (MSG), to be launched in 2002, will have 12 channels, including two water vapor channels centered at 6.2 and 7.3 μm (Schmetz et al. 1998).

The uses of the eight core bands, and the four additional bands, are briefly described in the following section.

Corresponding author address: Timothy J. Schmit, 1225 West Dayton Street, Madison, WI 53706; email: Tim.J.Schmit@noaa.gov.

2. ABI CHANNEL SELECTION

The 0.64 μm visible band is used for: daytime cloud imaging; snow and ice cover; detection of severe weather onset detection; low-level cloud drift winds; fog; smoke; volcanic ash, hurricane analysis; and winter storm analysis.

During the day, the 1.6 μm band can be used for: cloud/snow/ice discrimination; total cloud cover; aviation weather analyses for cloud-top phase (Hutchison 1999); and detecting smoke from low-burn-rate fires.

The shortwave IR window (3.9 μm) band has many uses: fog (Ellrod et al. 1998) and low-cloud discrimination at night; fire identification (Prins et al., 1998); volcanic eruption and ash detection; and daytime reflectivity for snow/ice.

The 6.15 μm and 7.0 μm bands will be used for upper and mid-tropospheric water vapor tracking; jet stream identification (Weldon et al., 1991); hurricane track forecasting; mid-latitude storm forecasting; severe weather analysis and for estimating upper level moisture (Soden et al., 1993; Moody et al., 1999).

The longwave infrared window (11.2 μm) band will provide day/night cloud analyses for general forecasting and broadcasting applications; precipitation estimates (Vicente et al., 1998); severe weather analyses; cloud drift winds (Velden et al. 1998a); hurricane strength (Velden et al. 1998b) and track analyses; cloud top heights; volcanic ash detection (Prata 1989); fog detection (in multi-band products); winter storms; and cloud phase/particle size estimates (in multi-band products).

The 12.3 μm band will offer nearly continuous cloud monitoring for numerous applications; low-level moisture determinations; volcanic ash identification detection (Davies and Rose 1998); Sea Surface Temperature measurements (Wu et al. 1999) and cloud particle size (in multi-band products).

The 13.3 μm band will be used for cloud top height assignments for cloud-drift winds;

cloud products for ASOS supplement (Schreiner et al. 1993; Wylie and Menzel 1999); tropopause delineation; and estimating cloud opacity.

Four bands have been proposed as additions to the core eight, with the goal of meeting NWS requirements and enhancing many products/applications. The 8.5 μm band, in conjunction with the 11.2 μm band, will enable detection of volcanic dust cloud containing sulfuric acid aerosols (Realmuto et al. 1997; Baran et al. 1993; Ackerman and Strabala 1994). In addition, the 8.5 μm band can be combined with the 11.2 and 12.3 μm bands to derive cloud phase (Strabala et al. 1994).

The 10.35 μm band will help to derive low-level moisture, cloud particle size and surface properties. Chung et al. (2000) showed how the 10 - 11 μm region is important for determining particle sizes of ice-clouds.

A visible band at 0.86 μm will help the detection of aerosols and vegetation. Characterizing aerosols and their optical properties is essential for improving a number of satellite products, for example land and sea surface temperatures. This band may enable localized vegetation stress monitoring, fire danger monitoring, and albedo retrieval. Other applications include suspended sediment detection (Aquirre-Gomez, 2000).

Finally, a near-infrared channel at 1.38 μm is proposed to detect very thin cirrus not detected by other bands. The 1.38 μm band is similar to a band on MODIS (MODerate resolution Imaging Spectroradiometer). Radiation from this band does not sense into the lower troposphere due to water vapor absorption and thus it provides excellent daytime sensitivity to very thin cirrus.

The spectral widths of the ABI infrared bands are shown both in Table 1 and Fig. 1. A number of these same bands were selected by NASA for the Advanced Geosynchronous Studies Imager (AGSI) (Hinkal et al. 1999).

Table 1. ABI channel selection. The four shaded bands denote the proposed additional bands.

Wavelength (μm)	Description
0.64 +/- 0.05	Visible
0.86 +/- 0.05	Visible
1.375 +/- 0.015	Near IR
1.61 +/- 0.03	Near IR
3.9 +/- 0.1	Shortwave IR
6.15 +/- 0.45	Water Vapor 1
7.0 +/- 0.2	Water Vapor 2
8.5 +/- 0.2	IR Window 1
10.35 +/- 0.25	IR Window 2
11.2 +/- 0.4	IR Window 3
12.3 +/- 0.5	IR Window 4
13.3 +/- 0.3	Carbon Dioxide

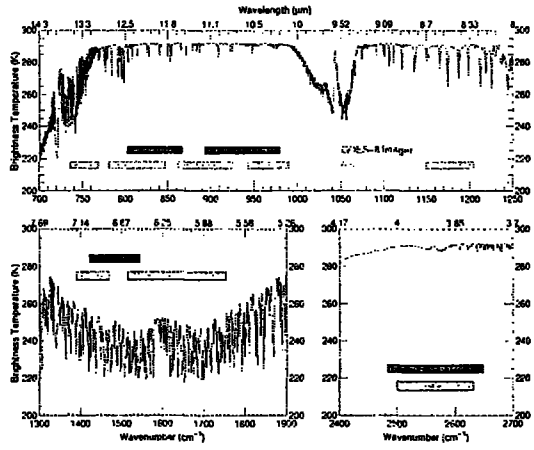

Fig. 1 The GOES-8 IR spectral bands (top bars) and the ABI IR spectral bands (lower bars). A high-spectral resolution earth-emitted spectra is also plotted.

The corresponding ABI weighting functions (for the IR bands) are shown in Fig. 2.

3. ABI SIMULATIONS BASED ON MODIS DATA

There are two main methods to simulate the expected signal from a future instrument. One method uses a radiative transfer model along with some estimate of the state of the atmosphere to calculate the expected (noise free) signal and then add noise. The second method, employed in this study, is to use higher-resolution data to simulate ABI. This method allows for more realistic simulations, especially of the clouds. Bands on the high-spatial resolution NASA MODIS data (Ackerman et al. 1998) have been used to simulate the ABI bands. The 10.35 μm band could not be simulated since there is no corresponding MODIS band.

The simulation of the ABI from MODIS data consists of two steps. First, apply a point spread function (PSF) to the MODIS data to account for diffraction and other blurring affects. PSF data were obtained from MIT/Lincoln Labs (personal communication, Edward Wack). Second, remap the MODIS 1 km to the ABI 2 km spatial resolution. No corrections were made to account for different spectral response functions between MODIS and ABI. Also, given the similarities between MODIS and ABI bit depth and instrument noise, no adjustments were made for either parameter.

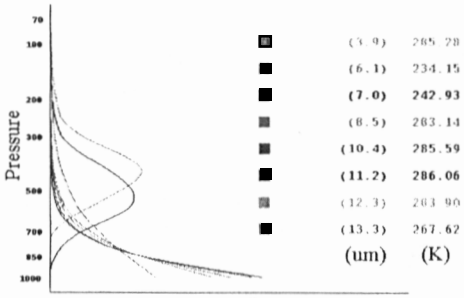

Fig. 2. The contribution weighting functions are plotted for each of the IR ABI bands for the standard atmosphere at a 40 degree local zenith angle.

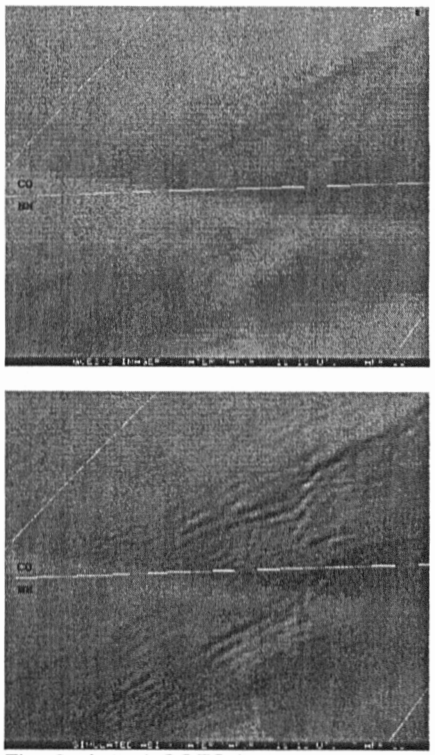

Fig. 3. Actual GOES Imager water vapor image (top) and the simulated ABI image (bottom). Both images are shown in the GOES projection. The gravity waves are clearly depicted in the ABI image. This case is from 7 April 2000, 1815 UTC.

Figure 3 shows current GOES and simulated ABI (from MODIS imagery) water vapor images in cloud free skies. These mountain waves over Colorado and New Mexico were induced by strong northwesterly flow associated with a pair of upper-tropospheric jet streaks moving across the elevated terrain of the southern and central Rocky Mountains. The mountain waves appear better defined over Colorado; in fact, several aircraft reported moderate to severe turbulence over that region.

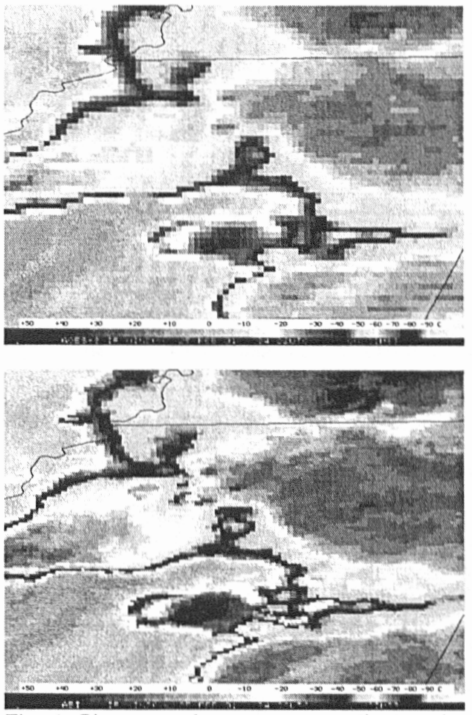

Fig. 4. Close-up of severe convection as depicted in the longwave IR window from 25 February 2001. GOES Imager (top) and simulated ABI (bottom) are shown.

Figure 4 shows GOES Imager and ABI close-ups of a severe thunderstorm. The details of the cold-tops are more evident in the ABI image. Additional comparisons are being made for a wide range of meteorological phenomena. These phenomena include wave clouds, severe convection, hurricanes, volcanoes, fires, lake ice, cloud phase and fog. For example, a thin ash plume from the Mt. Cleveland (Alaska) volcano was more readily identified in an 8.5 μm minus 11 μm image than in the traditional split window 11 minus 12 μm image.

4. SUMMARY

The ABI represents an exciting expansion in geostationary remote sensing capabilities, especially the 12 band version. Other improvements include faster coverage and improved spatial resolution. Even with 12 bands, the instrument could benefit from the addition of two more bands, at 0.47 μm and 9.6 μm. The 0.47 μm band would be used for aerosol detection and would enable daytime "true color" composites. The 9.6 μm band would monitor total ozone on space and time scales never before possible; MSG will also have such an ozone-sensitive band. Similar bands were proposed on the AGSI (Hinkal et al. 1999).

5. REFERENCES

Ackerman, S. A., K. I. Strabala, W. P. Menzel, R. A. Frey, C. C. Moeller, and L. E. Gumley, 1998: Discriminating clear sky from clouds with MODIS. *J. Geophys. Res.*, **103**, 32141-32157.

Ackerman, S. and K. I. Strabala, 1994: Satellite remote sensing of H2SO4 aerosol using the 8 to 12 μm window region: Application to Mount Pinatubo. *J. Geo. Res.*, **99**, 18,639-18,649.

Aquirre-Gomez, R., 2000: Detection of total suspended sediments in the North Sea using AVHRR and ship data. *Int. J. Remote Sensing*, **21**, 1583-1596.

Baran, A. J., J. S. Foot and P. C. Dibben, 1993: Satellite detection of volcanic sulfuric acid aerosol. *Geophys. Res. Letters*, **20**, 1799-1801.

Chung S., S. Ackerman, and P. F. van Delst, 2000: Model calculations and interferometer measurements of ice-cloud characteristics. *J. Appl. Met.*, **39**, 634-644.

Davies, M. A., and W. I. Rose, 1998: GOES imagery fills gaps in Montserrat volcanic cloud observations. *EOS, Transactions, American Geophysical Union*, **79**, 505-507.

Ellrod, G. P., R. V. Achutuni, J. M. Daniels, E. M. Prins, and J. P. Nelson III, 1998: An assessment of GOES-8 Imager data quality, *Bull. Amer. Meteor. Soc.*, **79**, 2509-2526.

Gurka, J. J., and G. J. Dittberner, 2001: The next generation GOES instruments: status and potential impact. Preprint Volume. 5th Symposium on Integrated Observing Systems. 14-18 January, Albuquerque, NM, Amer. Meteor. Soc., Boston.

Hinkal, S., Jenstrom, D.; Florez, J., Bremer, J. C.; Hersh, M.; Neuberger, D., and Kindsfather, R., 1999: Advanced Geosynchronous Studies Imager: Instrument system design. Earth Observing Systems IV, Proceedings of the Conference, Denver, CO, 18-20 July 1999. Bellingham, WA, Society of Photo-Optical Instrumentation Engineers (SPIE). SPIE Proceedings volume 3750, pp2-10.

Hutchison, K. D., 1999: Application of AVHRR/3 imagery for improved detection of thin cirrus clouds and specification of cloud-top phase. *J. Atmos. Oceanic Tech.*, **16**, 1885-1899.

Menzel, W. P., and J. F. W. Purdom, 1994: Introducing GOES-I: The first of a new generation of geostationary operational environmental satellites. *Bull. Amer. Meteor. Soc.*, **75**, 757-781.

Moody J. L., A. J. Wimmers, and J. C. Davenport, 1999: Remotely sensed specific humidity: development of a derived product from the GOES Imager channel 3, *Geo. Phys. Res. Let.*, **26**, 59-62.

Prins, E. M., J. M. Feltz, W. P. Menzel, and D. E. Ward, 1998: An overview of GOES-8 diurnal fire and smoke results for SCAR-B and 1995 fire season in South America, *J. Geophys. Res.*, **103** (D24), 31821-31835.

Prata, A. J., 1989: Observations of volcanic ash clouds in the 10-12 µm window using AVHRR/2 data. *Int. J. Remote Sens.*, **10**, 751-761.

Realmuto, V. J., A. J. Sutton, T. Elias, 1997: Multispectral thermal infrared mapping of sulfur dioxide plumes: A case study from the East Rift Zone of Kilauea Volcano, Hawaii, *J. Geophys. Res.*, **102**, 15,057-15,072.

Schmetz, J., H. Woick, S. Tjemkes, and J. Rattenborg, 1998: From Meteosat to Meteosat Second Generation, Proceedings, *Ninth Conference on Satellite Meteorology and Oceanography*, Paris, France, Amer. Meteor. Soc., 335-338.

Schmit, T. J., E. M. Prins, T. J. Schreiner, and J. J. Gurka, 2001: Introducing the GOES-M Imager. Submitted to the *National Weather Association-Digest.*

Schreiner, A. J., D. A. Unger, W. P. Menzel, G. P. Ellrod, K. I. Strabala, and J. L. Pellett, 1993: A comparison of ground and satellite observations of cloud cover. *Bull. Amer. Meteor. Soc.*, 74, 1851-1861.

Soden, B. J., and F. P. Bretherton, 1993: Upper tropospheric relative humidity from the GOES 6.7 µm channel: Method and climatology for July 1987. *J. Geophys. Res.*, **98**, 16669-16688.

Strabala, K. I., S. A. Ackerman, and W. P. Menzel, 1994: Cloud properties inferred from 8-12 µm data. *J. Appl. Meteor*, **33**, 212-229.

Velden, C. S., T. L. Olander, and S. Wanzong, 1998a: The impact of multispectral GOES-8 wind information on Atlantic tropical cyclone track forecasts in 1995. Part I: dataset methodology, description, and case analysis. *Mon. Wea. Rev.*, **126**, 1202–1218.

Velden, C. S., T. L. Olander, and R. M. Zehr, 1998b: Development of an objective scheme to estimate tropical cyclone intensity from digital geostationary satellite infrared imagery. *Wea. Forecasting*, **13**, 172–186.

Vicente, G. A., R. A. Scofield, and W. P. Menzel, 1998: The operational GOES infrared rainfall estimation technique, *Bull. Amer. Meteor. Soc.*, **79**, 1883–1898.

Weldon, R. B, and S. J. Holmes, 1991: Water vapor imagery -- interpretation and applications to weather analysis and forecasting, NOAA Technical Report NESDIS 57.

Wu, Xiangqian, W. P. Menzel, and Gary S. Wade, 1999: Estimation of sea surface temperatures using GOES-8/9 radiance measurements. *Bull. Amer. Meteor. Soc.*, **80** (6), 1127-1138.

Wylie, D. P., and W. P. Menzel, 1999: Eight years of high cloud statistics using HIRS. *J. Climate*, **12**, 170-184.

P5.23

Simulation of GOES-M 5-band Imager Using MODIS Data For Volcanic Ash

Donald W. Hillger*
NOAA/NESDIS/ORA/RAMMT
CIRA / Colorado State University
Fort Collins CO

James Clark
NOAA/NESDIS/OSDPD/SSD
Satellite Analysis Branch
Camp Spring MD

1. Introduction

The next three satellites in the GOES series, GOES-M through O, with the first to be launched in 2001, will have slightly-changed Imager instruments, with a new band at 13.3 □m (Schmit et al 2001). The new band was introduced to improve cloud height determinations. Unfortunately this band is not an additional band. Instead, it replaces the 12.0 □m band currently used, along with the GOES longwave infrared band at 11 □m, to identify volcanic ash. This technique was pioneered by Prata (1989), but has been applied by many (Oppenheimer 1998; Ellrod et al 2001).

To simulate the effect of the new band on usage of GOES for volcanic ash detection, selected bands of Moderate Resolution Imaging Spectroradiometer (MODIS) data were used. Table 1 lists the GOES Imager band number arrangement. The new 13.3 □m band will be called band 6 even on the new 5-band arrangement (bands 1 through 4 and 6). The current 12.0 □m band will continue to be called band 5, to avoid confusion between band numbers on current and new versions of the GOES Imager.

Table 1: Simulation of GOES-M Imager using MODIS bands

GOES Imager		MODIS	
Band number	**Central wavelength (□m)**	**Band number**	**Central wavelength (□m)**
1	0.65	1	0.645
2	3.9	22	3.96
3	6.7	27	6.7
4	10.7	31	11.0
5	12.0	32	12.0
6	13.3	33	13.3

Table 1 also lists the MODIS bands that correspond to the six bands available between the two versions of the GOES Imager. MODIS contains 36 bands, and six of those bands have central wavelengths that correspond to the six GOES bands (bands 1, 22, 27, 31, 32, and 33 respectively). In general the MODIS bandwidths are narrower than those of the equivalent GOES bands, but simulating both the current and new bands using MODIS minimizes any differences this may cause.

2. Analysis Using Principal Components

To determine the effect of the change from band 5 to band 6 on GOES-M, that band was substituted into a volcanic ash product used operationally by the Washington Volcanic Ash Advisory Center (VAAC). That product consists of Principal Component Image (PCI) analysis of the three GOES thermal infrared bands (bands 2, 4, and 5). PCI analysis creates images that explain all of the variance in the original bands by separating the common from the difference information in the original bands (Hillger* 1996; Hillger and Ellrod 2001). PCI-1 contains the common signal from the three GOES bands that are input, generally cloud/no-cloud information. The band 2/4 (shortwave/longwave) difference usually seen in PCI-2 is useful for detecting volcanic hot spots, and the band 4/5 (split window) difference usually seen in PCI-3 is good for detecting volcanic ash.

Two test versions of the PCIs were generated, one using simulated current-GOES bands 2, 4, and 5;

* Corresponding author address: Dr. Donald W. Hillger, NOAA/NESDIS/RAMMT, CIRA/Colorado State University, Fort Collins CO 80523-1375. E-mail: hillger@cira.colostate.edu

and the other using simulated GOES-M bands 2, 4, and 6. The case for this study was a large eruption of ash on 20 December 2000 from the Popocatepetl volcano (hereafter abbreviated Popo, 19.02°N, 98.62°W) at 5426 m elevation near Mexico City. For this case MODIS data were available at 1715 UTC from the polar-orbiting EOS AM-1/Terra satellite. The MODIS data were analyzed at 2 km spatial resolution (at nadir) and afterward remapped into a GOES projection at 4 km resolution to match the ash analyses that are available for verification.

Figure 1 is an analysis issued by the Washington VAAC (Operations 1999) giving the extent of the ash plume based on GOES multi-spectral imagery for 1715 UTC. This analysis time matches the time of the MODIS imagery that was analyzed using PCIs. The ash extends mainly east and south of the volcanic source, to as far away as the Yucatan Peninsula. In the ash analysis the plume is given in two parts, at different flight levels (FL250 [25,000 ft / 7600 m] and FL320 [32,000 ft / 9800 m]). These levels were estimated by effectively matching the derived vector motion of the ash as seen in GOES imagery to the appropriate height levels from the Mexico City upper-air sounding and a model sounding. The extent of the ash in this analysis is a guide for the simulated GOES analyses to follow.

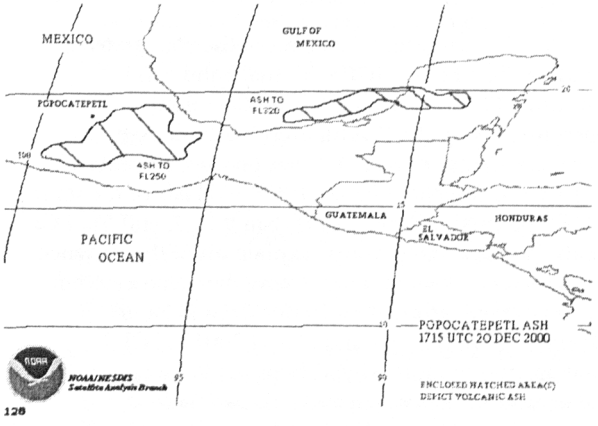

Figure 1: Volcanic ash analysis for 1715 UTC on 20 December 2000 for Popocatepetl volcano near Mexico City. Analysis based on GOES multi-spectral imagery by the Satellite Analysis Branch (SAB) Washington VAAC.

There was no volcanic hot spot detected for Popo for this case since clouds obscured the volcanic vent. Otherwise PCI-2 is often effective for detecting hot spots or thermal anomalies. Since PCI-2 is generally a longwave vs. shortwave band difference, the change from band 5 to band 6 does not cause a significant change in this PCI. Similarly PCI-1, since it shows the overall cloud setting common to all three infrared bands (and not any of the volcanic features that are often seen only in image differences), does not change much. Therefore the remainder of the discussion will focus on PCI-3, a product that will change primarily from a band 4/5 difference to a band 4/6 difference, with much less contribution from GOES band 2.

Figure 2 contains PCI-3 as it is now available from a simulation of current GOES Imager bands 2, 4, and 5. This multi-spectral image product generally depicts the volcanic ash very well. Ash is seen as white, in contrast to the image background and other image features. The ash is concentrated mainly to the east and southeast of Popo where there is a maximum in the ash signal. A secondary maximum exists to the east over the Yucatan Peninsula. Some ash can be seen connecting the two maxima, but that ash has much less contrast to the background of the image.

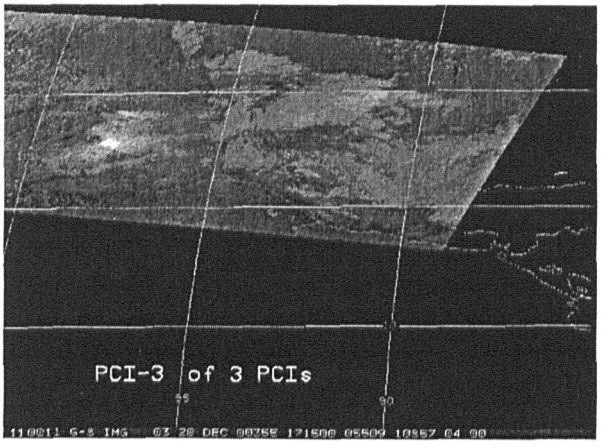

Figure 2: PCI-3 of three PCIs that were generated from a simulation of the three thermal infrared bands of GOES-8 through 11 (bands 2, 4, and 5) using MODIS data for 1715 UTC on 20 December 2000 over Popocatepetl volcano near Mexico City. PCI-3 shows the ash plume as white by heavily utilizing GOES band 5.

For comparison, Figure 3 is PCI-3 generated from simulated GOES bands 2, 4, and 6 in place of bands 2, 4, and 5 used in Figure 2. In this figure the densest part of the ash plume can still be seen east and south of Popo, including ash at the far eastward extent over the Yucatan. However, the immediate difference compared to the current version of PCI-3 in Figure 2 is the lessened contrast of the ash to the image background and the more significant contribution from clouds. These cloud features tend to obscure the ash

plume except at locations where the ash concentration is the greatest. The secondary maximum east off the coast of Yucatan easily seen in Figure 2 is hard to discern in this new image due to low clouds underlying the ash. This cloud contamination is a major drawback to this three-band product with the change in bands planned for GOES-M.

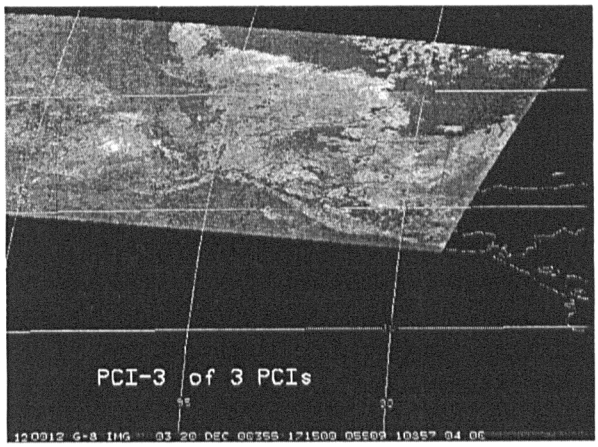

Figure 3: Same as Figure 2 except generated from a simulation of the three thermal infrared bands of GOES-M through O (bands 2, 4, and 6). PCI-3 shows only the parts of the ash plume where the ash is most concentrated, when compared to the current version of PCI-3 in Figure 2, and also suffers from contamination by low clouds.

In an attempt to isolate the cloud problem, the contributions of the bands to the current and new versions of the three-band product will be examined. Table 2 gives the contributions of the GOES bands to the PCIs for both current and new simulations of this volcanic ash case. In the new version of PCI-3, band 2 contributes 11% of the explained variance, compared to approximately 0% for the current version of PCI-3. If it is assumed that the cloud contamination is due to the increased contribution from GOES band 2 in PCI-3, the immediate thought for fixing the cloud contamination is to eliminate band 2 from the analysis to generate a two-band (band 4/6) difference image that may not suffer from this low-cloud contamination. The reasoning is that PCI-3 generated from current GOES bands 2, 4, and 5 is basically a two-band difference with little or no contribution from GOES band 2. When generated, the two-band difference is nearly identical to PCI-3 in Figure 2 and is therefore not shown.

Figure 4 is a two-band difference generated from simulated bands 4 and 6. This image product shows the ash plume only very faintly southeast of Popo where the ash concentration is the greatest. The two-band difference is not as good for ash detection as the three-band product in this case and continues to have significant cloud contamination. The clouds therefore are not due to the contribution from band 2, but are inherent in the difference between bands 4 and 6. Band 6 was added to detect clouds, the kind that are contaminating both the two-band and the three-band products in attempts to see volcanic ash. That cloud signal comes at the expense of detection of ash that is easily accomplished with the current split window bands. It is at least some consolation that PCI-3 generated from the new combination of bands (Figure 3), although inferior for ash detection to PCI-3 generated from the current combination of bands (Figure 2), is far superior to a two-band difference that uses the new band 6 (Figure 4).

Table 2: Contributions of MODIS-simulated GOES infrared bands to PCIs used for Volcanic Ash Detection

PCI	GOES-8 through 11 bands			GOES-M through O bands		
	Explained Variance (%) and Sign (negative contributions in parentheses) of GOES Band Contributions					
	2	4	5	2	4	6
1	46	26	27	37	22	41
2	54	(20)	(26)	52	~0	(48)
3	(~0)	53	(47)	(11)	78	(11)

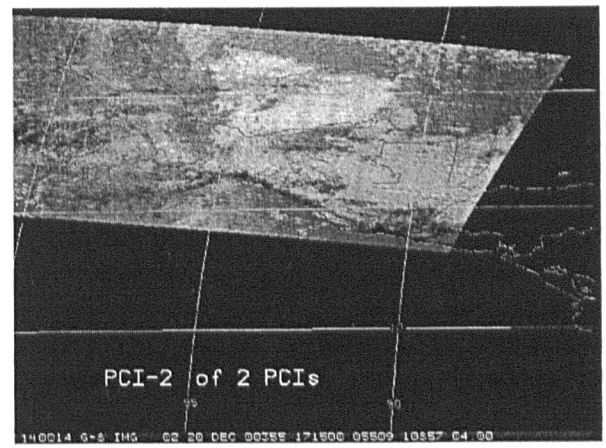

Figure 4: A two-band (band 4/6) difference image generated from a simulation of the two longwave infrared bands of GOES-M through O using MODIS data for 1715 UTC on 20 December 2000 over Popocatepetl volcano near Mexico City. This image product is far inferior for volcanic ash detection compared to the three-band product in Figure 3.

3. Summary and Conclusions

This study provided a simulated case using MODIS data where a two-band volcanic ash product (when differenced with GOES band 4) is not suitable for ash detection with the new GOES-M band 6 substituted for the current-GOES band 5. Rather, a three-band product of GOES-M bands 2, 4, and 6 depicts the ash plume better, although not as well as a similar three-band product generated from the current set of GOES infrared bands. The choice for the ash analyst is to either generate PCIs directly from the new set of GOES-M thermal infrared bands or utilize similarly-configured combinations of the three bands, as suggested by the assessed contributions of the bands to PCI-3. However the main drawback of the new band 6 remains, a greatly increased chance of contamination by clouds that can obscure the extent of the ash plume, causing decreased ability to monitor diffuse ash and increased chance of false ash detection.

Acknowledgements

The MODIS data for this study were provided by Chris Moeller of the CIMSS at the University of Wisconsin in Madison. Funding for this study is made available through NOAA Grant NA67RJ0152.

4. References

Ellrod, G.P., B.H. Connell, and D.W. Hillger, 2001: Improved volcanic ash detection using multi-spectral infrared satellite data. Submitted to *Journal of Geophysical Research: Solid Earth.*

Hillger, D.W., 1996: Meteorological analysis using principal component image transformation of GOES imagery. *International Radiation Symposium - IRS'96: Current Problems in Atmospheric Radiation,* (W.L. Smith and K. Stamnes, Editors; A. Deepak Publishing), 19-24 August, Fairbanks AK, 480-483.

Hillger, D.W., and G.P. Ellrod, 2001: Detection of unusual atmospheric and surface features by employing Principal Component Image transformation of GOES imagery, *Tenth Conference on Satellite Meteorology and Oceanography*, AMS, 9-14 January, Long Beach CA, 461-464.

Oppenheimer, C., 1998: Volcanological applications of meteorological satellites, *International Journal of Remote Sensing*, 19, 2829-2864.

Operations of the Washington Volcanic Ash Advisory Center, 1999: *Third Caribbean/South American Regional Air Navigation Meeting,* International Civil Aviation Organization, October 05-15, 5-p.

Prata, A.J., 1989: Observations of volcanic ash clouds in the 10-12 □m window using AVHRR/2 data, *International Journal of Remote Sensing*, 10, 751-761.

Schmit, T.J., E.M. Prins, A.J. Schreiner, and J.J. Gurka, 2001: Introducing the GOES-M Imager, Submitted to *National Weather Association Digest.*

P5.35

NOAA/NESDIS Operational Advanced-TOVS (ATOVS) Polar Orbiter Sounding Products

Anthony L. Reale
NOAA/NESDIS,Suitland, Maryland

Americo S. Allegrino
Raytheon Information Technology and Scientific Services, Lanham, Maryland

1.0 INTRODUCTION

Since 1979, the NESDIS operational sounding products from NOAA's polar orbiting satellites have provided a continuous suite of infrared and microwave radiation sounder measurements, and derived temperature and moisture sounding products on a global scale. These data represent a unique source of global, atmospheric, weather information, with a demonstrated positive impact on Numerical Weather Prediction (NWP) forecasts, NOAA's primary mission for sounding products. In May, 1998, the ATOVS instrument configuration onboard NOAA-15 was successfully deployed, followed by NOAA-16 in September, 2000. ATOVS consists of the new 15-channel Advanced Microwave Sounding Unit-A (AMSU-A), the new 5-channel AMSU-B for atmospheric moisture, the HIRS/3 and the AVHRR /3. ATOVS sounding products from NOAA-15 were operationally implemented by NESDIS in April, 1999 (Reale et al. 1999a and 1999b). AMSU-B processing was delayed until May, 2000 (Chalfant et al.1999 and Reale et al. 2000b). This report summarizes the ATOVS sounding product systems and scientific algorithms operated by NESDIS.

2.0 ATOVS SCIENTIFIC ALGORITHMS

Two product systems are currently operated, **ATOVS-A,** which processes sounding products using the HIRS, AMSU-A and AVHRR radiometers (Reale et al. 2000a), and **ATOVS-B,** which processes (moisture) sounding products using the AMSU-B radiometer (Chalfant et al. 1999). The scientific procedures for each system are comprised of two primary subsystems for **Orbital** and **Offline** support processing, respectively.

2.1 Orbital Processing

The orbital processing system consists of five steps:

- Preprocessing
- Radiance Temperature Adjustments
- Contamination Detection
- First Guess Computation
- Retrieval Computation

Preprocessing for each orbital system is done on the raw, level-1b satellite data. Preprocessing steps include the application of the calibration coefficients and, the computation of the radiance and radiance temperature measurements. In addition, preprocessing for ATOVS-B includes the correction of AMSU-B measurements for Radio Frequency Interference (RFI) from data transmitters onboard NOAA-15 (Atkinson 1999 and 2000). AMSU-B data from NOAA-16 have no RFI.

Limb adjustments are then applied to the calibrated, radiance temperature measurements from HIRS/3, AMSU-A and AMSU-B (Wark 1993 and Allegrino et al. 1999. The limb corrected measurements for AMSU-B are also adjusted to remove perceived bias relative to radiative transfer model calculations (Fleming et al. 1991).

The contamination detection step is done separately for microwave and infrared sensor data. Microwave contamination detection primarily consists of identifying localized anomalies in AMSU sounding channels sensitive in the lower troposphere typically due to precipitation and large ice particles (Grody et al. 1999). Infrared measurements are screened for cloud contamination by methods described in Ferguson and Reale, 2000.

The first guess computation is uniquely determined for each ATOVS-A and ATOVS-B sounding using a library search technique (Goldberg et al. 1988). The first guess libraries consist of collocated radiosonde and satellite observations, which are directly accessed during orbital processing and updated daily.

The matrix equation for the library search is given in (1):

$$D = (R - R_k)^t \; B^{-1} \; (R - R_k) \qquad (1)$$

where the subscript t indicates the matrix transpose and

D: scalar closeness parameter,
B: sounding channel radiance covariance matrix
R: adjusted, observed radiance temperature vector
R_k: adjusted, library radiance temperature vector

The first guess temperature, moisture and radiance temperature profiles for a given sounding are computed by averaging the 10 closest collocations; that is, those with the smallest "D". Radiosonde averages are used for temperature and moisture, and the adjusted

measurements from the sounder are averaged for radiance temperature.

In the retrieval step, the general form of the retrieval equation is given by (2):

$$T - T_g = C(R - R_g) \qquad (2)$$

where T and R are product and measurement parameters, the subscript "g" an apriori estimate, and C is the solution.

The ATOVS-A retrieval method is the Minimum-Variance-Simultaneous (MVS) solution (Smith et al. 1984 and Fleming et al. 1986) given by matrix equation (3):

$$\begin{aligned} T - T_g &= S A^t (A S A^t + N)^{-1} (R - R_g) \qquad (3) \\ &= X \quad (\quad Y \quad)^{-1} (R - R_g) \end{aligned}$$

where the subscript t indicates the matrix transpose, and:

T: final soundings products vector, (151),
T_g: first guess products vector, (151)
S: first guess covariance matrix, (151 x 151),
A: sounder channel weighting matrix, (35 x 151),
N: measurement noise covariance matrix, (35 x 35),
R: observed radiance temperature vector
R_g: first guess radiance temperature vector
X,Y: pre-computed retrieval operator components.

The product vector (T) contains 100 levels of atmospheric temperature (1000 mb to .1 mb), 50 levels of moisture (1000 mb to 200 mb), and the surface level. The dimension 35 for the A and N matrices denotes all the ATOVS channels; not all are used. The first guess and observed channels used in the retrieval solution, depend on the sounding type.

The ATOVS-B retrieval utilizes an ordinary least squares solution of equation 2, where:

T: water vapor mixing ratio sounding products vector
T_g: first guess mixing ratio vector
C: statistical regression coefficients
R: observed radiance temperature vector
R_g: first guess radiance temperature vector

The product vector (T) includes 15 levels of atmospheric moisture (1000 to 300 mb). Two sets of regression coefficients are available, for sea and non-sea soundings respectively.

The original calibrated sounder measurements, the adjusted sounder measurements, the first guess information, the derived temperature and moisture soundings and the appended ancillary data (i.e. cloud mask, AVHRR, SST, etc.) are operational products that are routinely distributed to users. The dedicated links for these data are NOAA-EMC, the United Kingdom Meteorological Office (UKMO) (Bracknell, England), the Global Telecommunications System (GTS) and the Shared Processing Network (SPN).

2.2 Offline Processing

The offline systems contribute the tuning and validation functions required to maintain the scientific integrity of the sounding products. Offline systems routinely compile and maintain data sets comprised of

- Satellite Radiance Databases
- Satellite and Radiosonde Collocations
- Coefficients

The Satellite Radiance Database Sets are separately maintained for HIRS/3, AMSU-A and AMSU-B radiometer data. These data sets contain adjusted and non-adjusted radiance temperature measurements for the respective instruments, typically spanning the latest 30 to 60 days. Each data set is updated at the conclusion of orbital processing at about a 50% sub-sampling rate, excluding polar-redundant and high terrain (>1000m) observations.

Collocated radiosonde and satellite observations are extensively used in the derivation and validation of the operational sounding products. The steps to compile and utilize collocated radiosonde and satellite observations include the radiosonde collocation processing and, updating the Matchup Data Bases (MDB) and the First Guess Libraries.

In the radiosonde collocation process, the radiosonde reports are processed daily. Accepted radiosonde reports are candidates for collocation with satellite data. A collocated radiosonde and satellite observation is compiled if the candidate radiosonde and satellite sounding data meet the criteria described in Tilley et. al., 2000.

The Matchup Data Bases (MDB), supporting the ATOVS-A and ATOVS-B products systems, respectively, provide the longer term data sets of radiosonde and satellite data collocations used for the tuning and validation of derived sounding products (Tilley et al. 2000 and Reale et al. 1990). Each MDB is updated daily. The ATOVS-A system maintains separate MDB's for clear and cloudy collocations, which are stratified among 23 geographical categories. On the other hand, the ATOVS-B system maintains a single MDB where collocations are stratified by sea and non-sea.

The First Guess Libraries are updated daily based on the MDBs, and directly accessed during orbital processing. The first guess libraries have about half of the capacity of the MDBs, with an additional requirement that the vertical extent of a candidate radiosonde report be complete from (at least) 950 mb to 50 mb for ATOVS-A, and from 950 mb to 400 mb for ATOVS-B, respectively. A new approach based on a statistical regression of the collocated AMSU-A measurements (Goldberg 1999) was deployed for

NOAA-15 during April 2000 to extend each radiosonde from the highest report level to .1 mb. The downward extension of a radiosonde is only required if the first significant level is between 950 and 1000 mb, and is done using a weighted, averaged, lapse rate and constant dewpoint depression for temperature and moisture, respectively, based on the lowest reported levels.

Various offline systems also compute coefficients for the derivation of operational sounding products. Coefficients are required for limb adjustment, cloud detection (Ferguson and Reale, 2000), the first guess (Goldberg et al. 1988), the retrieval (Fleming et al, 1986 for ATOVS-A and Goldberg et al. 1998 for ATOVS-B), AMSU-B radiance bias adjustment (Fleming et al. 1991 and McMillin et al. 1989, using the approach of Crone et al. 1996), and, RFI correction (AMSU-B for NOAA-15). Except for limb adjustment and RFI correction, all coefficients are updated weekly.

3.0 RESULTS

The scientific monitoring and evaluation of operational sounding products is maintained on a continuous basis at NESDIS. The primary evaluation strategy is the vertical accuracy statistics. Vertical accuracy statistics, based on satellite minus radiosondes differences computed from collocations stored on the MDB, are illustrated in Figures 1 and 2. These provide estimates of the expected performance of NESDIS operational soundings on a global scale. Figure 1 shows differences for ATOVS-A clear temperature soundings from the 60N to 60S latitude belt. Figure 3 shows differences for ATOVS-B moisture soundings for the 30N to 30S latitude belt. The thicker curves for each plot are for the final soundings, and the thinner lines for the corresponding first guess profiles, respectively. Figure 2 provides mean and standard deviation differences in degrees K, whereas the Figure 3 plots are percent differences in water vapor mixing ratio (g/kg), with the mean profiles used to compute percentages shown along the inside of the left axis. Pressure (mb) and sample size are indicated along the left and right vertical axis for all plots.

Figure 1 indicates that satellite minus radiosonde differences approach 2.5 K (RMS) near the surface and troposphere, 1.5 K in the middle troposphere where the sounders are most reliable, and about 2.0 K in the stratosphere. Little or no bias is present except at the tropopause. Figure 2 indicates expected uncertainties for moisture near the surface to be about 15 percent in the tropics. However, when multiplied by the mean mixing ratio values, the actual differences in water mixing ratio units is about 2 g/kg in the tropics. The steady increase in the percentage uncertainty of moisture with height is also attributable to the relatively low mixing ratio values aloft. Factoring in the spatial and temporal windows for each collocation, the inherent variability of moisture measurements, and radiosonde moisture errors, the accuracy estimates shown in Figure 2 are reasonable.

Significantly improved accuracy of the final soundings (thick curves) compared to the guess (thin curves) in Fig. 1 confirms the scientific approach, in particular, the consistency of the first guess radiance temperature and temperature observations provided for the retrieval step (Fleming et al. 1986).

4.0 FUTURE PLANS

The primary scientific activity planned over the next year is the merging of the ATOVS-A and B systems into a single, simultaneous, temperature and moisture products generation system. This will include studies to replace the library search with a statistical regression technique based on AMSU, and if successful, the replacement of pre-computed with real-time retrieval operators. Referred to as System-2002, the proposed upgrade would result in dual sounding products, consisting of climate oriented first guess information, and real-time weather oriented derived products, the later optimized for assimilation into NWP. There are also new requirements to provide ATOVS processing fall back contingencies, particularly in the event of a HIRS sounder failure

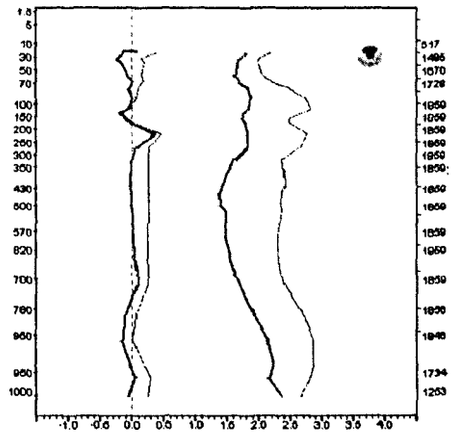

Figure 1: ATOVS-A Clear Statistics

Figure 2: ATOVS-B Tropical Statistics

5.0 REFERENCES

Allegrino, A., A.L. Reale, M.W. Chalfant and D.Q.Wark, 1999: Application of limb adjustment techniques for polar orbiting sounding data. Technical Proceedings of the 10th International TOVS Study Conference, Jan 26- Feb 2, Boulder, Colorado, USA., 1-10.

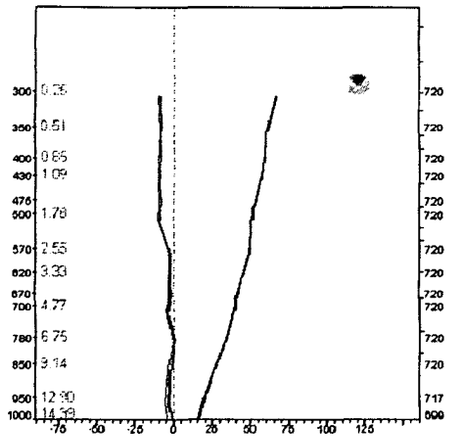

Atkinson, N.C., 2000: Calibration, monitoring and validation of AMSU-B. 33rd Committee on Space Research (COSPAR) Scientific Assembly, Warsaw, 16-23 July, to be published in Advances in Space Research.

Atkinson, N.C., 1999: Calibration and in-orbit performance of AMSU-B. Technical Proceedings of the ECMWF/EUMETSAT Workshop on Use of ATOVS Data for NWP Assimilation, 2-5 November, 105-108.

Chalfant, M.W., A. Reale, and F. Tilley, 1999: Status of NOAA Advanced Microwave Sounding Unit-B products. Technical Proceedings of the 10th International TOVS Study Conference, Jan 26- Feb 2, Boulder, Colorado, USA., 60-71.

Crone, L.J., L.M. McMillin, and D.S. Crosby, 1996: Constrained Regression in satellite meteorology. Journal of Applied Meteorology, AMS, Vol 35, No. 11, 2023-2035.

Ferguson, M.P., and A.L. Reale, 2000: Cloud detection techniques in NESDIS Advanced-TOVS sounding products systems. 10th Conference on Satellite Meteorology and Oceanography, 9-14 January, Long Beach, Ca., 252-254.e

Fleming, H.E., et. al., 1991: The forward problem and corrections for the SSM/T satellite microwave temperature sounder. IEEE Transactions on Geoscience and remote Sensing, Vol. 29, No. 4, 571-584.

Fleming, H.E., D.S. Crosby, and A.C. Neuendorffer, 1986: Correction of satellite temperature retrieval errors due to errors in atmospheric transmittances. Journal of Climate and Applied Meteorology, Vol 25, No. 6, 869-882.

Goldberg, M.D., 1999: Generation of retrieval products from AMSU-A: methodology and validation Technical Proceedings of the 10th International TOVS Study Conference, Jan 26- Feb 2, Boulder, Colorado, USA., 219-229.

Goldberg, M, J. Daniels and H. Fleming, 1988: A method for obtaining an improved initial approximation for the temperature/moisture retrieval problem. Preprints, 3rd Conference on satellite Meteorology and Oceanography, Anaheim, Ca, 16-19.

Goldberg, M.D., A. Reale and G. Kratz, 1998: The use of pattern recognition to derive SSM/T2 moisture retrievals. Adv. Space res., Vol. 21, 385-398.

Grody, N., et. al., 1999: Applications of AMSU for obtaining water vapor, cloud liquid water, precipitation, snow cover and sea ice concentration. Technical Proceedings of the 10th International TOV Study Conference, Jan 26- Feb 2, Boulder, Colorado, 230-240.

McMillin, L.M., L.J. Crone and D.S. Crosby, 1989: Adjusting satellite radiance by regression with an orthogonal transformation to a prior estimate. Jour. Appl. Meteor., Vol 28, No 9, 969-975.

Reale, A.L., M.W. Chalfant, and L.M. Wilson, 2000a: NESDIS advanced TOVS sounding products. 10th Conference on Satellite Meteorology and Oceanography, 9-14 January, Long Beach, Ca., 259-262.

Reale, A.L., M.W. Chalfant, and F.H. Tilley, 2000b: NESDIS moisture sounding products from AMSU-B and SSM/T2. 10th Conference on Satellite Meteorology and Oceanography, 9-14 January, Long Beach, Ca., 263-266.

Reale, A., M. Chalfant and L. Wilson, 1999a: Scientific status of NOAA advanced TOVS sounding products. Technical Proceedings of the 10th International TOVS Study Conference, Jan 26- Feb 2, Boulder, Colorado, USA., 437-448.

Reale, A., M. Chalfant and L. Wilson, 1999b: Scientific status of NESDIS advanced TOVS sounding products. Technical Proceedings of the ECMWF/EUMETSAT Workshop on Use of ATOVS Data for NWP Assimilation, 2-5 November, 1999, 153-160.

Reale, A., H. Fleming, D. Wark, C. Novak, M. Gelman, F. Zbar, J. Neilon, and H. Bloom, 1990: Baseline upper air network final report. NOAA Technical Report NESDIS 52, U.S. Dept. Of Commerce, Washington D.C., 57 pp.

Smith, W.L., H.M. Woolf, C.M. Hayden, D.Q. Wark, A.J. Schreiner and J.F. LeMarshall, 1984: The physical retrieval TOVS export package. Proc. Of the First International TOVS Study Conference, Madison, Wi., Cooperative Institute for Meteorological Satellite Studies, 227-278.

Tilley, F.H., M.E. Pettey, M.P. Ferguson, and A.L. Reale, 2000: Use of radiosondes in NESDIS advanced-TOVS (ATOVS) sounding products. 10th Conference on Satellite Meteorology and Oceanography, 9-14 January, Long Beach, Ca., 255-258.

Wark, D.W., 1993: Adjustment of TIROS operational vertical sounder data to a vertical view. NOAA Technical Report NESDIS-64, U.S. Dept. Of Comm., Washington D.C., 36 pp.

P5.38

RETRIEVAL OF ATMOSPHERIC INVERSIONS USING GEOSTATIONARY HIGH-SPECTRAL-RESOLUTION SOUNDER RADIANCE INFORMATION

Jun Li
Cooperative Institute for Meteorological Satellite Studies (CIMSS)
University of Wisconsin-Madison

Timothy J. Schmit
NOAA/NESDIS, Office of Research and Applications, Advanced Satellite Products Team (ASPT)

Hung-Lung Huang, and Harold M. Woolf
Cooperative Institute for Meteorological Satellite Studies (CIMSS)
University of Wisconsin-Madison, Madison, WI

1. INTRODUCTION

The era of high-spectral-resolution radiance measurements from the geostationary perspective is approaching. The first instrument to usher in this new era is the experimental Geosynchronous Imaging Fourier Transform Spectrometer (GIFTS), which is to be followed by an operational Advanced Sounder Baseline (ABS). The advanced sounders will have thousands of channels with widths on the order of single wavenumbers, while the current GOES Sounder (Menzel and Purdom, 1994) has only 18 bands with widths on the order of tens of wavenumbers. High-spectral-resolution sounder measurements from geostationary orbit will allow for monitoring the evolution of temperature and moisture inversions in clear skies. The current GOES sounder radiance measurements are, in general, not able to depict atmospheric inversion structure because of their lower spectral-resolution. Being able to characterize inversions is important for many reasons, including the detection of severe weather potential and possible fog formation, numerical model initialization, and sounding retrieval. High-spectral-resolution sounder radiances, as well as current GOES sounder radiances, will be simulated, with instrument noise included, for a number of radiosonde profiles with varying inversion strengths. A physical retrieval algorithm will be employed to retrieve temperature and moisture profiles with both sounders. The retrievals will be compared to the true profiles that were used to create the radiances in order to determine the strength of an inversion that can be retrieved from both current and the next-generation geostationary radiances.

Corresponding author address: Jun Li, Space Science and Engineering Center, Uiniversity of Wisconsin-Madison, 1225 West Dayton Street, Madison, WI 53706; e-mail: JunL@ssec.wisc.edu

2. RETRIEVAL SIMULATIONS

A fast and accurate transmittance models called Pressure Layer Optical Depth (PLOD) or Pressure layer Fast Algorithm for Atmospheric Transmittances (PFAAST) (Hannon et al. 1996) is used for the Advanced Baseline Sounder (ABS) or Cross-track Infrared Sounder (CrIS) (Bloom, 2001) simulations. The calculations are made at 101 pressure levels (0.01–105 kPa) and take into account the satellite zenith angle, absorption by well-mixed gases (including nitrogen, oxygen, and carbon dioxide), water vapor (including the water vapor continuum), and ozone.

A two-step algorithm, a Principle Component Regression (PCR; Huang and Antonelli 2001) followed by a non-linear physical retrieval method (Li and Huang 1999; Li et al. 2000), will be adopted for retrieval of atmospheric temperature and moisture profiles from ABS or CrIS simulated radiances which are added with the instrument noise. The regression retrieval serves as the first guess (or background) in the physical retrieval. PCR uses the projections of the predictor

variables (brightness temperature) onto a subset of principle components. Once a first guess is obtained from a numerical model forecast or generated from the regression technique described above, a non-linear iterative procedure is applied to the radiative transfer equation to further improve the profiles. Approximately half of the channels (optimal channels) are used in the physical retrieval procedure.

A data set containing more than 6000 global radiosonde profiles between 65S and 65N latitude is used for ABS retrieval simulation. 90% of the profiles are used for training - to create the regression coefficients, while the remaining 10% of the profiles are used to test the retrieval performance. The radiative transfer calculations of the ABS spectral band radiances are performed for each profile from the training data set to provide a temperature-moisture-ozone profile/ABS radiance pair for use in the statistical regression analysis. The ABS instrument noise is added into the calculated spectral band radiances. The eigenvector or Empirical Orthogonal Function (EOF) regression equation is then generated based on these calculated radiances and the matching atmospheric profiles. To complete the regression retrieval, the regression equation can be applied to the ABS independent radiances to obtain the estimated atmospheric profile retrieval, the regression retrieval is further updated with the nonlinear physical retrieval procedure. Comparison between the true and retrieved profiles gives the accuracy of retrieval performance.

3. RESULTS

Figure 1 shows an example of CrIS brightness temperature spectra and GOES band brightness temperatures (lower panel) calculated from profile with low level temperature inversion. The ABS Technical Requirement Document (TRD) noise (upper panel) is included in the CrIS radiances, while the GOES-8 spec noise is added in the GOES radiances. It can be see that the temperature inversion signal is well depicted by the CrIS spectra, while it is smoothed by the GOES brightness temperatures due to the low spectral resolution of the current GOES sounder. Figure 2 shows the true atmospheric temperature profile used in the simulation, the CrIS and GOES retrieved temperature profiles. Since CrIS spectra is able to well reflect the atmospheric inversion signal, significant improvement of CrIS low level temperature retrieval over the GOES sounder retrieval is found.

Figure 3 is the 1km vertical resolution temperature RMS (left panel) and 2km vertical resolution water vapor mixing ratio RMS (right panel) from the 605 independent profile retrievals with EOF regression physical procedures. There is substantial improvement of physical retrieval procedure over the EOF regression procedure for the boundary layer temperatures, while the accuracy of moisture retrievals is significantly improved from the physical procedure over the EOF regression procedure (2 ~ 5% improvement for atmospheric water vapor mixing ratio). Figure 4 shows the residual RMS from the EOF regression first guess profiles, the physical retrieval profiles, along with instrument noise (NEDT RMS). It can be seen that the EOF regression first guess fits the radiances very well (the residual is close to the instrument noise) in the longwave CO_2 region, this is due to the fact that CO_2 absorption region's radiances are more linear to atmospheric temperature profile since there is only CO_2 absorption in that region. For the longwave window region and the midwave water vapor region, the radiances are highly nonlinear to the water vapor mixing ratio. The regression first guess is not able to fit the observed radiances, while the nonlinear physical approach can reduce the first guess residual to the noise level in those spectral regions.

4. CONCLUSIONS

Retrievals from simulated CrIS radiances with the ABS TRD noise indicates that

(1) Nonlinear physical retrieval procedure improves eigenvector regression derived first guess profile, especially for atmospheric moisture profile;
(2) Simulations from CrIS radiances demonstrates that the next GOES advanced sounder (ABS) meets the NWS requirement for atmospheric profile products (1K of temperature for 1km vertical resolution and 15% of

water vapor mixing ratio for 2km vertical resolution);

(3) The ABS is able to depict the atmospheric temperature inversion structure on which the current GOES sounder has limited information.

5. REFERENCES

Bloom, H. J., 2001: The Cross-track Infrared Sounder (CrIS): A sensor for operational meteorological remote sensing, Technical Digest of Optical Remote Sensing of the Atmosphere, 74-76, February 5-8, 2001, Coeur d'Alene, Idado.

Hannon, S., L. L. Strow, and W. W. McMillan, 1996: Atmospheric infrared fast transmittance models: A comparison of two approaches. *Proceedings of SPIE*, 2830, 94-105.

Huang, H. L., and Antonelli, 2001: Application of principal component analysis to high-resolution infrared measurement compression and retrieval, *J. Appl. Meteor.* 40, 365-388.

Li, J., and H. L. Huang, 1999: Retrieval of atmospheric profiles from satellite sounder measurements using the discrepancy principle. *Appl. Optics*, 38, 916-923.

Li, J., W. Wolf, W. P. Menzel, W. Zhang, H.-L. Huang, and T. H. Achtor, 2000: Global soundings of the atmosphere from ATOVS measurements: the algorithm and validation. *J. Appl. Meteor.* 39, 1248 - 1268.

Menzel, W. P., and J. F. W. Purdom, 1994: Introducing GOES-I: The first of a new generation of geostationary operational environmental satellites. *Bull. Amer. Meteor. Soc.*, **75**, 757-781.

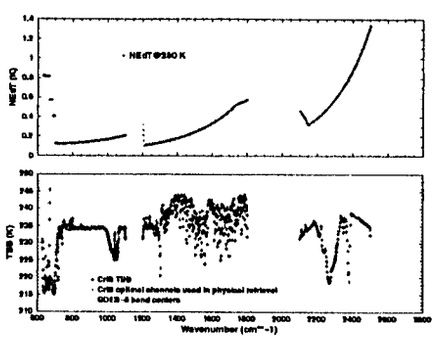

Figure 1, CrIS brightness temperature spectra and GOES band brightness temperatures (lower panel) calculated from profile with low level temperature inversion. The ABS TRD noise (upper panel) is included in the CrIS radiances, while the GOES-8 spec noise is added in the GOES radiances.

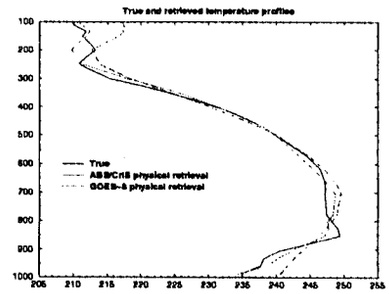

Figure 2, the true atmospheric temperature profile used in the simulation, along with the CrIS and GOES retrieved temperature profiles.

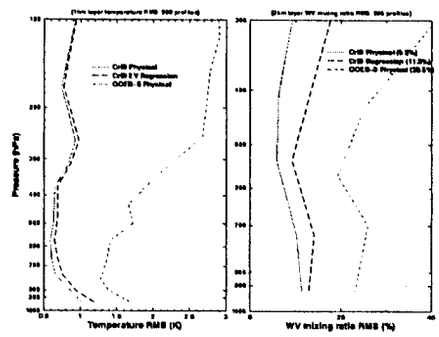

Figure 3, 1km vertical resolution temperature RMS (left panel) and 2km vertical resolution water vapor mixing ratio RMS (right panel) with EOF regression physical procedures (CrIS and GOES).

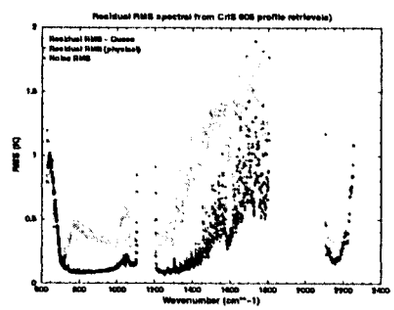

Figure 4, the CrIS residual RMS from the EOF regression first guess profiles, the physical retrieval profiles, along with instrument noise (NEDT RMS).

A METHOD FOR CORRELATED NOISE MODELING IN SATELLITE RADIANCE SIMULATION

Thomas J. Kleespies
David Crosby
NOAA/NESDIS
Thomas.J.Kleespies@noaa.gov

1. INTRODUCTION

This work is motivated by an Observing Systems Simulation Experiment in which NESDIS is collaborating with NCEP/EMC and the NASA Data Assimilation Office. The immediate goal is to determine the incremental improvement on the forecast of a Doppler Wind Lidar instrument over present day observing systems. In order for the current satellite instruments to be accurately simulated, it is necessary to model instrument noise, both independent and correlated. This paper presents such a method, and notes a high level of correlation in the inter channel noise in one of the High Resolution Infrared Sounder (HIRS) instruments.

2. METHODOLOGY

A number of standard methods of modeling correlated noise are available. We chose one such method presented in Searle (1982). Let S be the sample covariance matrix from the measured noise, then the vector of simulated correlated noise is given by

$$Y = G\sqrt{\Lambda}X \qquad 1)$$

where
G is the eigenvectors of S
$\sqrt{\Lambda}$ is a matrix whose diagonal is composed of the square root of the eigenvalues of S
X is a vector of gaussian random numbers with mean =0.0, variance=1.0

The sample of the measured noise is from HIRS space calibration observations for an entire day. An example of inter channel noise for NOAA 11 is given in figure 1. The gaussian random numbers are computed by (Box and Muller, 1958),

$$x = (-2\ln U_1)^{1/2}\cos(2\pi U_2) \qquad 2)$$

where U_1 and U_2 are numbers drawn from a uniform random distribution. We used the FORTRAN RAN function for this purpose. This approach was applied to a realization of size 100,000 and the inter channel correlation coefficients were computed. Results for selected channel pairs are presented in Table 1.

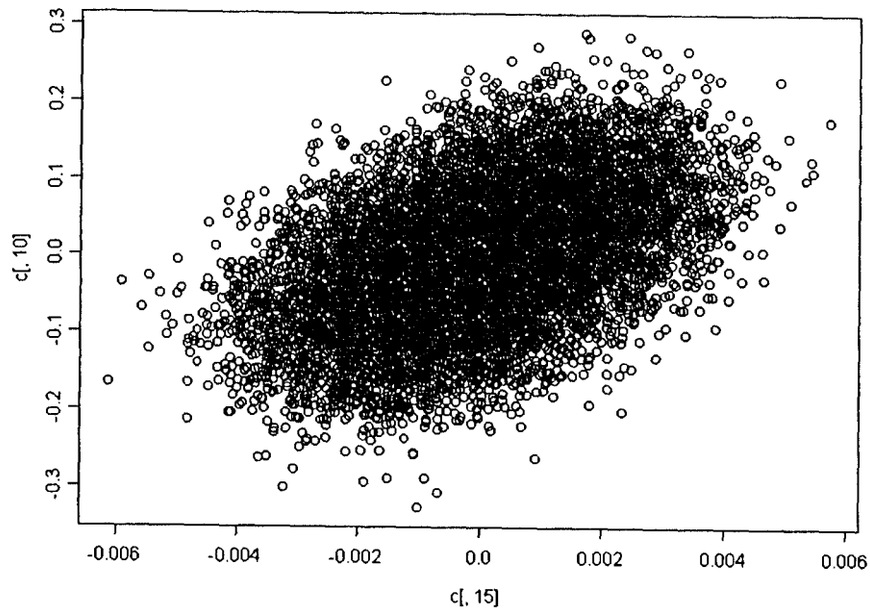

Figure 1. HIRS 11 Space calibration radiances, Ch 10 vs Ch 15, n=16032, r=.492
units are mw /(cm^2 sr cm^{-1})

NOAA 11 N=100000		Observed	Simulated
Chan	Chan	r	r
6	4	0.487	0.481
9	2	0.408	0.410
9	8	0.428	0.430
11	5	0.483	0.481
11	8	-0.409	-0.413
12	10	-0.434	-0.436
13	4	-0.417	-0.418
14	10	-0.438	-0.438
14	11	0.475	0.474
15	10	0.492	0.495
15	11	-0.417	-0.416
15	14	-0.462	-0.464
17	4	0.416	0.415
17	13	-0.411	-0.411

Table 1. Correlation coefficient for selected channels of NOAA 11 HIRS observed and simulated space calibration observations.

3. CONCLUSIONS

We have presented a method for simulating correlated noise and applied it to radiances from the NOAA 11 HIRS instruments. This method accurately reproduces the observed correlation structure. The NOAA 11 HIRS exhibits inter channel noise correlations that approach 0.5 . This fact has implications for the use of off diagonal elements in the observational error covariance matrix used in variational data assimilation.

4. REFERENCES

Box, G. E. P. and M. E. Muller, 1958: A note on the generation of random normal deviates. Annals of Mathematical Statistics, 29, pp 610-611.

Searle, S. R., 1982: Matrix Algebra Useful for Statistics, Ch. 13, Wiley&Sons.

AN IMPACT STUDY OF FIVE REMOTELY SENSED AND FIVE IN-SITU DATA TYPES IN THE ETA DATA ASSIMILATION SYSTEM

Tom H. Zapotocny*, W. Paul Menzel, James P. Nelson III and James A. Jung
Cooperative Institute for Meteorological Satellite Studies
University of Wisconsin-Madison

1. INTRODUCTION

The primary role of geostationary and polar orbiting satellites in the atmospheric sciences is to provide frequent observations over a large geographical extent. In otherwise data sparse maritime regions, satellite observations have become the primary source of information. Currently the National Environmental Satellite, Data, and Information Service (NESDIS) produces hourly Geostationary Operational Environmental Satellite (GOES) temperature and moisture retrievals, as well as temperature profiles down to cloud top from the TIROS Operational Vertical Sounder (TOVS) and vertically integrated precipitable water from the Special Sensor Microwave/Imager (SSM/I). These three satellite systems provide a wealth of nearly continuous remotely sensed data, which generously supplements in-situ data.

In order to assess the quality of such satellite data, the Cooperative Institute for Meteorological Satellite Studies (CIMSS) acquired the complete Eta Data Assimilation/Forecast System (EDAS) (Black 1994) from the National Centers for Environmental Prediction (NCEP). A primary goal of the CIMSS EDAS effort is to maintain a system that, except for horizontal and vertical resolution, is consistent with the operational EDAS. The CIMSS EDAS is used in coordination with NCEP personnel for investigating the impact of current and planned satellite data sources on NWP forecasts.

This paper describes the results of an experiment utilizing the EDAS to study the 24-hr forecast impact of five remotely sensed and five in-situ data types during 11-day periods for three seasons and is a follow-on to Zapotocny et al. (2000). The three 11-day periods are 13-23 December 1998, 10-20 April 1999, and 13-23 July 1999.

This extended length study involves running the EDAS repeatedly on the same cases with varied sets of input data. A control run utilizes all EDAS data types. Separate experiments, with one of the ten data types denied in each, were then run. Summing the difference between the control and experimental runs for the multiple time periods yields a measure of the forecast impact from each data type.

2. EXPERIMENTAL DESIGN

The five remotely sensed data types studied are SSM/I vertically integrated precipitable water (SSM/I), TOVS temperature profiles down to cloud top (TOVCD), GOES Sounder three layer clear air precipitable water (GOESPW), GOES Imager infrared cloud drift winds (GOESCD), and GOES Imager cloud top water vapor winds (GOESWV). All five of these data types are used only within a marine environment within the EDAS. The five in-situ data types analyzed are rawinsonde temperature and moisture observations (RAOBM), Aircraft Communications Addressing and Reporting System (ACARS) temperature data (ACARM), rawinsonde wind observations (RAOBW), ACARS wind observations (ACARW), and surface land observations of pressure, temperature and moisture (SFCLM).

For this three season experiment, a total of 726 separate EDAS runs were required to isolate the contributions from all data types examined (10 denials plus a control run for 66 time periods). The operational EDAS was executing at a resolution of 32 km during all three 11-day time periods studied. However, initial model conditions in the experiments reported here were obtained from an 80 km horizontal resolution, 38 level vertical resolution EDAS which was also being executed at NCEP twice-daily "parallel" to the 32 km operational EDAS. All 726 EDAS runs performed herein were also run with a 80 km, 38 level EDAS. Furthermore, while the experiments were run on the native 80 km Eta grid, all results were interpolated to, diagnosed and displayed on the 80 km NGM Super C grid. Horizontal and vertical interpolations of the Eta model variables to isobaric surfaces and the C grid were performed within the Eta post-processor (Treadon 1993). Presenting results on isobaric surfaces should be more amenable to most readers, and removes the horizontal staggering of variables on the Eta model E grid. Finally, it is important to note that the 80 km results presented here may not be applicable to higher operational resolutions.

The RMS forecast impact (FI) of an individual data type is evaluated as the RMS error of the denied forecast minus the RMS error of the control forecast. Dividing this difference by the RMS error of the control forecast and multiplying by 100 normalizes the results and provides a percent improvement with respect to RMS FI. A positive FI means the forecast is better with the data type included than with it denied. The time-averaged 24-hr FI diagnostics exclude the first day of each 11-day period, removing more impact of the denied data type from the first guess.

All three 11-day periods used in this study were run with the EDAS operating in "full-cycling" mode. This

* Corresponding author address: Tom H. Zapotocny, Univ. of Wisconsin-Madison, 1225 W. Dayton St. Madison, WI 53706; email: tomz@ssec.wisc.edu.

involves denying the particular data type for 11 consecutive days and carrying the results of each 12-hr assimilation cycle forward to the starting point for the next 12-hr assimilation. This mode of operation was chosen to duplicates the NCEP twice-daily run cycle.

For completeness, diagnostic evaluations use both the entire horizontal model domain as represented by the 104 grid and a subsection closely outlining CONUS The entire domain diagnostics show data effects over large geographical distributions, while the CONUS subsection reduces the impact lateral boundary conditions play as the forecast proceeds and avoids possible problems with temporally-correlated observation errors from remotely sensed data.

3. RESULTS

In these experiments data were assimilated via 3DVAR at T-12, T-9, T-6, T-3, and T-0, using 3-hour Eta model forecasts between each assimilation step. Differences between the various time-averaged forecast runs and the control forecast run provide a measure of the FI of the EDAS to each data type. In the bar charts that follow, the five isobaric levels for each data type proceed from 300 hPa on the left to 1000 hPa on the right. Moreover, grid points on isobaric surfaces underground are not used in the diagnostics.

3.1. The 24-hr domain wide RMS FI statistics

Figure 1 presents a three season summary of the three 11 day time periods and indicates that nearly all data types provide a positive FI. In fact, only the 300 hPa u-component FI from SSM/I is negative for the 60 time period summation. Except for the u-component, RAOBM provides the largest positive FI by level and field on a fairly regular basis. However, because of their large July values, the precipitable water data types of SSM/I and GOESPW provide relatively large cumulative positive contributions to relative humidity at and above 850 hPa. GOESCD and RAOBW contributions, which are fairly uniform from season to season (not shown), also make relatively large positive FIs to all three fields. Of these ten data types, GOESWV and ACARM regularly provide the smallest overall FI for each of the three fields; however, even their contributions are slightly positive when summed over the three periods.

In general, it was found that the cumulative impact of most in-situ data types decreased in summer relative to winter. The opposite was true for the remotely sensed data types (not shown).

The only data type to have its largest three time period positive FI at 1000 hPa is the SFCLM temperature data type. The generally small 1000 hPa FI results are not surprising. Levels that close to the earth's surface are dominated by the physical parameterizations of sensible and latent heat addition, skin friction, and stronger PBL effects, all of which will tend to quickly drive the state fields to the same general solution, no matter what data type has been denied.

3.2. The 24-hr CONUS RMS FI statistics

This subsection examines the 24-hr FI results within a subsection closely outlining CONUS and a small percentage of adjacent coastal waters. CONUS subsection results are presented for two reasons. First, since the COUNUS subsection is far removed from the EDAS domain boundaries, the impact of the lateral boundary conditions is reduced as the forecast proceeds. Second, use of the CONUS subsection reduces the problem of temporally-correlated observation errors with remotely sensed data. The subsection used is approximately 84% land covered, compared with the entire domain being approximately 70% water covered. Finally, note that the CONUS bar charts use the same y-axis scales as the entire domain results of Fig. 1.

With respect to temperature impact (Fig. 2A), the two upper levels of RAOBM are the largest positive contributors, with impacts of 6 to 10%. Interestingly, one of the largest negative contributors to temperature forecast impact exists for RAOBM at 1000 hPa. RAOBW is the second largest overall contributor with GOESCD, ACARW and GOESPW the next largest contributors. The remaining five data types (SSM/I, TOVCD, GOESWV, ACARM, and SFCLM) cumulatively all have small positive or negative FI contributions to the temperature forecast.

For the five levels displayed, RAOBW cumulatively has the largest positive contribution to the u-component (Fig. 2B), with its most positive contributions at and above 700 hPa. The next three largest contributors cumulatively are RAOBM, GOESCD and ACARW. The GOESCD contributions are fairly uniform at each of the five levels, in contrast to RAOBW, RAOBM and ACARW. The six remaining data types (SSM/I, GOESPW, TOVCD, GOESWV, ACARM, and SFCLM) all show small positive or negative FI contributions in the CONUS subsection.

RAOBM provides the largest cumulative positive FI for relative humidity (Fig. 2C). GOESCD, RAOBW and GOESPW are the next largest contributors. The remaining six data types provide very small contributions either way.

A comparison of the in-situ domain wide results (Fig. 1) and the CONUS subsection results (Fig. 2) reveals that the positive contribution from RAOBW is similar in a cumulative sense over both diagnostic domains. However, all other data types provide smaller FI in the subsection than over the entire domain. There are also more negative FIs in the subsection than in the entire domain.

Finally, from a remotely sensed perspective, it is interesting to note that in both the subsection and entire domain the GOESWV impacts are less than the GOESCD impacts, even though they use identical observational error weights and are somewhat redundant spatially. A long-standing concern, which could help explain the different impacts, revolves around

the different height assignment methods used for infrared cloud drift winds and water vapor cloud top winds. Velden et al. (1998) and Rao et al. (2000) provide detailed descriptions of the error characteristics and on how the height assignment is made for both of these remotely sensed data sets. The vertical distribution of these data types is also a key contributor. GOESCD infrared data tends to span the troposphere, with relative density maxima at cirrus level and stratus level. However, GOESWV data is predominately located between 350 and 200 hPa (Velden et al. 1997). As such, since GOESCD samples low level information, it tends to capture trade wind easterlies and open celled cumulus that GOESWV cannot. A final factor is the amount of data. GOESCD typically has more observations than GOESWV for most time periods.

4. SUMMARY

This paper summarizes the 24-hr forecast impacts (FIs) of five remotely sensed satellite data types and five in-situ data types in the Eta Data Assimilation System during 11-day periods in a winter, summer and transition season. The five satellite data types are used only in a marine environment and are SSM/I vertically integrated precipitable water (SSM/I), GOES sounder three layer clear air precipitable water (GOESPW), TOVS temperature profiles down to cloud top (TOVCD), GOES imager infrared cloud drift winds (GOESCD), and GOES imager cloud top water vapor winds (GOESWV). The five in-situ data types are rawinsonde temperature and moisture (RAOBM), rawinsonde winds (RAOBW), aircraft temperatures (ACARM), aircraft winds (ACARW) and surface land observations (SFCLM). The three 11-day periods are 13-23 December 1998, 10-20 April 1999, and 13-23 July 1999. FI statistics are presented for three standard meteorological fields, at each of five isobaric levels over both the entire domain and CONUS. The fields consist of temperature, u-component of the wind and relative humidity. While only the u-component statistics are presented, the v-component FI statistics were found to be very similar.

The domain wide 24-hr FI results (Fig. 1) indicate that all of the data types provided some positive impact. RAOBM cumulatively had the largest positive contribution, with GOESCD another consistent contributor throughout. The precipitable water data types of SSM/I and GOESPW had the most positive FI during summer in terms of relative humidity, but their importance was reduced during winter (not shown). GOESWV and ACARM had the smallest cumulative impact of all ten data types, with their overall contribution being just slightly positive.

While the positive FIs are termed modest for all data types, it is important to note that very few negative FIs were observed in the domain wide diagnostics, even when examining individual time periods (not shown). Finally, also while not shown, it is important to note that the cumulative impact of most in-situ data types decreased in summer relative to winter, while the opposite was true for the remotely sensed data.

In the CONUS subsection (Fig. 2), the overall importance of in-situ data were larger than the remotely sensed data for most data types. RAOBW provided the most consistently positive FI from season to season, while the importance of RAOBM dropped dramatically from winter to summer (not shown). The most consistently positive FI from the remotely sensed data season to season was from GOESCD; however, GOESPW had some of the largest positive impacts in July of any data type for relative humidity (not shown). Overall, the number of negative FIs was found to be larger in the CONUS subsection than the entire domain for both the in-situ and remotely sensed data.

Several future studies could prove to be very beneficial. First, would a similar study of data in global models reveal the same results? Second, what is the impact of using radiances versus retrievals in operational models? In any event, a more complete understanding of how to utilize existing and future data types is required if modeling improvements related to the available data are to be realized.

5. REFERENCES

Black, T. L., 1994: The new NMC mesoscale Eta model: Description and forecast examples. *Wea. Forecasting*, **9**, 265-278.

Rao, P. A., Z.-X. Pu, S. A. Braun, and C. S. Velden, 2000: Error characteristics of satellite derived water vapor winds as compared to ECMWF model analyses. Preprints, *10th Conf. on Satellite Meteorology and Oceanography*, Long Beach, CA, Amer. Meteor. Soc., 16-19.

Treadon, R., 1993: The NMC Eta model post processor: A documentation. Office Note 394, National Oceanic and Atmospheric Administration, 42 pp. [Available from NASA Goddard Space Flight Center, Wallops Flight Facility, Wallops Island, VA 23337.]

Velden, C. S., S. J. Nieman, W. P. Menzel, and S. T. Wanzong, 1997: Upper-tropospheric winds derived from geostationary satellite water vapor observations. *Bull. Amer. Meteor. Soc.*, **78**, 173-195.

Velden, C. S., T. L. Olander, and S. T. Wanzong, 1998: The impact of multispectral GOES-8 wind information on Atlantic tropical cyclone track forecasts in 1995. Part I: Dataset methodology, description and case analysis. *Mon. Wea. Rev.*, **126**, 1202-1218.

Zapotocny, T. H., and Coauthors, 2000: A case study of the sensitivity of the Eta data assimilation system. *Wea. Forecasting*, **15**, 603-621.

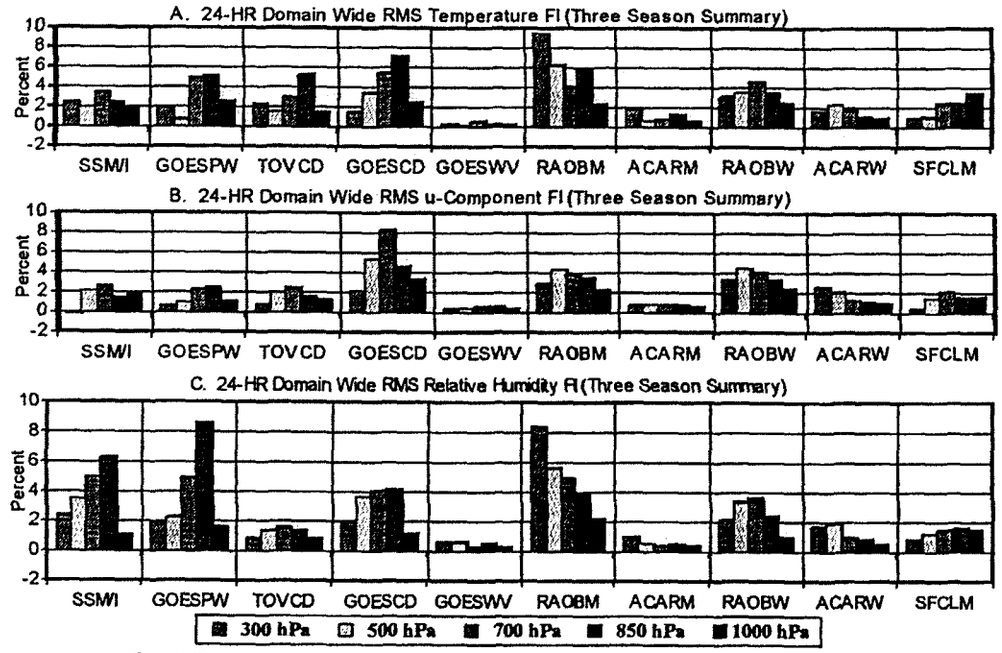

Fig. 1. Entire domain FI (%) of the ten data types after 24-hrs of ETA model integration.

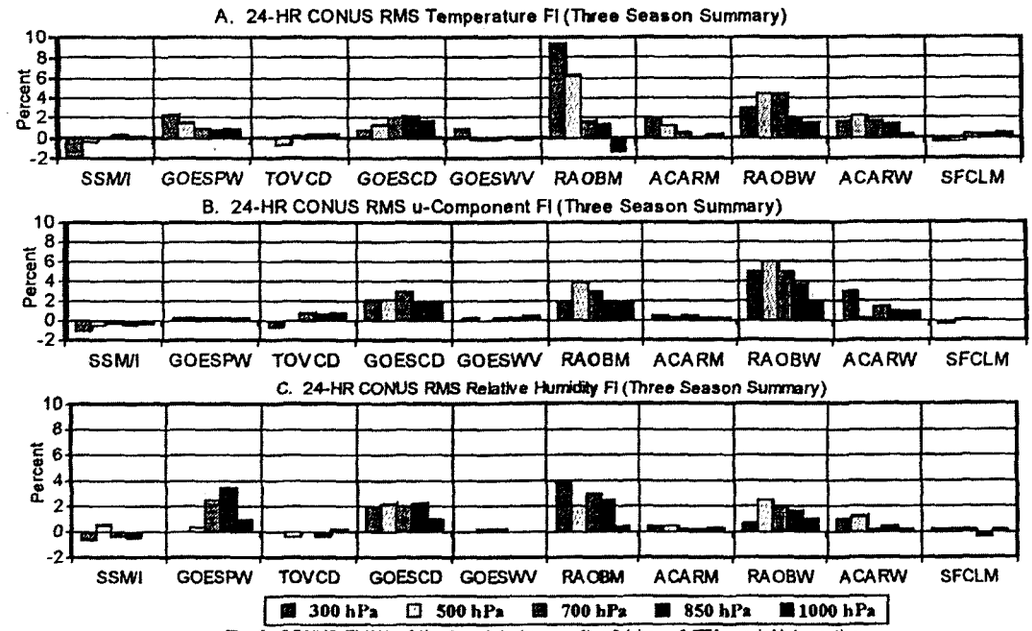

Fig. 2. CONUS FI (%) of the ten data types after 24-hrs of ETA model integration.

NOAA/NESDIS GOES and Polar Products and Services Web Sites

NOAA/NESDIS Offices and User Guides

Office of Systems Development (OSD)
http://www.osd.noaa.gov

Office of Satellite Data Processing and Distribution (OSDPD)
http://www.osdpd.noaa.gov

OSDPD Satellite Services Division
http://www.ssd.noaa.gov

OSDPD Information Processing Division
http://www.osdpd.noaa.gov/IPD/IPD.html

Satellite Active Archive (SAA)
http://www.saa.noaa.gov

Office of Research and Applications (ORA)
http://orbit-net.nesdis.noaa.gov/ora

Cooperative Institute for Meteorological Satellite Studies (CIMSS)
http://cimss.ssec.wisc.edu/

Cooperative Institute for Research in the Atmosphere (CIRA)
http://www.cira.colostate.edu

National Climatic Data Center
http://www.ncdc.noaa.gov

GOES I-M Databook
http://rsd.gsfc.nasa.gov/goes/text/goes.databook.html

GOES Products and Services Catalog
http://orbit35i.nesdis.noaa.gov/arad/fpdt/goescat/index.html

NOAA-KLM User's Guide
http://www2.ncdc.noaa.gov/docs/klm

Satellite Product Overview Display (SATPROD)
http://osdacces.nesdis.noaa.gov:8081/satprod

Products and Services

Aerosols

POES Aerosol Products
http://www.osdpd.noaa.gov/PSB/EPS/Aerosol/Aerosol.html

ASOS Cloud Products

GOES ASOS Satellite Cloud Products
http://orbit-net.nesdis.noaa.gov/goes/asos/

Atmospheric Moisture and Temperature (Soundings)

GOES Lifted Index, CAPE Index, Convective Inhibition, Total Precipitable Water, and Skew-T Plots
http://orbit-net.nesdis.noaa.gov/goes/soundings/

POES Temperature and Water Vapor
http://poes.nesdis.noaa.gov/atovs/

Polar Orbiting Satellite Sounding Evaluator (POSSE)
http://poes.nesdis.noaa.gov/posse/

Aviation

Fog/Low Cloud
http://orbit-net.nesdis.noaa.gov/arad/fpdt/fog.html

Aircraft Icing
http://orbit-net.nesdis.noaa.gov/arad/fpdt/icg.html

Turbulence
http://orbit-net.nesdis.noaa.gov/arad/fpdt/turb.html

Microbursts
http://orbit-net.nesdis.noaa.gov/arad/fpdt/mb.html

Volcanic Ash
http://orbit-net.nesdis.noaa.gov/arad/fpdt/volc.html

Operational Volcano Information
http://www.ssd.noaa.gov/VAAC/index.html

Biomass Burning

CIMSS Biomass Burning
http://cimss.ssec.wisc.edu/goes/burn/abba.html

CoastWatch

CoastWatch Home Page
http://coastwatch.noaa.gov

CoastWatch from OSDPD
http://www.osdpd.noaa.gov/PSB/EPS/CW/coastwatch.html

Derived Product Images

GOES Lifted Index, Cloud Top Pressure, Total Precipitable Water, Surface Skin Temperature
http://orbit-net.nesdis.noaa.gov/goes/sdpi/

CIMSS Realtime GOES Page
http://cimss.ssec.wisc.edu/goes/realtime/realtime.html

Global Energy and Water Cycle Experiment (GEWEX)

ORA GEWEX
http://orbit-net.nesdis.noaa.gov/goes/gcip/

Images

Geostationary Satellite Server
http://www.goes.noaa.gov

POES Image Products
http://www.osdpd.noaa.gov/PSB/IMAGES/IMAGES.html

Ozone

POES/SBUV Ozone Products
http://www.osdpd.noaa.gov/PSB/OZONE/OZONE.html

GOES Total Atmospheric Ozone
http://cimss.ssec.wisc.edu/goes/realtime/grtmain.html#ozone

POES/ATOVS Ozone Products
http://poes.nesdis.noaa.gov/atovs/data/ozone.html

Precipitation

Operational Precipitation Data
http://www.ssd.noaa.gov/PS/PCPN/index.html

Operational AMSU Precipitation Products
http://www.osdpd.noaa.gov/PSB/IMAGES/MSPPS_day2.html

AMSU Precipitation Products
http://orbit-net.nesdis.noaa.gov/arad2/MSPPS/index.html

DMSP SSM/I Precipitation Products
http://orbit-net.nesdis.noaa.gov/arad2/index.html

Radiation Budget

Radiation Budget Products
http://www.osdpd.noaa.gov/PSB/EPS/RB/RB.html

Sea Surface Temperature

POES SST
http://www.osdpd.noaa.gov/PSB/EPS/SST/SST.html

GOES SST
http://cimss.ssec.wisc.edu/goes/realtime/grtmain.html#gesst

Significant Event Imagery

Dust Storms, Fires, Flooding, Oil Spills, Snow Storms/Snow Cover, Tropical Events, and Volcanoes
http://www.osei.noaa.gov/

Snow and Ice

Operational AMSU Snow Cover and Sea Ice Products
http://www.osdpd.noaa.gov/PSB/IMAGES/MSPPS_day2.html

AMSU Snow Cover and Sea Ice Products
http://orbit-net.nesdis.noaa.gov/arad2/MSPPS/index.html

DMSP SSM/I Snow Cover and Sea Ice Products
http://orbit-net.nesdis.noaa.gov/arad2/index.html

Operational Snow and Ice Data
http://www.ssd.noaa.gov/PS/SNOW/index.html

Tropical Cyclones

Operational Tropical Cyclone Data
http://www.ssd.noaa.gov/PS/TROP/index.html

Vegetation Index

Global Vegetation Index User's Guide
http://www2.ncdc.noaa.gov/docs/gviug/index.htm

Vegetation Index Products from OSDPD
http://www.osdpd.noaa.gov/PSB/IMAGES/gvi.html

Vegetation Condition Index from ORA Land Surface Team
http://orbit-net.nesdis.noaa.gov/crad/sat/surf/html/lst_avhrr.html

Drought Monitoring
http://orbit-net.nesdis.noaa.gov/crad/sat/surf/vci/index.html

Winds

Operational High Density Satellite Derived Winds
http://www.ssd.noaa.gov/PS/WIND/hdw-table.html

Ocean Surface Winds
http://manati.wwb.noaa.gov/doc/oceanwinds1.html

High Density Derived Winds
http://orbit-net.nesdis.noaa.gov/goes/winds/

Tropical Cyclone Winds and Analyses
http://cimss.ssec.wisc.edu/tropic/tropic.html

Satellite Derived Motion Vectors
http://cimss.ssec.wisc.edu/goes/satwind/satwind.html

MODIS
http://www.osdpd.noaa.gov/MODIS/
http://www.osdpd.noaa.gov/MODIS/CONUS/index_CONUS.html

Search and Rescue
http://www.sarsat.noaa.gov

Data Collection System

ARGOS DCS
http://noaasis.noaa.gov/ARGOS

GOES DCS
http://noaasis.noaa.gov/DCS